

**LARGE EDDY SIMULATION OF MIXED CONVECTION IN A
VERTICAL SLOT AND GEOMETRICAL STATISTICS OF
WALL-BOUNDED THERMAL FLOW**

A Thesis Submitted to
the College of Graduate Studies and Research
in Partial Fulfillment of the Requirements
for the Degree of Doctor of Philosophy
in the Department of Mechanical Engineering
University of Saskatchewan
Saskatoon, Saskatchewan

by

Jing Yin

Permission to Use

In presenting this thesis in partial fulfillment of the requirements for a Post-graduate degree from the University of Saskatchewan, I agree that the Libraries of this University may make it freely available for inspection. I further agree that permission for copying of this thesis in any manner, in whole or in part, for scholarly purposes may be granted by the professor or professors who supervised my thesis work or, in their absence, by the Head of the Department or the Dean of the College in which my thesis work was done. It is understood that any copying or publication or use of this thesis or parts thereof for financial gain shall not be allowed without my written permission. It is also understood that due recognition shall be given to me and to the University of Saskatchewan in any scholarly use which may be made of any material in my thesis.

Requests for permission to copy or to make other use of material in this thesis in whole or part should be addressed to:

Head of the Department of Mechanical Engineering
University of Saskatchewan
Saskatoon, Saskatchewan, Canada
S7N 5A9

Abstract

Buoyant flows are characterized with unsteady large-scale structures and thus time-dependent large eddy simulation (LES) is generally favored. In this dissertation, to further explore LES for buoyant flow, an LES code based on a collocated grid system is first developed. A multigrid solver using a control strategy is developed for the pressure Poisson equations. The control strategy significantly accelerated the convergence rate. A temperature solver using a fourth-order Runge-Kutta approach is also developed. The LES code is extensively tested before it is applied. Although the collocated grid system will introduce conservation errors, in tests of a steady lid-driven cavity flow and transient start-up flow, the effect of the non-conservation of the collocated grid system was not significant.

In LES, the effect of SGS scales is represented by SGS models. A novel dynamic nonlinear model (DNM) for SGS stress is tested using isothermal channel flow at $Re_\tau = 395$. The kinetic energy dissipation and geometrical characteristics of the resolved scale and SGS scale with respect to the DNM are investigated. In general, the DNM is reliable and has relatively realistic geometrical properties in comparison with the conventional dynamic model in the present study. In contrast to a pure advecting velocity field, a scalar (temperature) field displays very different characteristics. The modelling of SGS heat flux has not been as extensively studied as that of SGS stress partly due to the complexity of the scalar transport. In this dissertation, LES for a turbulent combined forced and natural convection is studied. The DNM model and a nonlinear dynamic tensor diffusivity model (DTDM-HF) are applied for SGS stress and heat flux, respectively. The combined effect of the nonlinear models is compared to that of linear models. Notable differences between the nonlinear and linear SGS models are observed at the subgrid-scale level. At the resolved scale, the difference is smaller but relatively more distinguishable in terms of quantities related to the temperature field.

Finally, the geometrical properties of the resolved velocity and temperature fields of the thermal flow are investigated based on the LES prediction. Some universal geometrical patterns have been reproduced, e.g. the positively skewed resolved

enstrophy generation and the alignment between the vorticity and vortex stretching vectors. The present research demonstrates that LES is an effective tool for the study of the geometrical properties of a turbulent flow at the resolved-scales. The wall imposed anisotropy on the flow structures and orientation of the SGS heat flux vector are also specifically examined. In contrast to the dynamic eddy diffusivity model, the DTDM-HF successfully predicts the near-wall physics and demonstrates a non-alignment pattern between the SGS heat flux and temperature gradient vector.

Acknowledgements

I would like to express my great appreciation to my supervisor, Professor Donald J. Bergstrom, for his support and insightful guidance in my research, and also for his generous help in the non-academic area which greatly encouraged me in a foreign country. My thanks also go to my committee members, Professor J. D. Bugg, Professor R. Sumner, Professor D.A.Torvi, and Professor R. Evitts for their invaluable advice and help on my research.

Since I started my graduate study, many students have played an important role in my research work. I would like to specially thank Bingchen Wang for many fruitful discussions. I would also like to thank Franklin Krampa-Morlu, Olajide G Akinlade and Philip LePoudre for all the academic discussion and happy time working with them.

Finally, I would like to express my deep love and appreciation to my husband, my parents, my sister and brother-in-law, for their lifetime, unconditional love, care, support and encouragement.

Dedicated to my daughter
April Yu-Shan Li

Table of Contents

Permission to Use	i
Abstract	ii
Acknowledgements	iv
Dedication	v
Table of Contents	vi
List of Tables	x
List of Figures	xi
Nomenclature	xvii
1 Introduction	1
1.1 Motivation	1
1.2 Subgrid-scale Modelling in LES	3
1.3 Assessment of instantaneous structures: Turbulence Geometrical Statistics	6
1.4 Objectives of the Dissertation	9
1.5 Outline of the Dissertation	10

2	Filtered Equations and SGS Models	12
2.1	The Filtering Operation	12
2.2	Filtered Governing Equations for LES	13
2.3	SGS Stress Modelling	14
2.3.1	Dynamic Smagorinsky Model	15
2.3.2	Scale Similarity and Mixed Model	18
2.3.3	Dynamic Nonlinear Model	20
2.4	SGS Heat Flux Modelling	21
2.4.1	Dynamic Eddy Diffusivity Model	22
2.4.2	Dynamic Tensor Diffusivity Model	24
2.4.3	Dynamic Mixed Model	25
2.5	Summary	27
3	Numerical Algorithm and Test Problems	29
3.1	Numerical Algorithm for LES	29
3.2	Multigrid Solver Using a Control Strategy	32
3.2.1	Formation of the Coarse-grid Equations	33
3.2.2	Implementation of Multigrid Method	35
3.2.3	Performance of Multigrid Method Using a Control Strategy	36
3.3	Kinetic Energy Conservation	38
3.3.1	Conservation Properties of Collocated Grid Systems	39
3.3.2	Numerical Tests on Kinetic Energy Conservation	42
3.4	Test Problems	44
3.4.1	Lid Driven Cavity Flow	44
3.4.1.1	Steady Laminar Flow ($Re_D = 400$)	45

3.4.1.2	Start-up LDC Flow ($Re_D = 1000$)	47
3.4.2	Turbulent Channel Flow at $Re_\tau = 180$	49
3.4.2.1	Governing Equations for the Large-scale Field	50
3.4.2.2	Analysis of Results	50
3.5	Summary	53
4	LES of Channel Flow at $Re_\tau = 395$ and Investigation of the Dynamic Nonlinear SGS Stress Model	55
4.1	Introduction	55
4.2	Basic Concepts Related to Turbulence Geometrical Statistics	57
4.3	SGS Stress Modelling	61
4.4	Numerical Method and Flow Configuration	62
4.5	Analysis of Results	63
4.5.1	Resolved Mean and Fluctuation Properties	64
4.5.2	SGS Kinetic Energy Dissipation	66
4.5.3	Geometrical Properties of the Resolved Strain Rate and SGS Stress Tensor	68
4.5.4	Relations between the State Parameters S^* and S_τ^* and SGS Dissipation Rate	71
4.6	Summary	74
5	LES of Combined Forced and Natural Convection in a Vertical Plane Channel using Different SGS Models	76
5.1	Introduction	76
5.2	Governing Equations and SGS Models	77
5.3	Physical Model and Numerical Method	78

5.4	Analysis of Results	80
5.4.1	Mean Resolved Temperature and Velocity Profiles	81
5.4.2	Resolved Shear Stresses and Heat Fluxes	82
5.4.3	Velocity and Temperature Fluctuations	87
5.4.4	SGS Effects	88
5.5	Summary	89
6	Geometrical Properties of the Resolved-Scale Velocity and Temperature Fields of Buoyant Channel Flow	91
6.1	Introduction	91
6.2	Physical Model and Numerical method	92
6.3	Analysis of Results	93
6.3.1	Structural Configurations of Local Fluid Element Deformation	93
6.3.2	Resolved Enstrophy Generation and Helicity	95
6.3.3	Attitude of the Resolved Vorticity Vector with Respect to the Eigenframe of the Resolved Strain Rate Tensor	98
6.3.4	Attitude of the Resolved Temperature Gradient Vector with Respect to the Eigenframe of the Resolved Strain Rate Tensor	105
6.3.5	Orientation of the SGS Heat Flux Vector \mathbf{h}	109
6.4	Summary	112
7	Conclusions and Future Work	114
7.1	Summary of the Dissertation	114
7.2	Contributions of the Dissertation	115
7.3	Future Studies	121
	References	123

List of Tables

3.1	Number of iterations and computing time to reduce the residuals by four orders of magnitude	38
3.2	Conservation properties of analytical and discrete equations	42
3.3	Mass residuals and residuals of the pressure field	45
3.4	Peak values for 3-D LDC flow at $Re_D = 400$	47
3.5	Peak values for start-up LDC flow at $Re_D = 1000$	48
3.6	Peak values of channel flow at $Re_\tau = 180$	52
5.1	Physical quantities of the flow	81

List of Figures

3.1	A 2-dimensional sketch of a typical control volume for a collocated grid system.	30
3.2	Coarse grid formed from assembly of 1×2 blocks	33
3.3	V cycle	36
3.4	Implementation of the control strategy	36
3.5	Convergence histories on the finest grid before update of the coefficients	38
3.6	A 1-D uniform discrete system.	41
3.7	Error of the average kinetic energy.	44
3.8	Geometry and boundary conditions of LDC flow	45
3.9	Streamlines on the $x_1 - x_3$ plane at $x_2/D = 0.5$ using grid size $48 \times 48 \times 48$ ($Re_D = 400$)	46
3.10	Velocity vectors of the $x_1 - x_3$ plane at $x_2/D = 0.5$ using grid size $48 \times 48 \times 48$ ($Re_D = 400$)	46
3.11	Velocity vectors of the $x_2 - x_3$ plane at $x_1/D = 0.5$ using grid size $48 \times 48 \times 48$ ($Re_D = 400$)	46
3.12	Profiles of velocity components on the central lines of the cavity ($Re_D = 400$).	47
3.13	Profiles of velocity components on the central lines of the cavity at $t = 4$ ($Re_D = 1000$).	49
3.14	Computational domain and coordinate system ($Re_\tau = 180$).	50
3.15	Mean velocity profile using wall coordinates ($Re_\tau = 180$).	51

3.16	Resolved velocity fluctuations in wall coordinates: (a) streamwise; (b) wall-normal; (c) spanwise. ($Re_\tau = 180$).	51
3.17	Resolved Reynolds shear stress distribution in wall-normal direction: (a) for half-channel (b) in wall coordinates ($Re_\tau = 180$).	52
3.18	Non-dimensional shear stress distribution across the channel ($Re_\tau = 180$).	52
4.1	Computational domain and coordinate system ($Re_\tau = 395$).	62
4.2	Mean velocity profile using wall coordinates ($Re_\tau = 395$).	64
4.3	Resolved velocity fluctuations in wall coordinates: (a) streamwise; (b) wall-normal; (c) spanwise. ($Re_\tau = 395$).	65
4.4	Resolved Reynolds shear stress distribution in wall-normal direction ($Re_\tau = 395$).	66
4.5	Instantaneous velocity vectors and streamwise vorticity contour in the spanwise plane ($x_2 - x_3$) across the channel center ($Re_\tau = 395$). . . .	66
4.6	Instantaneous SGS dissipation of TKE normalized by u_τ^4/ν in a plane parallel to the wall at $y^+ = 24.4$ ($Re_\tau = 395$).	67
4.7	Averaged SGS dissipation rate normalized by u_τ^4/ν in wall coordinate ($Re_\tau = 395$).	67
4.8	PDF of the nondimensional state parameters at the channel center (a) S^* of resolved strain rate tensor \bar{S}_{ij} ; (b) S_τ^* of SGS shear stress $-\tau_{ij}$ ($Re_\tau = 395$).	69
4.9	PDF of the nondimensional state parameters in the buffer layer ($x_2^+ = 24.4$) (a) S^* of resolved strain rate tensor \bar{S}_{ij} ; (b) S_τ^* of SGS shear stress $-\tau_{ij}$ ($Re_\tau = 395$).	70
4.10	PDF of the nondimensional state parameters in the viscous sublayer ($x_2^+ = 3.9$) (a) S^* of resolved strain rate tensor \bar{S}_{ij} ; (b) S_τ^* of SGS shear stress $-\tau_{ij}$ ($Re_\tau = 395$).	70

4.11	JPDF of the nondimensional status parameter S^* and S_τ^* at the channel center ($Re_\tau = 395$).	71
4.12	JPDF of S^* and the normalized SGS dissipation at the channel center using the linear DM_L ($Re_\tau = 395$).	71
4.13	JPDF of S^* and the normalized SGS dissipation at the channel center using the nonlinear DNM ($Re_\tau = 395$).	72
4.14	JPDF of S_τ^* and the normalized SGS dissipation at the channel center using the nonlinear DNM ($Re_\tau = 395$).	73
4.15	Experimental measurement of the JPDF of S^* and S_τ^* with SGS dissipation (by Tao <i>et. al.</i> , 2002, for duct flow).	73
4.16	JPDF of S^* and the normalized SGS dissipation in the buffer layer using the nonlinear DNM ($Re_\tau = 395$).	73
4.17	JPDF of S_τ^* and the normalized SGS dissipation in the buffer layer using the nonlinear DNM ($Re_\tau = 395$).	73
5.1	Illustration of the physical domain of the combined forced and natural convective channel flow.	79
5.2	Mean resolved velocity and temperature profiles across the channel: (a) non-dimensional mean streamwise velocity $\langle \bar{u}_1 \rangle / u_\tau^a$; (b) non-dimensional mean temperature $\frac{\langle \bar{\theta} \rangle - \theta_{wc}}{\theta_{wh} - \theta_{wc}}$. Solid line: DM&DEDM-HF; dash line: DNM&DTDM-HF.	82
5.3	Mean resolved velocity and temperature profiles across the channel displayed using wall coordinates: (a) velocity; (b) temperature. Solid line: DM&DEDM-HF; dash line: DNM&DTDM-HF.	82
5.4	Instantaneous velocity vectors and temperature contour in a central transverse plane predicted by the set of dynamic nonlinear SGS models ($Gr = 9.6 \times 10^5$ and $Re_\tau^a = 150$). The temperature is non-dimensionalized as $\frac{\langle \bar{\theta} \rangle - \theta_{wc}}{\theta_{wh} - \theta_{wc}}$	82

5.5	Non-dimensional shear stresses predicted by the two sets of linear and nonlinear SGS models. Solid line: DM&DEDM-HF; dash line: DNM&DTDM-HF.	83
5.6	Resolved Reynolds shear stress shown using wall coordinates. Solid line: DM&DEDM-HF; dash line: DNM&DTDM-HF.	84
5.7	Non-dimensional wall-normal heat fluxes predicted by the two sets of linear and nonlinear SGS models ($Gr = 9.6 \times 10^5$ and $Re_\tau^a = 150$). Dash dot line: DNS ($Gr = 0$, Davidson <i>et al.</i> [1]); symbols (\bullet and \circ): DNS ($Gr = 7.68 \times 10^6$, Davidson <i>et al.</i> [1]); solid line: DM&DEDM-HF; dash line: DNM&DTDM-HF.	84
5.8	Resolved turbulent heat fluxes shown using wall coordinates: (a) streamwise; (b) wall-normal. Solid line: DM&DEDM-HF; dash line: DNM&DTDM-HF.	85
5.9	Resolved turbulent heat fluxes shown using logarithmic wall coordinates ($Gr = 9.6 \times 10^5$ and $Re_\tau^a = 150$): (a) streamwise component; (b) wall-normal component.	86
5.10	Effective eddy diffusivity for the wall-normal turbulent heat flux ($Gr = 9.6 \times 10^5$ and $Re_\tau^a = 150$).	86
5.11	Resolved velocity fluctuations in wall coordinates: (a) streamwise; (b) wall-normal; (c) spanwise. Solid line: DM&DEDM-HF; dash line: DNM&DTDM-HF.	87
5.12	Resolved temperature fluctuations in wall coordinates. Solid line: DM&DEDM-HF; dash line: DNM&DTDM-HF.	88
5.13	SGS shear stress produced by SGS models ($Gr = 9.6 \times 10^5$ and $Re_\tau^a = 150$). Solid line: DM&DEDM-HF; dash line: DNM&DTDM-HF. . . .	88
5.14	SGS heat fluxes produced by SGS models ($Gr = 9.6 \times 10^5$ and $Re_\tau^a = 150$).	89
6.1	PDF of S^* and β^* in the logarithmic layer predicted using DNM&DTDM-HF.	94

6.2	PDF of S^* for three different flow regimes predicted using the DNM&DTDM-HF.	95
6.3	PDF of the resolved normalized enstrophy generation predicted using the DNM&DTDM-HF.	96
6.4	PDF of the resolved-scale relative helicity predicted using the DNM&DTDM-HF.	97
6.5	Illustration of the random relative orientation between two unit vectors \mathbf{e} and $\bar{\boldsymbol{\omega}}^o$ in the 2-D and 3-D sample spaces.	99
6.6	PDF $P_\Psi(\psi)$ of the alignment angle between $\bar{\boldsymbol{\omega}}$ and $\mathbf{e}_{S\beta}$ in logarithmic layer ($x_2^+ = 80$) predicted using the DNM&DTDM-HF.	100
6.7	PDF of the alignment angle between $\bar{\boldsymbol{\omega}}$ and $\mathbf{e}_{S\alpha}$ predicted using the DNM&DTDM-HF.	101
6.8	PDF of the alignment angle between $\bar{\boldsymbol{\omega}}$ and $\mathbf{e}_{S\beta}$ predicted using the DNM&DTDM-HF.	102
6.9	PDF of the alignment angle between $\bar{\boldsymbol{\omega}}$ and $\mathbf{e}_{S\gamma}$ predicted using the DNM&DTDM-HF.	102
6.10	Geometrical description of the attitude of $\bar{\boldsymbol{\omega}}^o$ with respect to the eigen-frame of \bar{S}_{ij}	103
6.11	JPDF(θ, ϕ) for describing the attitude of $\bar{\boldsymbol{\omega}}$ with respect to the eigen-frame of \bar{S}_{ij} in the hot wall region predicted using the DNM&DTDM-HF.	105
6.12	PDFs of the alignment angle between the resolved temperature gradient $\nabla \bar{T}$ and $\mathbf{e}_{S\alpha}$ predicted using two sets of SGS models: DM&DEDM-HF and DNM&DTDM-HF.	106
6.13	PDFs of the alignment angle between the resolved temperature gradient $\nabla \bar{T}$ and $\mathbf{e}_{S\beta}$ predicted using two sets of SGS models: DM&DEDM-HF and DNM&DTDM-HF.	106

6.14	PDFs of the alignment angle between the resolved temperature gradient $\nabla\bar{T}$ and $\mathbf{e}_{S\gamma}$ predicted using two sets of SGS models: DM&DEDM-HF and DNM&DTDM-HF.	107
6.15	JPDF(θ, ϕ) for describing the attitude of $\nabla\bar{T}$ with respect to the eigenframe of \bar{S}_{ij} in the hot wall region predicted using the DNM&DTDM-HF.	108
6.16	PDFs of the alignment angle between the SGS heat flux \mathbf{h} and the resolved temperature gradient $\nabla\bar{T}$	110
6.17	JPDF(θ, ϕ) for describing the attitude of \mathbf{h} with respect to the eigenframe of \bar{S}_{ij} in the hot wall region predicted using the DNM&DTDM-HF.	111

Nomenclature

English Symbols

a	coefficients of the pressure correction equation; or parameter of a hyperbolic tangent function
a_j	base vectors
a_j^E, a_j^G	base vectors for test grid scale mixed model
b	source term of the pressure correction equation
b_j	base vectors
b_j^E, b_j^G	base vectors for sub-grid scale mixed model
b_m	net mass flux
c_P	specific heat at constant pressure
C_1, C_2	coefficients of the dynamic mixed SGS stress model
C_e	coefficient of the dynamic mixed model
C_f	friction coefficient: $2\tau_w / \rho U_D^2$
C_g	coefficient of the dynamic mixed model
C_{ij}	cross stress tensor: $\overline{u'_i \bar{u}_j} + \overline{\bar{u}_i u'_j}$
C_W, C_N	coefficients of the dynamic nonlinear SGS stress model
C_s	coefficient of the Smagorinsky model
C_S	coefficient of the dynamic Smagorinsky model; or coefficient of dynamic nonlinear SGS stress model
C_{SIM}, C_{SIM}^L	coefficient of the scale similarity SGS stress model
C_θ	coefficient of the dynamic eddy diffusivity model
C_θ^G	coefficient of the nonlinear gradient model
C_θ^T	coefficient of the dynamic tensor diffusivity model for SGS heat flux
C_θ^{SIM}	coefficient of the scale similarity SGS heat flux model

D	distance from the wall to the maximum streamwise velocity location; or width of cavity
e_{ij}	local error tensor function
E	local error tensor
F	a function: or face velocity
g_i	gravitational acceleration vector: $[-g, 0, 0]^T$
Gr	Grashof number: $g\beta\Delta\theta(2\delta)^3/\nu^2$
h_j	grid level SGS heat flux vector
h_n	relative helicity: $\cos\Theta(\mathbf{u}, \boldsymbol{\omega})$
H	helicity (density): $u_i\omega_i$
H_i	combination of the convection-diffusion terms of the N-S equations
H_j	test-grid level SGS heat flux vector
$G(\mathbf{x}, \mathbf{y})$	filter kernel function
K	turbulence kinetic energy; $(u_i u_i)/2$
i	index: $i = 1, 2, \dots$
j	index: $j = 1, 2, \dots$
L_{ij}	Leonard stress: $\overline{\bar{u}_i \bar{u}_j} - \bar{u}_i \bar{u}_j$
\mathcal{L}_{ij}	resolved Leonard-type stress: $\widetilde{\bar{u}_i \bar{u}_j} - \tilde{\bar{u}}_i \tilde{\bar{u}}_j$
\mathcal{L}_j	vector: $\widetilde{\bar{u}_j \bar{\theta}} - \tilde{\bar{u}}_j \tilde{\bar{\theta}}$
M_{ij}	differential tensorial function: $\alpha_{ij} - \tilde{\beta}_{ij}$
M	dimension of discretized domain
M_j	differential vector: $a_j - \tilde{b}_j$
n	index: $n = 1, 2, \dots$; or the n th order
N	dimension of discretized domain
N_{ij}	differential tensorial function: $\zeta_{ij} - \tilde{\eta}_{ij}$
Nu	Nusselt number: $2q_w/[\lambda(\theta_D - \theta_w)/D]$
p	resolved fluctuating pressure
p'	pressure correction
P	probability (function); or mean pressure
\mathcal{P}_r	SGS TKE dissipation rate: $-\tau_{ij}\bar{S}_{ij}$
q_w	wall heat flux

Q	local error density function
R_{ij}	SGS Reynolds stress: $\overline{u'_i u'_j}$
Re_b	Reynolds number based on bulk velocity: $U_b \delta / \nu$
Re_D	Reynolds number based on cavity width: UD / ν
R_m	mass residual
$R_{p'}$	residual of pressure correction equations
Re_τ	Reynolds number: $u_\tau \cdot \delta / \nu$
Re_τ^a	Reynolds number: $u_\tau^a \cdot \delta / \nu$
s^*	nondimensional parameter of resolved strain rate tensor
s_τ^*	nondimensional parameter of SGS stress tensor
S_{ij}	strain rate tensor
\bar{S}_{ij}	resolved strain rate tensor: $(\partial \bar{u}_i / \partial x_j + \partial \bar{u}_j / \partial x_i) / 2$
$ \bar{S} $	norm of \bar{S}_{ij}
t	time
Δt	time step
T	average temperature
T_τ	wall friction temperature: $q_w / (\rho c_P u_\tau)$
T_{ij}	test-grid level SGS stress tensor
\mathcal{T}_{ij}	viscous shear stress: $\nu (\partial u_i / \partial x_j)$
u_i	velocity components: $i = 1, 2, 3$
u'_i	SGS velocity component: $u'_i = u_i - \bar{u}_i$
u_i^*	estimated velocity
\bar{u}_i''	residual velocity: $\bar{u}_i'' = \bar{u}_i - \langle \bar{u}_i \rangle$
u_i^+	nondimensional velocity component: $\langle u_i \rangle / u_\tau$
u_τ	wall friction velocity: $\sqrt{\tau_w / \rho}$
$u_\tau c$	cold wall friction velocity: $\sqrt{\tau_w c / \rho}$
$u_\tau h$	hot wall friction velocity: $\sqrt{\tau_w h / \rho}$
u_τ^a	average wall friction velocity: $(u_\tau h + u_\tau c) / 2$
$-\langle \bar{u}_1'' \bar{u}_2'' \rangle$	resolved Reynolds shear stress for LES of channel flow
U	constant lid velocity
U_b	bulk velocity across the channel: $\int_0^{2\delta} \langle \bar{u}_1 \rangle dx_2 / (2\delta)$
U_D	bulk averaged velocity over the distance D : $\int_0^D \langle \bar{u}_1 \rangle dx_2 / D$

V	computational domain
ΔV	control volume
\mathbf{w}	vortex stretching vector: $w_i = \omega_j S_{ij}$
W_{ij}	differential tensorial function: $\lambda_{ij} - \tilde{\gamma}_{ij}$
x_i	coordinates ($i = 1, 2, 3$)
Δx_i	grid size in the x_i direction
x_2^+	wall coordinate: $x_2 u_\tau / \nu$

Greek Symbols

α	molecular thermal diffusivity: $\lambda / (\rho c_P)$
α_{ij}	tensor: $2\tilde{\Delta}^2 \tilde{S} \tilde{S}_{ij}$
α_S	largest eigenvalue of resolved strain-rate tensor
α_{sgs}	SGS eddy thermal diffusivity
$\alpha_{-\tau}$	largest eigenvalue of SGS stress tensor
β	thermal expansion coefficient
β_{ij}	tensor: $2\bar{\Delta}^2 \bar{S} \bar{S}_{ij}$
β_S	intermediate eigenvalue of resolved strain-rate tensor
$\beta_{-\tau}$	intermediate eigenvalue of SGS stress tensor
β^*	nondimensional parameter
γ_{ij}	grid level constituent tensor: $2\bar{\Delta}^2 (\bar{S}_{ik} \bar{\Omega}_{kj} - \bar{\Omega}_{ik} \bar{S}_{kj})$
γ_S	smallest eigenvalue of resolved strain-rate tensor
$\gamma_{-\tau}$	smallest eigenvalue of SGS stress tensor
Γ_2	effective eddy duffusivity
δ	half channel width
δ_{ij}	Kronecker delta
$\delta_D(\mathbf{x}, \mathbf{y})$	Dirac delta function
δ_{ij}	Kronecker delta
Δ	mesh or filter size

ϵ_K	conservation error
\mathbf{e}	orthonormal eigenvectors
ε_{ijk}	Levi-Civita permutation symbol
ε_r	resolved viscous dissipation rate: $2\nu\bar{S}_{ij}\bar{S}_{ij}$
$\mathcal{E}_{ij}(\mathbf{x}, \mathbf{x}_0)$	local error tensor, a function of \mathbf{x} for a specific location \mathbf{x}_0
ζ_{ij}	test-grid level constituent tensor: $4\tilde{\Delta}^2(\tilde{S}_{ik}\tilde{S}_{kj} - \frac{1}{3}\tilde{S}_{mn}\tilde{S}_{nm}\delta_{ij})$
η_{ij}	grid level constituent tensor: $4\bar{\Delta}^2(\bar{S}_{ik}\bar{S}_{kj} - \frac{1}{3}\bar{S}_{mn}\bar{S}_{nm}\delta_{ij})$
θ	temperature
Θ_r	arithmetic mean temperature: $\int_0^{2\delta} \langle \bar{\theta} \rangle dx_2 / (2\delta)$
Θ	angle
λ	eigenvalue
λ_{ij}	test-grid level constituent tensor: $2\tilde{\Delta}^2(\tilde{S}_{ik}\tilde{\Omega}_{kj} - \tilde{\Omega}_{ik}\tilde{S}_{kj})$
μ	coefficient of viscosity
ν	kinematic viscosity
ν_{sgs}	subgrid-scale viscosity
ν_T	eddy viscosity
Π_k	normalized TKE dissipation rate: $\mathcal{P}_r/(u_\tau^4/\nu)$
ρ	density
σ	enstrophy generation: $\boldsymbol{\omega} \cdot \mathbf{w}$
σ_n	normalized enstrophy generation: $\cos \Theta(\boldsymbol{\omega}, \mathbf{w})$
σ_{SGS}	SGS Prantdl number
τ	shear stress
τ_{ij}	grid level SGS stress
τ_w	wall friction stress
τ_{wc}	cold wall friction stress
τ_{wh}	hot wall friction stress
$\boldsymbol{\omega}$	vorticity vector: $\omega_i = \varepsilon_{ijk}\Omega_{kj}$
ω^2	enstrophy: $\omega_i\omega_i$
Ω_{ij}	rotation rate tensor
ψ	streamline function

Subscripts and Superscripts

$()_1$	streamwise component
$()_2$	wall-normal component
$()_3$	spanwise component
$()_b$	component at the back face of the control volume
$()_c$	cold wall properties
$()_e$	component at the east face of the control volume
$()_E$	component at the east neighbor node
$()_f$	component at the front face of the control volume
$()_F$	component at the front neighbor node
$()_h$	hot wall properties
$()_n$	component at the north face of the control volume
$()_N$	component at the north neighbor node
$()_P$	component at the central node
$()_{rms}$	root mean square
$()_S$	properties related to the strain rate tensor
$()_w$	component at the west face of the control volume; or wall properties
$()_{wc}$	cold wall properties
$()_{wh}$	hot wall properties
$()_W$	component at the west neighbor node
$()_{ij}$	tensor: $i, j = 1, 2, 3$
$()_i$	vector component: $i = 1, 2, 3$
$()_{,i}$	spatial derivative: $\partial()/\partial x_i$
$()_{i,j}$	spatial derivative: $\partial()_i/\partial x_j$
$()_{ij}^*$	tracefree form of a tensor
$()^{I,J}$	indices for a discrete location
$()^n$	result at the n -th time step
$()_\alpha$	component related to the largest eigenvalue
$()_\beta$	component related to the intermediate eigenvalue
$()_\gamma$	component related to the smallest eigenvalue

$(\dot{})$	time derivative: $\partial()/\partial t$
$\overline{()}$	grid level filter; or resolved quantity
$\widetilde{()}$	test-grid level filter
$()'$	SGS or temporal residual component
$()''$	residual component
$()^+$	wall coordinates; or forward scatter
$()^-$	backscatter
$\langle \rangle$	plane and time or spatially averaged quantity
$\langle \rangle_L$	local averaged quantity
$\langle \rangle_p$	plane averaged quantity

Abbreviations

1-D	One-Dimensional
2-D	Two-Dimensional
3-D	Three-Dimensional
CS	Control Strategy
CDS	Central Difference Scheme
CFD	Computational Fluid Dynamics
CPU	Central Processing Unit
DEDM-HF	Dynamic Eddy Diffusivity Model for SGS Heat Flux
DM	Dynamic Smagorinsky Model
DMM	Dynamic Mixed Model
DNM	Dynamic Nonlinear SGS stress Model
DNS	Direct Numerical Simulation
DTDM-HF	Dynamic Tensor Diffusivity Model for SGS Heat Flux
DTMM	Dynamic Two-Parameter Mixed Model
HF	Heat Flux
HPIV	Holographic Particle Image Velocimetry
JPDF	Joint Probability Density Function
LDC	Lid Driven Cavity Flow

LES	Large Eddy Simulation
LGS	Line Gausse-Seidel Iteration
LHS	Left Hand Side
NGM-HF	Nonlinear Gradient Model for SGS Heat Flux
NP	Neighbor Points
N-S	Navier-Stokes
PDF	Probability Density Function
PIV	Particle Image Velocimetry
PTD	Pure-Two-Dimensional
QTD	Quasi-Two-Dimensional
RANS	Reynolds Averaged Navier-Stokes method
RHS	Right Hand Side
SGS	Subgrid Scale
STS	subtest-grid Scale
SM	Smagorinsky SGS stress Model
TKE	Turbulence Kinetic Energy

Chapter 1

Introduction

1.1 Motivation

Purely forced convection is an isothermal flow driven by a pressure gradient. In non-isothermal cases, buoyancy forces due to density difference induced by temperature gradients also act as a driving force for fluid motion. The case when buoyancy is the only driving force is referred as natural convection. In many engineering and environmental applications, such as airflow in an air-conditioned room, heat exchangers, turbine blades, electronic cooling system, and nuclear reactors, the flow is neither pure forced nor natural convection but instead a combination of both regimes called mixed convection. Natural and forced convection can be combined in two different ways: the buoyancy and pressure forces act in the same direction which is called aiding flow, or they are in different directions which is called opposing flow. The impact of the buoyancy can be significantly different in the aiding and opposing flow regions. In aiding flow region, the shear stress, turbulence production and turbulent heat transfer are reduced compared to the forced convection. In contrast, the shear stress, turbulence production and turbulent heat transfer in opposing flow are enhanced due to the effect of the buoyancy force. Compared to forced convection, mixed convection is more complicated, because buoyancy can significantly alter the turbulence [1]. Therefore, thermal flows exhibit some specific features which are not encountered in isothermal flows including the following:

i) Multiple flow regimes may coexist in one flow domain. For example, it is common to find unsteady laminar circulation and transitional flow in a fully developed

turbulent flow at relatively high Reynolds number [2]. In contrast, low Reynolds number phenomena are usually encountered only near a wall for isothermal flows.

ii) Buoyancy exhibits the strongest effects in a very thin boundary layer along the wall, where many properties of practical importance vary steeply and are difficult to measure or estimate.

iii) Buoyant flows are characterized by well-organized, 3-dimensional, unsteady large-scale structures, which are frequently noticed even in a steady situation. Due to these large-scale structures, turbulent diffusion may occur in a counter-gradient direction, which is opposite to standard gradient-diffusion behaviour [3].

Given such specific features as these, buoyant flows are relatively more difficult to predict. Among the three major computational methods, i.e. direct numerical simulation (DNS), Reynolds-averaged Navier-Stokes (RANS) and large eddy simulation (LES), RANS is the most widely used method for engineering flows since the full spectrum of turbulence is modeled and thus fewer computational resources are required. However, although RANS have been successfully applied for a variety of engineering flows, it often fails for turbulent buoyant flows. One typical example is related to simulation of a prototypical thermal flow in a vertical channel with differentially heated sidewalls. In such a flow, the main temperature gradient is horizontal and perpendicular to the buoyancy. It is well known that a RANS calculation with the widely used linear isotropic eddy diffusivity model will fail to reproduce the streamwise turbulent heat flux of the flow, since the eddy diffusivity model requires that the turbulent heat flux be aligned to the mean temperature gradient which is zero in the streamwise direction. In general, the standard $k - \varepsilon$ and traditional eddy-viscosity models for a RANS simulation are based on the equilibrium assumption and use only a single time or length scale, and thus cannot account for nonequilibrium effects and multi-scale phenomena in buoyant flows. On the other hand, second-moment closures in RANS contain a large number of terms that need to be modeled. Therefore, to reproduce buoyant flows, and especially to capture the unsteady large-scale structures, a time-dependent simulation, such as LES or DNS, is generally required.

1.2 Subgrid-scale Modelling in LES

DNS is the most straightforward approach and solves all scales of turbulence. However, its application is limited to low Reynolds number flows due to the excessive computational resources required. In RANS, all scales of turbulence are modeled which generally eliminates the details of the turbulence in both space and time. In comparison, LES is a technique standing between DNS and RANS. In LES, the flow field is separated into large- and small-scale motions. The contribution of the large energy-containing scales are resolved exactly, and only the effects of the small scales of turbulence are modeled. LES is appropriate to capture the unsteady effect of turbulence since only fluctuations smaller than the cutoff scale are smoothed out using a local, spatial averaging filter. Since the cutoff scales are expected to be problem independent (i.e. independent of the large-scales and of a universal character), the filter size, which is usually equal to the grid size, should be located in the inertial sub-range in the kinetic energy spectrum where turbulence is statistically in equilibrium and universal in character.

In LES of thermal flows, additional terms, i.e. SGS stress and heat flux terms, are present in the LES transport equations due to the filtering operation. These SGS terms represent the effect of the cutoff scales of motion and need to be modeled. The first SGS stress model was derived by Smagorinsky [4], in which the SGS stress tensor is related to the filtered rate of strain. For homogeneous, isotropic turbulence, Lilly [5] showed that the coefficient of the Smagorinsky model has a simple, universal value of 0.17. However, it was soon found that this value of the constant was too dissipative and the coefficient should be case dependent. In 1991, Germano *et al.* [6] suggested a Smagorinsky-type Dynamic Model (DM) using a dynamic procedure to determine the local value of the coefficient. The widely used DM [6, 7] is known for its capability of self-calibration, general balancing of the TKE between the resolved and unresolved scales, and being free from any empirical constants and artificial near-wall damping functions. However, the DM originates from the Smagorinsky constitutive relation which is based on the molecular transport analogy and requires the principal axes of the negative SGS stress tensor to be strictly aligned with those of the filtered strain rate tensor. This rigid and overly simplified geometrical relation between the

stress and strain rate tensors is not realistic in terms of physics and can lead to other problems. For instance, simulations based on the DM can be numerically unstable due to excessive backscatter of TKE from the subgrid to resolved scales if the model coefficient is not properly bounded [8]. A plane-averaging scheme is often applied for bounding the coefficient [6,7]. However, to apply the plane-averaging scheme, the flow has to be homogeneous in one or two directions. Since the above mentioned deficiencies of the DM stem from its constitutive relation, improved dynamic SGS stress models often consider non-Smagorinsky type constitutive relations. One approach to achieve this goal is to use nonlinear tensor functions to build the constitutive relation. A dynamic nonlinear model (DNM) was proposed by Wang and Bergstrom [9] based on the three-parameter quadratic constitutive relation of Speziale and Gatski [10,11]. The DNM is observed to have obvious advantages in comparison with the conventional DM: it significantly increases the numerical stability, i.e., its coefficients are calculated dynamically during simulation without any artificially ‘tuning’; it allows for a more realistic geometrical representation of the SGS stress tensor [12] and provides more degrees of freedom for reflecting both forward and backward scatter of TKE between the resolved and unresolved scales. Other nonlinear SGS stress models can also be found in the recent works of Lund and Novikov [13], Wong [14], Kosović [15], Winckelmans *et al.* [16] and Liu *et al.* [17].

The closure of the filtered scalar (temperature) transport equation requires modelling of the SGS scalar (heat) flux. In contrast to the velocity field, a scalar field displays different characteristics. In a comprehensive review of scalar transport, Warhaft [18] addressed both large- and small-scale behaviour and demonstrated that the large- and small-scales in a scalar field are strongly coupled and the traditional cascade picture, which promotes the notion of universality of the small scale motions, is a crude representation. Unlike the velocity field, even at high Reynolds number, the scalar field remains anisotropic at the dissipation and inertial scales in the presence of a main scalar gradient. Kang and Meneveau [19] also demonstrated that in the presence of a scalar gradient, whereas the TKE dissipation tensor tends towards isotropy at small scales, the SGS scalar-variance dissipation remains anisotropic independent of filter scale. The promise of LES strongly relies on the assumption of small-scale universality and isotropy, i.e. the statistics of the small-scale turbulence

are independent of forcing and boundary conditions. This anisotropic behavior of a scalar field presents a significant challenge for LES modelling: not only the mean scalar-variance dissipation rate, but also the geometrical properties of the SGS scalar field should be reproduced by a SGS model. Furthermore, the performance of SGS scalar flux models may be case dependent. Partly due to the complexity of the physics of scalar transport, modelling of the SGS heat (scalar) flux has not been as extensively studied and developed as that of the SGS stress. The concept of a dynamic SGS eddy diffusivity model (DEDM) for the SGS heat flux was initially introduced by Moin *et al.* [20] in 1991 immediately after the proposal of the dynamic procedure by Germano *et al.* [6], in which the SGS heat flux vector is made proportional to the negative resolved temperature gradient based on the analogy to the molecular heat diffusion/conduction process governed by Fourier’s law. Since the transport of the SGS thermal energy due to unresolved turbulent motions is fundamentally different and much more complex than that due to a molecular heat conduction process, the predictions of the conventional DEDM [20] are much more isotropic than the actual phenomenon [19]. Nevertheless, the DEDM is still the most popular model in the literature and has been applied for predicting some of the mean properties of turbulent scalar fields [21–29].

In order to improve the performance of the SGS heat flux model in terms of its physical and geometrical representation of the SGS heat flux vector, some innovative modelling approaches have been proposed in the literature. Using a statistical approach, Yoshizawa [30] derived a SGS heat flux model based on the gravitational acceleration vector and resolved temperature and velocity gradients (It should be noted that Yoshizawa’s model does not rely on the dynamic modelling approach, which is different than the SGS heat flux models to be discussed below). By applying the Taylor expansion to the classic scale-similarity model introduced by Bardina *et al.* in 1980 [31], Leonard [32] suggested a gradient SGS heat flux model. However, it was soon found that the scale-similarity-type models do not dissipate enough energy and typically lead to inaccurate results. Since the eddy diffusivity model with a positive coefficient is a purely dissipative model, mixed models which combine the former two models were introduced into the LES community. Salvetti and Banerjee [33] introduced a dynamic two-parameter mixed SGS heat flux model, in which the coef-

ficients of the eddy diffusivity and scale-similarity term are determined dynamically. The model of Salvetti and Banerjee was an extension of the work of Zang *et al.* [34] on a dynamic mixed SGS stress model, and has been recently applied by Tyagi and Acharya [35] for studying heat transfer of rotating rib roughened square duct flow, and by Jaber and Colucci [36] for studying reacting and non-reacting turbulent flows using both the *a priori* and *a posteriori* LES methods^a. Based on a Taylor series analysis of the discrete filtering process related to the SGS heat flux term, Porté-Agel *et al.* [37, 38], and Kang and Meneveau [39] introduced a mixed model, which dynamically combines the linear eddy diffusivity SGS heat flux model with a gradient SGS heat flux model. This model has been applied for studying heat fluxes and dissipation in an atmospheric boundary layer and heated wind tunnel wake flow using the *a priori* LES approach. Peng and Davidson [40] proposed a dynamic tensor diffusivity model for representing the SGS heat flux and used it to predict a buoyancy driven channel flow. Their model takes into account the temperature gradients in all directions, and was able to sustain the streamwise SGS heat flux even when the streamwise temperature gradient is zero.

1.3 Assessment of instantaneous structures: Turbulence Geometrical Statistics

In the conventional approach within the LES community, turbulence is assessed in terms of properties obtained after temporal and spatial averaging, such as mean and fluctuating velocity and temperature fields, resolved and SGS shear stress and scalar flux profiles, etc. Although it is well known that turbulence is characterized by various internal organizations (coherent structures), the conventional analysis approach provides very poor information on the flow structures and dynamic interaction between them. In contrast, various geometrical alignments (relative orientation) between vectors composed of velocity gradients obtained using the methodology of turbulence geometrical statistics clearly point to the presence of the internal organizations. For

^aThe so-called *a priori* LES denotes filtered DNS in which LES quantities are obtained by imposing a range of filters on the DNS data. In contrast to the *a priori* LES, the analysis based on the LES prediction is specified as the *a posteriori* LES. The results of a *a posteriori* LES are affected by modelling and numerical errors.

example, there is a distinct difference between the alignment patterns of the resolved vorticity $\bar{\omega}$ and the eigenvectors λ_i of the strain rate tensor for a random Gaussian field and turbulent flows, e.g. the PDFs of $\cos(\bar{\omega}, \lambda_i)$ are flat for a random Gaussian field [41], while $\bar{\omega}$ tends to be aligned with the intermediate eigenvector of the strain rate tensor for turbulent flows. The PDF of enstrophy generation is also different: it is asymmetric and preferentially positive for real turbulent flows while it is symmetric for a random Gaussian field [41]. The above alignments not only manifest the existence of organization, but also reveal the dynamics of turbulence. For instance, the positiveness of the enstrophy generation indicates the prevalence of vortex stretching over vortex compressing in turbulence. Although internal organization in turbulent flows can also be observed individually by some visualization techniques, geometrical statistics provides more unambiguous information on such structures and thus is more appropriate for revealing the characteristics of the structures and physical process of turbulent flows. Furthermore, since most of the geometrical invariant quantities and relations, such as enstrophy generation, vortex stretching and compression, and alignments between various tensors and vectors [42–45], studied in turbulence geometrical statistics are frame invariant, i.e. they are independent of the reference system.

Due to the richness of the topic, in the following context, I only focus on reviewing the literature that is relevant to this research, viz., recent advances in applying LES for studying the geometrical properties of turbulent flow and scalar fields. Since the pioneering works of Vieillefosse [46], Pelz *et al.* [47], Ashurst *et al.* [48] and Kerr [49] in the 1980's, the methodology of turbulence geometrical statistics has been successfully introduced for studying turbulence structures and dynamics. However, previous approaches have primarily utilized DNS [47–53] and experimental [44, 45] approaches based on unfiltered turbulent flows. Recently, study of the statistical geometry of turbulence at the filtered- (or, resolved-) scale based on LES has become a relevant research topic. This is due to the evidence that many important physical phenomena (both local and global) of fluid flows can be observed and reproduced at a given filtered level, temporally and spatially. Tao *et al.* [54] analyzed the holographic particle image velocimetry (HPIV) measurements of a quasi-isotropic flow at the center of a square duct using the *a priori* LES approach, and observed that many geometrical alignment trends of the filtered turbulence agree with those of unfiltered

turbulence [48–53]. For example, Tao *et al.* [54] were able to reproduce the canonical preferential alignment pattern between the resolved vorticity vector ($\bar{\omega}$) and the eigenvector ($\mathbf{e}_{S\beta}$) corresponding to the intermediate eigenvalue of the resolved strain rate tensor in the context of LES. This specific alignment pattern has been noted in many studies ever since the seminal work of Ashurst *et al.* [48] and Kerr [49]. Following the study of Tao *et al.* [54], *a priori* LES investigations of the alignment patterns between the resolved vorticity vector, vortex stretching vector and eigenvectors of the resolved strain rate tensor have appeared in the literature including the recent works by Horiuti [55] and Borue and Orszag [56] who analyzed DNS data of isotropic flows, and by Higgins *et al.* [57] and Porté-Agel *et al.* [38] who analyzed experimental measurements of atmospheric boundary layer flows.

An important application of *a priori* LES studies is to provide physical insight for the *a posteriori* LES approach for numerical simulations in terms of the design of improved SGS modelling approaches and understanding of the mechanism of interactions between the resolved- and subgrid-scale (SGS) motions. In contrast to the above-mentioned *a priori* LES study of the geometrical properties of fluid tensors and vectors, the *a posteriori* LES approach has also been recently applied to this type of study, which includes the work of Fureby and Grinstein [58] who investigated the resolved-scale vorticity magnitude and vortex stretching rate using numerical simulations, and the works of Wang *et al.* [12, 59] who studied the geometrical property of the SGS stress tensor and resolved vorticity, and the near-wall anisotropic effect on vortex stretching patterns based on LES of turbulent Couette flow. In comparison with DNS, the study of turbulence geometrical statistics using an LES approach is beneficial in that it provides a reduction in the computational cost, and more importantly, the results of the analysis can potentially lead to the development of improved SGS modelling strategies. For example, the phenomenological discovery of Vieillefosse [46], Kerr [49], and Ashurst *et al.* [48] that $\bar{\omega}$ is preferentially aligned with $\mathbf{e}_{S\beta}$ has been recently used for construction of some innovative local geometrical structure-based SGS stress models for LES [60–62].

Closely coupled with the geometrical property of the fluid vectors and tensors, the geometrical characteristics of the scalar gradient has also been investigated based on the DNS approach over the past decade. A number of papers have been

published, for instance, Nomura and Elghobashi [63] studied turbulent mixing of an inhomogeneous passive scalar in the context of a nonpremixed reacting flow, Martín *et al.* [64] proposed a simplified stochastic equation for modelling the scalar gradient evolution process and compared their statistical results with the DNS data, and Boratav *et al.* [65] studied the alignment feature between the vorticity, scalar gradient and eigenframe of the strain rate tensor based on DNS of turbulent buoyant non-premixed flames. Recently, the method of LES has also been applied for studying the geometrical properties of the turbulent scalar gradient vector. For instance, Higgins *et al.* [66] examined the geometrical alignments between the real SGS heat fluxes and those predicted by a SGS model based on *a priori* LES analysis of a turbulent atmospheric boundary layer flow.

1.4 Objectives of the Dissertation

- i) The first objective of this dissertation is to study mixed convection in a vertical slot for aiding and opposing flow conditions. To examine the effect of buoyancy, the resolved velocity and temperature fields and second-order statistics including Reynolds stress components and turbulent heat fluxes are analyzed following the conventional method in the LES community.
- ii) Although the methodology of turbulence geometrical statistics has been an effective tool for studying the structures of turbulence, its applications are mainly based on DNS or filtered DNS (*a priori* LES). The relevant studies based on *a posteriori* LES are still limited, possibly due to concerns over the accuracy since the *a posteriori* LES is inherently connected to modelling and numerical errors. The second objective is to reproduce those universal geometrical properties of turbulent flows based on the *a posteriori* LES of mixed convection.
- iii) According to DNS and LES studies of wall-bounded flows [43, 52, 53, 59], the presence of the wall in a flow field has a significant anisotropic effect on the local flow structures. The third objective of this dissertation is to examine the flow structures in the near-wall regimes (i.e., viscous sublayer, buffer layer and logarithmic region) in terms of the statistical geometry of quantities related to the coherent structures

and dynamics of turbulence, such as helicity, enstrophy generation, the alignment pattern of the vorticity vector with respect to the eigenframe of the resolved strain rate tensor, and the ratio of the eigenvalues of the resolved strain rate tensor.

iv) For mixed convection, the scalar (temperature) is driven by a mean scalar (temperature) gradient and advected by turbulence. The geometrical characteristics of the scalar field are of fundamental importance to understand the dynamics of the scalar transport (mixing) processes, and thus are specifically investigated in this dissertation together with the geometrical properties of the fluid vectors and tensors, such as eigenvectors of the strain rate tensor.

v) The final objective of this work is to examine the performance of different SGS stress and heat flux models, and their combined effect on the LES prediction of a buoyant flow. In this dissertation, SGS stress models are not only assessed by the conventional approach, i.e. by comparing their LES prediction to the DNS data, but also by their geometrical properties studied using turbulence geometrical statistics. Note that SGS dissipation is closely related to the local flow structures. Therefore, both mean and instantaneous TKE dissipation as well as the statistical relationship between the SGS dissipation and characteristic parameters of the local flow structures are examined. Specifically, the performance of the SGS heat flux model is investigated with respect to the orientation of the SGS heat flux vector.

1.5 Outline of the Dissertation

The dissertation is organized as follows. In chapter 2, the methodology of LES is introduced, e.g. the filtering operation for LES, the algorithm for solving the filtered governing equations, and classic SGS stress and heat flux models for the closure of the LES equations are reviewed.

In chapter 3, the numerical algorithm including the discretization on a collocated grid system using the finite volume method, use of a fractional-step method suggested by Kim and Moin [67] and application of a multigrid solver using a control strategy for solving the pressure Poisson equation are introduced. In this chapter, the conservation properties of the collocated grid system are tested in comparison

with that of the staggered grid system. At the end of the chapter, the present 3-D LES code is evaluated using two benchmark flows, i.e. lid driven cavity flow and low Reynolds number channel flow.

In chapter 4, an LES study of a channel flow at $Re_\tau = 395$ is reported. The new dynamic nonlinear SGS stress model of Wang and Bergstrom [9] is investigated and compared to the conventional linear dynamic Smagorinsky model. In this chapter, the local geometrical properties of the small-scale flow structures are reported, and the issue of TKE dissipation produced by these two SGS models is investigated using both the conventional LES approach and the methodology of turbulence geometrical statistics.

In chapter 5, the combined forced and natural convective flow between two vertical plates at different temperatures is investigated using the LES approach. Two sets of dynamic SGS models, i.e. a combination of linear SGS models and a combination of nonlinear SGS models, were applied in this chapter. The LES predictions of the thermal fluid flow field are compared with DNS data reported in the literature using conventional LES approaches.

In chapter 6, the geometrical properties of the velocity and temperature field of the mixed flow investigated in chapter 5 are studied. This chapter focuses on a variety of characteristic geometrical patterns of local flow structures. The effect of buoyancy on the flow field is examined in terms of three different near-wall flow regimes in both the hot and cold wall regions. The near-wall restriction on the geometrical properties of the thermal flow field is reported. In this chapter, the performance of SGS heat flux model is also investigated with respect to the orientation of the SGS heat flux vector.

Finally, a summary of the major contributions of the dissertation and a discussion of directions for the future research are presented in chapter 7.

Chapter 2

Filtered Equations and SGS Models

2.1 The Filtering Operation

LES is based on the fact that the flow field consists of multiple scales of motion and can be separated into large- and small-scales by applying a filtering operation. A filtered variable denoted by an overbar is defined as

$$\bar{f}(\mathbf{x}) = \int_D f(\mathbf{y}) G(\mathbf{x}, \mathbf{y}) d\mathbf{y}, \quad (2.1)$$

where $G(\mathbf{x}, \mathbf{y})$ is the filter function, which determines the size of the small-scales, and D is the entire domain. The most commonly used filter functions are: the sharp Fourier cutoff filter

$$\hat{G}(k) = \begin{cases} 1 & \text{if } k \leq \pi/\bar{\Delta} \\ 0 & \text{otherwise} \end{cases}, \quad (2.2)$$

the Gaussian filter

$$G(x) = \sqrt{\frac{6}{\pi\bar{\Delta}^2}} \exp\left(-\frac{6x^2}{\bar{\Delta}^2}\right), \quad (2.3)$$

and the tophat filter

$$G(x) = \begin{cases} 1/\bar{\Delta} & \text{if } |x| \leq \bar{\Delta}/2 \\ 0 & \text{otherwise} \end{cases}, \quad (2.4)$$

where the caret $\hat{\cdot}$ denotes the complex Fourier transform of the original quantity and $\bar{\Delta}$ denotes the filter width. An exhaustive discussion of various filters and their properties can be found in Pope's work [68]. In general, the sharp Fourier cutoff filter clearly separates scales, but it causes non-local oscillatory behavior when filtering

spatially localized phenomena [69]. The tophat filter has good spatial localization, but does not separate the scales unambiguously. The Gaussian filter has an intermediate character between the sharp Fourier filter and the tophat filter.

2.2 Filtered Governing Equations for LES

After applying the filtering operation (2.1), the continuity, Navier-Stokes (N-S) and energy equations for incompressible flows will take the following forms:

$$\bar{u}_{i,i} = 0, \quad (2.5)$$

$$\dot{\bar{u}}_i + (\bar{u}_i \bar{u}_j)_{,j} = -\bar{p}_{,i} / \rho + \nu \bar{u}_{i,jj} - \tau_{ij,j}, \quad (2.6)$$

and

$$\dot{\bar{\theta}} + (\bar{u}_j \bar{\theta})_{,j} = \alpha \bar{\theta}_{,jj} - h_{j,j}, \quad (2.7)$$

where

$$\tau_{ij} \stackrel{\text{def}}{=} \overline{u_i u_j} - \bar{u}_i \bar{u}_j \quad (2.8)$$

and

$$h_j \stackrel{\text{def}}{=} \overline{u_j \theta} - \bar{u}_j \bar{\theta}. \quad (2.9)$$

The additional SGS stress and heat flux terms, i.e. τ_{ij} and h_j , appearing in the above filtered governing equations represent the effect of the small scales and must be modeled.

In the context of the energy cascade, energy is generated in the inertial range at the large-scale level and then transmitted to and dissipated at the viscous dissipative scales. In LES, the dissipative scales of motion are resolved poorly. Therefore, the main function of SGS stress models is to ‘drain’ energy from the resolved scales, mimicking the actual energy dissipation. To demonstrate the mechanisms of energy transfer between the resolved and SGS scales, the transport equations for kinetic energy $K = (\bar{u}_i \bar{u}_i)/2$ are given as follows:

$$\begin{aligned}
\dot{K} + \underbrace{(K\bar{u}_j)_{,j}}_{\text{Advection of } K} &= \underbrace{-(\bar{p}\bar{u}_j)_{,j}/\rho}_{\text{Pressure diffusion}} + \underbrace{\nu K_{,jj}}_{\text{Viscous diffusion}} - \underbrace{(\tau_{ij}\bar{u}_i)_{,j}}_{\text{SGS diffusion}} \\
&\quad - \underbrace{\nu\bar{u}_{i,j}\bar{u}_{i,j}}_{\text{Viscous dissipation}} + \underbrace{\tau_{ij}\bar{S}_{ij}}_{\text{SGS dissipation}}
\end{aligned} \tag{2.10}$$

The advection and diffusion terms in the above equation do not create or drain energy but only redistribute it within resolved scales. The last two terms in the above equation, i.e., viscous and SGS dissipation, represent the energy dissipated by viscosity and net energy transfer between the resolved and SGS scale, respectively. The latter, i.e., SGS dissipation $\tau_{ij}\bar{S}_{ij}$, can be either positive or negative locally, where the negative values of the $\tau_{ij}\bar{S}_{ij}$ represents the energy transfer from resolved to SGS scales (forward scatter), and the positive values of the $\tau_{ij}\bar{S}_{ij}$ represents the energy transfer in the reverse direction (backward scatter). In general, energy cascades in the direction from large- to small-scales, therefore, the SGS dissipation ($\tau_{ij}\bar{S}_{ij}$) is negative on average [70].

2.3 SGS Stress Modelling

Since the small-scale motions have shorter time scales than the large, energy-carrying eddies, it can be hypothesized that they adjust more rapidly and recover equilibrium nearly instantaneously. The small-scale velocity field, therefore, is assumed to be homogeneous and isotropic. The classic Smagorinsky Model (SM) is based on the equilibrium assumption and assumes a linear constitutive relation between the unknown SGS stress term and resolved strain rate tensor. There are several main drawbacks related to the model. For instance: i) measurements of the local SGS dissipation often exhibit some negative dissipation regimes [71, 72], in contrast, the SM is purely dissipative due to the positive coefficient; ii) a comparison between the SGS shear stress predicted by the SM and that obtained using experimental and DNS data exhibits significant differences [72]; iii) for the laminar flow regime, the SM with the standard coefficient over estimates the SGS stress and dissipation, often preventing transition to turbulence [71]. Similarly, in the near-wall region, the model is too dissipative to predict the correct asymptotic behavior without wall damping

functions [69]. Noting the above drawbacks, Germano *et al.* [6] and Lilly [7] suggested the dynamic Smagorinsky model (DM), which employed a dynamic procedure to improve the performance of the SM significantly. Although the DM has been widely applied in LES due to its simplicity and robustness, a few drawbacks are also linked to the linear constitutive relation adopted in its modelling approach. The model coefficient obtained through a dynamic procedure needs to be properly bounded to avoid large values, which generally lead to a potential numerical instability due to excessive backscatter of TKE. To prevent instability, a plane averaging technique is often applied [7, 20, 73], which then limits the application of this model to flows with homogeneous planes. On observing the deficiencies of the linear Smagorinsky type models, nonlinear SGS modelling approaches were introduced into the LES community. Earlier works include the classic scale-similarity model of Bardina *et al.* [31], a mixed model which adds a dissipative Smagorinsky term to the scale-similarity model [33, 34, 72, 74–76] and other nonlinear models [9, 15, 32, 77–79]. Recent reviews of different SGS stress models can be found in the literature [68, 70, 80]. In the next section, several classic SGS stress models, such as the DM, scale-similarity model, mixed model, and nonlinear dynamic model are reviewed.

2.3.1 Dynamic Smagorinsky Model

The conventional DM introduced by Germano *et al.* [6] and Lilly [7] has been widely used in the LES community due to its simplicity and robustness. The constitutive relation for the DM is based on a linear tensorial function of the resolved strain rate tensor \bar{S}_{ij} , i.e.

$$\tau_{ij}^* = \tau_{ij} - \frac{\tau_{kk}}{3}\delta_{ij} = -2C_s\bar{\Delta}^2|\bar{S}|\bar{S}_{ij}, \quad (2.11)$$

where $\bar{S}_{ij} \stackrel{\text{def}}{=} (\partial\bar{u}_i/\partial x_j + \partial\bar{u}_j/\partial x_i)/2$, $|\bar{S}| = (2\bar{S}_{ij}\bar{S}_{ji})^{1/2}$ is the norm of the resolved strain rate tensor, and an asterisk represents a trace-free tensor, i.e. $(\cdot)_{ij}^* \stackrel{\text{def}}{=} (\cdot)_{ij} - (\cdot)_{kk}\delta_{ij}/3$. In the DM, the model coefficient C_s is computed dynamically during the simulation, rather than input a *priori* as in the SM. The DM has made significant progress compared to the SM. It is free from any empirical constant and can adjust to the flow condition automatically. Theoretically, its coefficient can be locally negative and thus allow for backscatter of the kinetic energy. As for the near-wall flow, no

additional damping function is needed to ensure the correct near-wall behavior of the SGS stress.

The dynamic process proposed by Germano *et al.* [6] is based on a second, coarser test-grid-level filtering process. By applying the second test-grid-level filter denoted by a tilde, i.e. $(\tilde{\cdot})$, to the filtered governing equations, we obtain a new subtest-grid scale (STS) stress, T_{ij} , which is

$$T_{ij} = \widetilde{\overline{u_i u_j}} - \tilde{u}_i \tilde{u}_j \quad (2.12)$$

The characteristic size of the test-grid filter is denoted by $\tilde{\Delta}$. As suggested by Germano *et al.* [6], the ratio of the width of the test-grid filter to that of the grid filter is typically set to 2. Applying the closure defined by Eq.(2.11) to the test-grid filtered equations, the STS stress is similarly approximated by

$$T_{ij}^* = T_{ij} - \frac{\delta_{ij}}{3} T_{kk} = -2C_S \tilde{\Delta}^2 \left| \tilde{S} \right| \tilde{S}_{ij} \quad (2.13)$$

The Germano identity [6] is obtained by subtraction of the test-grid filtered τ_{ij} from T_{ij} , i.e.

$$\mathcal{L}_{ij} = T_{ij} - \tilde{\tau}_{ij} = \widetilde{\overline{u_i u_j}} - \tilde{u}_i \tilde{u}_j \quad (2.14)$$

Substituting Eqs.(2.11) and (2.13) into the Eq.(2.14), the following equation is obtained

$$\mathcal{L}_{ij} - \frac{1}{3} \mathcal{L}_{kk} = -\alpha_{ij} C_S + \widetilde{\beta_{ij} C_S} \quad (2.15)$$

where

$$\alpha_{ij} = 2\tilde{\Delta}^2 \left| \tilde{S} \right| \tilde{S}_{ij} \quad (2.16)$$

$$\beta_{ij} = 2\bar{\Delta}^2 \left| \bar{S} \right| \bar{S}_{ij} \quad (2.17)$$

Note that \mathcal{L}_{ij} can be numerically calculated and thus the coefficient C_S is only unknown variable in Eq.(2.15). However, the above Eq.(2.15) is over-determined since five independent equations are available to determine a single coefficient. Therefore, the Germano identity Eq.(2.14) can be satisfied only approximately. The error is

$$e_{ij} = \mathcal{L}_{ij}^* + \alpha_{ij} C_S - \widetilde{\beta_{ij} C_S} \quad (2.18)$$

where \mathcal{L}_{ij}^* is the tracefree form of \mathcal{L}_{ij} , i.e. $\mathcal{L}_{ij}^* = \mathcal{L}_{ij} - \frac{1}{3}\mathcal{L}_{kk}$. By assuming that the coefficient C_S is spatially invariant within the test window, C_S can be extracted from the test-grid filtering operation. Eq.(2.18) then becomes

$$e_{ij} = \mathcal{L}_{ij}^* + C_S M_{ij} \quad (2.19)$$

where

$$M_{ij} = \alpha_{ij} - \tilde{\beta}_{ij} \quad (2.20)$$

An optimal value for C_S can be obtained by minimizing the error of the Germano identity using the least squares method:

$$\frac{\partial E^2}{\partial C_S} = \frac{\partial \langle e_{ij} e_{ij} \rangle}{\partial C_S} = 0 \quad (2.21)$$

Note that the trace of \mathcal{L}_{ij} vanishes because $\bar{S}_{ii} = 0$ for an incompressible flow. The following expression for the model coefficient C_S is obtained:

$$C_S = -\frac{M_{ij}\mathcal{L}_{ij}}{M_{ij}M_{ij}}, \quad (2.22)$$

The dynamic procedure can be applied to models with more than one coefficient as well.

The DM has been applied to many flows, generally with good results. However, as discussed before, it may become numerically unstable. To prevent unrealistic backscatter of the TKE due to large negative coefficients, the coefficient field is generally filtered using a plane averaging scheme or the negative coefficients are simply clipped during the simulation [6, 7]. Difficulties in applying a plane averaging scheme arise in flows that do not possess directions of statistical homogeneity. Another disadvantage related to the plane averaging scheme is that it will smear the local characteristics of the model.

2.3.2 Scale Similarity and Mixed Model

In LES, the instantaneous velocity u_i is decomposed into resolved velocity \bar{u}_i and SGS fluctuations u'_i , i.e.

$$u_i = \bar{u}_i + u'_i \quad (2.23)$$

Using the above decomposition, the SGS stress τ_{ij} can be split as:

$$\begin{aligned} \tau_{ij} &= \overline{u_i u_j} - \bar{u}_i \bar{u}_j = \overline{(\bar{u}_i + u'_i)(\bar{u}_j + u'_j)} - \bar{u}_i \bar{u}_j \\ &= \overline{\bar{u}_i \bar{u}_j} + \overline{\bar{u}_i u'_j} + \overline{u'_i \bar{u}_j} + \overline{u'_i u'_j} - \bar{u}_i \bar{u}_j \\ &= (\overline{\bar{u}_i \bar{u}_j} - \bar{u}_i \bar{u}_j) + (\overline{\bar{u}_i u'_j} + \overline{u'_i \bar{u}_j}) + \overline{u'_i u'_j} \end{aligned} \quad (2.24)$$

where the terms in the first and second bracket are denoted as Leonard stresses and cross terms, respectively, and the last term is the Reynolds SGS stress. Namely,

$$\tau_{ij} = L_{ij} + C_{ij} + R_{ij} \quad (2.25)$$

where

$$L_{ij} = \overline{\bar{u}_i \bar{u}_j} - \bar{u}_i \bar{u}_j, \quad (2.26)$$

$$C_{ij} = \overline{\bar{u}_i u'_j} + \overline{u'_i \bar{u}_j}, \quad (2.27)$$

and

$$R_{ij} = \overline{u'_i u'_j}. \quad (2.28)$$

Eq. (2.23) is filtered to obtain the filtered SGS components, i.e. $\overline{u'_i} = \bar{u}_i - \bar{\bar{u}}_i$, and then the scale-similarity model of Bardina [31] assumes the cross term and SGS Reynolds stress can be approximately as

$$C_{ij} = \overline{\bar{u}'_i \bar{u}_j} + \overline{\bar{u}_i \bar{u}'_j} \approx \bar{\bar{u}}_j (\bar{u}_i - \bar{\bar{u}}_i) + \bar{\bar{u}}_i (\bar{u}_j - \bar{\bar{u}}_j) \quad (2.29)$$

and

$$R_{ij} = \overline{u'_i u'_j} \approx (\bar{u}_i - \bar{\bar{u}}_i)(\bar{u}_j - \bar{\bar{u}}_j). \quad (2.30)$$

Substituting Eq. (2.26), (2.29) and (2.30) into (2.25), yields:

$$\begin{aligned}
\tau_{ij} &= (\overline{u_i u_j} - \bar{u}_i \bar{u}_j) + (\overline{u'_i u_j} + \overline{u_i u'_j}) + \overline{u'_i u'_j} \\
&\approx (\overline{u_i u_j} - \bar{u}_i \bar{u}_j) + [\bar{u}_i (\bar{u}_j - \bar{\bar{u}}_j) + \bar{\bar{u}}_j (\bar{u}_i - \bar{\bar{u}}_i)] + (\bar{u}_i - \bar{\bar{u}}_i)(\bar{u}_j - \bar{\bar{u}}_j) \\
&\approx \overline{u_i u_j} - \bar{\bar{u}}_i \bar{\bar{u}}_j
\end{aligned} \tag{2.31}$$

Consequently, the scale-similarity model introduced by Bardina *et al.* [31] takes the following form:

$$\tau_{ij} = C_{SIM} (\overline{u_i u_j} - \bar{\bar{u}}_i \bar{\bar{u}}_j) \tag{2.32}$$

where C_{SIM} is the numerical coefficient.

Another form of the scale-similarity model can be obtained by applying a test filter. Since the most active subgrid scales are those closest to the cutoff scale (the characteristic width of a filter) and interact primarily with the scales right above the cutoff scale, a consequent thought is to relate the SGS stress, τ_{ij} , to the resolved Leonard stress $\widetilde{\bar{u}_i \bar{u}_j} - \tilde{\bar{u}}_i \tilde{\bar{u}}_j$, which is obtained by subtraction of the test-grid filtered τ_{ij} from T_{ij} (see Eq. 2.14) and relates to the turbulent stresses right above the cutoff scale. Based on their Particle Image Velocimetry (PIV) measurements in a round jet, Liu *et al.* [72] confirmed that τ_{ij} is highly correlated with the resolved Leonard stress and thus proposed the following scale-similarity model:

$$\tau_{ij} = C_{SIM}^L (\widetilde{\bar{u}_i \bar{u}_j} - \tilde{\bar{u}}_i \tilde{\bar{u}}_j) \tag{2.33}$$

where C_{SIM}^L is the model coefficient, the tilde represents the test-grid filtering operation with characteristic width $\tilde{\Delta} > \bar{\Delta}$. The value of C_{SIM}^L depends on the filtering operation. A discussion on the determination of the coefficient can be found in Cook's work [81]. Although a high correlations between the actual SGS stress and that modeled by the scale-similarity model is found in the *a priori* tests [31, 72], and the model is also able to produce backscatter of TKE, it is found not to dissipate enough energy which typically leads to inaccurate results. Therefore, a mixed model is suggested which adds a dissipative Smagorinsky term to the scale-similarity model [31, 72], i.e.

$$\tau_{ij} = C_1 (\widetilde{\bar{u}_i \bar{u}_j} - \tilde{\bar{u}}_i \tilde{\bar{u}}_j) - 2 (C_2 \bar{\Delta})^2 |\bar{S}| \bar{S}_{ij} \tag{2.34}$$

In the simulation of recirculating flows, Zang *et al.* [34] implemented a dynamic mixed model (DMM) with C_1 of fixed value and C_2 determined dynamically with good results. A value of $C_1 \approx 1$ was suggested in early papers [34, 74, 81]. Instead of specifying C_1 , Vreman *et al.* [82] proposed a dynamic two parameter mixed model (DTMM), in which both C_1 and C_2 are determined dynamically. The coefficients of the mixed model could be determined using the dynamical procedure described in section 2.3.1.

2.3.3 Dynamic Nonlinear Model

The dynamic nonlinear model (DNM) proposed by Wang and Bergstrom [9] is based on the explicit quadratic tensorial polynomial constitutive relation originally introduced by Speziale and Gatski [10, 11] for the RANS approach, and takes the following form within the context of LES:

$$\tau_{ij}^* = -C_S \beta_{ij} - C_W \gamma_{ij} - C_N \eta_{ij}, \quad (2.35)$$

where

$$\begin{aligned} \beta_{ij} &= 2\bar{\Delta}^2 |\bar{S}| \bar{S}_{ij} \\ \gamma_{ij} &= 2\bar{\Delta}^2 (\bar{S}_{ik} \bar{\Omega}_{kj} - \bar{\Omega}_{ik} \bar{S}_{kj}) \\ \eta_{ij} &= 4\bar{\Delta}^2 (\bar{S}_{ik} \bar{S}_{kj} - \frac{1}{3} \bar{S}_{mn} \bar{S}_{nm} \delta_{ij}) \end{aligned} \quad (2.36)$$

where $S_{ij} = (u_{i,j} + u_{j,i})/2$ and $\Omega_{ij} = (u_{i,j} - u_{j,i})/2$. As part of a dynamical procedure, a test-grid filter is applied to obtain the STS stress T_{ij} . The trace free form of T_{ij} is

$$T_{ij}^* = -C_S \alpha_{ij} - C_W \lambda_{ij} - C_N \zeta_{ij} \quad (2.37)$$

where

$$\begin{aligned} \alpha_{ij} &= 2\tilde{\Delta}^2 |\tilde{S}| \tilde{S}_{ij} \\ \lambda_{ij} &= 2\tilde{\Delta}^2 (\tilde{S}_{ik} \tilde{\Omega}_{kj} - \tilde{\Omega}_{ik} \tilde{S}_{kj}) \\ \zeta_{ij} &= 4\tilde{\Delta}^2 (\tilde{S}_{ik} \tilde{S}_{kj} - \frac{1}{3} \tilde{S}_{mn} \tilde{S}_{nm} \delta_{ij}) \end{aligned} \quad (2.38)$$

where the tilde denotes the test-grid filtering operation. The optimal values of the three dynamic model coefficients C_S , C_W and C_N can be obtained using the least squares approach, which requires solution of the following matrix equation:

$$\begin{bmatrix} M_{ij}M_{ij} & M_{ij}W_{ij} & M_{ij}N_{ij} \\ W_{ij}M_{ij} & W_{ij}W_{ij} & W_{ij}N_{ij} \\ N_{ij}M_{ij} & N_{ij}W_{ij} & N_{ij}N_{ij} \end{bmatrix} \cdot \begin{bmatrix} C_S \\ C_W \\ C_N \end{bmatrix} = - \begin{bmatrix} \mathcal{L}_{ij}^* M_{ij} \\ \mathcal{L}_{ij}^* W_{ij} \\ \mathcal{L}_{ij}^* N_{ij} \end{bmatrix}. \quad (2.39)$$

Similar to the previous definition of M_{ij} (Eq. 2.20), W_{ij} and N_{ij} are two differential tensors defined as:

$$W_{ij} \stackrel{\text{def}}{=} \lambda_{ij} - \tilde{\gamma}_{ij} \quad (2.40)$$

and

$$N_{ij} \stackrel{\text{def}}{=} \zeta_{ij} - \tilde{\eta}_{ij}, \quad (2.41)$$

The design of the modelling constitutive relation is based on the Speziale-Gatski constitutive relation. The three tensorial base components (i.e., β_{ij} , γ_{ij} and η_{ij}) are independent and individually related to three important SGS physical features, e.g. the overall SGS dissipation level, a high correlation coefficient between the modelled and exact SGS stress in an *a priori* LES test, and realistic reflection of TKE backscatter [9]. Due to its nonlinear characteristics, the DNM is numerically robust and can be applied locally without the need for bounding of its coefficients in the simulation, which contrasts sharply with the performance of the DM. However, in terms of the efficiency, it is found that the DNM is approximately 25% more computationally expensive than the DM [9]. Wang and Bergstrom investigated the model using LES of turbulent Couette flow at relatively low Reynolds numbers [9]. The model was found to be more robust compared to the DM. It can adjust to the local flow conditions automatically and allow for both forward and backward scattering processes of TKE between the resolved and unresolved scales.

2.4 SGS Heat Flux Modelling

Most pioneering works used the linear eddy diffusivity model (DEDM-HF) for the heat flux term (e.g. Mion *et al.* [20], Cabot [83], Wong and Lilly [84]). The DEDM-

HF assumes that the heat flux term is proportional to the temperature gradient. More specifically, it suggests a linear constitutive relation between the SGS heat flux and temperature gradient. Although the linear DEDM-HF cannot predict the anisotropic behavior of the scalar field [19, 72], it has been applied for various turbulent scalar transport problems with good results [21, 22, 24–27]. Recently, nonlinear SGS heat flux models have been studied. Peng and Davidson [40] proposed a dynamic nonlinear tensor diffusivity model (DTDM-HF) for the SGS heat flux term for studying turbulent buoyant flow. In their approach, the eddy diffusivity tensor is related to the resolved strain rate tensor. DTDM-HF is actually similar to the nonlinear gradient model (NGM-HF) proposed by Leonard [32], which is derived from Bardina’s scale-similarity model [31]. Recall that the scale-similarity model is acknowledged to provide insufficient dissipation of KTE, the DTDM-HF and NGM-HF, derived from the scale-similarity model, may inherit the same deficiency. Instead, Salvetti and Banerjee [33], Portè-Agel *et al.* [37, 38] and Kang and Meneveau [19] suggested dynamic mixed SGS heat flux models (DMM-HF) which combine the scale-similarity model with a conventional linear eddy diffusivity model for the SGS scalar flux. The DMM-HF compensates for the deficiency of the scale-similarity type model by adding the Smagorinsky dissipative term. Since the magnitude of the Smagorinsky term is much smaller than the similarity term, most of the advantageous features of the scale-similarity model are retained in the mixed model. Compared to the linear diffusivity model, the nonlinear models are able to capture the characteristic features of the scalar field [33, 72].

2.4.1 Dynamic Eddy Diffusivity Model

The DEDM-HF introduced by Moin *et al.* [20] is based on the concept of a linear eddy thermal diffusivity in analogy to Fourier’s law. In the literature, this model is still the most popular for LES of scalar transport processes. The DEDM-HF adopts the following constitutive relation for modelling the SGS HF vector:

$$h_j = -\alpha_{sgs} \frac{\partial \bar{\theta}}{\partial x_j} \quad (2.42)$$

where α_{sgs} is the SGS (eddy) thermal diffusivity. It is expressed as:

$$\alpha_{sgs} = -\frac{\nu_{sgs}}{\sigma_{sgs}} \quad (2.43)$$

where ν_{sgs} is the SGS viscosity and σ_{sgs} is the SGS Prandtl number. Suggested by Lilly [7], the Smagorinsky closure, i.e. $\nu_{SGS} = C_S \bar{\Delta}^2 |\bar{S}|$, is applied to Eq.(2.43), i.e.,

$$\alpha_{sgs} = -\frac{C_S}{\sigma_{sgs}} \bar{\Delta}^2 |\bar{S}| \quad (2.44)$$

Where C_S is obtained dynamically by solving the DM, and the SGS Prandtl number σ_{sgs} remains to be determined. By substituting Eq. (2.44) into (2.42), the obtained DEDM-HF will take the following form:

$$h_j = \frac{C_S}{\sigma_{SGS}} \bar{\Delta}^2 |\bar{S}| \frac{\partial \bar{\theta}}{\partial x_j} = \frac{C_S}{\sigma_{SGS}} b_j \quad (2.45)$$

where

$$b_j = \bar{\Delta}^2 |\bar{S}| \frac{\partial \bar{\theta}}{\partial x_j}. \quad (2.46)$$

Similary, the heat flux at the test-grid scale is

$$H_j = \frac{C_S}{\sigma_{SGS}} \tilde{\Delta}^2 |\tilde{S}| \frac{\partial \tilde{\theta}}{\partial x_j} = \frac{C_S}{\sigma_{SGS}} a_j \quad (2.47)$$

where

$$a_j = \tilde{\Delta}^2 |\tilde{S}| \frac{\partial \tilde{\theta}}{\partial x_j}. \quad (2.48)$$

Following the dynamic procedure of Germano *et al.* [6], a similar identity exists to relate h_j to H_j , i.e.

$$\mathcal{L}_j = H_j - \tilde{h}_j = \widetilde{\bar{u}_j \bar{\theta}} - \tilde{u}_j \tilde{\theta} \quad (2.49)$$

By substituting Eqs. (2.45) and (2.47) into Eq. (2.49) and minimizing the error of the resulting equations using the least squares method (assuming that C_S/σ_{SGS} is spatially invariant within the test-grid scale), the SGS Prandtl number is obtained as

$$\frac{1}{\sigma_{SGS}} = \frac{1}{C_S} \frac{\mathcal{L}_j M_j}{M_j M_j} \quad (2.50)$$

where $M_j = a_j - \tilde{b}_j$. Note that C_S is calculated by Eq. 2.22. Actually, there is no need to calculate σ_{SGS} and C_S explicitly. For instance, let $C_\theta = -C_S/\sigma_{sgs}$, and then

the heat flux model (2.45) and (2.47) take the following form:

$$h_j = C_\theta \bar{\Delta}^2 |\bar{S}| \frac{\partial \bar{\theta}}{\partial x_j} = C_\theta b_j \quad (2.51)$$

where

$$b_j = \bar{\Delta}^2 |\bar{S}| \frac{\partial \bar{\theta}}{\partial x_j} \quad (2.52)$$

and

$$H_j = C_\theta \tilde{\Delta}^2 |\tilde{S}| \frac{\partial \tilde{\theta}}{\partial x_j} = C_\theta a_j \quad (2.53)$$

where

$$a_j = \tilde{\Delta}^2 |\tilde{S}| \frac{\partial \tilde{\theta}}{\partial x_j}. \quad (2.54)$$

By using the same procedure, i.e. substitute Eqs. (2.51) and (2.53) into Eq. (2.49) and minimize the error of the resulting equations by using the least squares method (assuming that C_θ is spatially invariant within the test-grid scale), we obtain

$$C_\theta = -\frac{\mathcal{L}_j M_j}{M_j M_j}. \quad (2.55)$$

Note that Eqs. (2.50) and (2.55) are actually equivalent. As discussed above, the DEDM-HF is based on the concept of a linear eddy thermal diffusivity in analogy to Fourier's law. It is inconsistent with the physics of turbulent convection. The forced alignment between the resolved scalar gradient and the modelled SGS scalar flux is, in general, unphysical, as has been confirmed by the recent study of Abe and Suga [85].

2.4.2 Dynamic Tensor Diffusivity Model

On noting the limitation of the DEDM-HF, Peng and Davidson [40] proposed a novel dynamic tensor diffusivity model (DTDM-HF) based on the concept of a dynamic tensor thermal diffusivity, which no longer relies on the analogy of molecular diffusion and allows for non-alignment between the SGS HF vector and resolved temperature gradient vector. The constitutive relation for the DTDM-HF of Peng and Davidson [40] at the grid level takes the following form:

$$h_j = -C_\theta^T \bar{\Delta}^2 \bar{S}_{jk} \frac{\partial \bar{\theta}}{\partial x_k}, \quad (2.56)$$

where C_θ^T is the model coefficient and the tensor diffusivity is based on the resolved strain rate tensor, viz. $D_{jk} = C_\theta^T \bar{\Delta}^2 \bar{S}_{jk}$. For the dynamic procedure, the test-grid level SGS HF vector is modelled as

$$H_j = -C_\theta^T \tilde{\Delta}^2 \tilde{S}_{jk} \frac{\partial \tilde{\theta}}{\partial x_k}. \quad (2.57)$$

Following the dynamic modelling approach of Germano *et al.* [6], the dynamic coefficient for the DTDM-HF is given as:

$$C_\theta^T = -\frac{\mathcal{L}_j M_j}{M_j M_j}, \quad (2.58)$$

where $M_j = a_j - \tilde{b}_j$ with the base vectors defined as

$$b_j = \bar{\Delta}^2 \bar{S}_{jk} \frac{\partial \bar{\theta}}{\partial x_k} \quad \text{and} \quad a_j = \tilde{\Delta}^2 \tilde{S}_{jk} \frac{\partial \tilde{\theta}}{\partial x_k}. \quad (2.59)$$

Unlike the DEDM-HF [cf. Eq. (2.51)], the DTDM-HF of Peng and Davidson [40] [cf. Eq. (2.56)] does not require the SGS heat flux be aligned with the negative resolved temperature gradient vector, instead, it models the heat flux vector h_j in response to both the resolved strain rate tensor and temperature gradient in all three coordinate directions through the contraction between \bar{S}_{jk} and $\partial \bar{\theta} / \partial x_k$. As such, in theory, the SGS heat flux component in a direction with zero mean temperature gradient can still be non-trivial due to the temperature gradients present in the other two directions.

2.4.3 Dynamic Mixed Model

Based on the scale-similarity model of Bardina *et al.* [31] for the SGS stress tensor, Portè-Agel *et al.* [37, 38] and Kang and Meneveau [19] proposed a similar scale-similarity model for the SGS scalar flux vector as follows:

$$h_j = C_\theta^{SIM} \left(\widetilde{\bar{u}_j \bar{\theta}} - \tilde{u}_j \tilde{\theta} \right) \quad (2.60)$$

where C_θ^{SIM} is a numerical coefficient. Following the approach of Leonard [32] and Clark *et al.* [77], Portè-Agel *et al.* [37, 38] applied a Taylor expansion to the filtering

operation and obtained a nonlinear gradient model from Eq. (2.60). The nonlinear gradient model takes the following form:

$$h_j = C_\theta^G \bar{\Delta}^2 \frac{\partial \bar{u}_j}{\partial x_k} \frac{\partial \bar{\theta}}{\partial x_k} \quad (2.61)$$

where C_θ^G is a model coefficient to be determined using a dynamic procedure. By combining the nonlinear gradient model (Eq. 2.61) and eddy diffusivity model (Eq. 2.53), Portè-Agel *et al.* [37, 38] and Kang and Meneveau [19] suggested a dynamic two-parameter mixed model (DTMM-HF) which takes the following form:

$$h_j = C_e \bar{\Delta}^2 |\bar{S}| \frac{\partial \bar{\theta}}{\partial x_j} + C_g \bar{\Delta}^2 \frac{\partial \bar{u}_j}{\partial x_k} \frac{\partial \bar{\theta}}{\partial x_k} = C_e b_j^E + C_g b_j^G \quad (2.62)$$

where $b_j^E = \bar{\Delta}^2 |\bar{S}| \partial \bar{\theta} / \partial x_j$ and $b_j^G = \bar{\Delta}^2 \partial \bar{u}_j / \partial x_k \partial \bar{\theta} / \partial x_k$; and C_e and C_g are model coefficients, which are determined dynamically during the simulation. The test-grid scale stress of the mixed model takes the following form:

$$H_j = C_e \tilde{\Delta}^2 |\tilde{S}| \frac{\partial \tilde{\theta}}{\partial x_j} + C_g \tilde{\Delta}^2 \frac{\partial \tilde{u}_j}{\partial x_k} \frac{\partial \tilde{\theta}}{\partial x_k} = C_e a_j^E + C_g a_j^G \quad (2.63)$$

where $a_j^E = \tilde{\Delta}^2 |\tilde{S}| \frac{\partial \tilde{\theta}}{\partial x_j}$ and $a_j^G = \tilde{\Delta}^2 \frac{\partial \tilde{u}_j}{\partial x_k} \frac{\partial \tilde{\theta}}{\partial x_k}$. By minimizing the error of the identity equation ($\mathcal{L}_j = H_j - \tilde{h}_j$) using the least squares method, the model coefficients can be calculated as:

$$\begin{bmatrix} L_j L_j & L_j M_j \\ L_j M_j & M_j M_j \end{bmatrix} \cdot \begin{bmatrix} C_e \\ C_g \end{bmatrix} = - \begin{bmatrix} L_j \mathcal{L}_j \\ M_j \mathcal{L}_j \end{bmatrix}. \quad (2.64)$$

where $L_j = a_j^E - \tilde{b}_j^E$ and $M_j = a_j^G - \tilde{b}_j^G$. Compared to the linear eddy diffusivity model, the dynamic mixed model has improved features that correspond better to the characteristics of the scalar field. However, its numerical implementation requires more CPU time than the eddy diffusivity model.

2.5 Summary

A successful SGS model should be able to satisfy the following requirements: i) predict the overall energy (or scalar variance for a scalar field) dissipation correctly; ii) predict both forward and backward transfer of energy (or scalar variance) between the resolved and SGS scales; and iii) properly reproduce the geometrical characteristics of the flow field. As mentioned before, since the linear eddy-viscosity type SGS stress models are not able to account for the backward transfer of kinetic energy due to their simple unphysical constitutive relations, a number of nonlinear SGS stress models, such as DMM [34, 74, 81], DTMM [82] and DNM [9], has been introduced to give improved results. For example, compared to the DM, the DNM [9] has advantageous features: it is based on a relatively realistic constitutive relation, and thus more robust than the DM; it can adjust to the local flow conditions automatically and predict both forward and backward scatter. Similarly, in the modelling of SGS scalar flux terms, the linear eddy diffusivity model cannot predict backscatter of the scalar variance either, whereas nonlinear SGS scalar flux models, such as the scale-similarity model, tensor diffusivity model and mixed models can predict backscatter. Note that the scalar field is anisotropic even at dissipative scales, a proper SGS scalar flux model should be able to reproduce the anisotropy character as well. By examining the SGS scalar variance dissipation predicted by the DEDM-HF and a mixed model, Kang and Meneveau [19] demonstrated that the DEDM-HF cannot predict the anisotropy of a scalar field, in contrast, the mixed model can be tuned to reproduce the correct amount of anisotropy. Besides the improvement, these SGS models are more complicated and require more CPU time, for example, the DNM is approximately 25% more computationally expensive than the DM [9] and dynamic mixed models require a CPU time 11% more than the Smagorinsky model [86]. For some cases, the benefits gained by nonlinear models may not outweigh their additional computational cost. Jiménez *et al.* [87] studied the scalar transport in a mixing layer and found that, the mixed SGS scalar flux model does not improve the LES prediction evidently (the dynamic mixed model and DEDM-HF yield similar prediction in their study), provided that a proper SGS stress model is adopted. In this dissertation, the DNM for SGS stress and DTDM-HF for SGS scalar flux are investigated based on LES of mixed

convection. The combination of the nonlinear models, i.e. DNM&DTDM-HF, yields a better prediction than the combination of the linear models, i.e. DM&DEDM-HF, especially with respect to the temperature field. It is also found that the DTDM-HF is able to successfully predict the near-wall geometrical properties of the SGS heat flux vector, whereas the DEDM-HF cannot.

Chapter 3

Numerical Algorithm and Test Problems

3.1 Numerical Algorithm for LES

A method based on the commonly used fractional time-step technique for DNS and LES calculation described in the works of Chorin [88] and Kim and Moin [67] is applied in this work, in which the filtered Navier-Stokes equations are solved in two steps: first, an estimated velocity field is obtained by solving the governing equation without updating the pressure field, and then a pressure correction Poisson equation derived from the continuity equation is calculated and the estimated velocity field is corrected to satisfy mass conservation. The filtered Navier-Stokes equations (2.6) can be written as

$$\dot{\bar{u}}_i = -\bar{p}_{,i}/\rho - H_i + \nu \bar{u}_{i,jj}, \quad (3.1)$$

where H_i is the nonlinear terms, i.e.

$$H_i = (\bar{u}_i \bar{u}_j)_{,j} + (\tau_{ij})_{,j}. \quad (3.2)$$

A typical time advancement method using a second-order Adams-Bashforth scheme for the nonlinear terms and a Crank-Nicolson scheme for the viscous stress terms is applied to calculate the velocity field after a time step Δt :

$$\begin{cases} \frac{\bar{u}_i^* - \bar{u}_i^n}{\Delta t} = -\frac{1}{2}[3H_i^{(n)} - H_i^{(n-1)}] + \nu(\bar{u}_{i,jj}^* + \bar{u}_{i,jj}^n)/2 \\ \bar{u}_i^{(n+1)} = \bar{u}_i^* - \frac{\Delta t}{\rho} \bar{p}_{,i}^{(n+1)} \end{cases} \quad (3.3)$$

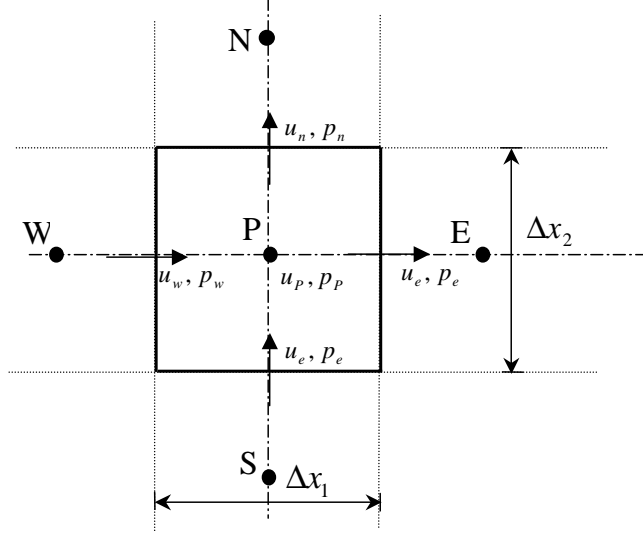


FIGURE 3.1: A 2-dimensional sketch of a typical control volume for a collocated grid system.

where n indicates the current time step and the superscript \star indicates an estimated value for the next time step (denoted by $n + 1$).

In the numerical solution of equations (3.3), a collocated grid system shown in Figure 3.1 is adopted. In a collocated grid system, both velocities and pressures are stored at cell centres, and the velocities at the interfaces of a control volume are approximated by a interpolation of the neighboring cell-centered velocities. The finite volume method and 2^{nd} -order central difference scheme used for the discretization of the equations (3.3) are classic and can be found in the literature (e. g. the work by Ferziger [89]), and thus will not be presented in this dissertation. We only demonstrate the strategy to obtain the new time-level pressure $\bar{p}^{(n+1)}$ in the second equation of (3.3). The $\bar{p}^{(n+1)}$ can be obtained by updating the old pressure $\bar{p}^{(n)}$ using a correcting pressure \bar{p}' , i.e.

$$\bar{p}^{(n+1)} = \bar{p}^{(n)} + \bar{p}'. \quad (3.4)$$

The unknown \bar{p}' is derived from the filtered continuity equation (2.5) by satisfying mass conservation. For instance, the continuity equation can be discretized using the finite volume method based on the collocated grid system shown in Figure 3.1, i.e.

$$\int_b^f \int_s^n \int_w^e \left(\frac{\partial \bar{u}_1}{\partial x_1} + \frac{\partial \bar{u}_2}{\partial x_2} + \frac{\partial \bar{u}_3}{\partial x_3} \right) dx_1 dx_2 dx_3 = 0. \quad (3.5)$$

By intergrating, we obtain:

$$(\bar{u}_e - \bar{u}_w)A_1 + (\bar{u}_n - \bar{u}_s)A_2 + (\bar{u}_f - \bar{u}_b)A_3 = 0, \quad (3.6)$$

where the subscripts ‘e’, ‘w’, ‘n’, ‘s’, ‘f’ and ‘b’ represent ‘east’, ‘west’, ‘north’, ‘south’, ‘front’ and ‘back’ faces of the control volume, respectively, and $A_1 = \Delta x_2 \cdot \Delta x_3$, $A_2 = \Delta x_1 \cdot \Delta x_3$ and $A_3 = \Delta x_1 \cdot \Delta x_2$ are the cross-sectional areas of the control volume perpendicular to the $w - e$, $s - n$ and $b - f$ directions, respectively. The face velocities in Eq. (3.6) are approximated by interpolation of neighboring node velocities. For example, the velocity at the east face is calculated as:

$$\bar{u}_e = \frac{\bar{u}_P^{(n+1)} + \bar{u}_E^{(n+1)}}{2}, \quad (3.7)$$

where the uppercase subscripts denote the neighboring nodes as shown in Figure 3.1. By substituting the second equation of (3.3) into above equation, we obtain:

$$\begin{aligned} \bar{u}_e &= \frac{1}{2} \left\{ \left[\bar{u}_P^* - \frac{\Delta t}{\rho} \frac{\partial \bar{p}^{(n+1)}}{\partial x} \Big|_P \right] + \left[\bar{u}_E^* - \frac{\Delta t}{\rho} \frac{\partial \bar{p}^{(n+1)}}{\partial x} \Big|_E \right] \right\} \\ &= \frac{\bar{u}_P^* + \bar{u}_E^*}{2} - \frac{\Delta t}{2\rho} \left[\frac{\partial \bar{p}^{(n+1)}}{\partial x} \Big|_P + \frac{\partial \bar{p}^{(n+1)}}{\partial x} \Big|_E \right] \\ &\approx \frac{\bar{u}_P^* + \bar{u}_E^*}{2} - \frac{\Delta t}{\rho} \frac{\partial \bar{p}^{(n+1)}}{\partial x} \Big|_e. \end{aligned} \quad (3.8)$$

Let

$$\frac{\partial \bar{p}^{(n+1)}}{\partial x} \Big|_e = \frac{\bar{p}_E^{(n+1)} - \bar{p}_P^{(n+1)}}{\Delta x_{PE}}, \quad (3.9)$$

where $\Delta x_{PE} = x_P - x_E$. Using Eq.(3.9) and (3.4), equation (3.8) can be rewritten as:

$$\begin{aligned} \bar{u}_e &= \frac{\bar{u}_P^* + \bar{u}_E^*}{2} - \frac{\Delta t}{\rho} \left[\frac{\bar{p}_E^{(n+1)} - \bar{p}_P^{(n+1)}}{\Delta x_{PE}} \right] \\ &= \frac{\bar{u}_P^* + \bar{u}_E^*}{2} - \frac{\Delta t}{\rho} \left[\frac{(\bar{p}_E^{(n)} + \bar{p}'_E) - (\bar{p}_P^{(n)} + \bar{p}'_P)}{\Delta x_{PE}} \right] \\ &= \frac{\bar{u}_P^* + \bar{u}_E^*}{2} - \frac{\Delta t}{\rho} \left[\frac{\bar{p}_E^{(n)} - \bar{p}_P^{(n)}}{\Delta x_{PE}} \right] - \frac{\Delta t}{\rho} \left[\frac{\bar{p}'_E - \bar{p}'_P}{\Delta x_{PE}} \right]. \end{aligned} \quad (3.10)$$

Let

$$\bar{u}_e^* = \frac{\bar{u}_P^* + \bar{u}_E^*}{2} - \frac{\Delta t}{\rho} \frac{(\bar{p}_E^{(n)} - \bar{p}_P^{(n)})}{\Delta x_{PE}} \quad (3.11)$$

and then Eq. (3.10) takes the following form:

$$\bar{u}_e = \bar{u}_e^* - \frac{\Delta t}{\rho} \frac{(\bar{p}'_E - \bar{p}'_P)}{\Delta x_{PE}}. \quad (3.12)$$

Substituting Eq.(3.12) into Eq.(3.6), the following discrete equation for the correcting pressure are obtained:

$$a_P \bar{p}'_P = \sum a_{NP} \bar{p}'_{NP} + b, \quad (3.13)$$

where the subscript NP represents the neighboring nodes, and a and b denote the coefficients and source term, respectively, all of which are:

$$\begin{aligned} a_E &= \frac{A_1 \Delta t}{\Delta x_{PE}}, & a_W &= \frac{A_1 \Delta t}{\Delta x_{WP}}, & a_S &= \frac{A_2 \Delta t}{\Delta x_{PS}}, \\ a_N &= \frac{A_2 \Delta t}{\Delta x_{NP}}, & a_F &= \frac{A_3 \Delta t}{\Delta x_{PF}}, & a_B &= \frac{A_3 \Delta t}{\Delta x_{BP}}, \\ b &= -\rho [A_1(\bar{u}_e^* - \bar{u}_w^*) + A_2(\bar{u}_n^* - \bar{u}_s^*) + A_3(\bar{u}_f^* - \bar{u}_b^*)], \\ a_P &= \sum a_{NP}. \end{aligned} \quad (3.14)$$

Note that in the above scheme, the face velocity is calculated in two steps: first, it is estimated using the old neighboring velocities and the pressure gradient $-\bar{p}_{,i}^{(n)}$ at the interface (see Eq. 3.11), and then it is corrected to satisfy mass conservation using the correcting pressure (see Eq. 3.12). This approach leads to a pressure correction Poisson equation (3.13) instead of a pressure Poisson equation.

3.2 Multigrid Solver Using a Control Strategy

Numerical solution of the incompressible Navier-Stokes equations requires solving the Poisson type equation. Several techniques, including multigrid and direct methods, are commonly used. Direct methods generally require large computer memory, while iterative methods require an effective convergence rate. Iterative methods such as classic Gauss-Seidel (GS) type solvers show strong convergence in the initial few sweeps, but subsequently the convergence rate decreases rapidly. It can be ex-

plained by a Fourier analysis of the error components [90]. GS solvers can effectively smooth out errors of wavelengths comparable to the mesh size, but are less effective in smoothing the longer wavelength (low frequency) errors, therefore, the convergence time dramatically increases after the initial few sweeps. The multigrid method (MG) was developed to overcome this problem. It employs a hierarchy of grids and solves the pressure field at different grid levels so that errors with different wavelengths are smoothed out easily on comparable grid sizes. Multi-grid methods can greatly accelerate the convergence rate, especially for large-scale multi-dimensional problems. For a complete review of the MG technique, one can refer to the works by Brandt [91] and Stüben and Trottenberg [92].

3.2.1 Formation of the Coarse-grid Equations

To apply a multigrid method, the equations for coarse-grids have to be known. The formation of the coarse-grid equations should satisfy two requirements. First the corrections suggested by the coarse-grid equations should go to zero when the fine-grid values represent the correct solution of the discretization equations. Second, the form of the coarse-grid equations should be consistent with that of the fine-grid equations to permit the same solver. Hutchinson *et al.* [93] and Sathiyamurthy and Patankar [94] described a procedure which combines a block of fine-grid equations to obtain the coarse-grid equations. Here, the simple case of a coarse grid formed from the assembly of 1×2 blocks of fine-grid control volumes shown in Figure 3.2 is used to demonstrate the procedure.

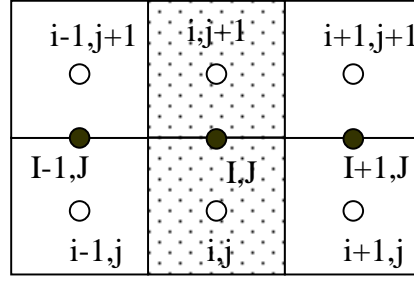
The fine-grid discretization equations for the node (i, j) and node $(i, j + 1)$ in Figure 3.2 can be written in the following general forms:

$$a_{i,j}^P \Phi_{i,j} = a_{i,j}^E \Phi_{i+1,j} + a_{i,j}^W \Phi_{i-1,j} + a_{i,j}^N \Phi_{i,j+1} + a_{i,j}^S \Phi_{i,j-1} + b_{i,j} \quad (3.15)$$

and

$$a_{i,j+1}^P \Phi_{i,j+1} = a_{i,j+1}^E \Phi_{i+1,j+1} + a_{i,j+1}^W \Phi_{i-1,j+1} + a_{i,j+1}^N \Phi_{i,j+2} + a_{i,j+1}^S \Phi_{i,j} + b_{i,j+1}, \quad (3.16)$$

where Φ is the variable to be solved, a denotes the coefficients of the discretization



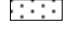
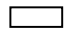


 Coarse grid control volume
 Fine grid control volume
 Node of coarse grid
 Node of fine grid

FIGURE 3.2: Coarse grid formed from assembly of 1×2 blocks

equation of the control volume, and b is a source term. The superscript P denotes the central node, and E , W , N and S denote the east, west, north and south neighbor nodes, respectively. To formulate the equation for the coarse-grid node (I,J) , we first sum up the fine-grid equations of nodes located in the coarse-grid control volume (I,J) , e.g. add the Eq. (3.15) and (3.16) and rearrange the resulting equation to obtain:

$$\begin{aligned}
 (a_{i,j}^P - a_{i,j+1}^S)\Phi_{i,j} + (a_{i,j+1}^P - a_{i,j}^N)\Phi_{i,j+1} &= a_{i,j}^E\Phi_{i+1,j} + a_{i,j+1}^E\Phi_{i+1,j+1} \\
 &+ a_{i,j}^W\Phi_{i-1,j} + a_{i,j+1}^W\Phi_{i-1,j+1} \\
 &+ a_{i,j+1}^N\Phi_{i,j+2} + a_{i,j}^S\Phi_{i,j-1} \\
 &+ b_{i,j} + b_{i,j+1}.
 \end{aligned} \tag{3.17}$$

Let $\delta_{I,J}$ be the average error of the fine-grid equations corresponding to the cells in the coarse-grid control volume (I,J) , and assume that the values of the variable Φ for all the fine-grid nodes in the block can be corrected by $\delta_{I,J}$, i.e.

$$\Phi_{i,j} = \Phi_{i,j}^0 + \delta_{I,J}, \tag{3.18}$$

and

$$\Phi_{i,j+1} = \Phi_{i,j+1}^0 + \delta_{I,J}, \tag{3.19}$$

where $\Phi_{i,j}^0$ and $\Phi_{i,j+1}^0$ are the approximate values of the variable for node (i,j) and

(i,j+1) on the fine grid, respectively. By substituting Eqs. (3.18) and (3.19) into (3.17) and rearranging, we obtain the equation for the coarse grid:

$$\begin{aligned}
& (a_{i,j}^P - a_{i,j+1}^S + a_{i,j+1}^P - a_{i,j}^N)\delta_{I,J} \\
& = (a_{i,j}^E + a_{i,j+1}^E)\delta_{I+1,J} + (a_{i,j}^W + a_{i,j+1}^W)\delta_{I-1,J} + a_{i,j+1}^N\delta_{I,J+1} + a_{i,j}^S\delta_{I,J-1} \\
& + a_{i,j}^E\Phi_{i+1,j}^0 + a_{i,j}^W\Phi_{i-1,j}^0 + a_{i,j}^N\Phi_{i,j+1}^0 + a_{i,j}^S\Phi_{i,j-1}^0 + b_{i,j} - a_{i,j}^P\Phi_{i,j}^0 \\
& + a_{i,j+1}^E\Phi_{i+1,j+1}^0 + a_{i,j+1}^W\Phi_{i-1,j+1}^0 + a_{i,j+1}^N\Phi_{i,j+2}^0 + a_{i,j+1}^S\Phi_{i,j}^0 + b_{i,j+1} \\
& - a_{i,j+1}^P\Phi_{i,j+1}^0.
\end{aligned} \tag{3.20}$$

Let $R_{i,j}^0$ and $R_{i,j+1}^0$ denote the residuals of the fine-grid Eqs.(3.15) and (3.16), i.e.

$$R_{i,j}^0 = a_{i,j}^E\Phi_{i+1,j}^0 + a_{i,j}^W\Phi_{i-1,j}^0 + a_{i,j}^N\Phi_{i,j+1}^0 + a_{i,j}^S\Phi_{i,j-1}^0 + b_{i,j} - a_{i,j}^P\Phi_{i,j}^0 \tag{3.21}$$

and

$$\begin{aligned}
R_{i,j+1}^0 & = a_{i,j+1}^E\Phi_{i+1,j+1}^0 + a_{i,j+1}^W\Phi_{i-1,j+1}^0 + a_{i,j+1}^N\Phi_{i,j+2}^0 + a_{i,j+1}^S\Phi_{i,j}^0 \\
& + b_{i,j+1} - a_{i,j+1}^P\Phi_{i,j+1}^0.
\end{aligned} \tag{3.22}$$

Using $a_{I,J}^P$, $a_{I,J}^E$, $a_{I,J}^W$, $a_{I,J}^N$, $a_{I,J}^S$ and $R_{I,J}$ to denote the coefficients and source term of Eq.(3.20), the coarse grid equation takes the following form:

$$a_{I,J}^P\delta_{I,J} = a_{I,J}^E\delta_{I+1,J} + a_{I,J}^W\delta_{I-1,J} + a_{I,J}^N\delta_{I,J+1} + a_{I,J}^S\delta_{I,J-1} + R_{I,J}, \tag{3.23}$$

where

$$\begin{aligned}
a_{I,J}^P & = a_{i,j}^P - a_{i,j+1}^S + a_{i,j+1}^P - a_{i,j}^N, \\
a_{I,J}^E & = a_{i,j}^E + a_{i,j+1}^E, \\
a_{I,J}^W & = a_{i,j}^W + a_{i,j+1}^W, \\
a_{I,J}^N & = a_{i,j+1}^N, \\
a_{I,J}^S & = a_{i,j}^S, \\
R_{I,J} & = R_{i,j}^0 + R_{i,j+1}^0.
\end{aligned} \tag{3.24}$$

With the above procedure, the coarse-grid equations can be obtained by simply combining the fine-grid equations. Note that the coarse-grid equation (Eq. 3.23) is of

identical form as the fine-grid equation (Eq. 3.15 and 3.16). The higher-level coarser-grid equations can be generated by combining the previously obtained coarse-grid equations using the same procedure. Therefore, arbitrary level grid equations can be generated if the lower level grid equations are known and no rediscrization is necessary at the coarse grid levels. An additional advantage of the technique is that since the coarse-grid equations are derived from conservative fine-grid equations, they will automatically retain the important conservation property of the fine grid.

3.2.2 Implementation of Multigrid Method

There are several strategies to implement multigrid methods, such as V cycle, W cycle, and FMV cycle. However, all of these strategies implement the MG with fixed iteration number on each grid and in a fixed sequence to employ different grid levels. For example, the simplest V cycle shown in Figure 3.3 moves sequentially from the finest grid to the coarsest grid and then from the coarsest grid to the finest grid. The sequence and iteration number on each grid remain unchanged during the outer iterations. For the strategies with fixed sequence and iteration number, sometimes, the number of iterations on a grid level is enough, and sometimes not. To overcome this disadvantage, a control strategy is suggested [93,95], in which the procedure is controlled by two parameters, α_i and ϵ_i . Here, α_i is a specified fraction of residual defined as:

$$\alpha_i = R_i/R_0, \quad (3.25)$$

where R_0 denotes the initial residual of the discretization equations on a grid level and R_i denotes the residual at the i th iteration on the same level. ϵ_i is a residual ratio defined as

$$\epsilon_i = R_i/R_{i-1}. \quad (3.26)$$

The implementation of the control strategy is outlined in Figure 3.4: on a level m , we first check the value of α_i and ϵ_i . If the value of α_i is larger than a certain value α_0 and ϵ_i is smaller than a specific constant ϵ_0 , continue the iteration on the present level m . Otherwise, i) if ϵ_i is larger than ϵ_0 , which implies that the residual

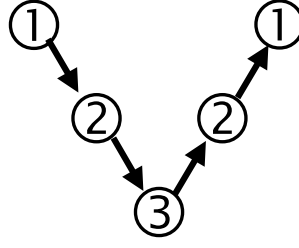


FIGURE 3.3: V cycle

reduction on the present grid level is very slow, it is worth shifting to the coarser grid level $m+1$ to obtain the correction $\delta_{I,J}$. ii) if α_i is smaller than α_0 , which implies that the residual reduction on the present grid level is adequate, move to the finer grid level $m-1$ to correct the variable. After correcting, further iterations on the finer grid level ($m-1$) should be performed to lead to a faster convergence rate. Repeat the above procedure until the errors of the finest grid equations are negligible.

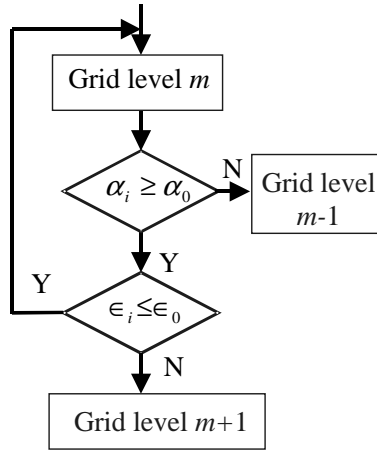


FIGURE 3.4: Implementation of the control strategy

3.2.3 Performance of Multigrid Method Using a Control Strategy

The lid-driven cavity flow at Reynolds number $Re = 400$ was chosen to test the performance of the multigrid method using the control strategy (MG-CS). The convergence property of the MG-CS is compared with that of the MG using the simplest V cycle (MG-V). To implement MG, four grid levels are employed. The grid sizes ranging from the finest to the coarsest are $48 \times 48 \times 48$, $24 \times 24 \times 24$, $12 \times 12 \times 12$,

and $6 \times 6 \times 6$, orderly. From the numerical experiments, it was found that for the MG-CS, the parameters $\alpha_0 = 0.25$ and $\epsilon_0 = 0.5$ provide good performance. These residual reduction criterions were also adopted by Hutchinson *et al.* [93].

The reduction of the residual of the pressure correction equations is investigated with respect to three different solvers, i.e. line Gauss-Seidel (LGS), MG-V and MG-CS. The residual of the pressure correction equations is calculated as

$$R_{p'} = \sum_{n=1}^N \left| \left(\sum a_{NP} \bar{p}'_{NP} + b - a_P \bar{p}'_P \right)_n \right|, \quad (3.27)$$

where N denotes the number of the control volumes of the pressure field; and the subscript NP represents the neighboring nodes; a_{NP} , a_P and b denote the coefficients and source term of the pressure correction equation (3.13), which are defined by Eq. (3.14). Usually, the iteration numbers on each grid in a V cycle are fixed. In this study using a V cycle, when the fraction of residual on a coarse grid, α_i , is smaller than 0.1, it will move to the next grid level. Otherwise, it will stay at the present grid level until the allowed maximum iteration number is reached. The maximum number for each level was 3. The number of iterations on the finest grid and the computing time needed to reduce the residuals by four orders of magnitude using the MG-V and MG-CS solver are shown in Table 3.1. It is evident that the control strategy significantly improved the performance of the multigrid technique. To reduce the residuals of the pressure field by four orders of magnitude, the finest grid takes 33 iterations for the MG-CS, while for the MG-V, the finest grid takes 120 iterations. The computational cost of the MG-CS is only about one third of that of the MG-V. The convergence histories of the LGS, MG-V and MG-CS are plotted in Figure 3.5. The convergence rate of the LGS is unacceptably slow after the first few iterations. In comparison, the slopes of the residual reduction curves of both the MG-V and MG-CS are almost constant and much steep. Evidently, the convergence rate of the MG-CS is much faster than that of the MG-V.

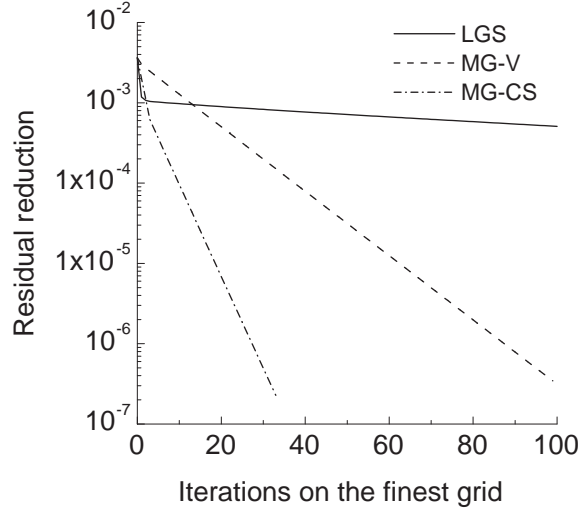


FIGURE 3.5: Convergence histories on the finest grid before update of the coefficients

TABLE 3.1: Number of iterations and computing time to reduce the residuals by four orders of magnitude

	Numbers of iterations on the finest grid	Computing time (s)
MG-V	120	180
MG-CS	33	65

3.3 Kinetic Energy Conservation

All of the transport equations are based on conservation laws and have physical conservation requirements. Discrete numerical equations should also recover the same conservation requirements, otherwise numerical instability, dissipation or unphysical behavior could happen. Most discretization schemes only conserve mass and momentum, but not the kinetic energy. The mass and momentum equations alone are sufficient to obtain a solution and typically a kinetic energy equation is not solved. For this reason, in the past, people did not pay specific attention to the kinetic energy conservation issue. Initial concerns over kinetic energy conservation were caused by research on the instability occurring in numerical computation. Recently, Morinishi *et al.* [96] presented a comprehensive examination of the conservation properties of various finite difference schemes on collocated and staggered grids. They demonstrated that methods based on collocated grid systems are inherently non-conservative. Vasilyev [97] extended this work to non-uniform grids and developed higher order schemes

which exhibit good conservation properties, except in time. Ham *et al.* [98] presented a second order scheme for staggered non-uniform grids which conserves kinetic energy both in time and space, and examined the conservation properties of the scheme in LES of a channel flow. Another attempt to construct higher order conservative schemes was undertaken by Verstappen and Veldman [99, 100]. They proposed a symmetry-preserving discretization method which conserves the total mass, momentum and kinetic energy on both uniform and non-uniform staggered grids [100].

The collocated grid system is often favored over the staggered grid system due to its simpler form. Although the inherent non-conservative performance of a collocated grid system has been demonstrated, its effects are still not clear, especially in LES. The question of interest is: how significant is the effect of the non-conservative behavior with respect to kinetic energy of collocated grids on LES of turbulence? It is a challenging question. Since the local kinetic energy cannot be defined unambiguously in a staggered grid system and it is difficult to separate the conservation errors from other errors, such as SGS modelling errors.

3.3.1 Conservation Properties of Collocated Grid Systems

To demonstrate the conservation properties of the analytical equations, the governing equations of incompressible flow are written symbolically for convenience. The continuity and momentum equations will take the following forms:

$$(Cont.) = 0 \tag{3.28}$$

and

$$\frac{\partial u_i}{\partial t} + (Conv.)_i + (Pres.)_i + (Visc.)_i = 0, \tag{3.29}$$

where

$$(Cont.) = \frac{\partial u_i}{\partial x_i}, \tag{3.30}$$

$$(Conv.)_i = \frac{\partial(u_i u_j)}{\partial x_j}, \tag{3.31}$$

$$(Pres.)_i = \frac{\partial p}{\partial x_i}, \tag{3.32}$$

$$(Visc.)_i = \frac{\partial \mathcal{T}_{ij}}{\partial x_j}, \quad (3.33)$$

where $\mathcal{T}_{ij} = \nu \frac{\partial u_i}{\partial x_j}$ is the viscous shear stress. Note that all the terms in the above equations are in divergence form, e.g. $\partial f_j(\Phi) / \partial x_j$. Integrating the general term in space, we obtain:

$$\int \int \int_V \frac{\partial f_j(\Phi)}{\partial x_j} dV = \int \int_S f(\Phi) \cdot dS. \quad (3.34)$$

From equation (3.34), one can conclude that the total quantity of Φ in the domain V only depends on the boundary condition of the domain and will remain the same if the boundary conditions are conservative, i.e. the net mass flux across boundary is zero. This behavior of a term in divergence form is defined as conservative. Note that the continuity equation is conservative *a priori*, and the convective, pressure and viscous terms, i.e. $(Conv.)_i$, $(Pres.)_i$ and $(Visc.)_i$, in the momentum equation are also conservative. Now consider the derivation of the transport equation for the kinetic energy, $K = (u_i \cdot u_i) / 2$, from the momentum equation:

$$\frac{\partial K}{\partial t} + u_i \cdot (Conv.)_i + u_i \cdot (Pres.)_i + u_i \cdot (Visc.)_i = 0. \quad (3.35)$$

The convective, pressure and viscous terms can be rewritten as follows

$$u_i \cdot (Conv.)_i = \frac{\partial u_j u_i u_i}{\partial x_i} - (u_j u_i) \cdot (Cont.), \quad (3.36)$$

$$u_i \cdot (Pres.)_i = \frac{\partial p u_i}{\partial x_i} - p \cdot (Cont.), \quad (3.37)$$

and

$$u_i \cdot (Visc.)_i = \frac{\partial \mathcal{T}_{ij} u_i}{\partial x_i} - \mathcal{T}_{ij} \cdot (Cont.). \quad (3.38)$$

Provided that the flow field satisfies the continuity equation, then the convection and pressure terms in the kinetic energy equation are conservative. The viscous term is not conservative and represents the dissipation of kinetic energy by viscosity.

Any conservative discrete mass, momentum and kinetic energy equations should recover the conservation properties defined above. For convenience, the following analysis is based on uniform grids. (One can extend the analysis to a non-uniform grid in a similar way). Morinishi *et al.* [96] noted that, provided the discrete form

of a conservative term is still in the divergence form, its conservation behavior will be recovered. Morinishi *et al.* [96] defined the finite difference operator on a uniform grid as follows:

$$\left. \frac{\delta_n \Phi}{\delta_n x_1} \right|_{x_1, x_2, x_3} \equiv \frac{\Phi(x_1 + nh_1/2, x_2, x_3) - \Phi(x_1 - nh_1/2, x_2, x_3)}{nh_1}, \quad (3.39)$$

$$\overline{\Phi}^{nx_1} \Big|_{x_1, x_2, x_3} \equiv \frac{\Phi(x_1 + nh_1/2, x_2, x_3) + \Phi(x_1 - nh_1/2, x_2, x_3)}{2}. \quad (3.40)$$

To verify the proposal by Morinishi *et al.* [96], consider the discretization of a 1D

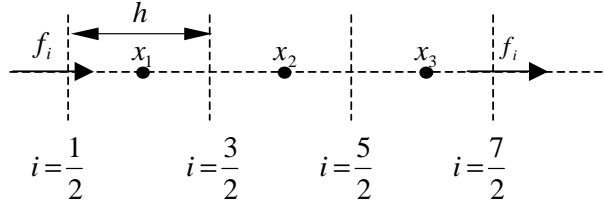


FIGURE 3.6: A 1-D uniform discrete system.

conservative term $\partial f(\Phi)/\partial x$ using a second-order central difference scheme (CDS), which yields the following divergence form in the discrete system:

$$\left. \frac{\partial f(\Phi)}{\partial x} \right|_i \approx \frac{f(\Phi_{x_i+h/2}) - f(\Phi_{x_i-h/2})}{h} = \left. \frac{\delta_1 f(\Phi)}{\delta_1 x} \right|_i. \quad (3.41)$$

Here, i represents the i th control volume. Now consider a simple discrete system with only three control volumes as shown in Figure 3.6. The integration of the conservative term $\partial f(\Phi)/\partial x$ over the domain is

$$\int_{x_{\frac{1}{2}}}^{x_{\frac{7}{2}}} \frac{\partial f(\Phi)}{\partial x} dx = \sum_{i=1}^3 \left. \frac{\delta_1 f(\Phi)}{\delta_1 x} \right|_i \cdot h = f_{\frac{7}{2}} - f_{\frac{1}{2}}. \quad (3.42)$$

This demonstrates that the discrete system (Eq. 3.41) recovers the analytical conservation behavior, i.e. the total quantity of a variable in a domain only depends on the boundary conditions. Following the conservation definition above, we investigate the conservation behavior of a collocated grid system using a 2^{nd} order CDS. On a collocated grid system, the discrete continuity equation uses the interpolated face

velocity, rather than the velocity defined at the nodes, i.e.

$$(Cont.)_i \equiv \frac{\delta_1 F_i}{\delta_1 x} = 0, \quad (3.43)$$

where F denotes the interpolated velocity on the face. For the momentum equation, the convective terms are

$$(Conv.)_i \equiv \frac{\delta_1 F_j \bar{u}_i^{1x_i}}{\delta_1 x_j}, \quad (3.44)$$

the pressure term is

$$(Pres.)_i \equiv \frac{\delta_1 \bar{p}^{1x_i}}{\delta_1 x_i}, \quad (3.45)$$

and the viscous term is

$$(Visc.)_i \equiv \frac{\delta_1}{\delta_1 x_j} \left(\nu \frac{\delta_1 \bar{u}_i^{1x_i}}{\delta_1 x_j} \right). \quad (3.46)$$

According to the conservation definition above, the discrete continuity and momentum equations are conservative on the collocated grid. The discrete kinetic energy equation can be obtained from the discrete momentum equation. The convective term is

$$\begin{aligned} u_i \cdot (Conv.)_i &= u_i \frac{\delta_1 F_j \bar{u}_i^{1x_j}}{\delta_1 x_j} \\ &= \frac{\delta_1 \left[F_j \cdot (\bar{u}_i^{1x_j})^2 / 2 \right]}{\delta_1 x_j} + (u_i^2 / 2) \frac{\delta_1 F_j}{\delta_1 x_j}. \end{aligned} \quad (3.47)$$

If the continuity equation (3.43) is satisfied, the second term of the RHS of Eq. (3.47) will disappear and the convective term is of conservative divergence form. The pressure term of the kinetic energy is

$$u_i \cdot (Pres.)_i = \frac{\delta_1 \bar{u}_i^{1x_i} \bar{p}^{1x_i}}{\delta_1 x_j} + p \frac{\delta_1 \bar{u}_i^{1x_i}}{\delta_1 x_j}. \quad (3.48)$$

Because the second term of the RHS of the equation (3.48) is not necessarily zero, therefore, the pressure term of the kinetic energy equation is not conservative. The conservation properties of the analytical and discrete equations on the collocated grid are summarized in the Table 3.2. Apparently, because in a collocated grid system, velocities are stored at the cell center while the discrete continuity equation uses the interpolated face velocity, the discrete kinetic energy equation on a collocated system cannot recover the conservation properties. In contrast, in staggered grid systems,

the velocities are stored at face of a control volume so that the discrete continuity equation uses the velocities themselves, most of them do not have this defect [96].

TABLE 3.2: Conservation properties of analytical and discrete equations

	<i>Cont.</i>	Momentum			Kinetic Energy		
		(<i>Conv.</i>)	(<i>Press.</i>)	(<i>Visc.</i>)	(<i>Conv.</i>)	(<i>Press.</i>)	(<i>Visc.</i>)
Analytical	⊙	⊙	⊙	⊙	⊙	⊙	⊗
Discrete	⊙	⊙	⊙	⊙	⊙	⊗	⊗

Note ⊙ denotes conservative and ⊗ denotes non-conservative

3.3.2 Numerical Tests on Kinetic Energy Conservation

The analytic conservation requirements dictate that the sum of kinetic energy of an inviscid flow over a domain never changes with periodic boundaries. Therefore, inviscid flow is often used to verify the conservation of a discretization system [96,97]. Following the approach of Morinishi *et al* [96], we construct an initial velocity field, which satisfies the continuity equation, and solve the flow as an inviscid flow with periodic boundary conditions. We simulate the development of the velocity field using the numerical scheme described in section 3.1 on a collocated and staggered grid, respectively. After an integration time, the error of the average kinetic energy ϵ_K defined as

$$\epsilon_K = |K(t) - K(t_0)| \quad (3.49)$$

will reflect the conservation properties of the system. Here, $K(t)$ is the total average kinetic energy of the computational domain, where t and t_0 denote the current and initial time, respectively. The 2D initial velocity field can be generated by a stream-function, such as $\psi = 2 \sin(x) \cos(y)$. Here, we employ a $2\pi \times 2\pi$ square domain and a 20×20 uniform grid. The initial velocity field is:

$$u = \frac{\partial \psi}{\partial y} = -2 \sin(x) \sin(y) \quad (3.50)$$

$$v = -\frac{\partial \psi}{\partial x} = -2 \cos(x) \cos(y), \quad (3.51)$$

which is implemented in the discrete form

$$u_{ij} = -2 \sin \left[\frac{2\pi}{N} \left(i - \frac{1}{2} \right) \right] \sin \left[\frac{2\pi}{N} \left(j - \frac{1}{2} \right) \right] \quad (3.52)$$

$$v_{ij} = -2 \cos \left[\frac{2\pi}{N} \left(i - \frac{1}{2} \right) \right] \cos \left[\frac{2\pi}{N} \left(j - \frac{1}{2} \right) \right]. \quad (3.53)$$

The total average kinetic energy of the computational domain is calculated as follows:

$$K(t) = \frac{1}{V} \sum_{i=1}^N \sum_{j=1}^M \left[\frac{1}{2} (u_{ij}^2 + v_{ij}^2) \cdot V_{ij} \right], \quad (3.54)$$

where $N = 20$ and $M = 20$ are dimensions of the computational domain, V denotes the area of the computational domain and V_{ij} is the area of the control volume (i, j) . Note that for a staggered grid system, the total kinetic energy defined by Eq. (3.54) is not unambiguous since the individual velocity components are stored in different locations.

Figure 3.7 shows the error of the total kinetic energy, ϵ_K , after an integration time of $\Delta t = 10L \left(2\pi \sqrt{K(t_0)} \right)$, where $L = 2\pi$ is the characteristic length of the square domain. Because the present code uses the second-order Adams-Bashforth time-stepping scheme which introduces a slight dissipative error, the kinetic energy is not exactly conserved even on the staggered grid system. However, as expected, the time-stepping error decreases with the square of Δt on the conservative staggered grid, whereas on the collocated grid, the error decreases with Δt , which implies that the scheme introduces not only 2^{nd} order time-stepping error but also errors due to the spatial discretization. We also note that the errors of the staggered grid system are much smaller than that for the collocated grid systems for the same time step.

3.4 Test Problems

3.4.1 Lid Driven Cavity Flow

Although the collocated grid system cannot conserve kinetic energy and the conservation errors lead to numerical dissipation (see section 3.3.1), the issue is: how

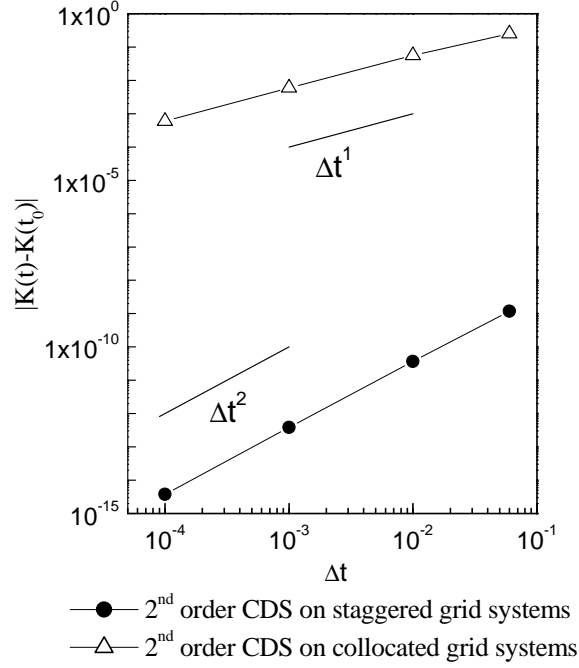


FIGURE 3.7: Error of the average kinetic energy.

significant is the numerical dissipation in comparison to the viscous and turbulent dissipation present in a real flow? In this dissertation, a benchmark flow, i.e. lid driven cavity (LDC) flow, is used as one of the test problems for the assessment of the collocated grid system and validation of the present LES code. As a benchmark flow, studies on LDC flows can be found in many references [101–104]. Figure 3.8 shows the geometry and boundary conditions of a 3-D lid driven flow in a cubical cavity, in which we assume that the lid is infinitely long and moves in horizontal direction. The flow condition is characterized by a Reynolds number, Re_D , which is defined as

$$Re_D = \frac{UD}{\nu}, \quad (3.55)$$

where U is the velocity of the lid and D denotes the width of the cavity.

3.4.1.1 Steady Laminar Flow ($Re_D = 400$)

The simulation of the LDC flow is first performed for $Re_D = 400$. The selected low Reynolds number $Re_D = 400$ ensures that the simulated flows are in the laminar regime. Therefore, the effect of SGS models is excluded in the test. The computational domain of the test problem is $15cm \times 15cm \times 15cm$, and two uniform grids of

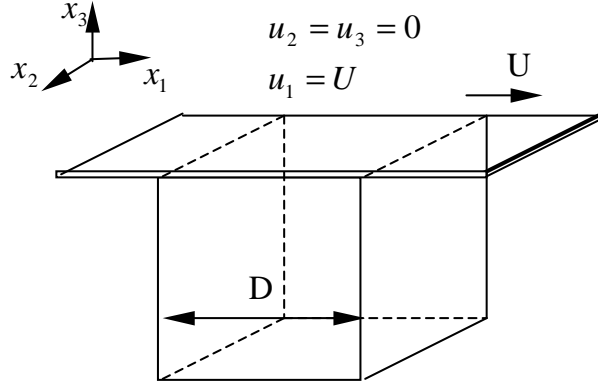


FIGURE 3.8: Geometry and boundary conditions of LDC flow

size $32 \times 32 \times 32$ and $48 \times 48 \times 48$ are adopted in the test. No-slip and no-penetration boundary conditions were imposed on the velocity components at the walls. The momentum equations were solved using the numerical method discribed in section 3.1.

The validity of the numerical solution is assessed by the residual of the pressure field, $R_{p'}$, defined by Eq.(3.27), and mass residual, R_m , defined as

$$R_m = \sum_{n=1}^N |b_m|, \quad (3.56)$$

where b_m is net mass flux out of the m th control volume, i.e.

$$b_m = (\dot{m}_e - \dot{m}_w) + (\dot{m}_s - \dot{m}_n) + (\dot{m}_f - \dot{m}_b), \quad (3.57)$$

where \dot{m} denotes the mass flux through the faces of the control volume. Table 3.3 shows the mass and pressure residuals of simulations on two different collocated grids, and indicates that the predicted fields satisfy these discrete transport equations.

TABLE 3.3: Mass residuals and residuals of the pressure field

Grid size	Number of outer iterations	R_m	R_p
$32 \times 32 \times 32$	5400	1.84×10^{-10}	1.01×10^{-10}
$48 \times 48 \times 48$	5800	4.28×10^{-10}	3.39×10^{-10}

The simulation results based on the collocated grid of size $48 \times 48 \times 48$ are

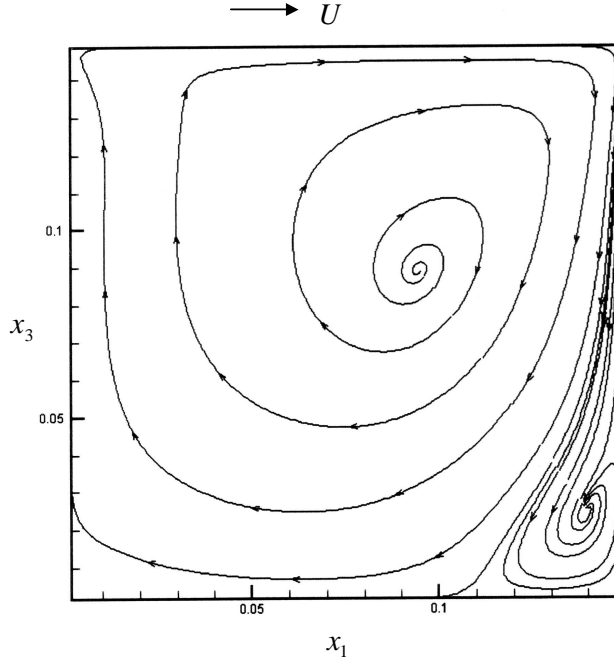


FIGURE 3.9: Streamlines on the $x_1 - x_3$ plane at $x_2/D = 0.5$ using grid size 48×48 ($Re_D = 400$)

shown in Figures 3.9-3.11. Figure 3.9 plots the streamlines on the $x_1 - x_3$ plane at $x_2/D = 0.5$. Driven by the lid, a primary vortex is observed near the center of the cavity. A counter-rotation recirculating flow is also found in the lower corner region. The velocity vectors on this plane are also plotted in Figure 3.10. The vectors are normalized by the largest vector in the plane to make the plots clearer. The pattern of the velocity vectors is consistent with the streamline patterns shown in Figure 3.9. The velocity vectors in the $x_2 - x_3$ plane at $x_1/D = 0.5$ is plotted in Figure 3.11. As shown in the figure, two distinct secondary vortices are observed near the bottom due to the effect of the side walls. The flow patterns obtained by the present 3-D code on the collocated grid presented here are similar to those in previous studies [102–105].

A more precise evaluation of the present collocated grid system is obtained by comparing the simulation results for the peak values of the velocity profiles on the centerlines of the cavity to the results of other authors. As shown in Table 3.4, the results of Ku *et al.* [102] are viewed as benchmark results, since in their work, the pseudo-spectral method was applied. In the present simulations, even a relatively coarse uniform collocated grid ($32 \times 32 \times 32$) can provide satisfying results due to the laminar flow characteristics at the low Reynolds number. In comparison, Huang [105] used a non-uniform grid, which was refined near the wall to capture the velocity

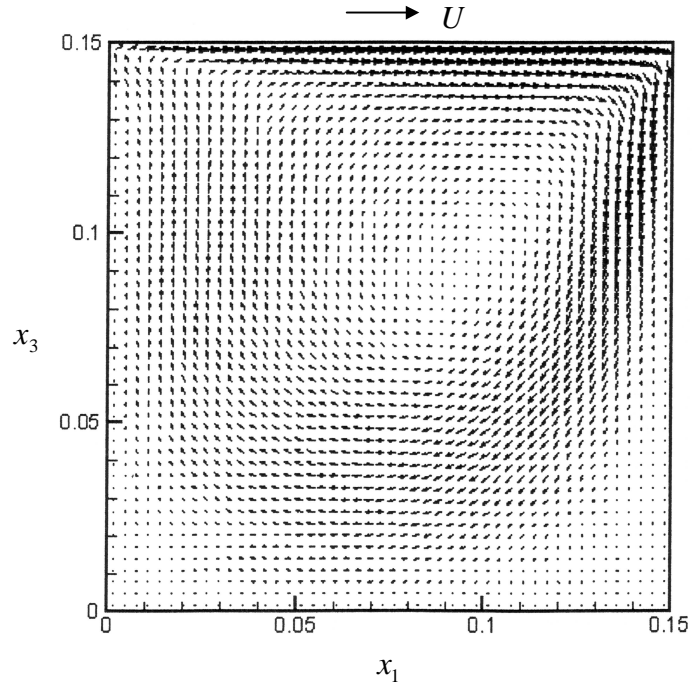


FIGURE 3.10: Velocity vectors of the $x_1 - x_3$ plane at $x_2/D = 0.5$ using grid size $48 \times 48 \times 48$ ($Re_D = 400$)

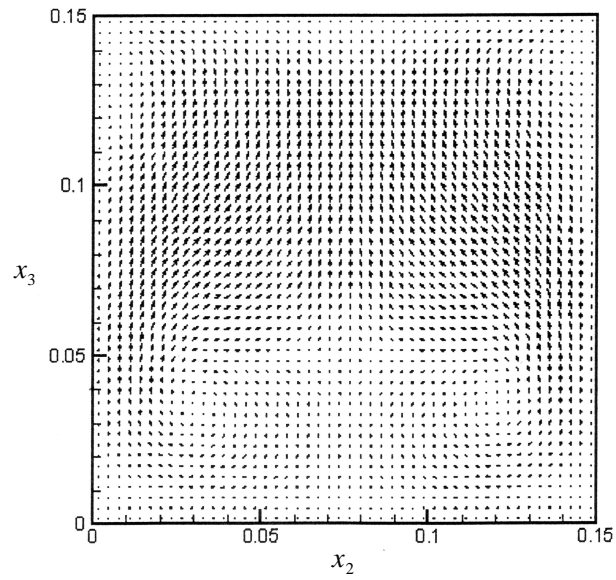


FIGURE 3.11: Velocity vectors of the $x_2 - x_3$ plane at $x_1/D = 0.5$ using grid size $48 \times 48 \times 48$ ($Re_D = 400$)

variation in the near-wall region more accurately, and thus give better predictions of the peak values.

TABLE 3.4: Peak values for 3-D LDC flow at $Re_D = 400$

Method	Grid size	u_{1min}	u_{3min}	u_{3max}
Present	$31 \times 31 \times 31$	-0.2105	-0.3465	0.1859
Present	$48 \times 48 \times 48$	-0.2226	-0.3646	0.1923
Huang(1998)	$31 \times 31 \times 31$	-0.232	-0.380	0.205
Deng <i>et al.</i> (1994)	$64 \times 64 \times 64$	-0.2330	-0.3765	0.2046
Babu <i>et al.</i> (1994)	$63 \times 63 \times 63$	-0.2083	-0.3084	0.1773
Ku <i>et al.</i> (1987)	— — —	-0.2378	-0.3791	0.2053

To further investigate the collocated grid system, we also compare the velocity profiles predicted by the collocated grid to those by a staggered grid system in Figure 3.12. Both collocated and staggered grid system are uniform and of size $32 \times 32 \times 32$. Figure 3.12 indicates that both collocated and staggered grid systems yield satisfying results which are consistent with the benchmark results of Ku *et al.* [102]. The difference between the solutions on the two different grid systems is minimal and perhaps insignificant (the difference between the peak values is less than 2%). This result indicates that the kinetic energy conservation issue may not be very important for steady flows in which the time accurate advancement is not important. The ability of the present collocated code to accurately advance in time an unsteady flow should be also investigated.

3.4.1.2 Start-up LDC Flow ($Re_D = 1000$)

Obviously, accurate time advancement is a necessary requirement for LES. The study of Guermond *et al.* on the 3-D LDC start-up flow ($Re_D = 1000$) [106] provides a good test case to evaluate the time accuracy of the numerical schemes on collocated and staggered grids. Their paper presented both experimental and numerical results of the flow development in a cavity with time. The flow is driven by a lid which is accelerated from rest to a constant velocity of $U_C = 0.018\text{m/s}$. The accelerating process adopted by the simulation is approximated by the equation

$$U(t) = 0.018 [1 - \exp(-100t)], \quad (3.58)$$

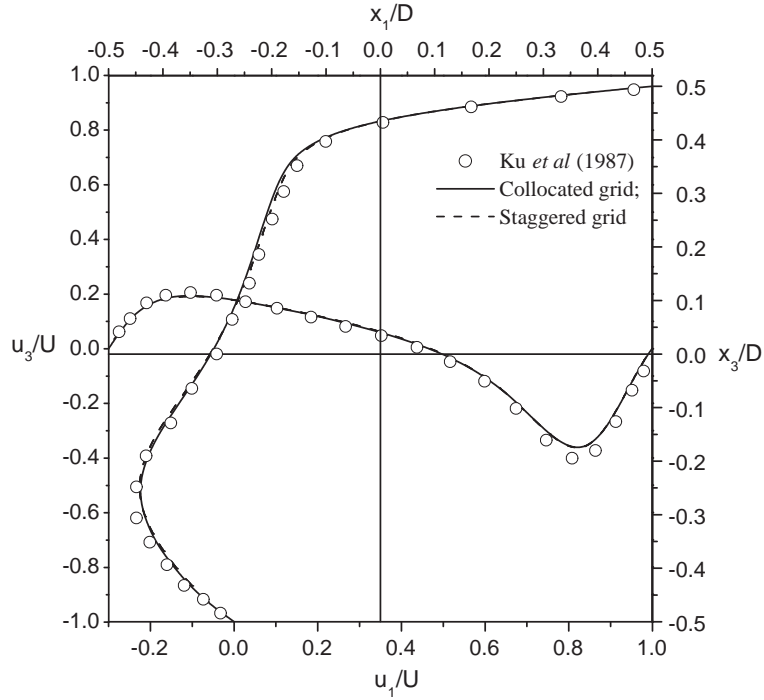


FIGURE 3.12: Profiles of velocity components on the central lines of the cavity ($Re_D = 400$).

where $U(t)$ is the lid velocity. Guermond *et al.* [106] measured and calculated the flow field at different times. Here, the flow field is advanced to $t = 4$ (using D/U_C as the reference time scale) using the 2^{nd} order explicit Adams-Bashforth scheme based on a uniform collocated and staggered grid of size $48 \times 48 \times 48$, respectively. In Figure 3.13, the profiles of the velocity components in the center plane are plotted and compared to the experimental data of Guermond *et al.* [106]. The results indicate that both the collocated and staggered grid give good predictions, and the difference between them is relatively small. As shown in Table 3.5, the difference between the peak values predicted by the two grids is less than 3%.

TABLE 3.5: Peak values for start-up LDC flow at $Re_D = 1000$

	u_{1min}/U_C	u_{3min}/U_C	u_{3max}/U_C
Collocated	-0.0766	-0.164	0.0466
Staggered	-0.0768	-0.160	0.0462
$ (u_{stag} - u_{coll})/u_{coll} $	0.26%	2.55%	0.85%

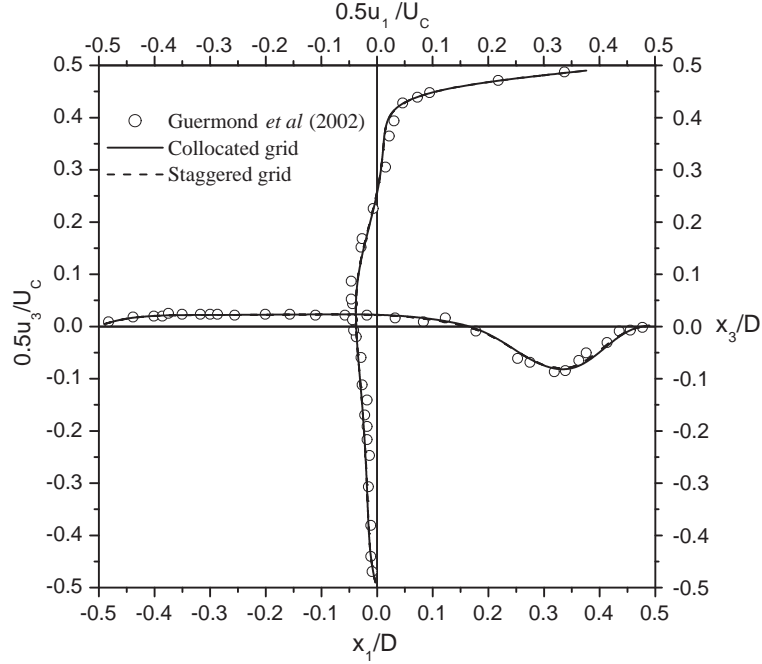


FIGURE 3.13: Profiles of velocity components on the central lines of the cavity at $t = 4$ ($Re_D = 1000$).

3.4.2 Turbulent Channel Flow at $Re_\tau = 180$

Besides the laminar test problems, a turbulent channel flow is also used for validation of the present LES code and assessment of SGS stress models. As one of the simplest wall-bounded flows, turbulent channel flows has been numerically studied by many authors [107–112]. The extensive DNS databases available make the flow a good benchmark flow to validate the LES code with respect to wall bounded turbulence. Here, we consider the channel flow at $Re_\tau = 180$, where $Re_\tau \stackrel{\text{def}}{=} u_\tau \delta / \nu$ and u_τ is the friction velocity on the wall. The geometry and computational domain of the test flow are shown in Figure 3.14. As suggested by Moser *et al* [109], the computational domain is $4\pi\delta \times 2\delta \times 4\pi\delta/3$, corresponding to the streamwise (x_1), wall-normal (x_2) and spanwise (x_3) directions, respectively. A grid of $48 \times 48 \times 64$ (in x_1, x_2, x_3) control volumes is adopted for discretization of the computational domain. The collocated grid is uniform in the streamwise and spanwise directions. In the wall-normal direction corresponding to the channel gap $-1 \leq x_2/\delta \leq 1$, the grid is refined near the wall using a hyperbolic-tangent function, i.e. the locations of interfaces of control volumes

in the direction are given as follows:

$$f_j = \frac{\tanh(a\xi_j)}{\tanh(a)}, \quad (3.59)$$

and

$$\xi_j = -1 + 2(j-1)/N_2 \quad (j = 1, 2, \dots, N_2 + 1). \quad (3.60)$$

where N_2 is the total number of control volumes in the wall-normal direction, and a is an adjustable parameter.

Fully developed turbulent channel flow is viewed as homogeneous in the stream-wise and spanwise directions, and periodic boundary conditions are used in these directions. Periodic boundary conditions assume that velocity, pressure, and their gradients on the boundaries are the same, which are effective only if the computational domain is large enough to include the largest eddies in the flow. As suggested by Moin and Kim [107], the computational domain is at least twice as large as the dimension of 3.2δ and 1.6δ in the x_1 and x_3 direction, respectively. The no-slip and no-penetration conditions are used in the normal direction at the solid walls.

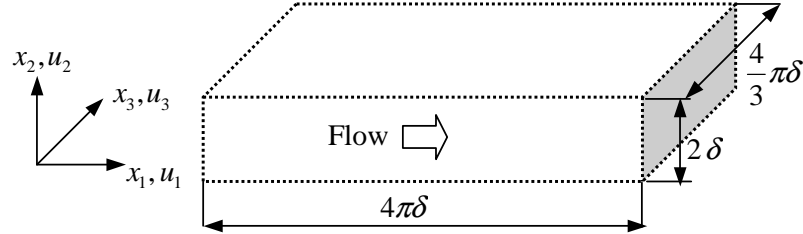


FIGURE 3.14: Computational domain and coordinate system ($Re_\tau = 180$).

3.4.2.1 Governing Equations for the Large-scale Field

In LES, the filtered continuity and Navier-Stokes equations for the large-scale field of a channel flow are

$$\frac{\partial \bar{u}_i}{\partial x_i} = 0, \quad (3.61)$$

$$\frac{\partial \bar{u}_i}{\partial t} + \frac{\partial}{\partial x_j} (\bar{u}_i \bar{u}_j) = -\frac{1}{\rho} \frac{\partial \bar{P}}{\partial x_i} \delta_{1i} + \nu \frac{\partial^2 \bar{u}_i}{\partial x_j \partial x_j} - \frac{\partial \tau_{ij}}{\partial x_j} - \frac{1}{\rho} \frac{\partial \bar{p}}{\partial x_i}, \quad (3.62)$$

where $(\partial \bar{P} / \partial x_i) \delta_{1i}$ is the main pressure gradient in the streamwise direction, which is determined by the flow Reynolds number, while $\partial \bar{p} / \partial x_i$ denotes the resolved fluctuating pressure gradient after extracting the mean pressure gradient. $\tau_{ij} \stackrel{\text{def}}{=} \overline{u_i u_j} - \bar{u}_i \bar{u}_j$ is the SGS stress tensor, which represents the effect of the SGS motions and needs to be modelled to close the above system of governing equations. Here the traditional SM [113] and DM described in section 2.3 are applied for the SGS stress tensor.

3.4.2.2 Analysis of Results

The LES predictions using the present collocated code are compared with the DNS data given by Kim *et al.* [108] and Moser *et al.* [109]. Note that the resolved quantities in LES ARE theoretically different from those in DNS, for instance, the DNS shear stress is actually balanced by the resolved shear stress and the SGS stress in LES. However, because in LES, the resolved scale is dominative in comparison with the SGS scale, it is still popular to compare the resolved scale directly to the DNS results in literature. Here, all quantities denoted by $\langle \cdot \rangle$ are obtained using both spatial averaging in the homogeneous plane and time averaging for more than 10000 time steps after the flow is fully developed. The superscript + denotes the quantities which are non-dimensionalized using the friction velocity u_τ .

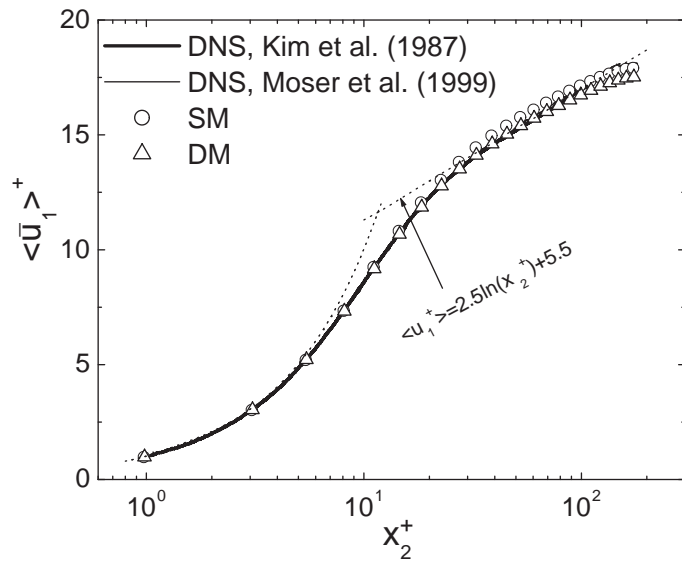


FIGURE 3.15: Mean velocity profile using wall coordinates ($Re_\tau = 180$).

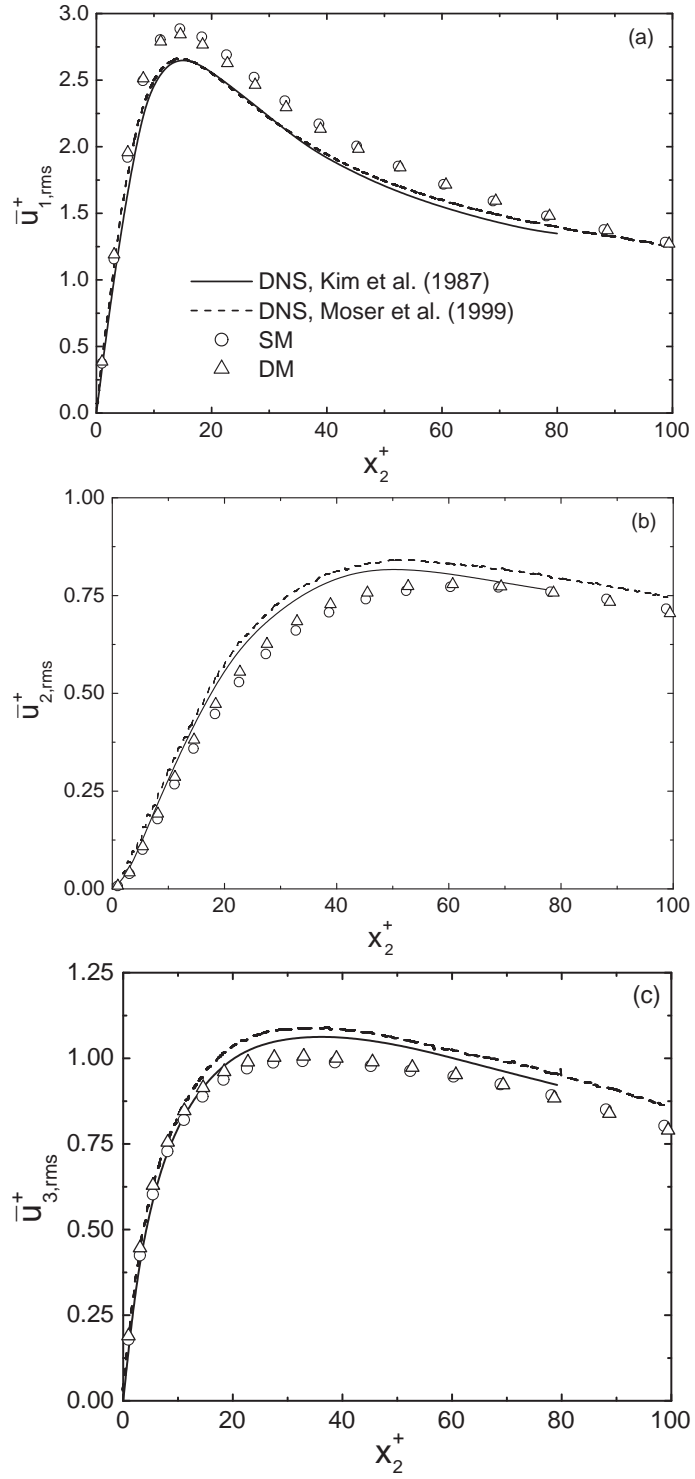


FIGURE 3.16: Resolved velocity fluctuations in wall coordinates: (a) streamwise; (b) wall-normal; (c) spanwise. ($Re_\tau = 180$).

The mean resolved streamwise velocity normalized by u_τ is shown in Figure 3.15 using wall coordinates. It is observed that both the SM and DM yield satisfactory predictions which are consistent with the DNS data (The DNS data of Kim *et al.* [108] and Moser *et al.* [109] almost overlap). Compared with that yielded by the DM, the profile of the mean resolved streamwise velocity predicted by the SM shifts upward slightly in the logarithmic region. Figure 3.16 plots the resolved velocity fluctuations and DNS data by Kim *et al.* [108] and Moser *et al.* [109] for comparison. Here, $\bar{u}_{1,rms}^+$, $\bar{u}_{2,rms}^+$ and $\bar{u}_{3,rms}^+$ denote the resolved root-mean-square streamwise (x_1), wall-normal (x_2) and spanwise (x_3) fluctuation components, respectively, which are normalized by the friction velocity u_τ . It can be seen in Figure 3.16a, both the SM and DM prediction of the resolved streamwise component in general agree with the DNS data, although they slightly overpredict the peak value near the wall. Figure 3.16b and c indicate that both the SM and DM underpredict the peak value of the resolved wall-normal and spanwise velocity fluctuations. The difference in peak value between the LES predictions and the DNS results is shown in Table 3.6. In general, DM predictions of the turbulence intensities are slightly closer to the DNS data.

TABLE 3.6: Peak values of channel flow at $Re_\tau = 180$

	$\bar{u}_{1,rms}^+$	$\bar{u}_{2,rms}^+$	$\bar{u}_{3,rms}^+$
DNS(Moser <i>et al</i> [109])	2.661	0.841	1.091
SM (*)	2.885 (8.4%)	0.772 (8.2%)	0.992 (9.1%)
DM (**)	2.843 (6.8%)	0.778 (7.5%)	1.005 (7.9%)

Note: * and ** denote the difference between the DNS data and LES predictions using the SM and DM, respectively.

The distribution of the resolved Reynolds shear stress is shown in Figure 3.17. The resolved Reynolds shear stress is normalized by $(u_\tau)^2$ and denoted as $-\langle \bar{u}_1'' \bar{u}_2'' \rangle^+$. Figure 3.17a plots the $\langle \bar{u}_1'' \bar{u}_2'' \rangle^+$ distribution across the channel. Results for only half of the channel are displayed due to the symmetrical property of the plot. Figure 3.17b shows the near-wall performance of $-\langle \bar{u}_1'' \bar{u}_2'' \rangle^+$ in wall coordinates. The magnitude of the SGS shear stress $-\langle \tau_{12} \rangle$ is an order of magnitude smaller than the resolved Reynolds shear stress, therefore, the resolved shear stress is compared to the DNS data directly. Figure 3.17a and b indicate that both the SM and DM yield satisfactory predictions of the Reynolds shear stress which are consistent with the DNS data. The

balance equation derived from the streamwise momentum equation is

$$\nu \frac{\partial \langle \bar{u}_1 \rangle}{\partial x_2} - \langle \bar{u}_1'' \bar{u}_2'' \rangle - \langle \tau_{12} \rangle = \frac{1}{\rho} \frac{\partial \langle \bar{p} \rangle}{\partial x_1} x_2 + \frac{\tau_w}{\rho}. \quad (3.63)$$

The three terms on the left-hand side (LHS) of Eq. (3.63) represent the resolved viscous shear stress, resolved Reynolds (or, turbulent) shear stress, and SGS shear stress, respectively. The two terms on the right-hand side (RHS) of the equation represent the resolved integrated driving force due to the mean streamwise pressure gradient, and the resolved viscous shear stress at the wall, respectively. The individual shear stresses identified in Eq. 3.63 are normalized by u_τ and shown in Figure 3.18. Since the SGS shear stress component $-\langle \tau_{12} \rangle$ is an order of magnitude smaller than the other two terms, it is not shown here. Again, the difference between the SM and DM predictions is almost insignificant.

3.5 Summary

In this chapter, a 3-D LES code using a collocated grid system has been developed and tested. The code is based on the fractional time-step technique [67, 88], in which the discretized Navier-Stokes equations are solved in two steps: first, the estimated velocity field is calculated without updating the pressure field, and then the pressure correction Poisson equation is solved to satisfy the continuity equation and the estimated velocity field is corrected using the new pressure field. In solving the pressure correction Poisson equation, a control strategy is adopted for the multigrid solver. It employs a flexible procedure which automatically adjusts to the convergence rate on each grid level. The performance of the MG-CS is tested using the LDC flow at $Re_D = 400$. Compared with the MG-V and LGS schemes, the MG-CS greatly accelerates the convergence rate of the pressure field. The computational cost of the MG-CS scheme is only about one third of that of the MG-V scheme.

The discretized equations should recover the inherent conservation nature of the analytical governing equations. Collocated grid systems do not conserve kinetic energy inherently [96]. The energy conservation properties of the present collocated grid system are investigated following previous works [96–98]. The development of a

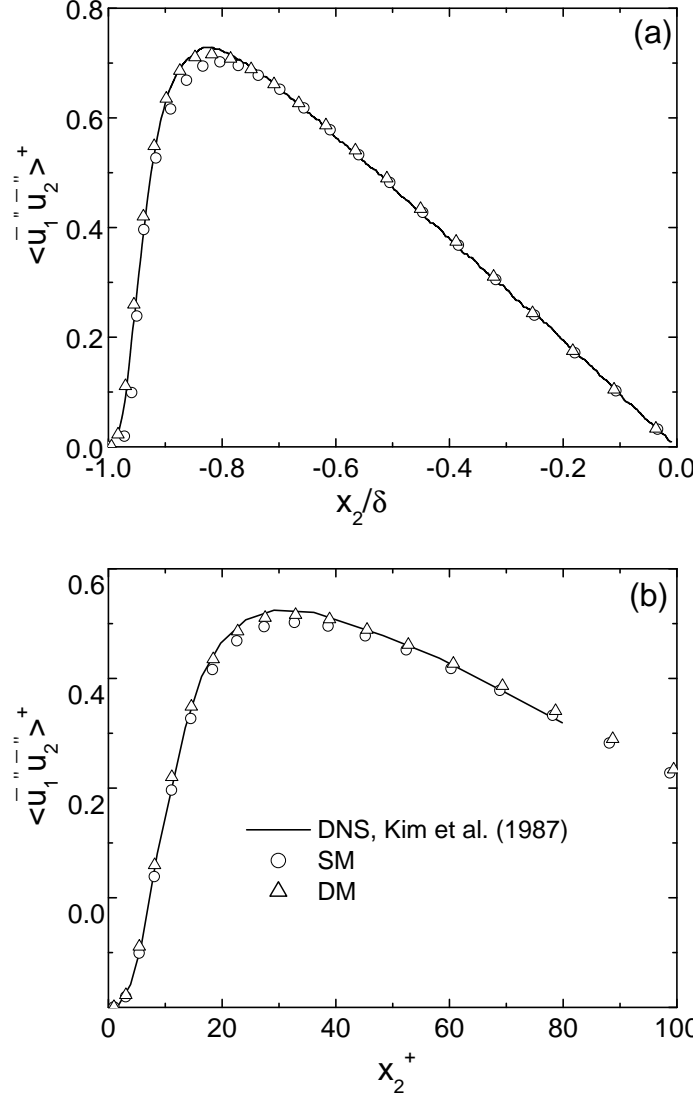


FIGURE 3.17: Resolved Reynolds shear stress distribution in wall-normal direction: (a) for half-channel (b) in wall coordinates ($Re_\tau = 180$).

periodic inviscid flow field is simulated on both staggered and collocated grid systems. After an integration time, the error of the average kinetic energy on the staggered grid system is second order with respect to the time step, whereas the error on the collocated grid is first order, which indicates that the collocated system introduces both the time-stepping and spatial discretization errors. To investigate the effect of the numerical dissipation on the prediction of a real flow, the collocated grid system is also tested using a steady laminar LDC at $Re_D = 400$ and a unsteady start-up flow at $Re_D = 1000$. It is found that, although the collocated grid system introduces conservation errors for the kinetic energy, it yields satisfactory predictions in comparison with those given by a staggered grid. This kinetic energy conservation issue is not very important for the steady LDC flow and unsteady start-up flow.

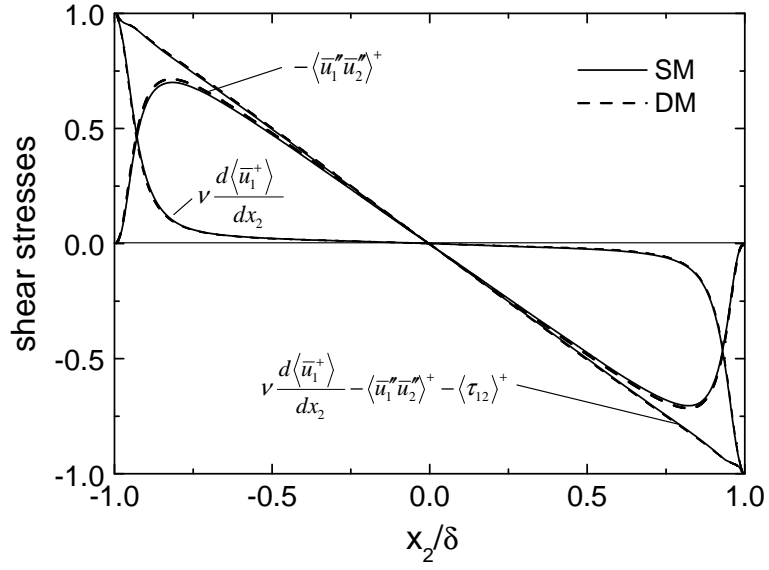


FIGURE 3.18: Non-dimensional shear stress distribution across the channel ($Re_\tau = 180$).

Finally, the present LES code based on the collocated grid system is tested using a low Reynolds number channel flow. The results indicate that the present LES code yields satisfactory predictions of the turbulent flow in comparison with DNS data. Based on the above investigations, a collocated grid system can be used with confidence for LES of turbulent flows.

Chapter 4

LES of Channel Flow at $Re_\tau = 395$ and Investigation of the Dynamic Nonlinear SGS Stress Model

4.1 Introduction

The presence of solid walls will affect the physics of the flow, especially the subgrid scale motions. For example, the growth of the small scales near the wall is inhibited and the exchange mechanisms between the large and small scales in this region are altered. Therefore, for LES of wall-bounded flows, the SGS models must be able to account for the significant effect of the wall. Fully developed channel flow is one of the most widely investigated wall-bounded flows, and due to its geometric simplicity, it is also a classic benchmark flow for numerical testing and physical understanding of the mechanics of wall-bounded turbulence. Because of the presence of high shear and small-scale turbulence near the wall, experimental measurement of near-wall flow is relatively difficult and the results are often inconsistent. With the development of numerical simulation techniques, turbulent channel flow at relatively low Reynolds number has been first extensively investigated in literature. The first application of LES to channel flow was made by Deardorff [114]. In his pioneering work, using only 6720 grid cells, he was able to capture several features of turbulent channel flow. His work indicated a potential application of LES in the study of three-dimensional turbulent flows. Following Deardorff's work, Schumann [115, 116] and Moin *et al.* [117] calculated turbulent channel flow using a much more refined grid. Moin and

Kim [107] later applied LES to channel flow at relatively higher Reynolds number $Re_\tau = 640$ and found that the resolution in the spanwise direction must be fine to obtain accurate solution. Instead of using a conventional Smagorinsky model for the SGS stress tensor, Moin and Kim [107] suggested a modified eddy viscosity model which added a second term to the Smagorinsky model to account for the inadequate resolution in the spanwise direction. Their work showed that with proper SGS models, LES is able to obtain detailed, instantaneous information of turbulent flow at an affordable resolution. Later, a DNS of a channel flow at $Re_\tau = 180$ was carried out by the same research group to provide benchmark data for comparison [118]. As an extension of their work, Moser *et al.* [109] conducted DNS of turbulent channel flow at several Reynolds numbers up to $Re_\tau = 590$. They reported that the wall-bounded turbulent flows at higher Reynolds numbers revealed some Reynolds number effects. For example, the mean velocity profiles at the $Re_\tau = 395$ and $Re_\tau = 590$ agree out to $y^+ = 200$ with an apparent logarithmic region, while the velocity profile at $Re_\tau = 180$ deviates from the higher Reynolds number cases beyond $x_2^+ = 10$.

In this chapter, an LES study of a channel flow at a Reynolds number of $Re_\tau = 395$ is reported. Here, $Re_\tau \stackrel{\text{def}}{=} u_\tau \delta / \nu$ and u_τ is the friction velocity. The newly proposed DNM [9] for the SGS stress is investigated and compared to the linear DM using two different averaging schemes, i.e. local and plane averaging. The present LES results are compared to the DNS results by Moser *et al.* [109]. In LES, since the small scales of motion are not numerically resolved, the SGS models need mimic the interaction between the large and small scale motions. Therefore, one of the important issues in SGS modelling is related to the turbulent kinetic energy (TKE) transfer between the large and small scales. In this chapter, the TKE dissipation produced by these two SGS models is investigated using both the conventional LES approach and the methodology of turbulence geometrical statistics reviewed in section 1.3. In contrast to the conventional methodology, turbulent geometrical statistics investigates the local geometrical properties and captures the statistical features of the small-scale flow structures.

4.2 Basic Concepts Related to Turbulence Geometrical Statistics

It is known that the local small-scale flow structures are more related to the velocity gradients rather than velocity itself. The velocity gradient tensor can be decomposed into a symmetric part and a skew-symmetric part, which are referred to as the strain rate tensor [i.e., $S_{ij} = (u_{i,j} + u_{j,i})/2$] and rotation rate tensor [i.e., $\Omega_{ij} = (u_{i,j} - u_{j,i})/2$], respectively. The vorticity vector, $\boldsymbol{\omega}$, can be derived from the rotation rate tensor, or, directly from the velocity gradient as $\omega_i = \varepsilon_{ijk}\Omega_{kj} = \varepsilon_{ijk}u_{k,j}$. Here, ε_{ijk} is the Levi-Civita symbol. The dynamical behavior of the velocity gradient tensor is of fundamental importance for many physical quantities. Besides S_{ij} , Ω_{ij} and ω_i , the velocity gradient also determines the vortex stretching vector, helicity density, enstrophy and enstrophy generation, and turbulent kinetic energy dissipation rate.

Because the second-order tensor S_{ij} is real and symmetric, it has three real eigenvalues which can be arranged in descending order as $\alpha_S \geq \beta_S \geq \gamma_S$. For incompressible flows, only two of the three eigenvalues of the resolved strain rate tensor are independent due to the continuity constraint, i.e.

$$\alpha_S + \beta_S + \gamma_S = 0. \quad (4.1)$$

The ratio between these three eigenvalues of S_{ij} is very useful for classifying the structural configurations of local fluid element deformations. The local fluid element deformation pattern is identified as *purely 2-dimensional* (PTD) if $\alpha_S : \beta_S : \gamma_S = 1 : 0 : -1$; *axisymmetric expansion* if $\alpha_S : \beta_S : \gamma_S = 1 : 1 : -2$; *axisymmetric compression* if $\alpha_S : \beta_S : \gamma_S = 2 : -1 : -1$; and *quasi-2-dimensional* (QTD) if $|\beta_S| \neq 0$, $|\beta_S| < |\alpha_S|$ and $|\beta_S| < |\gamma_S|$.

Since only two of the three eigenvalues of S_{ij} are independent for incompressible flow, the local fluid element deformation pattern derived from S_{ij} can be determined by a single non-dimensional parameter. Studies on the relative principal value of the strain rate tensor can be traced back to the pioneering work of Betchov [119], who analyzed the magnitude of the eigenvalues using some fundamental algebraic inequalities.

ities. Based on analysis of DNS data, Ashurst *et al.* [48] and Kerr [49] demonstrated that the ratio of the principal values of S_{ij} of homogeneous turbulence tends to be $\alpha_S : \beta_S : \gamma_S = 3 : 1 : -4$ indicating a dominant QTD flow pattern. In their statistical calculations [48, 49], the following non-dimensional parameter was suggested:

$$\beta^* = \frac{\sqrt{6}\beta_S}{(\alpha_S^2 + \beta_S^2 + \gamma_S^2)^{1/2}} \quad (4.2)$$

The experiment of Tsinober *et al.* [44] based on hot-wire measurements of grid generated turbulence in a wind tunnel further confirmed the result of Ashurst *et al.* [48] and Kerr [49], i.e. $\beta^* \approx 0.4$ which corresponds to $\alpha_S : \beta_S : \gamma_S \approx 3.74 : 1 : -4.74$ (the ratio $3.1 : 1 : -3.8$ was instead presented in their paper). A similar observation was reported in the work of She *et al.* [50] based on analyzing a DNS database of homogeneous turbulence. However, Lund and Rogers [42] later pointed out that the statistical results based on Eq.(4.2) can be biased and it leads to the incorrect conclusion that a state of local axisymmetric expansion does not exist in turbulent flows. Instead, they proposed an alternative non-dimensional parameter given by:

$$s^* = \frac{-3\sqrt{6}\alpha_S\beta_S\gamma_S}{(\alpha_S^2 + \beta_S^2 + \gamma_S^2)^{3/2}} \quad (4.3)$$

With the new parameterization, Lund and Rogers [42] investigated a DNS database of isotropic incompressible turbulence. They observed that the most probable state is $S^* = 1$ for flow regions with a low dissipation rate, and $S^* = 0.9$ for flow regions with a high dissipation rate. The state of $S^* = 1$ corresponds to axisymmetric expansion pattern (i.e., $\alpha_S : \beta_S : \gamma_S = 1 : 1 : -2$) and the state of $S^* = 0.9$ corresponds to the ratio $\alpha_S : \beta_S : \gamma_S = 1.7 : 1 : -2.7$. In general, any local fluid element deformation patterns corresponding to $S^* \geq 0.9$ can be approximately classified as axisymmetric expansion. The result of Lund and Rogers [42] that the axisymmetric expansion is the most probable state in isotropic turbulence was later confirmed by a number of researchers, including Soria *et al.* [120] and Blackburn *et al.* [53] who studied the eigenvalue ratio using the phase plane of tensorial invariants; and Tao *et al.* [54] who analyzed HPIV measurements using an *a priori* LES approach.

The non-dimensional parameter is clearly not unique, but there must be a one-to-one relationship between any two of them. A unique dependence between β^* and

s^* exists and is given by [42]:

$$s^* = \beta^*(3 - \beta^*/2) \quad (4.4)$$

The inverse relation is

$$\beta^* = 2 \cos \left[\frac{5}{3}\pi - \frac{1}{3} \cos^{-1}(s^*) \right] \quad (4.5)$$

The relation between β^* and β_S/α_S is:

$$\frac{\beta_S}{\alpha_S} = \frac{2\beta^*}{\sqrt{3(4 - \beta^{*2})} - \beta^*} \quad (4.6)$$

The relationship between s^* and β_S/α_S can be obtained by combining Eq.(4.6) and Eq.(4.4) or Eq.(4.5). Since there are only two independent eigenvalues for S_{ij} for incompressible flow, the most probable ratio of $\alpha_S : \beta_S : \gamma_S$ can be calculated using the above relationship Eq.(4.1, 4.4 - 4.6), provide that the most probable value of either β^* , s^* or β_S/α_S is determined. For instance, if the most probable value of β_S is 0.480, using Eq.(4.6), we obtain $\beta_S/\alpha_S = 0.333$. Due to the continuity constraint (Eq.4.1), $\gamma_S/\alpha_S = -1 - \beta_S/\alpha_S = -1 - 0.333 = -1.333$, therefore, $\alpha_S : \beta_S : \gamma_S = 1 : 0.333 : -1.333 \approx 3 : 1 : -4$.

The velocity gradient tensor $u_{i,j}$ can be decomposed into a symmetric part S_{ij} and a skew-symmetric part Ω_{ij} , which represent the strain-rate and rotation-rate tensor, respectively. The vorticity vector $\boldsymbol{\omega}$ can be derived from the rotation rate tensor or directly from the velocity gradient as $\omega_i = \varepsilon_{ijk}\Omega_{kj} = \varepsilon_{ijk}u_{k,j}$. The dynamical behavior of the velocity gradient tensor is of fundamental importance for understanding coherent structures because it governs a variety of physical phenomena such as local vortex stretching and TKE dissipation. If the resolved scale strain rate tensor acts to stretch the material line element aligned with the resolved-scale vorticity $\boldsymbol{\omega}$, then the magnitude of $\boldsymbol{\omega}$ increases. This is the phenomenon of vortex stretching, and corresponding *vortex stretching vector* \mathbf{w} is defined as [68]:

$$w_i = \omega_j S_{ij} \quad (4.7)$$

The increase of angular velocity by vortex stretching is a consequence of angular

momentum conservation. Stretching causes the cross-sectional area of a material fluid element to decrease, thus the angular velocity in the stretching direction must increase to conserve angular momentum [121]. A variable closely related to the phenomena is *enstrophy generation* σ , which is defined as

$$\sigma = \boldsymbol{\omega} \cdot \mathbf{w} \equiv \omega_i \omega_j S_{ij} = \omega^2 \lambda_i \cos^2(\boldsymbol{\omega}, \mathbf{e}_i) = \sum_i \sigma_i \quad (4.8)$$

where λ_i and \mathbf{e}_i are the eigenvalue and eigenvector of the strain rate tensor, respectively. The subscript i takes the values 1, 2 and 3, which correspond to the largest (or, the most extensive), intermediate and smallest (or, the most contracting) eigenvalues, respectively. As mentioned earlier, following the usual convention used by the fluids community, the eigenvalues mentioned above will be labeled in descending order of magnitude as α_S , β_S , and γ_S , respectively.

A positive enstrophy generation corresponds to the vortex stretching pattern, i.e. $\omega_i \omega_j S_{ij} > 0$, while negative enstrophy generation corresponds to the vortex compressing pattern, i.e. $\omega_i \omega_j S_{ij} < 0$. For PTD flows, both the vortex stretching vector and enstrophy generation vanish, i.e. $\mathbf{w} = 0$ and $\sigma_{PTD} = 0$. The only non-zero component of vorticity evolves as a conserved scalar. Three-dimensional and QTD turbulence are qualitatively different from PTD flow in that they possess essentially nonvanishing enstrophy generation. The *normalized enstrophy generation* σ_n describes the relative orientation between the vorticity and the vortex stretching vector:

$$\sigma_n = \cos \Theta(\boldsymbol{\omega}, \mathbf{w}) = \frac{\boldsymbol{\omega} \cdot \mathbf{w}}{|\boldsymbol{\omega}| \cdot |\mathbf{w}|} \quad (4.9)$$

Based on measurements of turbulent grid flow, Taylor [122] first demonstrated that the mean enstrophy generation for isotropic turbulence is positive. Taylor's conclusion is specific for (quasi-)homogeneous isotropic flows and has been confirmed through recent experimental studies [44] and a number of numerical tests based on DNS [123–125]. The predominant positiveness of the mean value of enstrophy generation indicates that the most probable state for isotropic turbulence is related to a vortex stretching instead of a vortex compressing flow configuration.

Helicity is an important fluid parameter which characterizes helical structures

and plays a key role in magnetohydrodynamics, small-scale intermittency, TKE dissipation processes, and the evolution of flow coherent structures [43, 47, 126, 127]. It is defined as

$$H = u_i \omega_i \quad (4.10)$$

The *relative helicity* h_n describes the relative orientation between the velocity vector \mathbf{u} and vorticity vector $\boldsymbol{\omega}$, i.e. the cosine of the angle Θ between these two vectors:

$$h_n = \cos \Theta(\mathbf{u}, \boldsymbol{\omega}) = \frac{\mathbf{u} \cdot \boldsymbol{\omega}}{|\mathbf{u}| \cdot |\boldsymbol{\omega}|} \quad (4.11)$$

According to the velocity identity $|\mathbf{u} \cdot \boldsymbol{\omega}|^2 + |\mathbf{u} \times \boldsymbol{\omega}|^2 = |\mathbf{u}|^2 |\boldsymbol{\omega}|^2$, helicity is related to the *Lamb vector* $\bar{\boldsymbol{\omega}} \times \bar{\mathbf{u}} = -\bar{\mathbf{u}} \times \bar{\boldsymbol{\omega}}$, which is the nonlinear convective term in the Navier-Stokes (N-S) equations in rotational form. If a region is strongly helical with velocity and vorticity vectors nearly aligned, i.e. h_n is close to ± 1 , then the magnitude of the Lamb vector $|\mathbf{u} \times \boldsymbol{\omega}|$ must be small. Since a small value of $|\mathbf{u} \times \boldsymbol{\omega}|$ indicates a low rate of TKE cascade to smaller-scales, helical behavior inhibits the TKE dissipation due to nonlinear interactions. Therefore, it is expected that the coherent structures with long lifetimes are associated with regions of large helicity and low dissipation rate; and in turn, large helicity is primarily located in regions with large-scale turbulent motions [43]. It is found that even if the large scales possess as much helicity as possible, the small scales develop much less helicity, which implies that helicity is primarily located at the large scales [128].

4.3 SGS Stress Modelling

The filtered continuity equation and Navier-Stokes equation for channel flows have been given in Section 3.4.2. Two dynamic SGS stress models, i.e. the DM of Lilly [7] and DNM of Wang and Bergstrom [9] (see Section 2.3), are tested in this chapter. It is well known that one of the main deficiencies of the DM is related to the numerical instability due to its construction, and consequently, the coefficient must be properly constrained. In the present study, we use two different approaches to constrain the model's coefficient. First the general plane averaging method, where the coefficient is averaged over the statistically homogeneous x_1 - x_3 plane, is adopted. Obviously, the

plane averaging approach will smear the local characteristics of the model. To retain local information, in the present study, we also adopted an ad hoc local averaging scheme, i.e. first bound the calculated coefficient of the DM by $-0.2 \leq C_S \leq 0.2$ (approximately 92% of the calculated coefficient values fall within this range), and then smooth the coefficient locally by using a 2-D discrete box filter (viz., local-plane-averaging based on a stencil of 3×3 nodes in the homogeneous x_1 and x_3 plane).

The second SGS stress model tested is the DNM proposed by Wang and Bergstrom [9] (see section 2.3), which is based on the explicit quadratic tensorial polynomial constitutive relation originally introduced by Speziale and Gatski [10,11] for the RANS approach. The fundamental features of this model have been examined using LES of turbulent Couette flow [9]. It is found that in comparison with the DM [6,7], the DNM can significantly increase the numerical stability. The model gave satisfactory predictions and no singularity problem was encountered in the simulation of Couette flow [9]. Wang and Bergstrom's study [9] only examined the DNM at a relatively low Reynolds number. As the extension to their work, the performance of the model in LES of channel flow at a higher Reynolds number ($Re_\tau = 395$) is examined in this chapter. For turbulent channel flow at the Reynolds number of $Re_\tau = 395$, the log layer is more extensive and the log law has a smaller intercept in comparison with low Reynolds number flow.

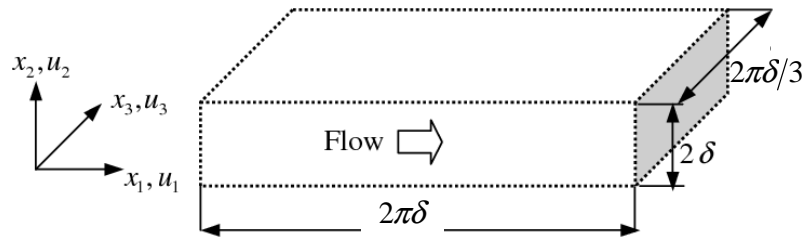


FIGURE 4.1: Computational domain and coordinate system ($Re_\tau = 395$).

4.4 Numerical Method and Flow Configuration

In this study, the governing equations are discretized using the finite volume method. Following the approach of Kim and Moin [67], the momentum equations were solved

using a fractional-step method where the nonlinear term was discretized using a second-order explicit Adams-Bashforth scheme and the viscous diffusion term was discretized using a second-order Crank-Nicolson scheme. A second-order central difference scheme was applied on a collocated grid for spatial discretization. At each time step, the pressure field was updated using a pressure correction method and the Poisson type pressure correction equation was solved using a multi-grid method with the control strategy described in section 3.2. The time period used to obtain the turbulent statistics was $10,000\Delta t$ after the flow became fully developed. Different time steps were explored before the simulation. It is found that $\Delta t \approx 0.0015\delta/u_\tau$ is small enough to obtain a stable solution and adopted in the calculation.

No-slip and no-penetration boundary conditions are imposed at the walls, and periodic boundary conditions are applied in the streamwise and spanwise directions. The computational domain which is shown in Figure 4.1 is set to be $2\pi\delta \times 2\delta \times 2\pi\delta/3$, corresponding to the streamwise (x_1), wall-normal (x_2) and spanwise (x_3) directions, respectively. The total number of control volumes is $48 \times 48 \times 64$ (in x_1, x_2, x_3). The grid is uniform with a spacing of $\Delta x_1^+ \approx 51.3$ and $\Delta x_3^+ \approx 12.7$, respectively, in the streamwise and spanwise directions. The mesh in the wall-normal direction corresponding to the channel gap is refined near the wall using a hyperbolic-tangent function described by Eq 3.59. In the present simulation, the first interior node off each wall is located at $x_2^+ \approx 0.4$. Since in the LES approach, not all scales of motion are resolved, the number of control volumes to be employed is significantly reduced in comparison with DNS approach. For instance, in the DNS study of Kim *et al.* [118], $192 \times 129 \times 160$ nodes were used for a Reynold number of $Re_\tau = 180$, and for the same test case ($Re_\tau = 395$), Moser *et al.* [109] used $256 \times 193 \times 192$ control volumes for their DNS approach.

4.5 Analysis of Results

In the absence of experimental measurements and filtered DNS data, the resolved-scale variables obtained here will be compared directly with the DNS results. All quantities denoted by $\langle \cdot \rangle$ are obtained using both spatial averaging in the homoge-

neous plane and time averaging for more than 10,000 time steps after the flow is fully developed. In presenting the results, the quantities are non-dimensionalized using the friction velocity u_τ .

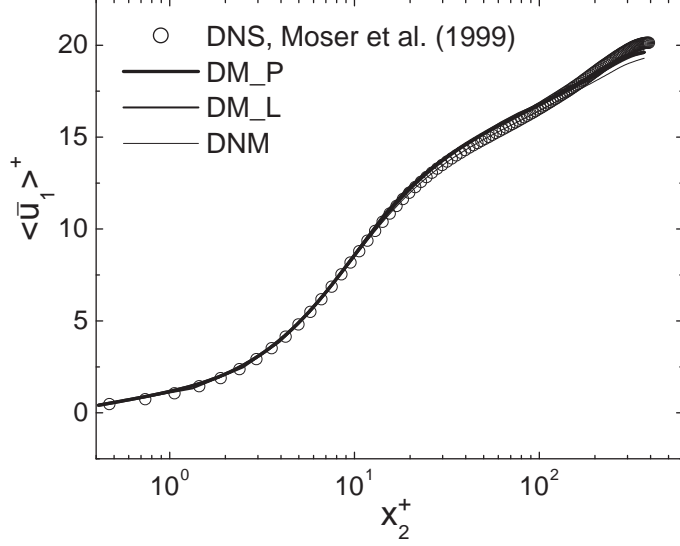


FIGURE 4.2: Mean velocity profile using wall coordinates ($Re_\tau = 395$).

4.5.1 Resolved Mean and Fluctuation Properties

The mean streamwise velocity profile using wall coordinates is shown in Figure 4.2. We use the suffixes $_P$ and $_L$ to denote the plane and local averaging schemes described above, respectively. Compared with the DNS data of Moser *et al.* [109], both the DNM and DM yield satisfactory predictions. None of the LES were able to pick up the wake region. The prediction of the DNM is closer to the DNS data, while the DM profiles are shifted slightly upward in the logarithmic region. The mean velocity profiles given by the DM using the plane and local averaging schemes almost overlap, which suggests that the choice of the bounding scheme does not have a significant effect on the prediction of the mean streamwise velocity.

Figure 4.3 plots the resolved velocity fluctuations and DNS data of Moser *et al.* [109] for comparison. Here, $\bar{u}_{1,rms}^+$, $\bar{u}_{2,rms}^+$ and $\bar{u}_{3,rms}^+$ denote the normalized root-mean-square streamwise (x_1), wall-normal (x_2) and spanwise (x_3) fluctuation component, respectively, which are defined as $\bar{u}_{i,rms}^+ \stackrel{\text{def}}{=} \langle (\frac{\bar{u}_i - \langle \bar{u}_i \rangle}{u_\tau})^2 \rangle^{1/2}$ for $i = 1, 2$ and 3 . It can be seen in Figure 4.3a, that both the DM and DNM prediction of the resolved

streamwise component are, in general, consistent with the DNS data, except that the DNM slightly overpredicts the peak value near the wall. Figure 4.3b indicates that both models underpredict the resolved wall-normal component near the wall. However, DNM yields a prediction that is relatively closer to the DNS results. In Figure 4.3c, both models underpredict the spanwise fluctuation component near the wall. However, towards the channel center, the DM tends to slightly overpredict the spanwise component, while the DNM prediction is in better agreement with the DNS data.

Figure 4.4 plots the distribution of the resolved Reynolds shear stress across the channel. The resolved Reynolds shear stress is normalized by $(u_\tau)^2$ and denoted as $-\langle \bar{u}_1'' \bar{u}_2'' \rangle^+$. The magnitude of the SGS shear stress $-\langle \tau_{12} \rangle$ is an order of magnitude smaller than the resolved Reynolds shear stress, its contribution to the total shear stress is insignificant for this case and is not shown here. Figure 4.4 indicates that all the models give a lower peak value near the wall. Compared to the predictions of the DM, the DNM prediction is closer to the DNS data. The prediction of the DM using the local averaging scheme is even worse than that of the DM using the plane averaging scheme, which suggests that the local bounding parameters may need to be adjusted for this specific flow.

Figure 4.5 shows the instantaneous velocity vectors and contours of streamwise vorticity fluctuations in the spanwise plane (x_2 - x_3) at the channel center. In the figure, it can be seen that the vortices with large magnitude of streamwise vorticity $\bar{\omega}_1$ are concentrated near the wall. The generation of the large amplitudes of $\bar{\omega}_1$ is due to the no-slip boundary condition which leads to large value of $\partial \bar{u}_3 / \partial x_2$ and the revolving fluid elements induced by the intense shear layer located at the interface between the energetic fluid streams moving toward and away from the wall.

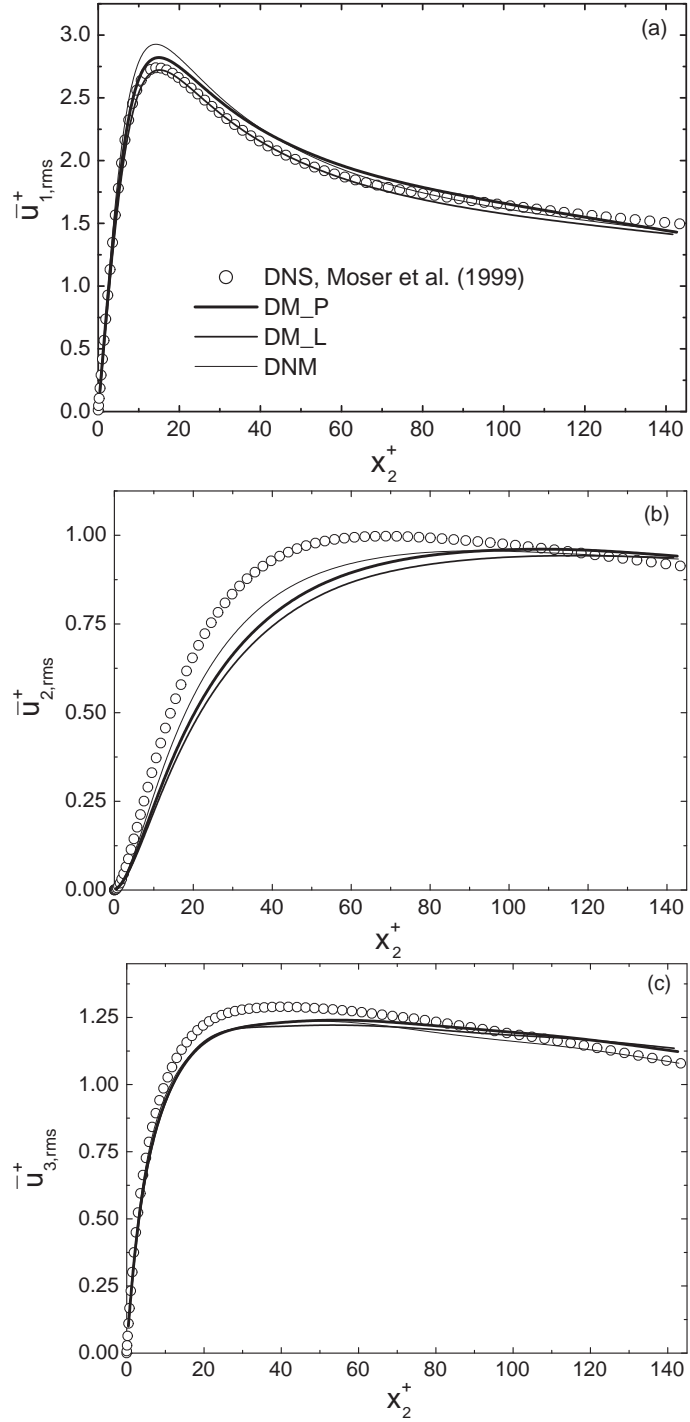


FIGURE 4.3: Resolved velocity fluctuations in wall coordinates: (a) streamwise; (b) wall-normal; (c) spanwise. ($Re_\tau = 395$).

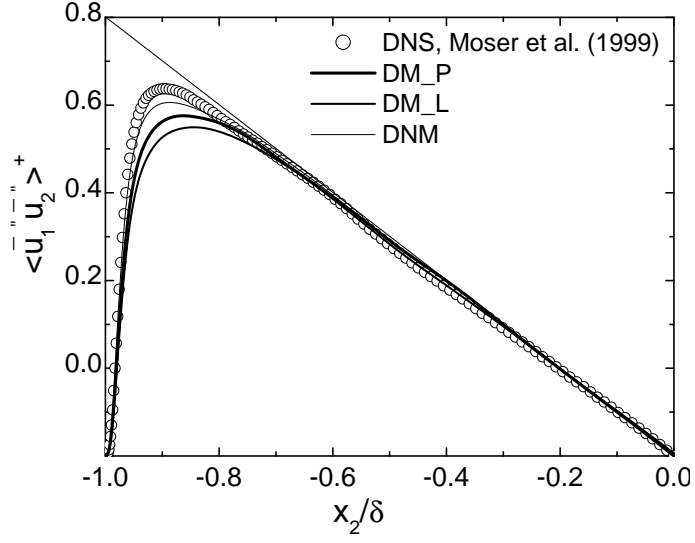


FIGURE 4.4:
($Re_\tau = 395$).

al direction

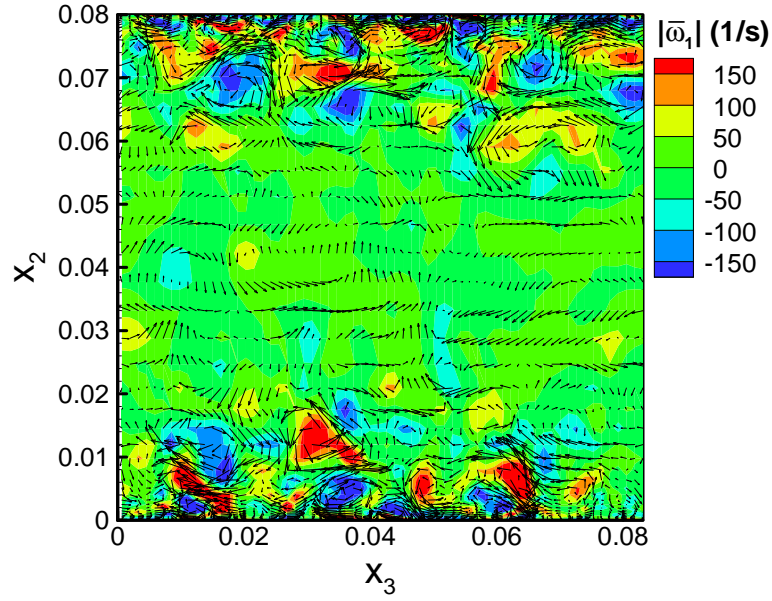


FIGURE 4.5: Instantaneous velocity vectors and streamwise vorticity contour in the spanwise plane ($x_2 - x_3$) across the channel center ($Re_\tau = 395$).

4.5.2 SGS Kinetic Energy Dissipation

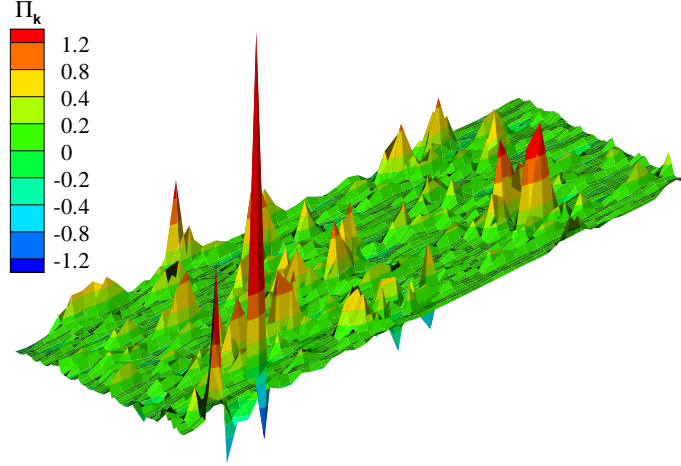
Kinetic energy transfer in LES is governed by the energy transport equation (2.10). The SGS dissipation term in the equation represents the unresolved kinetic energy, which should be mimicked by the SGS model. Here, we denote the SGS dissipation

(or TKE production) as \mathcal{P}_r , which is defined as [68]

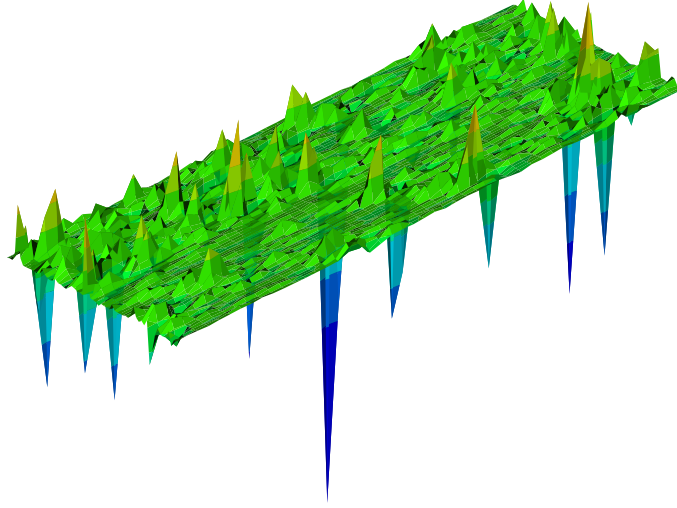
$$\mathcal{P}_r = -\tau_{ij}\bar{S}_{ij}. \quad (4.12)$$

To provide the correct level of overall SGS TKE dissipation to the large-scale motions is an essential function of SGS models. Although the mean SGS dissipation rate $\langle\mathcal{P}_r\rangle$ has a positive value, which represents a net turbulent kinetic energy cascade from the filtered (resolved) to subgrid scales of motions, experimental measurements [72, 129] and numerical studies [71, 130, 131] have shown that the local instantaneous TKE transfer occurs between resolved and subgrid scales in both directions. Therefore, SGS models are required to predict proper ‘backward scatter’ and ‘forward scatter’ of the TKE. It is well known that the simple eddy viscosity type model using a plane averaging scheme, which is not able to predict backward scatter, has poor performance in predicting transitional and near-wall flows, for which the backward transfer of TKE can be locally important [72, 87, 129, 130]. Another well-known problem of the eddy diffusivity type model is also related to this issue: the model is potentially unstable due to the improper TKE backward scatter [7]. In this section, the net SGS dissipation rate and TKE transfer between the resolved and SGS motions predicted by the DM and DNM are investigated.

Figure 4.6 shows the instantaneous SGS dissipation rate of TKE in a plane parallel to the wall at $x_2^+ = 24.4$ using the DNM and DM_L, respectively. Since the DM_P does not allow for backscatter, its prediction is not shown here. Here, Π_k denotes the instantaneous TKE dissipation rate normalized by u_τ^4/ν , i.e. $\Pi_k = \mathcal{P}_r/(u_\tau^4/\nu)$. Figure 4.6a indicates that the DM_L allows the TKE transfer in both forward and backward directions, however, the level of backward scatter is obviously smaller than that of the forward scatter. Although the level of the backscatter of TKE could be adjusted by changing the bounding parameters adopted for the local averaging scheme, it is an ad hoc ‘tuning’ and if a relatively large level of backscatter is allowed, a numerical instability may occur during the simulation. Figure 4.6b shows the SGS dissipation rate predicted by the DNM. Several large peak values of backscatter are observed in the figure, which implies that the DNM allows for a relatively high level of local backscatter without causing numerical instability. In



(a) DM using local average



(b) DNM

FIGURE 4.6: Instantaneous SGS dissipation of TKE normalized by u_τ^4/ν in a plane parallel to the wall at $y^+ = 24.4$ ($Re_\tau = 395$).

contrast to the DM, the DNM is free from the need for any artificial control of backward scatter.

Figure 4.7 shows the plane- and time-averaged distribution of \mathcal{P}_r along the wall-normal direction. In the figure, the averaged SGS TKE dissipation rates are normalized by u_τ^4/ν . ‘Forward’ denotes mean positive TKE production normalized by u_τ^4/ν , i.e. $\langle \mathcal{P}_r^+ \rangle / (u_\tau^4/\nu)$. ‘Backward’ denotes mean negative TKE production normalized by u_τ^4/ν , i.e. $\langle \mathcal{P}_r^- \rangle / (u_\tau^4/\nu)$. ‘Net’ denotes the net transfer of TKE normalized by u_τ^4/ν , i.e. $\langle \mathcal{P}_r \rangle / (u_\tau^4/\nu)$. It is interesting to observe that the DM with different bounding schemes yields quite different levels of TKE production. The difference

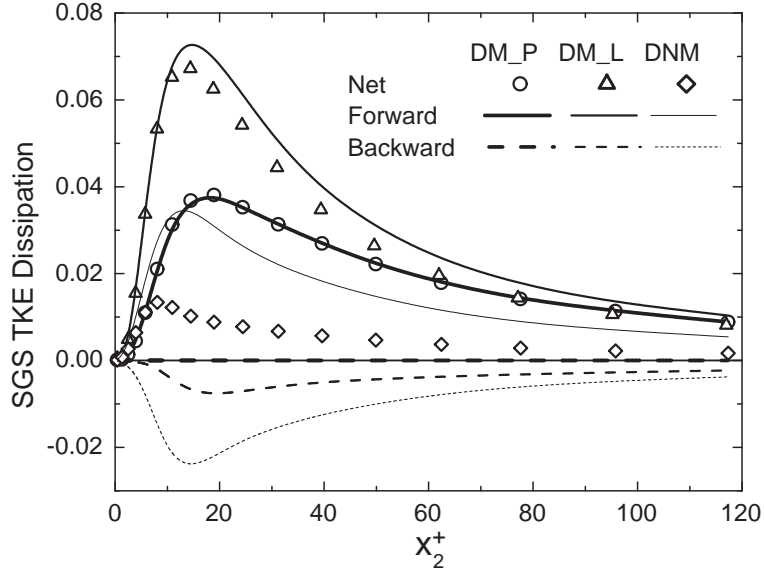


FIGURE 4.7: Averaged SGS dissipation rate normalized by u_τ^4/ν in wall coordinate ($Re_\tau = 395$).

between predicted values of the TKE production when different SGS models are applied was also observed by Cottet and Vasilyev's [132]. Compared to the DM, the DNM yields a relatively large level of mean backward scatter and thus a small level of net TKE production in the near-wall region. This is consistent with the previous observation of the instantaneous TKE transfer shown in Figure 4.6, e.g. the DNM allows a relatively high level of local negative transfer of TKE.

4.5.3 Geometrical Properties of the Resolved Strain Rate and SGS Stress Tensor

As reviewed in section 1.3, the method of turbulence geometrical statistics has been introduced to LES for studying the geometrical properties of the filtered flow field and the performance of SGS models. In this section, following the pioneering work by Tao *et al.* [54,133], turbulence geometrical statistics is applied to study the eigenvalue structure of the filtered strain rate and SGS stress tensor. Here, the concept of the nondimensional parameter S^* , suggested by Lund and Rogers [42] and defined by Eq. 4.3, is applied to study the resolved strain rate tensor, i.e. the symbol S^* used here denotes the nondimensional state parameter of \bar{S}_{ij} . In analogy to S^* , Tao *et al.* [134] suggested the variable S_τ^* to study the eigenvalue structure of the SGS stress

tensor. The stress state parameter S_τ^* is defined based on the deviatoric part of τ_{ij} , i.e.

$$S_\tau^* = \frac{3\sqrt{6}\alpha_{-\tau}\beta_{-\tau}\gamma_{-\tau}}{(\alpha_{-\tau}^2 + \beta_{-\tau}^2 + \gamma_{-\tau}^2)^{3/2}}, \quad (4.13)$$

where $\alpha_{-\tau}$, $\beta_{-\tau}$ and $\gamma_{-\tau}$ are eigenvalues of the deviatoric part of the SGS stress, $-\tau_{ij}^*$, where $\tau_{ij}^* = \tau_{ij} - \delta_{ij}\tau_{kk}/3$. Here $\alpha_{-\tau} \geq \beta_{-\tau} \geq \gamma_{-\tau}$ and $\alpha_{-\tau} + \beta_{-\tau} + \gamma_{-\tau} = 0$. As was the case for S^* , S_τ^* is bounded between ± 1 by its definition.

In this study, two statistical functions, the probability density function (PDF) and the joint probability density function (JPDF), are calculated based on a spatial and temporal average [135]. The PDF of the non-dimensional state parameters of the resolved strain rate and SGS stress tensor, S^* and S_τ^* , at the channel center is shown in Figure 4.8. The PDF profiles of S^* obtained by the DM_L and DNM are similar, and indicate that the most probable strain state is axisymmetric extension ($S^* = 1$), rather than axisymmetric compression ($S^* = -1$). However, the profile of the PDF of S^* drops slightly near $S^* = 1$. In contrast, Figure 4.8b shows that the mode of S_τ^* is located at $S_\tau^* = -1$, which indicates that the most probable stress state is axisymmetric compression, corresponding to an eigenvalue ratio of $\alpha_{-\tau} : \beta_{-\tau} : \gamma_{-\tau} = -1 : -1 : 2$. Although the modes of S_τ^* obtained by both the DM_L and DNM are located at $S_\tau^* = -1$, the DNM implies a higher probability of $S_\tau^* = -1$ than the DM_L. The DNM results also indicate that the probability of $S_\tau^* = -1$ is relatively prominent in comparison with the probability of $S^* = 1$, while the DM_L results indicate that the probability of $S_\tau^* = -1$ is almost the same as that of $S^* = 1$. Based on Figure 4.8b, the DNM yields a prediction which is closer to the observation of Tao *et al.* [54] based on the PIV measurement of a turbulent flow in a square duct.

Figure 4.9 shows the PDFs of S^* and S_τ^* near the wall in the buffer layer ($x_2^+ = 24.4$). In contrast to the PDF of S^* at the channel center (Figure 4.8a), Figure 4.9a shows that the modes of S^* in the buffer layer shift towards $S^* = 0$ (QTD near-wall flow). Note that in Figure 4.9b, the mode of S_τ^* in the buffer layer obtained by the DM_L also shifts towards $S_\tau^* = 0$, but the mode of S_τ^* obtained by the DNM is still located at $S_\tau^* = -1$. Figure 4.10a plots the PDFs of S^* in the viscous sublayer ($x_2^+ = 3.9$). Both the DNM and DM_L results indicate that in the viscous sublayer, the most probable state of the strain rate tensor is $S^* = 0$. In general, the presence of

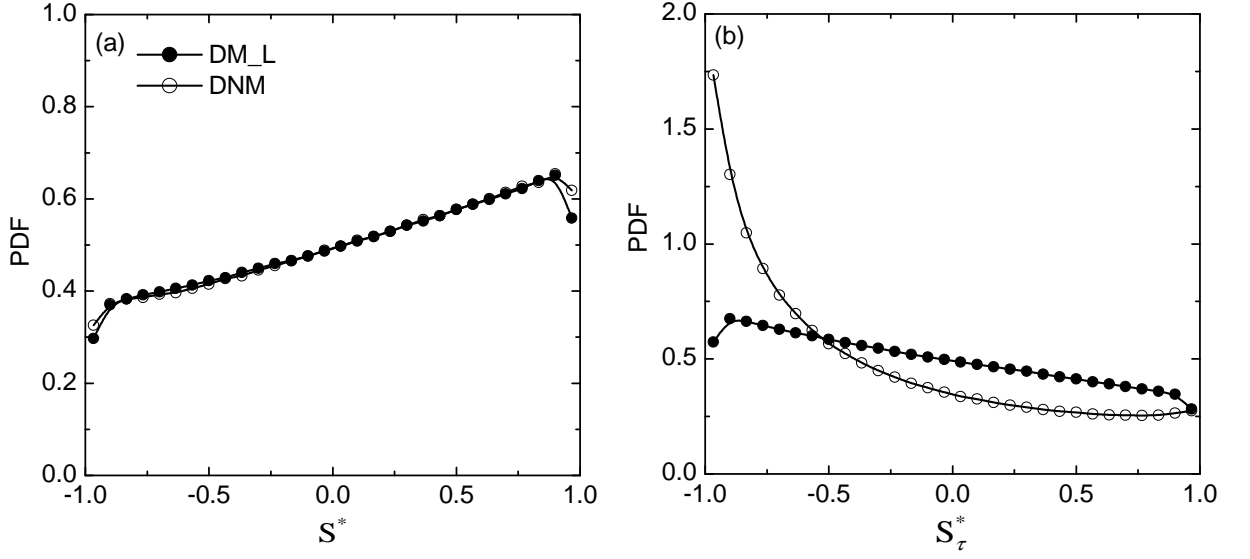


FIGURE 4.8: PDF of the nondimensional state parameters at the channel center (a) S^* of resolved strain rate tensor \bar{S}_{ij} ; (b) S_τ^* of SGS shear stress $-\tau_{ij}$ ($Re_\tau = 395$).

the wall tends to reinforce the tendency of $S^* = 0$, which corresponds to an eigenvalue ratio of $\alpha_S : \beta_S : \gamma_S = 1 : 0 : 1$. This observation reflects the intrinsic QTD nature of the near wall flow. The PDFs of S_τ^* in the viscous sublayer are shown in Figure 4.10b. It is observed that the mode of S_τ^* obtained by the DM_L is located at $S_\tau^* = 0$, while the PDF of S_τ^* obtained by the DNM still peaks at $S_\tau^* = -1$. Obviously, although the resolved strain structures predicted by the DM_L and DNM are similar, the SGS stress structures predicted by these two models are quite different, especially near the wall. It is not surprising that for the DM_L prediction, the PDF of S_τ^* is coupled with that of S^* , since the constitutive relation of the DM is based on linear relation to the resolved strain rate tensor.

To examine the relation between the preferred states of \bar{S}_{ij} and τ_{ij} predicted by the DNM, the JPDF of S^* and S_τ^* at the channel center is calculated and plotted in Figure 4.11. When the DNM is applied, the mode of the JPDF is located at $S^* = 1$ and $S_\tau^* = -1$. Corresponding to any S^* , the preferred state of the local SGS stress is always $S_\tau^* = -1$, whereas corresponding to any S_τ^* , the most probable state of the local strain is still $S^* = 1$, which implies that these two state parameters predicted by the DNM are not coupled. The DNM contradicts the DM, for which these two state parameters are coupled as $S^* = -S_\tau^*$ due to its constitutive relation. These observations on the JPDF of S^* and S_τ^* based on the DNM prediction (Figure 4.11)

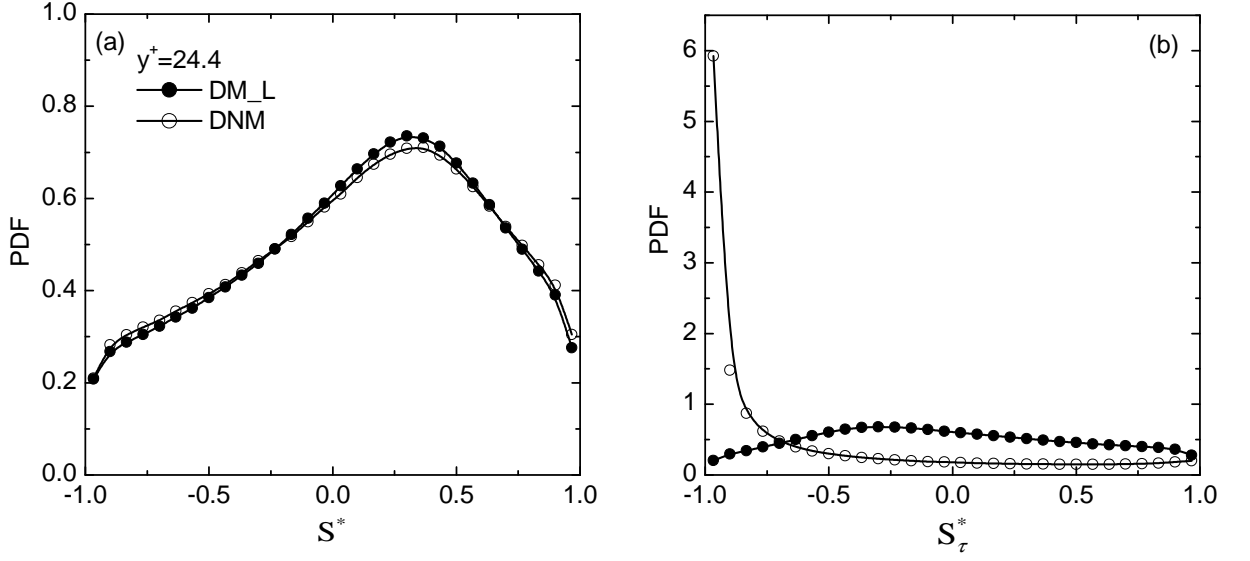


FIGURE 4.9: PDF of the nondimensional state parameters in the buffer layer ($x_2^+ = 24.4$) (a) S^* of resolved strain rate tensor \bar{S}_{ij} ; (b) S_τ^* of SGS shear stress $-\tau_{ij}$ ($Re_\tau = 395$).

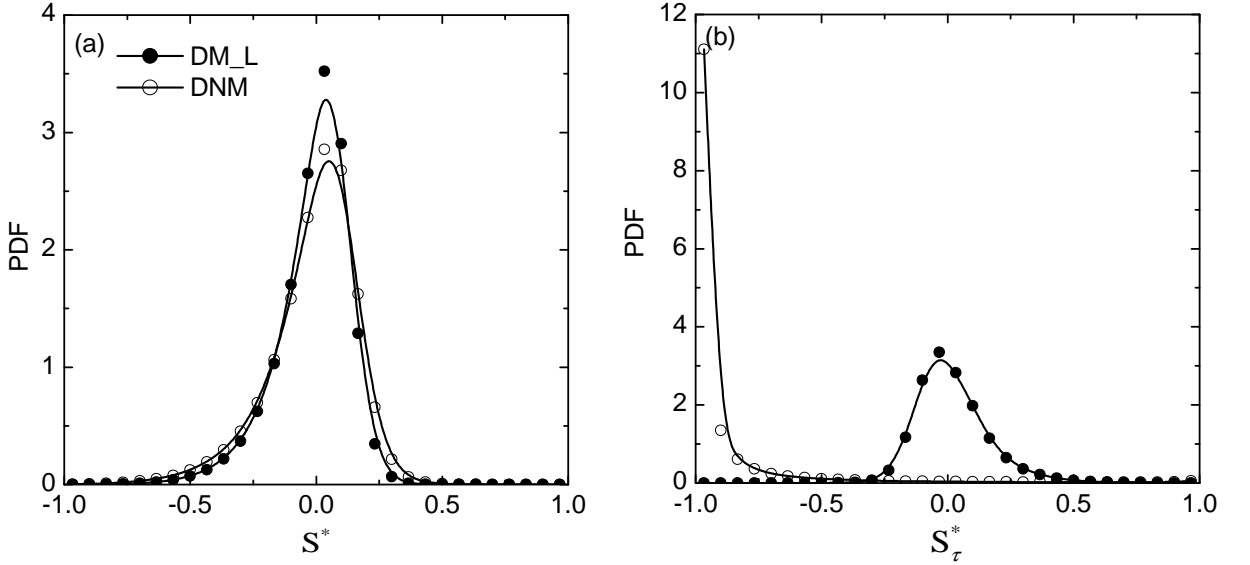


FIGURE 4.10: PDF of the nondimensional state parameters in the viscous sublayer ($x_2^+ = 3.9$) (a) S^* of resolved strain rate tensor \bar{S}_{ij} ; (b) S_τ^* of SGS shear stress $-\tau_{ij}$ ($Re_\tau = 395$).

are consistent with that based on the experimental measurements of a turbulent duct flow [54], which imply that the geometrical orientation of the SGS stress tensor predicted by the DNM may be close to the real orientation of the SGS stress tensor. Here, we have to emphasize that due to the absence of DNS and experimental data for the present test flow (channel flow), the experimental measurements of a duct flow

(Tao *et al.*) [54] is used for comparison. Therefore, it is not a strict comparison since two different flows are employed. However, we may expect that the main geometrical properties of turbulence are universal and not related to a specific flow. For example, the preferred alignment between the vorticity vector and the intermediate eigenvector of the strain rate tensor, and the preference of the axisymmetric extension state of strain structure are canonical and have been observed in many different flows.

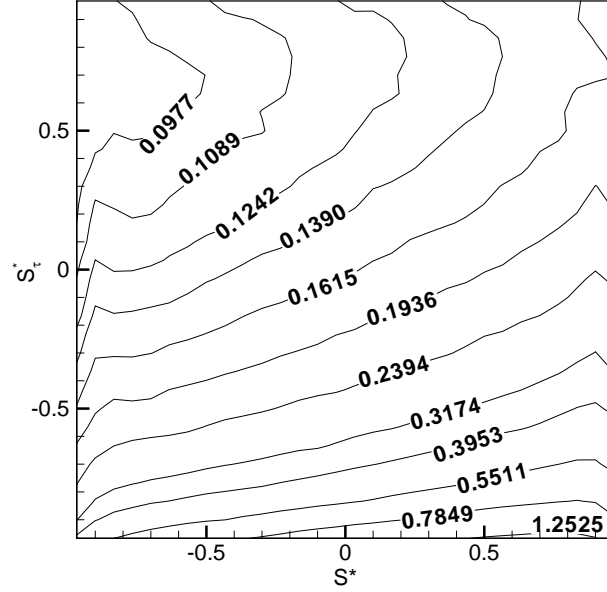


FIGURE 4.11: JPDF of the nondimensional status parameter S^* and S_τ^* at the channel center ($Re_\tau = 395$).

4.5.4 Relations between the State Parameters S^* and S_τ^* and SGS Dissipation Rate

In this section, the relations between the state parameters and the SGS dissipation are investigated, e.g. the topologies of S^* and S_τ^* with respect to the SGS dissipation when different SGS models are applied. A contour map of the JPDF of state parameters and SGS dissipation is generally used for this purpose. Here, Π denotes the normalized instantaneous SGS dissipation rate, which is defined as $\Pi = \mathcal{P}_r / (u_\tau^4 / \nu)$. In the statistics, the SGS dissipation rate is normalized by the mean SGS dissipation rate Π_{mean} , which is obtained by time and plane averaging over the homogeneous plane, i.e. $\Pi_{\text{mean}} = \langle \mathcal{P}_r / (u_\tau^4 / \nu) \rangle$.

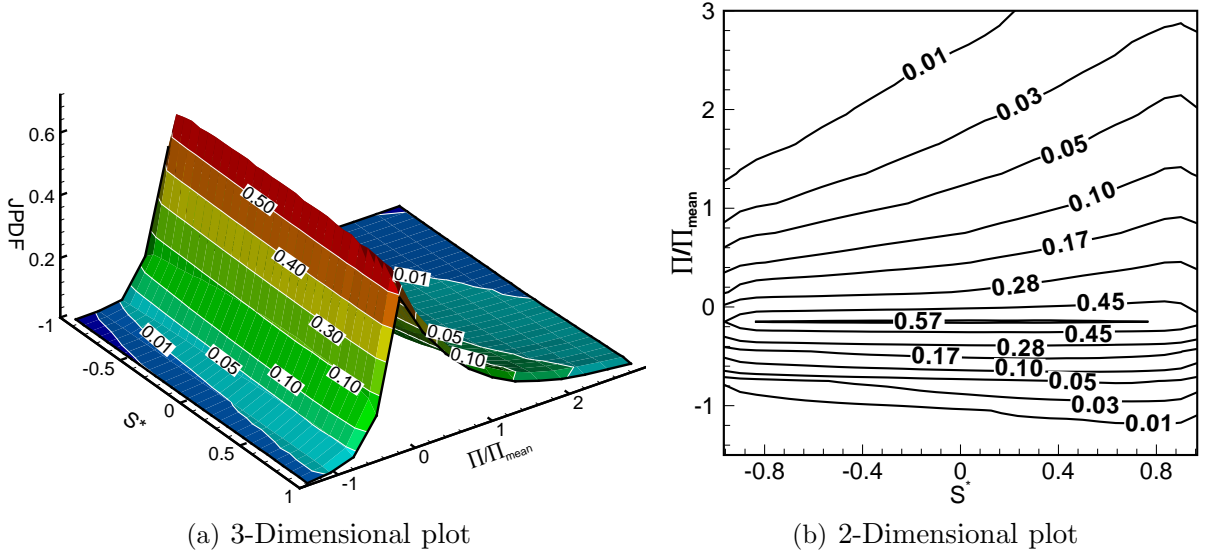


FIGURE 4.12: JPDF of S^* and the normalized SGS dissipation at the channel center using the linear DM_L ($Re_\tau = 395$).

Figure 4.12 plots the contour of the JPDF of S^* and Π/Π_{mean} using the DM_L at the channel center. Both a 3-D and 2-D plot are given in the figure. Evidently, both the positive (forward scatter) and negative (backscatter) dissipation exist over the entire range of S^* . In the positive dissipation region, axisymmetric extension ($S^* = 1$) is the preferred state of \bar{S}_{ij} , while in the negative dissipation region, the preference is not evident. Although the net SGS dissipation is positive (see Figure 4.7), Figure 4.12 shows that the mode of the JPDF of S^* and Π/Π_{mean} is located in the negative dissipation region. This implies that the frequency of backscatter is higher than that of forward scatter, but the average level of the magnitude of the backscatter is smaller than that of the forward scatter. It can be explained by the nature of the DM and the local-averaging scheme adopted. Naturally, the DM tends to overpredict the backscatter, which is known to cause numerical instability. Although the local-averaging scheme could constrain the total level of backscatter by clipping large negative coefficients, it cannot reduce the occurrence of the backscatter.

Figure 4.13 shows the contour of the JPDF of S^* and Π/Π_{mean} using the DNM at the channel center. The positive and negative dissipation exist over the whole range of S^* . For the positive dissipation region, $S^* = 1$ (axisymmetric extension state) is slightly preferred, while for most of the negative dissipation region, any preference is minimal. In contrast to the JPDF pattern of the DM_L, the peak values of the JPDF

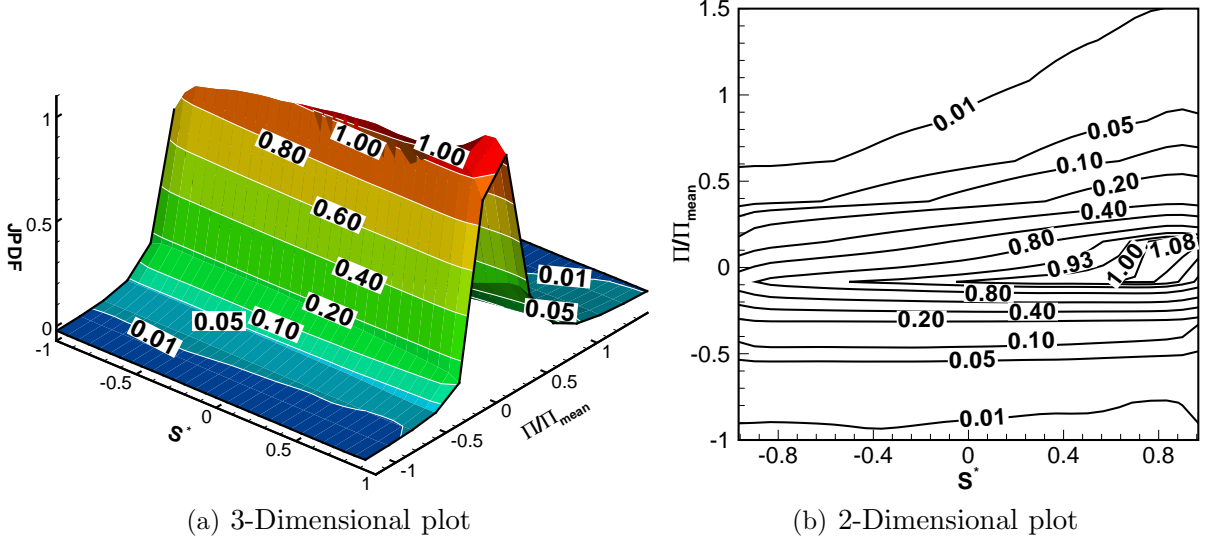


FIGURE 4.13: JPDF of S^* and the normalized SGS dissipation at the channel center using the nonlinear DNM ($Re_\tau = 395$).

of S^* and Π/Π_{mean} using the DNM are located in the positive SGS dissipation region, close to the axisymmetric extension state ($S^* = 1$). For the region $S^* < 0$, we notice that the peak value of the JPDF is located in the negative dissipation region, which implies that the DNM overpredicts the backscatter in this region. This conclusion is based on the study of Tao *et al.* [54], who measured a turbulent duct flow and found that for the whole range of S^* , the overall SGS dissipation should be positive.

The contour of the JPDF of S_τ^* and SGS dissipation Π/Π_{mean} using the DNM at the channel center is shown in Figure 4.14. In contrast to the state of strain rate tensor (Figure 4.13), The most probable SGS stress state is axisymmetric compression ($S_\tau^* = -1$) rather than axisymmetric extension ($S_\tau^* = 1$) for both the positive and negative dissipation region. Prediction of SGS dissipation is an important issue for SGS modelling. The topologies of SGS dissipation with respect to the state parameters S^* and S_τ^* based on the experimental measurements of Tao *et al.* [54] are shown in Figure 4.15 for comparison. We notice that the JPDF contour pattern predicted by the DNM is similar to those of the experimental measurements [54] (compare Figure 4.13b and Figure 4.14b to Figure 4.15a and 4.15b, respectively.). The topological similarity between the DNM predictions and the measured SGS dissipation is important in that it implies the local small structures predicted by the DNM are similar to the real ones. However, further investigations are necessary in order to draw a definitive conclusion.

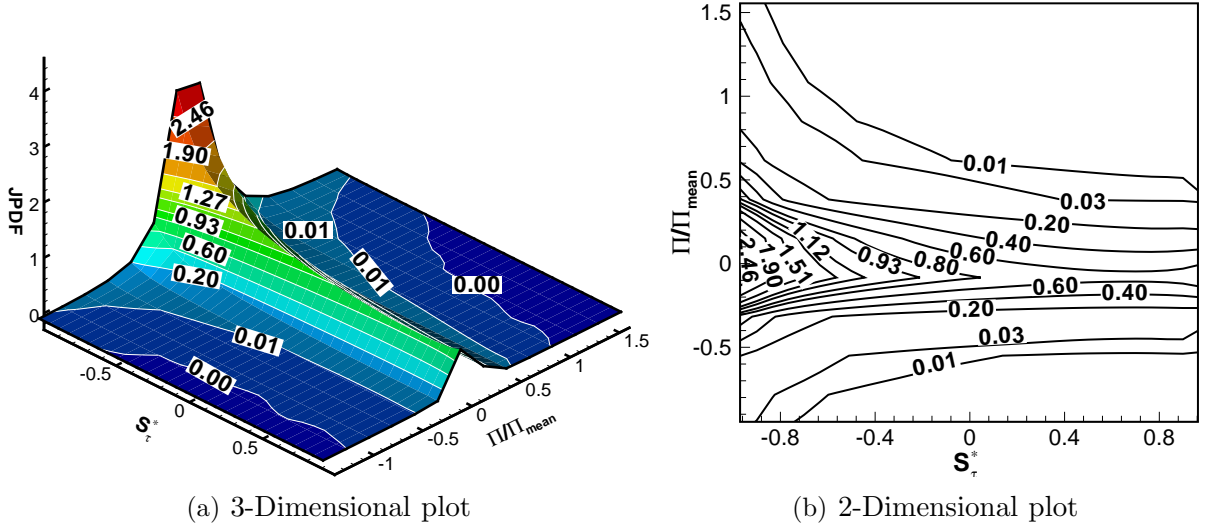


FIGURE 4.14: JPDF of S_τ^* and the normalized SGS dissipation at the channel center using the nonlinear DNM ($Re_\tau = 395$).

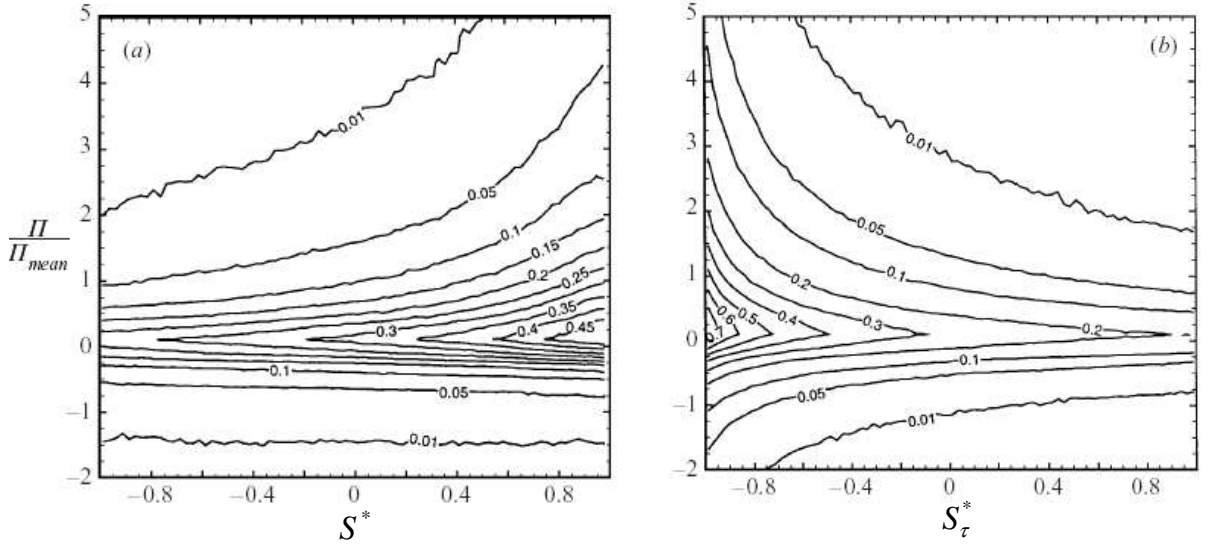


FIGURE 4.15: Experimental measurement of the JPDF of S^* and S_τ^* with SGS dissipation (by Tao *et. al.*, 2002, for duct flow).

The contour of the JPDF of S^* and Π/Π_{mean} in the buffer layer using the DNM is shown in Figure 4.16. It is observed that similar to the JPDF of S^* and Π/Π_{mean} at channel center, both forward and backward scatter of SGS dissipation occur over the entire range of S^* . However, compared to the channel center, the mode of the JPDF S^* and Π/Π_{mean} in the buffer layer moves away from the axisymmetric extension ($S^* = 1$) toward the QTD region ($S^* = 0$), which is mostly due to the 2-D nature of the near-wall flow. Figure 4.16 indicates that for the region $S^* > 0$, forward scatter is

still dominant, while for the region $S^* < 0$, backward scatter occurs more often and the peak values of the JPDF occur for negative dissipation in this region.

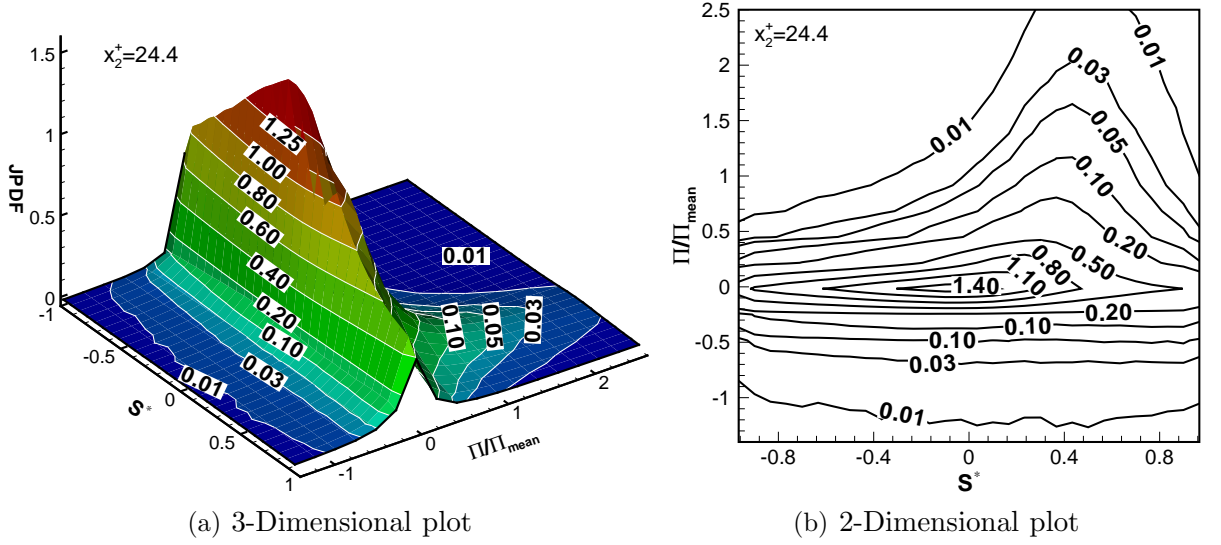


FIGURE 4.16: JPDF of S^* and the normalized SGS dissipation in the buffer layer using the nonlinear DNM ($Re_+ = 395$)

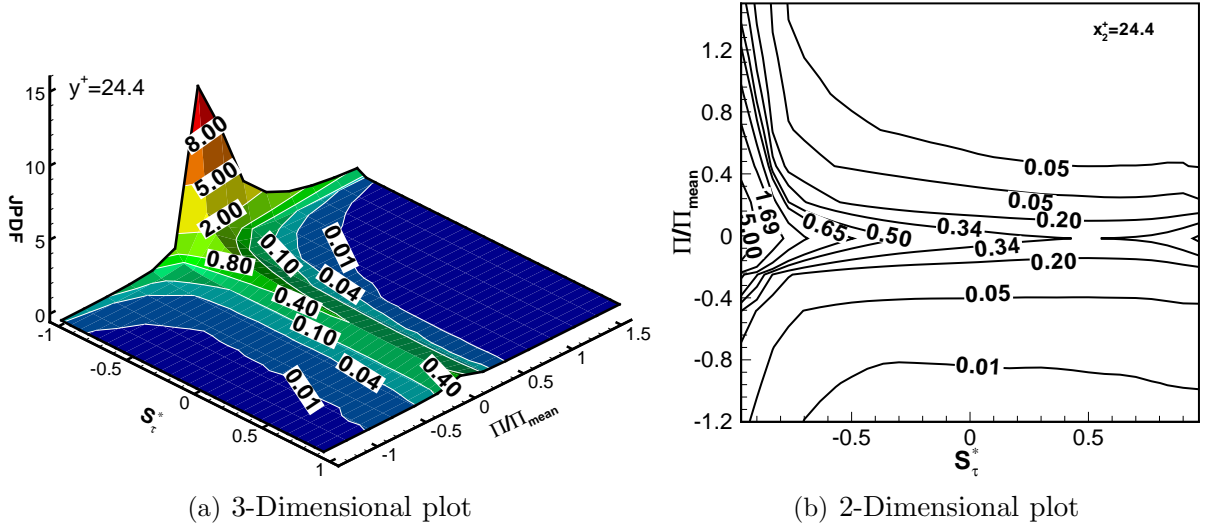


FIGURE 4.17: JPDF of S_τ^* and the normalized SGS dissipation in the buffer layer using the nonlinear DNM ($Re_\tau = 395$).

Figure 4.17 plots the contour of the JPDF of S_τ^* and Π/Π_{mean} in the buffer layer using the DNM. It is observed that the JPDF contour pattern in the buffer layer is similar to that at the channel center, i.e. both the positive and negative dissipation strongly favour the axisymmetric compression stress state ($S_\tau^* = -1$). However, compared to the JPDF at the channel center (Figure 4.14), the probability

of the axisymmetric compression state ($S_\tau^* = -1$) is evidently enhanced in the buffer layer.

4.6 Summary

In this chapter, the DM and DNM for SGS stress are investigated in LES of a channel flow at $Re_\tau = 395$. The present study of the mean and fluctuating properties of the flow indicates that the LES results are consistent with the DNS data. Both the DM and DNM models give satisfactory predictions with respect to the resolved velocity field. In general, the DNM yields predictions that are slightly closer to the DNS data and displays several attractive features, e.g. it is free from any artificial ‘tuning’.

The SGS dissipation is one of the important issues for LES. It is used in this study to evaluate the performance of the SGS models. It is observed that the DM with different bounding schemes yields quite different levels of TKE production. The DM with plane averaging cannot provide backscatter. Although the DM with local averaging could predict backscatter, the level of the backscatter is influenced by the local bounding scheme adopted for the model’s coefficient rather than the local flow structure. It is found that not only the level but also the local distribution of backscatter predicted by the DM is incorrect, which implies that it is not the model’s coefficient but the Smagorinsky type constitutive relation that should be modified. Compared to the DM, the nonlinear DNM allows for a relatively large level of backscatter and yet is stable in calculation due to its constitutive relation.

The methodology of turbulence geometrical statistics is used to investigate the local structures of the resolved and SGS field. The geometrical characteristics of the resolved strain structures predicted by both the DM and DNM are similar, i.e. at the channel center, the most probable strain state is axisymmetric extension ($S^* = 1$), while towards the wall, the flow tends to be QTD ($S^* = 0$) due to the effect of the solid wall. However, the SGS stress structures predicted by these two models are quite different. The DNM predictions are consistent with the experimental measurements, i.e. the state parameters S^* and S_τ^* predicted by the DNM are not coupled, while for the DM, the relation $S^* = -S_\tau^*$ is forced due to its constitutive relation.

At the channel center, the peak values of the JPDF of S^* and Π/Π_{mean} using the DM are located in the negative dissipation region, which implies that the DM tends to overpredict the backscatter. In contrast, the mode of the JPDF of S^* and Π/Π_{mean} using the DNM is located in the positive dissipation region. However, for the region $S^* < 0$, the peak values of the JPDF will fall in the negative dissipation region, which implies that for $S^* < 0$, the DNM may overpredict backscatter. Towards the wall, the mode of the JPDF of S^* and Π/Π_{mean} using the DNM move from the axisymmetric extension region ($S^* = 1$) to the QTD flow region ($S^* = 0$). In contrast, the JPDF profiles of S_τ^* and Π/Π_{mean} using the DNM is always peaked at $S_\tau^* = -1$ (axisymmetric compression) for all the flow region.

In general, both the DM and DNM yield satisfactory results with respect to the resolved mean and fluctuating properties. However, the DM cannot predict the proper level and distribution of backscatter. In contrast, the DNM allows for a relatively large level of backscatter and yet is stable. Both models capture the geometrical characteristics of the resolved strain structure. However, the geometrical properties related to the SGS field predicted by these two models are quite different. It is found that the SGS dissipation and SGS stress structures predicted by the DNM are topologically similar to the experimental measurements.

Chapter 5

LES of Combined Forced and Natural Convection in a Vertical Plane Channel using Different SGS Models

5.1 Introduction

In mechanical and environmental engineering, combined (mixed) forced and natural turbulent convection is a frequently encountered thermal-fluid phenomenon, which exists, for example, in the atmosphere, urban canopy flows, ocean currents, gas turbines, heat exchangers, nuclear reactors, and computer chip cooling systems. In the early development of the subject of convective heat transfer, forced and natural convection were studied separately and the interaction between these two physical processes was ignored. Modern research on combined forced and natural convection was initiated in the 1960's based on experimental approaches (see Metais and Eckert [136]). Since then, refined experimental measurements have become available [137,138], and the research methodology has been extended to numerical simulations based on the RANS, DNS, and LES [35, 139–145].

By their nature, buoyancy driven turbulent flows are unsteady and feature both large and fine scale flow structures. Therefore, a time dependent and fine scale resolved calculation based on DNS or LES can provide more details of the temperature and fluid flow fields. In LES of buoyant flows, the unknown SGS stress tensor and heat flux (HF) vector associated with the unresolved scales of motion need to be modelled to close the set of governing equations. Although in a direct sense, the SGS

stress model is for closing the filtered momentum equation and the SGS HF model is for closing the filtered thermal energy equation, these two types of SGS models jointly influence both the velocity and temperature fields. This is because the transport of momentum is tightly coupled with that of thermal energy in a combined forced and natural convective flow, both temporally and spatially.

In this chapter, LES of mixed flow for a Grashof number of $Gr = 9.6 \times 10^5$ and Reynolds number of $Re_\tau^a = 150$ is performed. The DM [7] and DNM [9] are used for closure of the filtered momentum equation, and the DEDM-HF [20] and DTDM-HF [40] are used for closure of the filtered energy equation. LES results are compared to the benchmark DNS study of Kasagi and Nishimura [141], Kuroda *et al.* [146] and Davidson *et al.* [1]. Attention is focused on evaluation of the performance of the linear and nonlinear SGS models in terms of their capability for predicting the resolved thermal-fluid fields. In particular, we compare the set of linear SGS models based on the DM and DEDM-HF, with the set of nonlinear SGS models based on the DNM and DTDM-HF.

5.2 Governing Equations and SGS Models

The filtered continuity equation (Eq.2.5) and thermal energy equation (Eq.2.7) have been presented in section 2.2. The filtered momentum equation for the mixed convective flow will consider the effect of buoyancy and takes the following form:

$$\frac{\partial \bar{u}_i}{\partial t} + \frac{\partial}{\partial x_j}(\bar{u}_i \bar{u}_j) = -\frac{1}{\rho} \frac{\partial \bar{p}}{\partial x_i} + \nu \frac{\partial^2 \bar{u}_i}{\partial x_j \partial x_j} - \frac{\partial \tau_{ij}}{\partial x_j} - \beta g_i (\bar{\theta} - \Theta_r), \quad (5.1)$$

where Θ_r is a reference temperature. $\tau_{ij} \stackrel{\text{def}}{=} \overline{u_i u_j} - \bar{u}_i \bar{u}_j$ is the SGS stress tensor. To close the momentum equations, the DM (Eq.2.11) and DNM (Eq.2.35) are used for the SGS stress term in this study. The details of these two SGS stress models can be found in section 2.3 and will not be described again in this chapter. To close the filtered energy equation (Eq.2.7), two dynamic SGS HF models are implemented in the simulation, namely, the DEDM-HF introduced by Moin *et al.* [20], and the DTDM-HF recently proposed by Peng and Davidson [40]. These two modelling formula have been summarized in section 2.4.

5.3 Physical Model and Numerical Method

The physical model tested in this research is a combined forced and natural convection (or, mixed convection) between two vertical parallel plates maintained at two different temperatures. Specifically, we consider a benchmark test case of Kasagi and Nishimura [141] and compare the LES results with the reported DNS results [1, 141, 146]. The physical domain of the test flow is described in Figure 5.1. The flow is characterized by a Grashof number of $Gr = 9.6 \times 10^5$ and a Reynolds number of $Re_\tau^a = 150$ (determined by the mean driving pressure gradient in the streamwise direction). Here, $Re_\tau^a \stackrel{\text{def}}{=} u_\tau^a \delta / \nu$ and u_τ^a is the average value of the friction velocities at the two walls. So, $Re_\tau^a = (Re_{\tau h} + Re_{\tau c})/2$. The pressure gradient drives the mean flow upward, while the buoyant force acts in the upward (aiding flow) and downward (opposing flow) directions near the hot and cold walls, respectively. Compared with the forced convection case ($Gr = 0$), the mean velocity profile for mixed convection becomes increasingly asymmetric as the Grashof number increases [1, 138, 141]. In general, the turbulent transport is enhanced in the opposing flow region and is suppressed in the aiding flow region. As mentioned in Davidson *et al.* [1], because the velocity profile is asymmetric in the wall-normal direction, the value of the friction velocity τ_w (and therefore, the Reynolds number Re_τ) at the hot wall is different than that at cold wall, i.e. $\tau_{wh} \neq \tau_{wc}$ (and $Re_{\tau h} \neq Re_{\tau c}$). As such, due to the buoyancy effect, it is expected that the value of Re_τ^a obtained from simulation deviates from the nominal value of 150, and we will revisit this subject later when discussing Table 5.1.

The momentum equations are solved using the method described in section 4.4. To solve the filtered thermal energy equation, a fourth-order Runge-Kutta method was used to advance the temperature field over a single time step. The time period used to obtain the turbulent statistics was 10,000 time steps after the flow becomes fully developed. In order to extract the value of a filtered variable at the test-grid level to perform the dynamic modelling procedure, the boundary thermal-fluid fields are processed using a second-order Gaussian filter and the interior fields are processed using a fourth-order discrete Gaussian filter. For the formulation of these discrete filters, the reader is referred to Sagaut and Grohens [147].

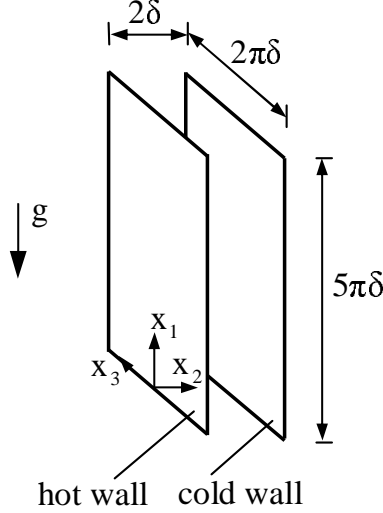


FIGURE 5.1: Illustration of the physical domain of the combined forced and natural convective channel flow.

No-slip and no-penetration boundary conditions were imposed on the velocity components at the walls, while the temperatures on the two side walls were set to fixed values derived from the given Grashof number. Periodic boundary conditions were imposed in the streamwise and spanwise directions. The computational domain was set to be $5\pi\delta \times 2\delta \times 2\pi\delta$, and $48 \times 32 \times 48$ control volumes were used for discretizing the domain in the streamwise (x_1), wall-normal (x_2) and spanwise (x_3) directions, respectively. The grid is uniform in the streamwise and spanwise directions and is refined in the wall-normal direction using a hyperbolic-tangent function (Eq.3.59), such that the first interior node off the wall is located at $x_2^+ \approx 1.2$. For the present LES, the number of the control volumes to be employed is significantly less than that used in a DNS approach. For instance, for a similar test case ($Gr = 7.68 \times 10^6$ and $Re_\tau^a = 150$), Davidson *et al.* [1] used $128 \times 96 \times 96$ control volumes in their DNS study of mixed convection. In the absence of filtered DNS data, the value of the resolved scale variables obtained from the simulation will be compared directly with the DNS results. All quantities denoted by $\langle \cdot \rangle$ are averaged both in time and over homogeneous planes. In presenting the results, the quantities are non-dimensionalized using the wall friction velocity u_τ and friction temperature T_τ .

5.4 Analysis of Results

Table 5.1 summarizes the flow conditions and some important parameters that characterize the thermal-fluid flow fields obtained from the LES and DNS approaches. Although slight differences exist, Table 5.1 indicates that the LES predictions of those characteristic flow parameters (such as the Reynolds number, and resolved wall friction coefficient and Nusselt number) based on both sets of linear and nonlinear models are, in general, consistent with the reported DNS data. The Reynolds numbers (Re_τ^a and Re_b) calculated from the LES are slightly smaller than those from the DNS performed by Kasagi and Nishimura [141], with a difference of less than 5%. The value of the resolved friction coefficient predicted using both the LES and DNS is larger at the hot wall and smaller at the cold wall. In contrast, the predicted value of the Nusselt number is smaller in the hot wall region and larger in the cold wall region. The reason that the value of the resolved wall friction coefficient increases at the hot wall and decreases at the cold wall, is due to the fact that buoyancy aids the upstream flow motion (consistent with the effect caused by the mean streamwise driving pressure gradient) near the hot wall while opposing it near the cold wall.

The Nusselt number in both the hot and cold wall regions is defined as the ratio of the actual heat transferred through the wall to the heat transfer that would occur through conduction [141], viz. $Nu = 2q_w/[\lambda(\theta_D - \theta_w)/D]$. Here, q_w represents the wall heat flux, θ_w is the wall temperature, D is the distance measured from the wall to the maximum streamwise velocity location, and $\theta_D \stackrel{\text{def}}{=} \int_0^D \langle \bar{\theta} \rangle dx_2 / D$ is the bulk averaged temperature over the distance D . Owing to the deformation of the mean velocity profile (see Figure 5.2a), the value of D for the hot wall region is smaller than that for the cold wall region. As such, the fluid heat conduction [i.e., $\lambda(\theta_D - \theta_w)/D$] near the hot wall is larger than that near the cold wall. Given the definition of the Nusselt number and the condition that the averaged value of q_w from the two walls must be equal to satisfy conservation of energy, the Nusselt number in the hot wall region is smaller than that in the cold wall region. These observations are in agreement with the previous investigations conducted by other researchers [1, 138, 141].

TABLE 5.1: Physical quantities of the flow

	Re_τ^a	Re_b	$\frac{Gr}{Re_b^2}$	u_τ		$C_f \times 10^{-3}$		Nu	
				Hot	Cold	Hot	Cold	Hot	Cold
DNS [141]	150	4494	0.0475	–	–	9.90	7.90	7.4	20.9
DM&DEDM-HF	145	4270	0.0526	0.0565	0.0522	9.59	7.96	7.1	21.6
DNM&DTDM-HF	147	4380	0.0500	0.0568	0.0535	9.55	7.98	7.3	21.4

5.4.1 Mean Resolved Temperature and Velocity Profiles

Figures 5.2a and 5.2b show the profiles of the mean resolved streamwise velocity and temperature across the channel for the mixed convective flow ($Gr = 9.6 \times 10^5$ and $Re_\tau^a = 150$). The DNS data of Kasagi and Nishimura [141] is used for validating the LES results. (Unless otherwise noted, in this chapter, DNS data refers to Kasagi and Nishimura.) In comparison with mixed convection, DNS data of forced convection ($Gr = 0$ and $Re_\tau = 150$) are also plotted in the figure. The DNS data of forced convection in Figure 5.3a refers to Kuroda *et al.* [146]. The mean velocity and temperature profiles are symmetric for the forced convection case and asymmetric for the mixed convection case. Compared with the DNS data [141], the results predicted by both sets of linear and nonlinear models are very similar: near the hot wall (or, in the aiding flow region), the mean velocity is slightly overpredicted and mean temperature is slightly underpredicted. From Figure 5.2b, it is observed that the mean temperature profile near the cold wall (or, in the opposing flow region) predicted by the set of nonlinear models agrees better with the DNS result than that predicted by the set of linear models.

Figures 5.3a and 5.3b show the mean velocity and temperature using wall coordinates. The suffixes $_h$ and $_c$ to denote quantities related to the hot and cold walls, respectively. DNS data of forced convection ($Gr = 0$ and $Re_\tau = 150$) in Figure 5.3a refers to Kuroda *et al.* [146]. Compared with the forced convection case, the mean resolved velocity profile for mixed convection deviates from the conventional logarithmic law in response to the buoyant force: the velocity shifts slightly downward near

the cold wall, whereas it becomes curved and shifts upward near the hot wall. The mean resolved temperature profile also deviates from the profile of forced convection: it shifts downward and upward near the cold and hot walls, respectively. Although both sets of linear and nonlinear SGS models yield almost the same prediction for the mean resolved velocity [cf. Figure 5.3a], it appears that the mean resolved temperature profile predicted by the set of nonlinear SGS models is closer to the DNS result [141] than that predicted by the set of linear SGS models, especially in the cold wall region [cf. Figure 5.3b].

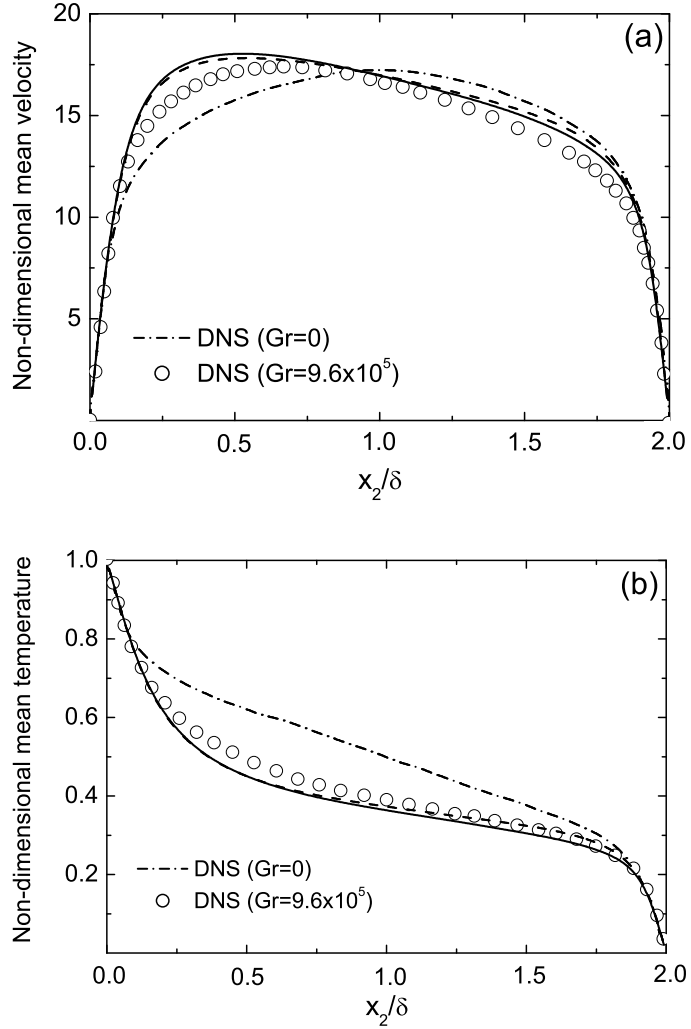


FIGURE 5.2: Mean resolved velocity and temperature profiles across the channel: (a) non-dimensional mean streamwise velocity $\langle \bar{u}_1 \rangle / u_\tau^a$; (b) non-dimensional mean temperature $\frac{\langle \bar{\theta} \rangle - \theta_{wc}}{\theta_{wh} - \theta_{wc}}$. Solid line: DM&DEDM-HF; dash line: DNM&DTDM-HF.

5.4.2 Resolved Shear Stresses and Heat Fluxes

To illustrate the basic characteristics of the flow in an intuitive manner, we show in Figure 5.4 the instantaneous velocity and temperature fields in the central transverse plane obtained using the set of nonlinear SGS models. From the figure, it is observed that the flow structures indicated by both the temperature contours and instantaneous velocity vectors near the cold wall are larger and more intense than those near the hot wall. This is because buoyancy aids the upstream flow motion in the region near the hot wall and opposes the upstream flow motion in the region near the cold wall with the consequent suppression and enhancement of turbulence in these two regions, respectively.

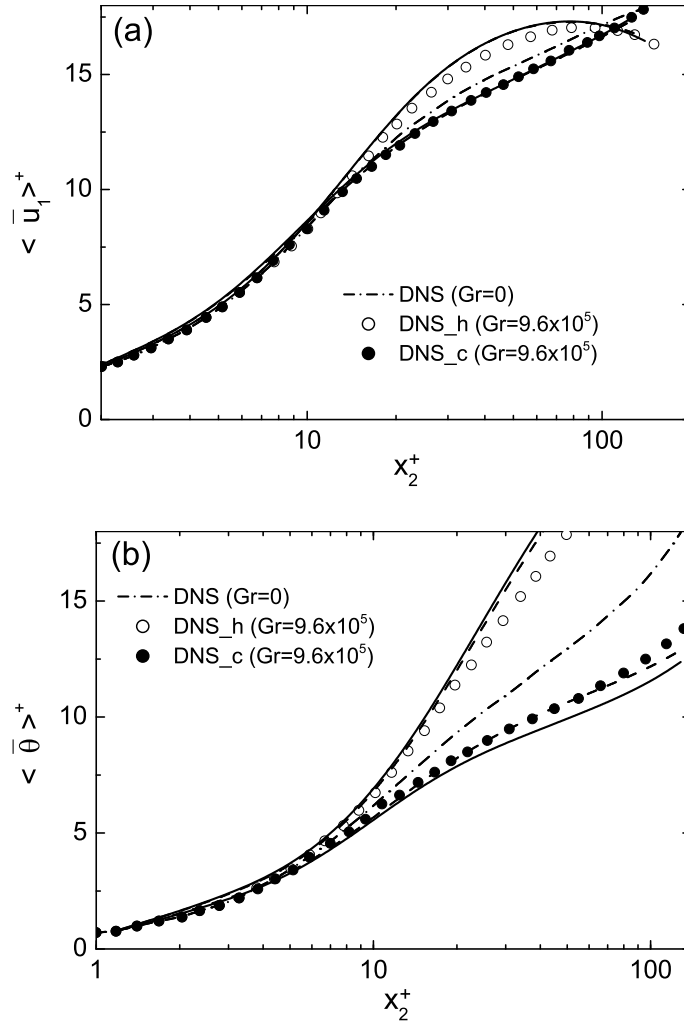


FIGURE 5.3: Mean resolved velocity and temperature profiles across the channel displayed using wall coordinates: (a) velocity; (b) temperature. Solid line: DM&DEDM-HF; dash line: DNM&DTDM-HF.

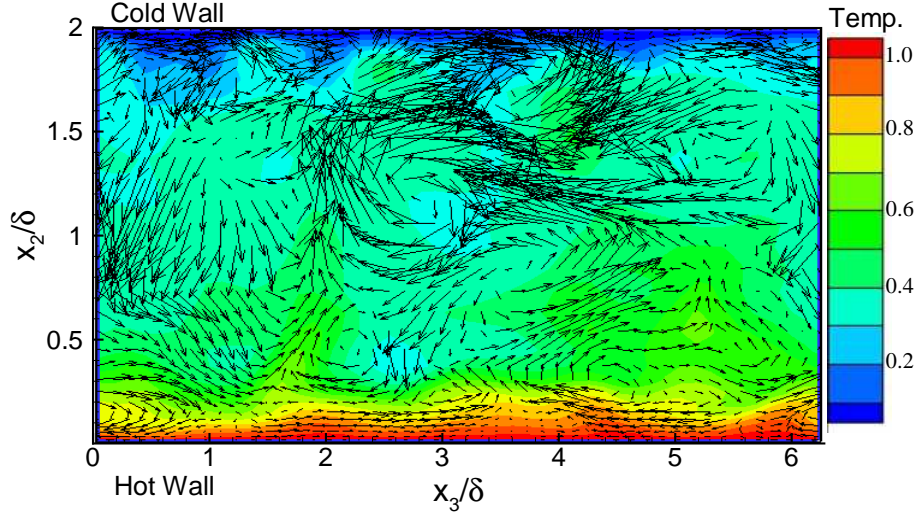


FIGURE 5.4: Instantaneous velocity vectors and temperature contour in a central transverse plane predicted by the set of dynamic nonlinear SGS models ($Gr = 9.6 \times 10^5$ and $Re_\tau^a = 150$). The temperature is non-dimensionalized as $\frac{\langle \bar{\theta} \rangle - \theta_{wc}}{\theta_{wh} - \theta_{wc}}$.

To investigate the effects of buoyancy on the balance of momentum and thermal energy, we decompose the instantaneous filtered quantity into the mean and residual components:

$$\bar{\phi} = \langle \bar{\phi} \rangle + \bar{\phi}'', \quad (5.2)$$

where $\langle \bar{\phi} \rangle$ denotes a filtered quantity averaged both in time and over the x_1 - x_3 plane, and $\bar{\phi}''$ denotes the residual component relative to $\langle \bar{\phi} \rangle$. By substituting Eq. (5.2) into the filtered streamwise momentum equation and then integrating the resulting equation from $x_2 = 0$ to a transverse location x_2 , the equation which balances the time- and plane-averaged shear stresses at an arbitrary wall-normal location x_2 is obtained

$$\nu \frac{\partial \langle \bar{u}_1 \rangle}{\partial x_2} - \langle \bar{u}_1'' \bar{u}_2'' \rangle + \int_0^{x_2} \beta g (\langle \bar{\theta} \rangle - \Theta_r) dx_2 - \langle \tau_{12} \rangle = \frac{1}{\rho} \frac{\partial \langle \bar{p} \rangle}{\partial x_1} x_2 + \frac{\tau_{wh}}{\rho}. \quad (5.3)$$

In order to derive the above approximate equation, two additional assumptions need to be made: the flow is (i) statistically stationary and (ii) homogeneous in the x_1 - x_3 plane. The four terms on the left-hand side (LHS) of Eq. (5.3) represent the resolved viscous shear stress, resolved Reynolds (or turbulent) shear stress, resolved buoyant shear stress, and SGS shear stress, respectively. The two terms on the right-hand side (RHS) of the equation represent the resolved integrated driving force due to the

mean streamwise pressure gradient, and the resolved viscous shear stress at the hot wall, respectively.

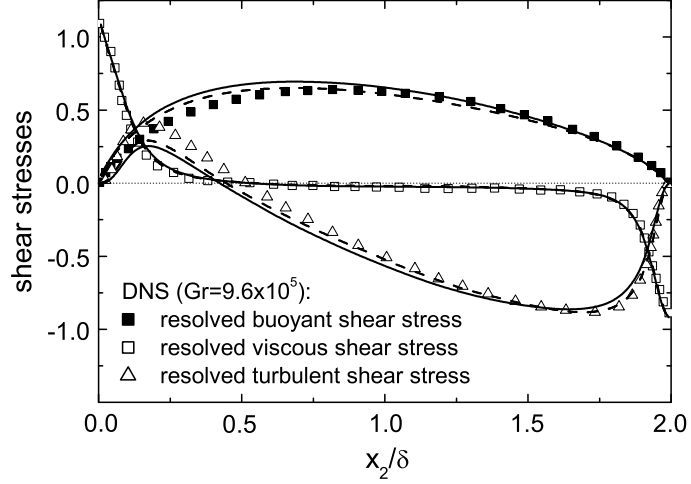


FIGURE 5.5: Non-dimensional shear stresses predicted by the two sets of linear and nonlinear SGS models. Solid line: DM&DEDM-HF; dash line: DNM&DTDM-HF.

The profiles of the first three terms on the LHS of Eq. (5.3), normalized by the value of the viscous shear stress term averaged over both walls [i.e., $\tau_w^a/\rho = (u_\tau^a)^2$], are shown in Figure 5.5 in comparison with the DNS results of Kasagi and Nishimura [141]. Since the SGS shear stress component $-\langle\tau_{12}\rangle$ is an order of magnitude smaller than these three terms, we will separately analyze this SGS effect in Subsection 5.4.4. In order for Eq. (5.3) to balance at both wall surfaces, the reference temperature Θ_r is taken as the bulk temperature, viz. $\Theta_r = \theta_b = \int_0^{2\delta} \langle\bar{\theta}\rangle dx_2 / (2\delta)$. With this convention, the resolved buoyant shear stress term in Eq. (5.3) vanishes at both wall surfaces. From Figure 5.5, it is observed that the LES prediction of the resolved viscous shear stress using both the linear and nonlinear sets of models is in good agreement with the DNS result [141]. However, the resolved buoyant shear stress is slightly overpredicted near the hot wall, and in contrast, the resolved Reynolds shear stress $-\langle\bar{u}_1''\bar{u}_2''\rangle$ is underpredicted in the same region. Figure 5.6 shows the absolute value of the resolved Reynolds shear stress using wall coordinates. From the figure, it is observed that due to the effect of buoyancy, $|\langle\bar{u}_1''\bar{u}_2''\rangle^+|$ is enhanced near the cold wall and suppressed near the hot wall. The LES results predicted by both sets of models agree better with the DNS result in the cold wall region than in the hot wall region. Furthermore, near the cold wall, the set of nonlinear models yields a prediction of $|\langle\bar{u}_1''\bar{u}_2''\rangle^+|$ closer to the DNS data than that predicted by the set of linear models.

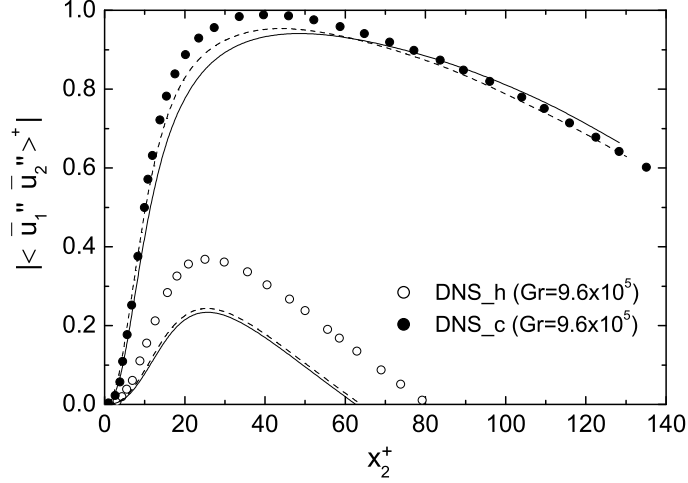


FIGURE 5.6: Resolved Reynolds shear stress shown using wall coordinates. Solid line: DM&DEDM-HF; dash line: DNM&DTDM-HF.

Following a similar procedure to derive Eq. (5.3), the time- and plane-averaged equation that balances the mean wall-normal heat fluxes at any arbitrary wall-normal location x_2 can be obtained from the filtered energy equation (2.7):

$$-\alpha \frac{\partial \langle \bar{\theta} \rangle}{\partial x_2} + \langle \bar{u}_2'' \bar{\theta}'' \rangle + \langle h_2 \rangle = \frac{q_{wh}}{\rho c_P}, \quad (5.4)$$

where $q_{wh} \stackrel{\text{def}}{=} -\lambda \frac{\partial \langle \bar{\theta} \rangle}{\partial x_2} \big|_{x_2=0}$ is the resolved molecular heat flux at the hot wall, and the three terms on the LHS of Eq. (5.4) correspond to the resolved molecular heat flux, resolved turbulent heat flux, and SGS wall-normal heat flux, respectively.

Figure 5.7 plots the resolved molecular and turbulent heat fluxes, which are normalized using the molecular heat flux at the hot wall $q_{wh}/(\rho c_P) = u_{\tau h} T_{\tau h}$ (we will discuss the SGS heat fluxes $\langle h_1 \rangle$ and $\langle h_2 \rangle$ separately in Subsection 5.4.4). As shown in the figure, in comparison with the molecular heat flux profile of the forced convection case ($Gr = 0$ and $Re_\tau = 150$, based on the DNS study of Davidson *et al.* [1]), the molecular heat flux of the mixed convection case predicted by both the current LES ($Gr = 9.6 \times 10^5$ and $Re_\tau^a = 150$) and DNS ($Gr = 7.68 \times 10^6$ and $Re_\tau^a = 150$) by Davidson *et al.* [1] increases noticeably near the hot wall, and decreases slightly near the cold wall; in contrast, the profile of the resolved turbulent heat flux displays the opposite trend. This is consistent with the notion that the turbulent motions are enhanced near the cold wall and suppressed near the hot wall. Also shown in the

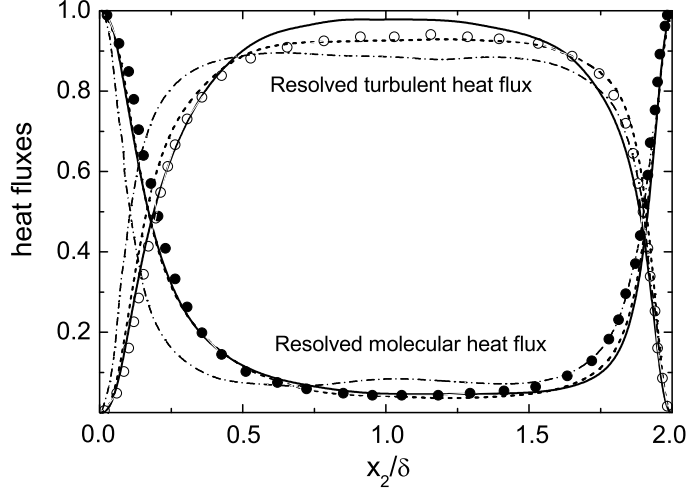


FIGURE 5.7: Non-dimensional wall-normal heat fluxes predicted by the two sets of linear and nonlinear SGS models ($Gr = 9.6 \times 10^5$ and $Re_\tau^a = 150$). Dash dot line: DNS ($Gr = 0$, Davidson *et al.* [1]); symbols (\bullet and \circ): DNS ($Gr = 7.68 \times 10^6$, Davidson *et al.* [1]); solid line: DM&DEDM-HF; dash line: DNM&DTDM-HF.

figure, the profiles of the resolved molecular heat flux predicted by both sets of the models are very similar; in contrast, the profiles of the resolved turbulent heat flux predicted by these two sets of models are notably different.

Figure 5.8 shows the resolved streamwise and wall-normal turbulent heat fluxes using the wall coordinate (i.e., $\langle \bar{u}_1'' \bar{\theta}'' \rangle^+$ and $\langle \bar{u}_2'' \bar{\theta}'' \rangle^+$, respectively). Both sets of linear and nonlinear models capture the trend of the DNS profile. Formally speaking, for a thermal convective flow in a plane channel, the time- and plane-averaged heat flux obtained from a DNS approach can be approximately recovered by an LES approach using the time- and plane-averaged resolved and SGS heat fluxes. However, because the resolved heat flux is an important physical quantity and its value usually dominates the SGS heat flux contribution in LES of many engineering and theoretical test flows, it is still popular to directly compare the resolved heat flux with the DNS results in literature. This direct comparison can be useful especially in a comparative study of different SGS modelling approaches. If the test condition is the same, the SGS modelling approach which produces results that are in better conformance with the DNS data can be considered as a more desirable approach. As shown in Figure 5.8a, in the cold wall region, the set of nonlinear models overpredicts the peak value of the streamwise turbulent heat flux $\langle \bar{u}_1'' \bar{\theta}'' \rangle^+$ in comparison with the DNS data [141]; in contrast, the set of linear SGS models underpredicts the peak value.

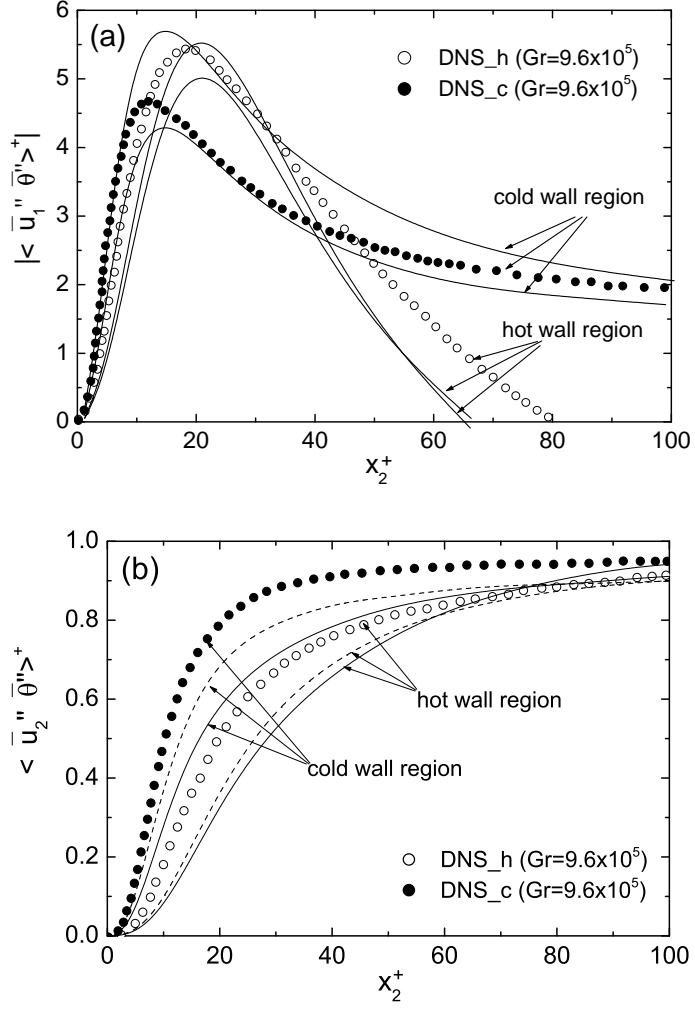


FIGURE 5.8: Resolved turbulent heat fluxes shown using wall coordinates: (a) streamwise; (b) wall-normal. Solid line: DM&DEDM-HF; dash line: DNM&DTDM-HF.

From Figure 5.8b, it is observed that the prediction of the wall-normal turbulent heat flux in both the hot and cold wall regions by the set of nonlinear SGS models is generally in better conformance with the DNS data [141] than that predicted by the set of linear SGS models. Figure 5.9 re-plots the profiles of the resolved streamwise and wall-normal turbulent heat fluxes using logarithmic coordinates based on the same data set for Figure 5.8. Following Na and Hanratty [148], it can be shown using a Taylor series expansion that in the vicinity of the wall, the following relations hold: $\langle \bar{u}_1'' \bar{\theta}'' \rangle^+ \propto x_2^{+2}$ and $\langle \bar{u}_2'' \bar{\theta}'' \rangle^+ \propto x_2^{+3}$. Such near-wall restrictions are evident in Figs. 5.9a and 5.9b, and valid in both the hot and cold wall regions.

The effective eddy diffusivity for the wall-normal turbulent heat flux is defined

as $\Gamma_2 = -\langle \bar{u}_2'' \bar{\theta}'' \rangle / (d\langle \bar{\theta} \rangle / dx_2)$. Figure 5.10 compares the value of Γ_2 predicted by the two sets of linear and nonlinear SGS models. In the figure, Γ_2 is non-dimensionalized with molecular thermal diffusivity. Common to both sets of SGS models, the predicted level of Γ_2 near the cold wall is larger than that near the hot wall. This is due to the fact that buoyancy enhances and suppresses the turbulent heat fluxes near the cold and hot walls, respectively [cf. Figure 5.8b]. As shown in Figure 5.10, the value of Γ_2 predicted using the set of nonlinear models is noticeably larger than that predicted using the set of linear SGS models, especially in the central region of the channel.

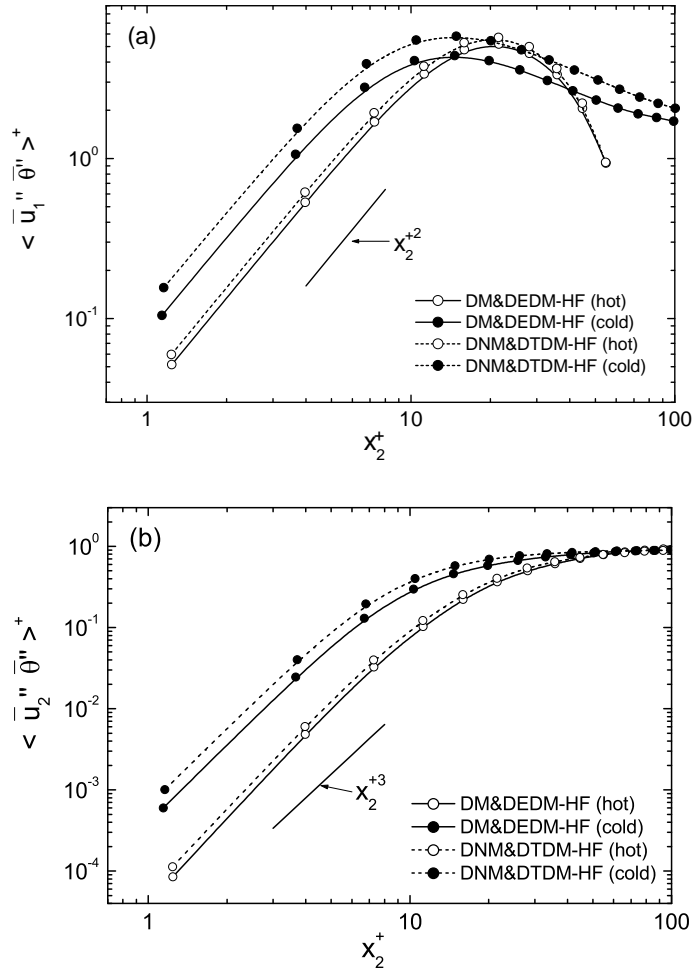


FIGURE 5.9: Resolved turbulent heat fluxes shown using logarithmic wall coordinates ($Gr = 9.6 \times 10^5$ and $Re_\tau^a = 150$): (a) streamwise component; (b) wall-normal component.

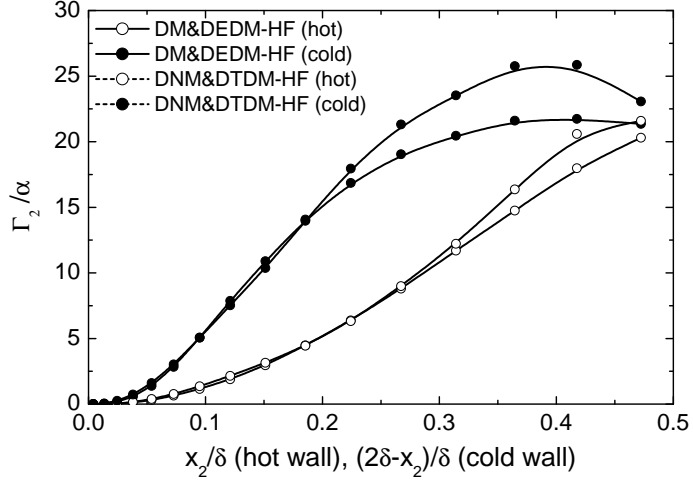


FIGURE 5.10: Effective eddy diffusivity for the wall-normal turbulent heat flux ($Gr = 9.6 \times 10^5$ and $Re_\tau^a = 150$).

5.4.3 Velocity and Temperature Fluctuations

For the forced convective flow with $Gr = 0$, the variance of the resolved temperature and velocity field (corresponding to resolved turbulence intensities for the latter case) is distributed in a symmetrical manner across the channel. However, for the mixed convection case of $Gr > 0$, the values of the resolved turbulence intensities near the hot and cold walls are expected to be different due to the existence of buoyancy. Figure 5.11 shows that the effect of buoyancy is to enhance the level of all three velocity fluctuation components (represented by $\bar{u}_{1,rms}^+$, $\bar{u}_{2,rms}^+$ and $\bar{u}_{3,rms}^+$, respectively) near the cold wall, and to reduce it near the hot wall. Here, the resolved velocity fluctuations are evaluated using the non-dimensionalized root-mean-square values defined as $\bar{u}_{i,rms}^+ \stackrel{\text{def}}{=} \langle (\frac{\bar{u}_i - \langle \bar{u}_i \rangle}{u_\tau})^2 \rangle^{1/2}$ for $i = 1, 2$ and 3 . From Figure 5.11, it is observed that the predictions from both sets of linear and nonlinear models in general agree with of the reported DNS results of Kasagi and Nishimura [141]. However, as indicated by Figure 5.11a, the set of nonlinear models yields a slightly better prediction for the streamwise velocity fluctuation $\bar{u}_{1,rms}^+$ in the opposing flow region than the set of linear models.

Figure 5.12 compares the resolved temperature fluctuation $\bar{\theta}_{rms}^+ \stackrel{\text{def}}{=} \langle (\frac{\bar{\theta} - \langle \bar{\theta} \rangle}{T_\tau})^2 \rangle^{1/2}$ predicted using the two sets of SGS models with the DNS data [141]. In general, it is observed that the prediction of $\bar{\theta}_{rms}^+$ from both sets of linear and nonlinear SGS models is similar to the DNS results. It is interesting to observe that the effect of buoyancy on

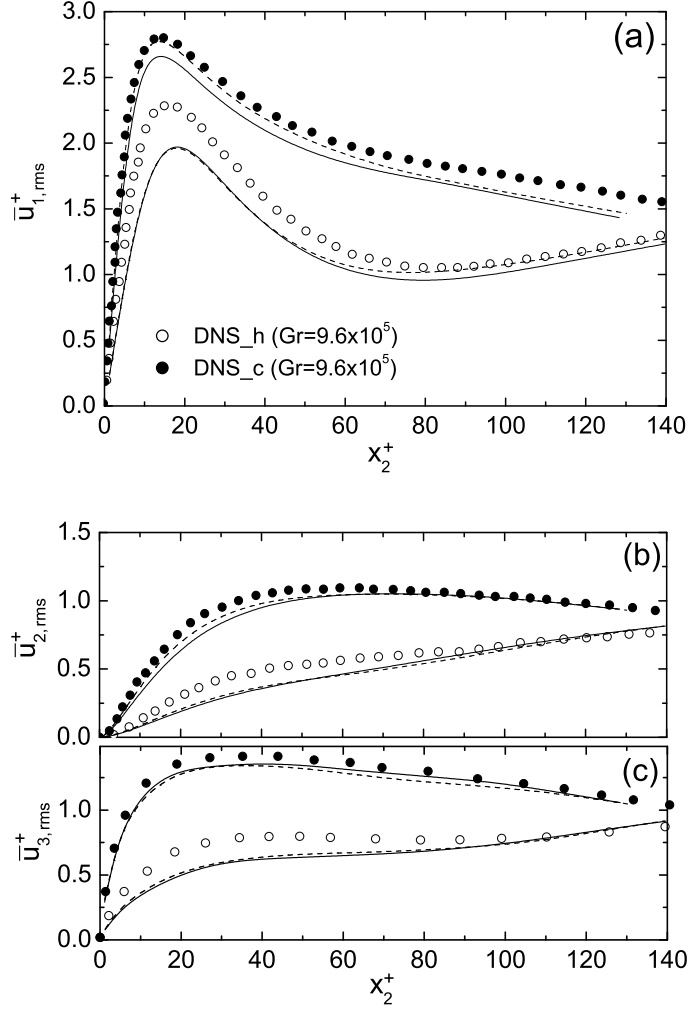


FIGURE 5.11: Resolved velocity fluctuations in wall coordinates: (a) streamwise; (b) wall-normal; (c) spanwise. Solid line: DM&DEDM-HF; dash line: DNM&DTDM-HF.

the resolved temperature fluctuation is exactly opposite to its effect on the resolved velocity functions as discussed above: $\bar{\theta}_{rms}^+$ is suppressed near the cold wall and enhanced near the hot wall. This result is consistent with the observation of Davidson *et al.* [1] in their DNS study of mixed convection. By definition, the production term, $-\langle \bar{u}_2'' \bar{\theta}'' \rangle (\partial \langle \bar{\theta} \rangle / \partial x_2)$, in the transport equation for the resolved temperature variance, is based on the wall-normal turbulent heat flux and the resolved temperature gradient [1]. For the mixed convection case, since the wall-normal turbulent heat flux $\langle \bar{u}_2'' \bar{\theta}'' \rangle$ is suppressed by buoyancy near the hot wall, the resolved wall-normal temperature gradient must increase in order to balance Eq. (5.4). Furthermore, the increase in the resolved temperature gradient $\partial \langle \bar{\theta} \rangle / \partial x_2$ must be much larger than the

decrease in $\langle \bar{u}_2'' \bar{\theta}'' \rangle$, since $\alpha \ll 1$. This explains why in Figure 5.12, $\bar{\theta}_{rms}^+$ is enhanced near the hot wall while it is suppressed near the cold wall in comparison with the forced convection case of $Gr = 0$.

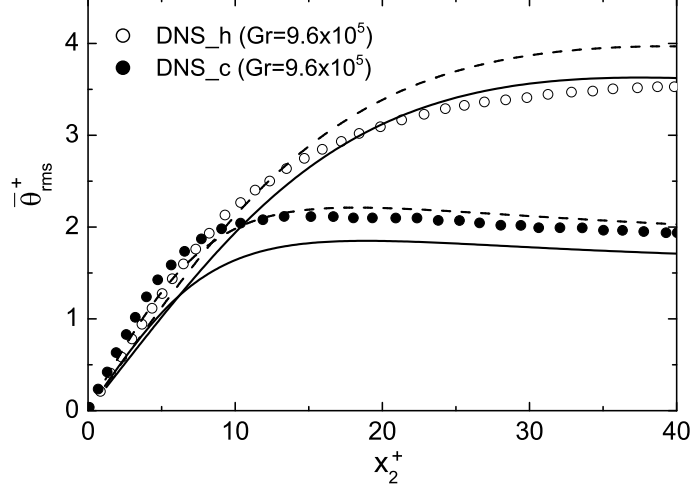


FIGURE 5.12: Resolved temperature fluctuations in wall coordinates. Solid line: DM&DEDM-HF; dash line: DNM&DTDM-HF.

5.4.4 SGS Effects

In Subsections 5.4.1–5.4.3, we have observed that although slight differences exist, some of the mean resolved scale quantities predicted by the two different sets of SGS models are similar in terms of their values, e.g. the mean resolved streamwise velocity and temperature shown in Figure 5.2 and the mean resolved viscous shear stress shown in Figure 5.5. This is not surprising, since in LES the large scale motions which contribute the most to the resolved fields are calculated directly. In order to understand a SGS model in greater detail, refined examination should be based on the statistics related to residual SGS motions, which of course, are expected to be more erratic than the resolved large-scale motions. For this purpose, Figs. 5.13–5.14 demonstrate some SGS effects involved in the current LES study of mixed convection.

Figure 5.13 compares the SGS shear stress $-\tau_{12}$ predicted by the two sets of linear and nonlinear SGS models. Although the predictions of both sets of SGS models show similar trends, the magnitude of the SGS shear stress predicted by the set of linear SGS models is higher than that predicted by the set of nonlinear SGS

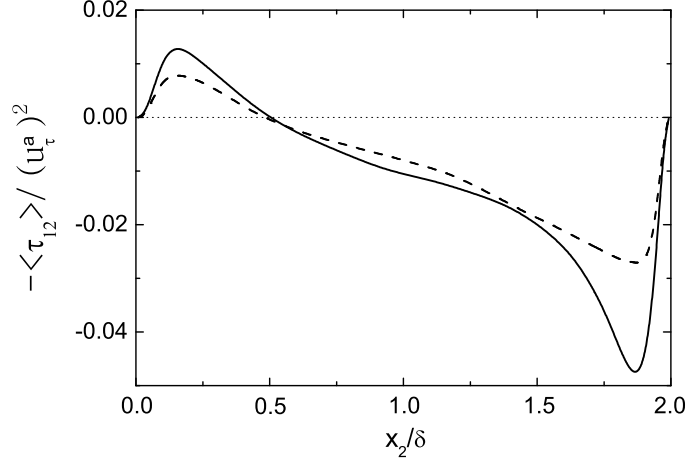


FIGURE 5.13: SGS shear stress produced by SGS models ($Gr = 9.6 \times 10^5$ and $Re_\tau^a = 150$). Solid line: DM&DEDM-HF; dash line: DNM&DTDM-HF.

models. Figure 5.14 compares the SGS heat fluxes predicted by the two sets of linear and nonlinear SGS models. As shown in the figure, the SGS heat fluxes produced by the two sets of SGS models are markedly different: the set of linear SGS models yields $|\langle h_1 \rangle| \leq |\langle h_2 \rangle|$, whereas the set of nonlinear SGS models yields $|\langle h_1 \rangle| \geq |\langle h_2 \rangle|$. According to Peng and Davidson [40], it is more reasonable to obtain $|\langle h_1 \rangle| \geq |\langle h_2 \rangle|$, which is in consistent with the observation that the level of the resolved streamwise turbulent heat flux $\langle \bar{u}_1'' \bar{\theta}'' \rangle$ is usually larger than that of the resolved wall-normal turbulent heat flux $\langle \bar{u}_2'' \bar{\theta}'' \rangle$. Furthermore, it is noted that the set of nonlinear SGS models enhances the magnitude of $\langle h_1 \rangle$, even though no mean temperature gradient exists in the streamwise direction. An explanation for this observation is that in comparison with the DEDM-HF, the DTDM-HF has more degrees of freedom for geometrical representation of the SGS HF vector, and allows for a non-alignment between h_j and $-\partial \bar{\theta} / \partial x_j$ to reflect the physics of turbulent thermal energy transport at the subgrid scale.

5.5 Summary

In this research, LES of a combined forced and natural convection between two vertical plates has been performed. Prototypical flow features of the resolved temperature and velocity fields, and mean turbulent shear stresses and heat fluxes have been re-

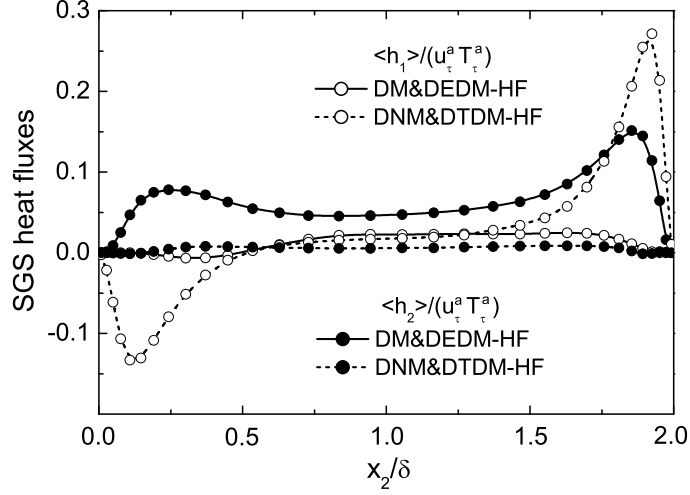


FIGURE 5.14: SGS heat fluxes produced by SGS models ($Gr = 9.6 \times 10^5$ and $Re_\tau^a = 150$).

produced at the resolved scale and compared with the DNS results. It is observed that, in contrast to forced convective flows driven purely by the mean pressure gradient, the existence of buoyancy in the current test case has a significant impact on both the resolved and subgrid-scale quantities. Due to buoyancy effects, the distribution of many flow parameters is asymmetrical across the channel, which includes the wall-normal distribution of the mean resolved temperature and velocity field, resolved turbulent and subgrid-scale shear stresses and heat fluxes, root-mean-square value of the fluctuation in the filtered velocity and temperature fields, and effective diffusivity for the resolved turbulent heat flux.

Two sets of dynamic SGS models were tested in the simulation, i.e. the set of linear SGS models with the DM for modelling the SGS stress and the DEDM-HF for modelling the SGS HF, and the set of nonlinear SGS models with the DNM modelling for the SGS stress and the DTDM-HF for modelling the SGS HF. The performances of these two sets of SGS models are different in terms of the SGS motions. In particular, their predictions for the SGS shear stress and SGS heat fluxes are markedly different. Although notable differences exist between these two sets of SGS models at the subgrid-scale level, it is observed that some flow quantities predicted by these two sets of SGS models are similar at the resolved scale. This is because in an LES approach, the large dominant turbulent motions and thermal energy transport processes are directly computed and the contribution from the SGS

motions is usually limited. In terms of the time- and plane-averaged values, the SGS shear stress ($-\tau_{12}$) predicted by both sets of SGS models is less than 3% of the resolved Reynolds shear stress; and the wall-normal SGS heat flux (h_2) predicted by the sets of nonlinear and linear SGS models is less than 2% and 8% of the resolved wall-normal turbulent heat flux, respectively. At the resolved scale, the difference between these two sets of SGS models is relatively more distinguishable in terms of the quantities related to the temperature field, especially in the cold wall region where the turbulent effect is the strongest due to the existence of buoyancy. It is found in the numerical simulation that the performance of the set of nonlinear SGS models is generally more satisfactory than that of the set of linear SGS models, however, there is also an accompanied slight increase in computational time.

Chapter 6

Geometrical Properties of the Resolved-Scale Velocity and Temperature Fields of Buoyant Channel Flow

6.1 Introduction

As introduced in section 1.3, *turbulence geometrical statistics* is a recently developed methodology for studying geometrical properties of local flow structures. The earliest works on this topic include those by Taylor [122], Townsend [149] and Betchov [119]. Previously, the study of the geometrical properties of turbulence has primarily used DNS and experimental data. Recently, the LES approach has also been used for studying turbulence for several reasons. Since LES costs much less in terms of computational resources and is not limited to low Reynolds number flows, it can be used where DNS cannot. The study of the geometrical properties can lead to a better understanding of the mechanism of interactions between the resolved and subgrid-scale motions. The analysis of the geometrical properties can potentially be used to improve SGS models. In LES, the flow motions can be decomposed into resolved scale and SGS components. Since LES computes the resolved scale motions directly and is expected to predict the major physics of turbulent flows at the resolved scale, those important geometrical characteristics obtained with the DNS and experimental approach are also expected to be manifested by the resolved scale flow field. As introduced in section 1.3, *a priori* LES approaches have been applied to study the geometrical properties of the resolved scale motions and the orientation of the SGS

models [54, 55, 57, 66, 133]. Following that work, *a posteriori* LES approaches have also been applied [12, 58, 59].

In this chapter, the methodology of turbulence geometrical statistics is applied to investigate the geometrical properties of both the velocity and temperature field based on *a posteriori* LES prediction of the wall-bounded thermal turbulent flow which has been investigated in chapter 5. This chapter focuses on the geometrical properties of the resolved velocity and temperature field and the geometrical alignment of the SGS models, i.e. the DNM and DM for the SGS stress term, and the DTDM-HF and DEDM-HF for the SGS heat flux term. The geometrical properties of the local flow structures, such as resolved helicity, enstrophy generation, local vortex stretching, and the alignment between the resolved velocity, vorticity, temperature gradient, subgrid-scale heat flux and the eigenvectors of the resolved strain rate tensor are studied. Unlike most other studies which did not explore the geometrical characteristics of near-wall flow, in this chapter, the effect of the presence of solid walls on the local flow structures is specifically studied. The buoyancy effect on the geometrical property of the thermal flow field is also investigated with respect to the different flow regimes in the hot and cold wall regions.

6.2 Physical Model and Numerical method

The physical model tested in this chapter is mixed convection in a vertical channel. Details of the flow and numerical methods can be found in chapter 5. In order to compare the LES predictions with the reported DNS and experimental results and also to examine the SGS effects, a number of SGS models are employed in our simulations for modelling the SGS stress tensor $\tau_{ij} \stackrel{\text{def}}{=} \overline{u_i u_j} - \bar{u}_i \bar{u}_j$ and the SGS HF vector $h_j \stackrel{\text{def}}{=} \overline{u_j \theta} - \bar{u}_j \bar{\theta}$. In particular, we compare the set of the linear SGS models based on the DM of Lilly [7] (for modelling τ_{ij}) and DEDM-HF of Moin *et al.* [20] (for modelling h_j), with the set of nonlinear SGS models based on the DNM of Wang and Bergstrom [9] (for modelling τ_{ij}) and DTDM-HF of Peng and Davidson [40] (for modelling h_j). A brief summary of these models can be found in Sections 2.3 and 2.4. To obtain the turbulent statistics, a time period of 10,000 time steps was used after

the flow becomes fully developed. For statistics, 30 bins were used for calculating the probability density function (PDF) and 30×30 bins were used for calculating the joint PDF (JPDF) of the sample data in the homogeneous (x_1 - x_3) plane.

6.3 Analysis of Results

This current research is a continuation of the previous chapter, which focused on addressing the basic features of the temperature and velocity fields of the test flow obtained using the LES approach in comparison with the DNS data of Kasagi and Nishimura [141], Kuroda *et al.* [146] and Davidson *et al.* [1]. Therefore, in this chapter, the analysis will focus on the geometrical properties of the thermal flow field, and skip the discussion of the details of the basic flow features.

6.3.1 Structural Configurations of Local Fluid Element Deformation

In this subsection, we investigate the local fluid element deformation configuration by analyzing the statistical results on the ratio of the three principal values of the resolved strain rate tensor \bar{S}_{ij} . As mentioned earlier, according to Lund and Rogers [42], the statistics based on β^* is biased due to improper normalization of the parameter, and they recommended using S^* for distinguishing local fluid element deformation configurations for turbulent flows. To verify the proposal of Lund and Rogers [42], the PDFs of the non-dimensional parameters S^* and β^* in the logarithmic layer near the hot wall are compared in Figure 6.1. Figure 6.1 shows that the most probable value for β^* is 0.433, indicating that the most probable flow configuration is a QTD state with $\alpha_S : \beta_S : \gamma_S = 3.4 : 1 : -4.4$, which is close to the classical ratio of $3 : 1 : -4$ initially proposed by Ashurst *et al.* [48] and Kerr [49]. In contrast to the above biased results based on the parameter β^* , Figure 6.1 shows that the mode of the PDF of S^* is located at $S^* = 1$, which indicates that the most probable flow configuration in the logarithmic layer is axisymmetric expansion ($\alpha_S : \beta_S : \gamma_S = 1 : 1 : -2$), a result that is consistent with the previous observations of other researchers based on isotropic and wall-bounded turbulent flows [42, 53, 54, 120].

Figures 6.2a–c compare the PDFs of S^* in the three different flow regimes in both the hot and cold wall regions. Since the prediction of the PDFs by the DM&DEDM-HF is similar to that by the DNM&DTDM-HF except for some differences in the magnitude of the PDFs, here we only present the results based on the later. As shown in Figure 6.2a, in the viscous sublayer, the mode of the PDFs occurs at $S^* = 0$, which reveals that the most probable local flow configuration in both the hot and cold wall regions is close to the PTD pattern ($\alpha_S : \beta_S : \gamma_S = 1 : 0 : -1$). This reflects the intrinsic 2-D nature of the near-wall viscous sublayer flow ($x_2^+ = 4$). From Figures 6.2a and b, it is observed that as the distance from the wall increases (as the value of x_2^+ increases), the value of S^* corresponding to the PDF mode increases, and the local flow configuration deviates from the PTD pattern towards a QTD pattern ($0 < S^* < 1$), eventually reaching the state of axisymmetric expansion ($S^* = 1$) in the logarithmic layer. From Figure 6.2a and b, and especially from Figure 6.2b, it is observed that the value of S^* corresponding to the mode is smaller in the hot wall region and larger in the cold wall region. This confirms our previous analysis (cf. Figure 5.4) that the turbulence is enhanced (and thus, more 3-D towards the axisymmetric expansion state) near the cold wall due to the effects of buoyancy.

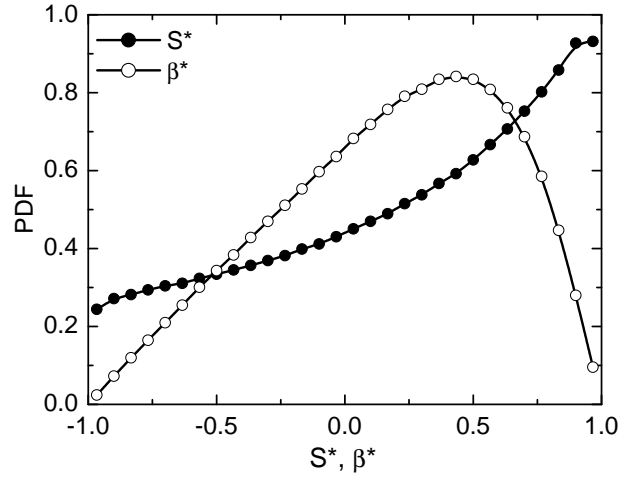


FIGURE 6.1: PDF of S^* and β^* in the logarithmic layer predicted using DNM&DTDM-HF.

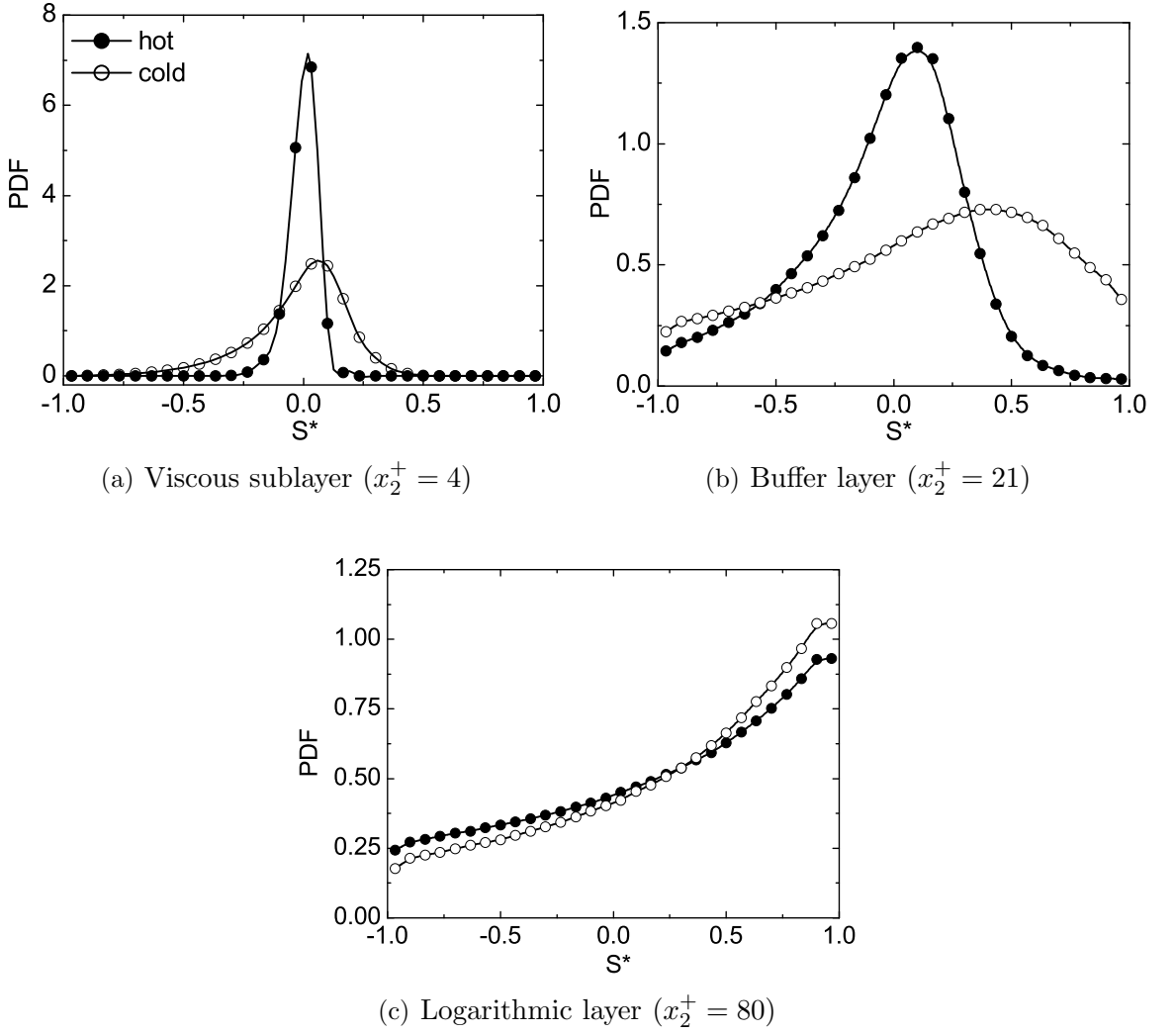


FIGURE 6.2: PDF of S^* for three different flow regimes predicted using the DNM&DTDM-HF.

6.3.2 Resolved Enstrophy Generation and Helicity

In this subsection, we analyze the geometrical property of the resolved vorticity vector ($\bar{\omega}$) in terms of its relative orientation with other fluid vectors. In particular, we focus on discussing two subjects: (i) resolved enstrophy generation and local vortex stretching patterns, and (ii) resolved helicity and local helical structures. We understand that resolved enstrophy generation characterizes the geometrical alignment pattern between the resolved vorticity and vortex stretching ($\bar{\mathbf{w}}$) vectors; whereas, resolved helicity characterizes the geometrical alignment pattern between the resolved

vorticity and velocity ($\bar{\mathbf{u}}$) vectors. Since the predicted PDF patterns of $\bar{\sigma}_n$ and \bar{h}_n by the DM&DEDM-HF are similar to those by the DNM&DTDM-HF except for some differences in the magnitude of the PDFs, we only present here the results obtained using the DNM&DTDM-HF.

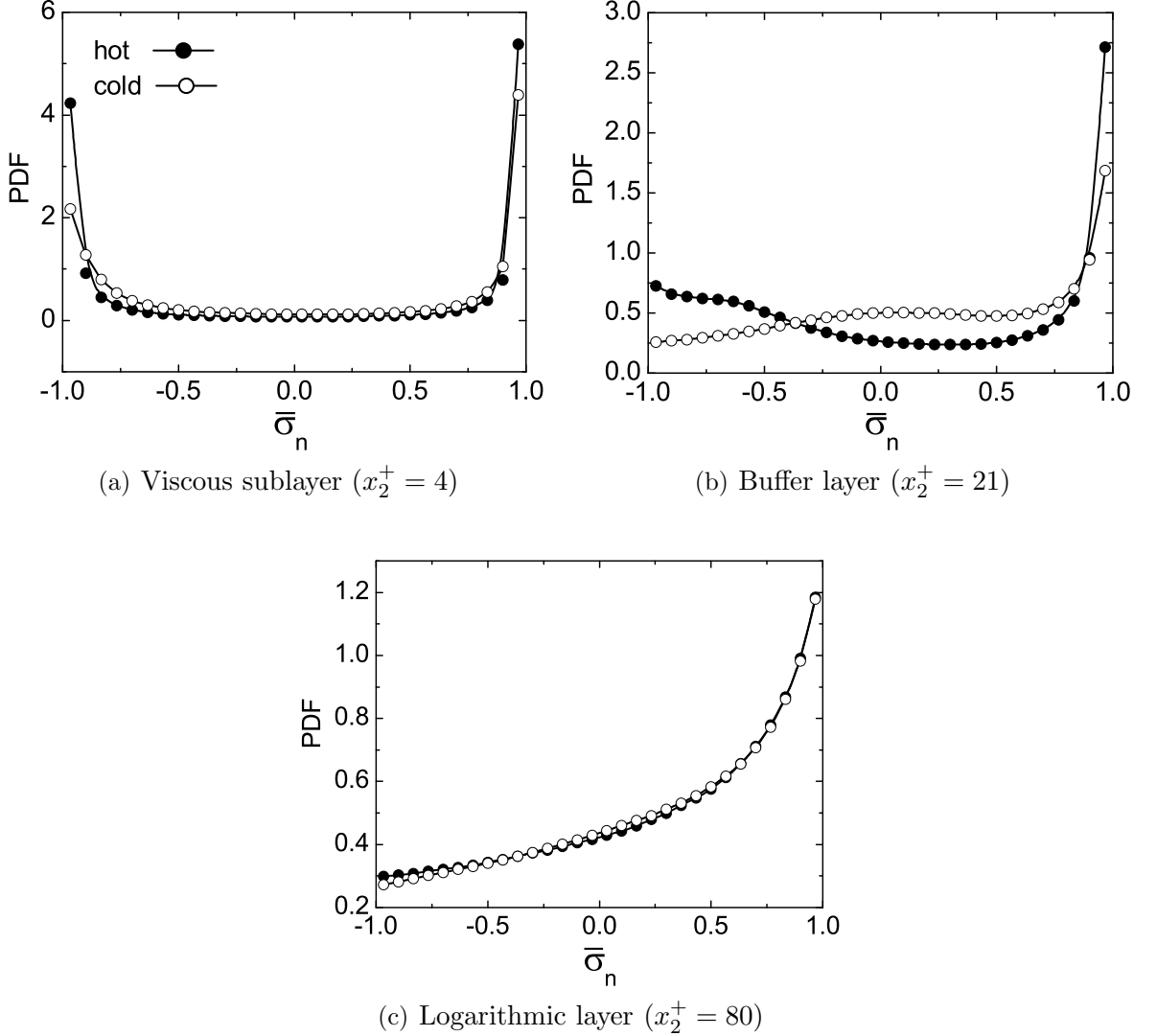


FIGURE 6.3: PDF of the resolved normalized enstrophy generation predicted using the DNM&DTDM-HF.

Figure 6.3 shows the PDF of the normalized enstrophy generation $\bar{\sigma}_n$ evaluated in the hot and cold wall regions based on the resolved velocity field. In Figure 6.3a, a bi-modal PDF pattern is observed, which indicates that both local vortex stretching ($\bar{\sigma}_n = 1$) and compressing ($\bar{\sigma}_n = -1$) are the most probable patterns in the viscous sublayer. This bi-modal PDF distribution for the viscous sublayer predicted by the current LES is consistent with the observation of Chong *et al.* [150] who analyzed DNS

data of a wall-bounded turbulent shear flow. From Figures 6.3b and c, it is evident that in both the buffer and logarithmic layers, the resolved vorticity vector $\bar{\omega}$ becomes preferentially aligned with the resolved vortex stretching vector $\bar{\mathbf{w}}$, suggesting that the local vortex stretching pattern becomes predominant as the distance from the wall increases. Similar observations of this preferential alignment between $\bar{\omega}$ and $\bar{\mathbf{w}}$ were obtained by Andreotti [124] who studied this alignment feature based on Burger’s models, and by Tsinober *et al.* [125] and Shtilman *et al.* [41] who analyzed DNS data of isotropic turbulence. In contrast to the PDF of S^* shown in Figure 6.2, the difference between the hot and cold wall regions in terms of the PDF of $\bar{\sigma}_n$ shown in Figure 6.3 is limited, implying that the temperature field of this specific test flow does not have a significant impact (through the buoyant force term in the filtered momentum equation) on the statistics of the local vortex stretching and compression patterns.

Figure 6.4 shows the PDF of the resolved helicity density \bar{h}_n and its flatness indicator $\langle \bar{h}_n^2 \rangle$ for three different flow layers: viscous sublayer, buffer layer, and logarithmic layer for both the hot and cold wall regions. The flatness indicator $\langle \bar{h}_n^2 \rangle \stackrel{\text{def}}{=} \frac{1}{N} \sum_{i=1}^N (\bar{h}_n^2)_i$ where N is the number of bins, was introduced by Rogers and Moin [43] for evaluating the strength of helical motions in the flow. Figure 6.4a and b indicate that a state of $\bar{h}_n = 0$ is the most prevalent in both the viscous sublayer and buffer layer, indicating a preferential orthogonal alignment between the resolved velocity $\bar{\mathbf{u}}$ and vorticity vector $\bar{\omega}$. The preference for this orthogonal alignment pattern is the most strongly expressed in the viscous sublayer. Such a near-wall anisotropic effect on helicity has been well documented based on DNS data of Poiseuille channel flow [43, 47]. In effect, by assuming that the streamwise velocity component and the wall-normal velocity gradient component are dominant in the near-wall region, the resolved vorticity can then be approximated as $\bar{\omega}|_{\text{wall}} \approx [0, 0, -\bar{u}_{1,2}]_{\text{wall}}^T$. This indicates that in the near-wall region, $\bar{\omega}$ is primarily aligned in the spanwise direction being perpendicular to the dominant streamwise velocity component \bar{u}_1 , resulting in $\bar{h}_n \approx 0$ in the vicinity of the wall. Figure 6.4c shows a relatively uniform (or, “flat”) distribution of \bar{h}_n in the logarithmic region (since the value of the probability density ranges only from 0.42 to 0.57), with the value of $\langle \bar{h}_n^2 \rangle$ being 0.303 and 0.336 in the hot and cold wall regions, respectively. Although a thermal effect is involved in our test case, it is

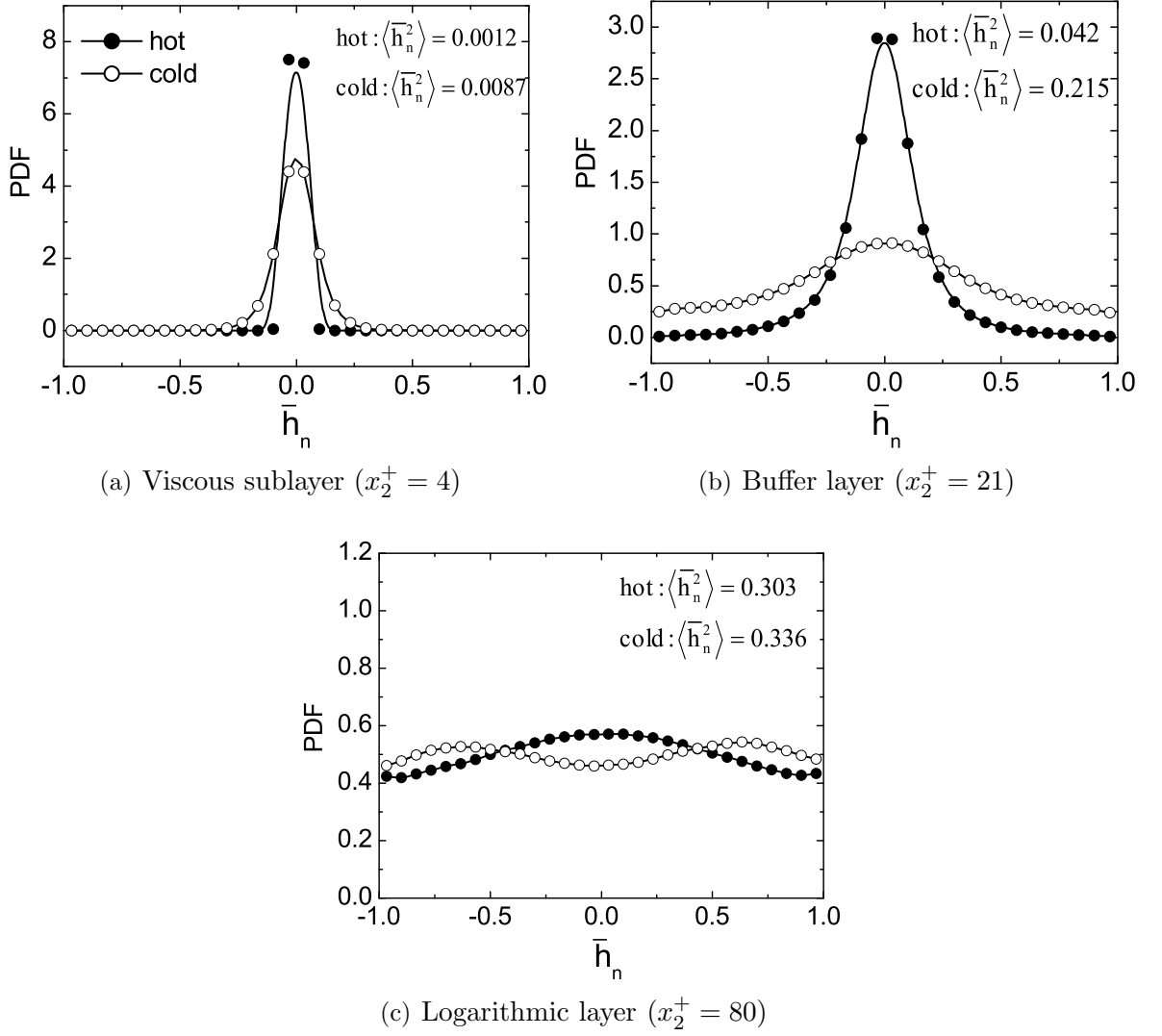


FIGURE 6.4: PDF of the resolved-scale relative helicity predicted using the DNM&DTDM-HF.

interesting to observe that these values are comparable to those for the logarithmic layer of the plane channel flow ($Re_\tau = 180$) obtained by Rogers and Moin [43] using a DNS approach; in their case, $\langle \bar{h}_n^2 \rangle$ ranged from 0.307 to 0.337. In comparison with the values of $\langle \bar{h}_n^2 \rangle$ shown in Figures 6.4a and b, it is concluded that as the distance from the wall increases (as the value of x_2^+ increases), helical activities as indicated by the value of $\langle \bar{h}_n^2 \rangle$ increase significantly for both the hot and cold wall regions. This observed strong wall anisotropic effect is consistent with the physical feature that for combined forced and natural convection in a vertical channel, large flow structures are formed in the core region of the channel, and as the wall is approached, the scales of the flow structure become smaller. An explanation for this feature is that because

helicity tends to reduce nonlinear interactions and inhibits the cascade of TKE to smaller scales, helical structures tend to remain coherent over a relatively long life-span. As a result, high-level helical activity is preferentially located in the regions with large-scale turbulent motions [43] (in the core region of the channel for this particular test case). Another important physical feature exhibited in Figures 6.4a, b and c is that the value of $\langle \bar{h}_n^2 \rangle$ is higher in the cold wall region than in the hot wall region for all three flow regimes. A stronger helical activity observed in the cold wall region implies that the large-scale motions are more prominent in the cold wall region, which is consistent with the characteristics of the velocity field demonstrated previously in Figure 5.4.

6.3.3 Attitude of the Resolved Vorticity Vector with Respect to the Eigenframe of the Resolved Strain Rate Tensor

As briefly mentioned in Section 1.3, the geometrical alignment pattern between the resolved vorticity $\bar{\omega}$ and the intermediate eigenvector $\mathbf{e}_{S\beta}$ of the resolved strain rate tensor \bar{S}_{ij} has been noted in many studies ever since the seminal works of Ashurst *et al.* [48] and Kerr [49] in the mid 1980's. Since then, this subject has been extensively studied based on a variety of analytical, experimental and numerical methodologies. The analytical methodologies include the restricted Euler equation approach of Cantwell [151], Burgers' vortex method of Andreotti [124] and development of the Lagrangian evolution equation by Dresselhaus and Tabor [152]. Experimental validations include the studies of Tsinober *et al.* [44, 125] who measured a turbulent grid flow and boundary-layer flow over a smooth plate using 12- and 20-wire probes, Honkan and Andreopoulos [45] who measured boundary-layer turbulence using three individual triple-wire gradient probes, Tao *et al.* [54] who processed HPIV measurements of the core field of a square duct flow using an *a priori* LES approach, and Higgins *et al.* [57] who processed field data measured using sonic anemometer arrays for an *a priori* LES study of the atmospheric surface layer. Numerical studies of this special alignment pattern between $\bar{\omega}$ and $\mathbf{e}_{S\beta}$ include the LES study of Couette flows [59] and a variety of DNS studies based on isotropic and wall-bounded turbulent flows [50, 51, 53, 55, 125, 153–155]. Up to now, research on the

alignment between $\bar{\omega}$ and $\mathbf{e}_{S\beta}$ has been restricted primarily to isotropic isothermal flows [48–51, 54, 55, 125, 153–155]. In this regard, investigations of wall-bounded flows and non-isothermal flows are still limited. Reports of the wall anisotropic effect on the preferred alignment between $\bar{\omega}$ and $\mathbf{e}_{S\beta}$ are only found in the previous DNS studies by Blackburn *et al.* [53], experimental investigations by Honkan and Andreopoulos [45], and LES studies by Higgins *et al.* [57] and Wang *et al.* [59].

In order to describe the alignment angle between two random vectors, some researchers evaluated the PDF of the cosine of the angle between these two vectors [44, 48, 50, 55, 57, 153], whereas some prefer to study the PDF of the angle itself [45]. The results obtained using these two approaches can be inconsistent especially when the alignment angle approaches zero. Blackburn *et al.* [53] studied both methods and indicated that the inconsistency in the results of these two methods is due to a “weighting effect” between the two different types of PDFs. Following the lead of Blackburn *et al.* [53], here we further clarify this issue based on spherical trigonometry analysis, and later, we will extend this analysis of the alignment angle between two vectors to a more general case for studying the attitude of a vector with respect to a 3-D Cartesian triad.

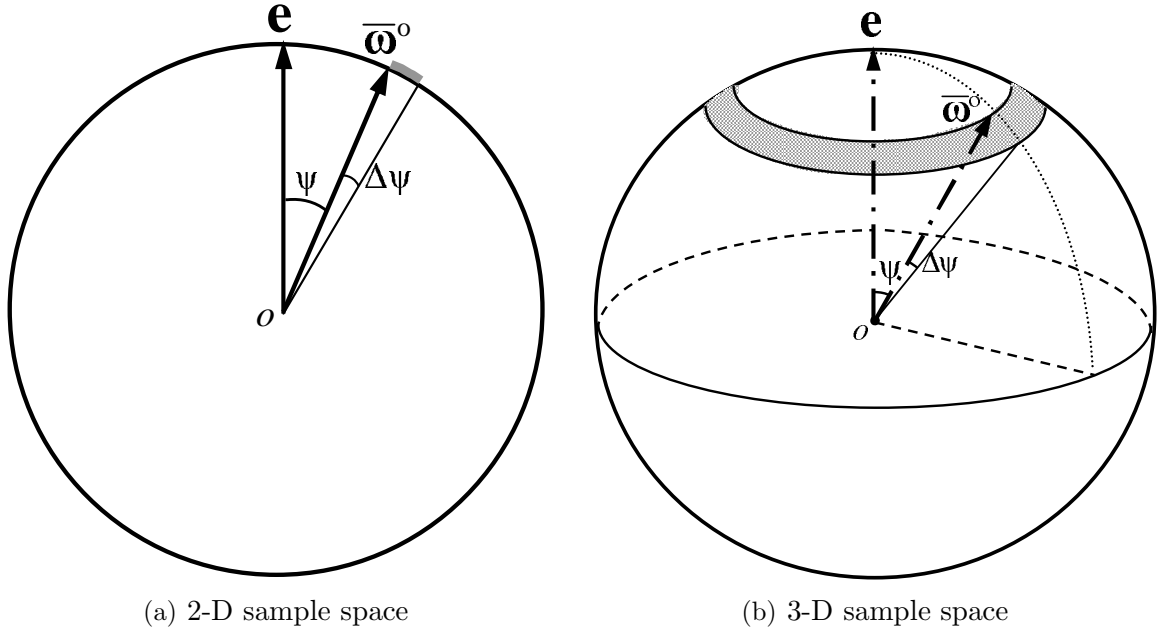


FIGURE 6.5: Illustration of the random relative orientation between two unit vectors \mathbf{e} and $\bar{\omega}^o$ in the 2-D and 3-D sample spaces.

Only one degree of freedom is needed for describing the relative orientation between two vectors. Figures 6.5a and b illustrate the relative orientation between two random unit vectors (i.e., \mathbf{e} and $\bar{\omega}^o$ for $|\mathbf{e}| = |\bar{\omega}^o| = 1$) in the 2-D and 3-D Cartesian spaces, respectively. Assume that \mathbf{e} is fixed in direction and the alignment angle between the two vectors is random, then the end of vector $\bar{\omega}^o$ is uniformly distributed along the periphery of the unit circle for the 2-D sample space case and uniformly distributed on the surface of the unit sphere for the 3-D sample space case. Let Ψ represent the random alignment angle and ψ denote the sample space variable corresponding to it. As shown in figure 6.5a, the sample area for the 2-D case is simply $\Delta S_{2D} = \Delta\psi$. In contrast, the sample area for the 3-D case shown in figure 6.5b is

$$\Delta S_{3D} = 2\pi \sin \psi \Delta\psi = -2\pi \Delta \cos \psi. \quad (6.1)$$

Obviously, the mapping relationship between these two sample areas (i.e., ΔS_{2D} and ΔS_{3D}) for the 2-D and 3-D cases is nonlinear. Therefore, the PDFs of the alignment angle based on the 2-D and 3-D sample spaces are, in general, different. Since $\Delta S_{3D} \propto \Delta \cos \psi$, it is understood that the PDF based on the cosine of the angle is associated with the 3-D sample space case; in contrast, that based on the angle itself corresponds to the 2-D sample space case. Because a turbulent flow field is inherently 3-D and so are the flow vectors, statistics based on a 2-D sample space is, in general, biased due to the so-called “weighting effect” by Blackburn *et al.* [53].

Figure 6.6 shows the distribution of $P_\Psi(\psi)$ calculated within the logarithmic layer using the 2-D and 3-D sampling areas discussed above. Consistent with the DNS results of Blackburn *et al.* [53], the value of P_Ψ obtained using the 2-D sampling area shown in Figure 6.6a drops drastically near $\psi = 0^\circ$ and the mode of Ψ as indicated by P_Ψ occurs at 15° – 21° . However, as analyzed above, the results obtained from Figure 6.6a are biased. In contrast, as shown in Figure 6.6b, the PDF of ψ evaluated using the 3-D sampling area for the same logarithmic layer demonstrates a strong tendency for $\bar{\omega}$ to be aligned with $\mathbf{e}_{S\beta}$ (i.e., the most probable state is $\Psi = 0^\circ$). This is a canonical pattern consistent with the observation of many other researchers based on DNS [44, 48, 50, 55, 153] and experimental studies [45, 54, 57]. In view of this, in the remainder of the chapter, the PDF of the random alignment

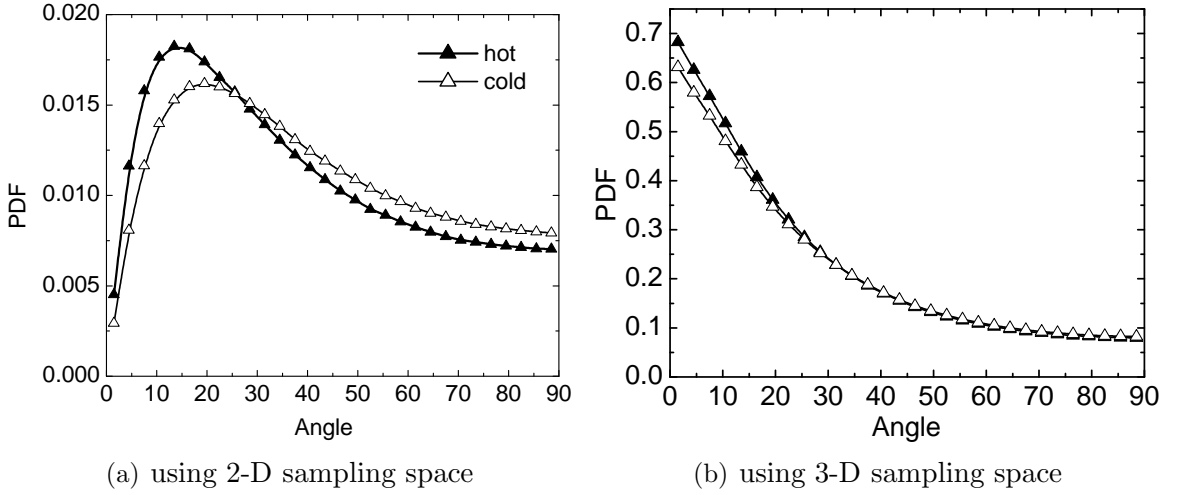


FIGURE 6.6: PDF $P_\Psi(\psi)$ of the alignment angle between $\bar{\omega}$ and $\mathbf{e}_{S\beta}$ in logarithmic layer ($x_2^+ = 80$) predicted using the DNM&DTDM-HF.

angle between two vectors is evaluated using Eq. (6.1) based on the 3-D sample space. Also, it should be indicated that because an eigenvector itself does not contain any information regarding its direction, the relative alignment angle between a vector and an eigenvector is restricted to $[0^\circ, 90^\circ]$ following the usual convention [54]; however, for the relative alignment angle between two vectors with definite directions, the angular interval is extended to $[0^\circ, 180^\circ]$.

Figures 6.7-6.9 show the alignment patterns between the resolved vorticity vector $\bar{\omega}$ and the eigenvectors, i.e. $\mathbf{e}_{S\alpha}$, $\mathbf{e}_{S\beta}$ and $\mathbf{e}_{S\gamma}$, of the resolved strain rate tensor \bar{S}_{ij} at three wall-normal locations, respectively. From Figure 6.7, it is observed that $\bar{\omega}$ is preferentially perpendicular to the most extensive eigenvector $\mathbf{e}_{S\alpha}$ in all three layers in both the hot and cold wall regions. Figures 6.8 and 6.9 show that $\bar{\omega}$ is preferentially aligned with the intermediate eigenvector $\mathbf{e}_{S\beta}$ while being perpendicular to the most contracting eigenvector $\mathbf{e}_{S\gamma}$. As reviewed earlier, these preferential alignment patterns (i.e., $\bar{\omega}$ being parallel to $\mathbf{e}_{S\beta}$ and perpendicular to $\mathbf{e}_{S\alpha}$ and $\mathbf{e}_{S\gamma}$) reproduced by the current LES are classical results previously observed by many researchers based on a variety of analytical, experimental and numerical (both DNS and LES) approaches. A general observation from figures 6.7-6.9 is that the presence of the wall has a significant anisotropic impact on these preferential alignment patterns, which become more and more strongly expressed as the wall is approached (as the

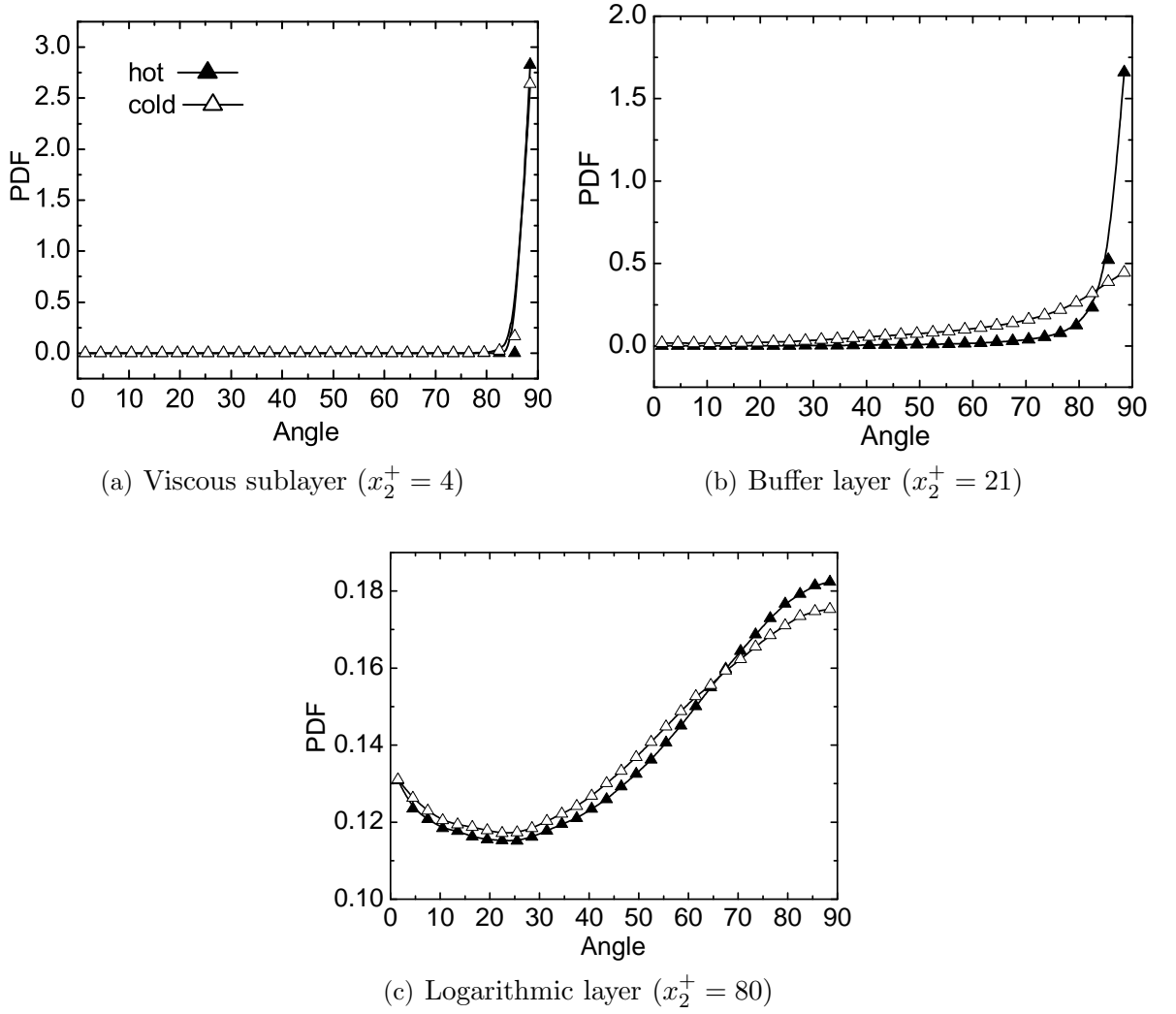


FIGURE 6.7: PDF of the alignment angle between $\bar{\omega}$ and $\mathbf{e}_{S\alpha}$ predicted using the DNM&DTDM-HF.

value of x_2^+ decreases). As the wall is approached, the PDFs of these alignment angles necessarily converge to Dirac delta functions [156]

$$P_{\Psi}(\psi)|_{\text{wall}} = \delta_{1D}(\psi), \quad (6.2)$$

for the alignment angle between $\bar{\omega}$ and $\mathbf{e}_{S\beta}$, and

$$P_{\Psi}(\psi)|_{\text{wall}} = \delta(\psi - 90^\circ), \quad (6.3)$$

for the alignment angle between $\bar{\omega}$ and $\mathbf{e}_{S\alpha}$, and that between $\bar{\omega}$ and $\mathbf{e}_{S\gamma}$. The strongly preferred alignment patterns and near-wall anisotropic behaviour demon-

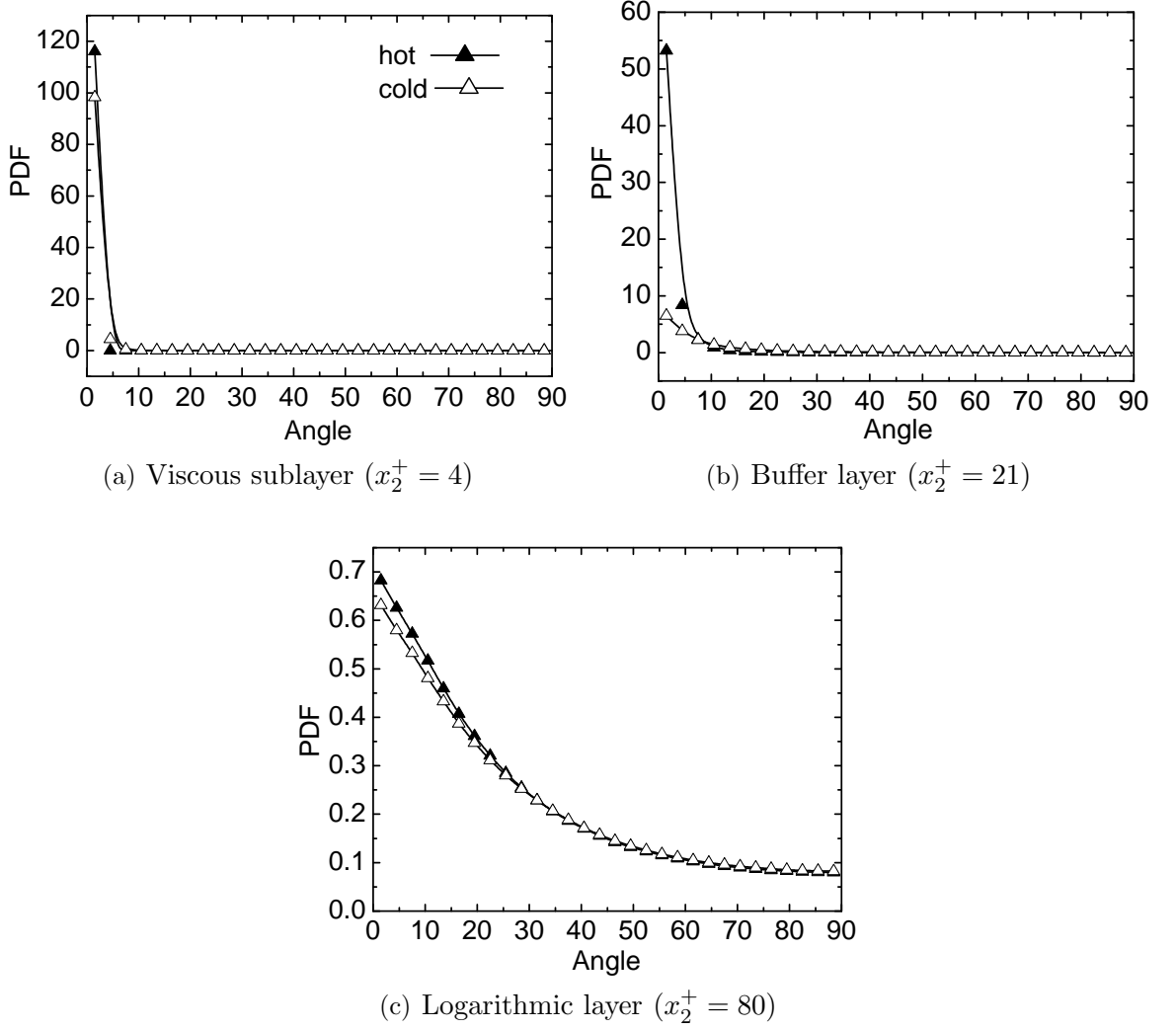


FIGURE 6.8: PDF of the alignment angle between $\bar{\omega}$ and $\mathbf{e}_{S\beta}$ predicted using the DNM&DTDM-HF.

strated in Figures 6.7-6.9 confirm the observations of Shtilman *et al.* [41] and Tsinober *et al.* [125] that the geometrical property of the fluid vectors (e.g., $\bar{\omega}$) and tensors (e.g., \bar{S}_{ij}) of (wall-bounded) turbulent flows are qualitatively different than those of a random Gaussian field, since local preferential geometrical structures do exist in realistic turbulent flows.

This discussion examined the relative orientation of the resolved vorticity vector $\bar{\omega}$ with respect to each individual eigenvector of \bar{S}_{ij} . However, in order to fully describe the attitude (or relative orientation) of $\bar{\omega}$ with respect to the eigenframe $[\mathbf{e}_{S\alpha}, \mathbf{e}_{S\beta}, \mathbf{e}_{S\gamma}]$ of \bar{S}_{ij} , a system of two independent parameters needs to be studied. Following the approach of Wang *et al.* [12], we use two independent random angles; namely, the *co-latitude* Θ , and the *co-longitude* Φ . The values taken on by the ran-

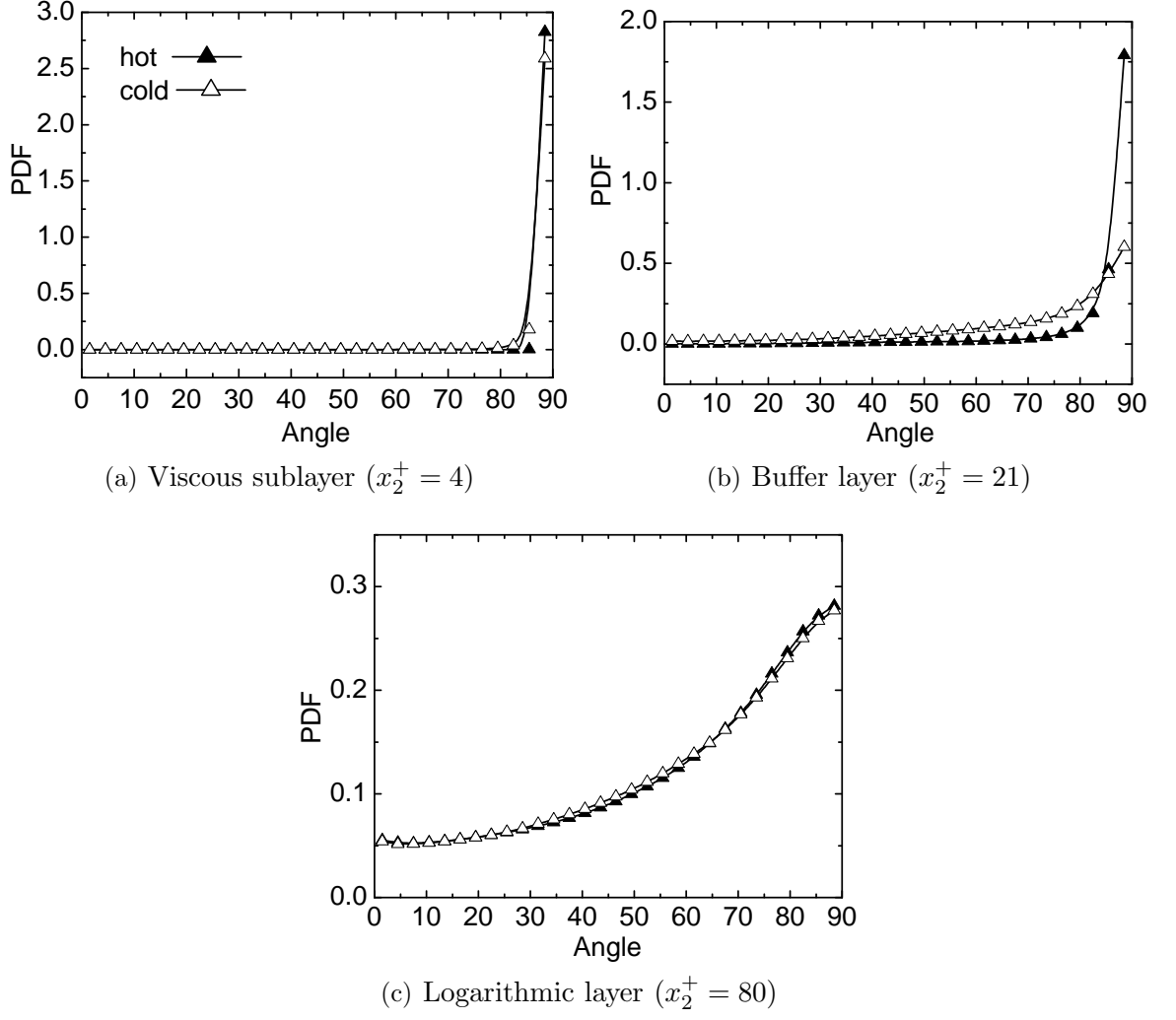


FIGURE 6.9: PDF of the alignment angle between $\bar{\omega}$ and $\mathbf{e}_{S\gamma}$ predicted using the DNM&DTDM-HF.

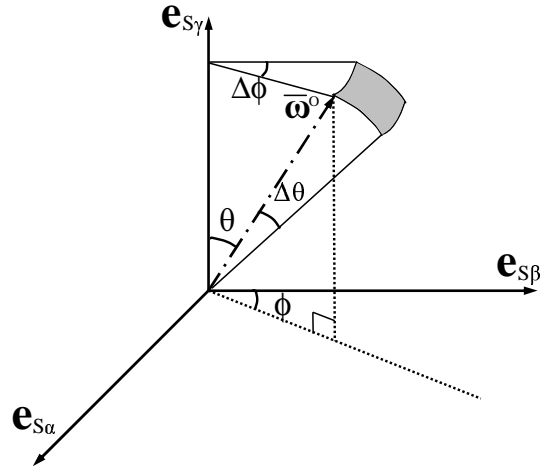


FIGURE 6.10: Geometrical description of the attitude of $\bar{\omega}^o$ with respect to the eigenframe of \bar{S}_{ij} .

dom angles Θ and Φ in the sample space are denoted by θ and ϕ , respectively (see Figure 6.10 for the geometrical description). If the orientation of the random vector $\bar{\omega}$ is uniformly distributed in a 3-D space, then the terminus of the normalized vector $\bar{\omega}^\circ$ is expected to be uniformly distributed on the surface of the unit sphere $|\bar{\omega}^\circ| = 1$, and correspondingly, the JPDF of θ and ϕ is a uniform distribution in terms of the *solid angle*:

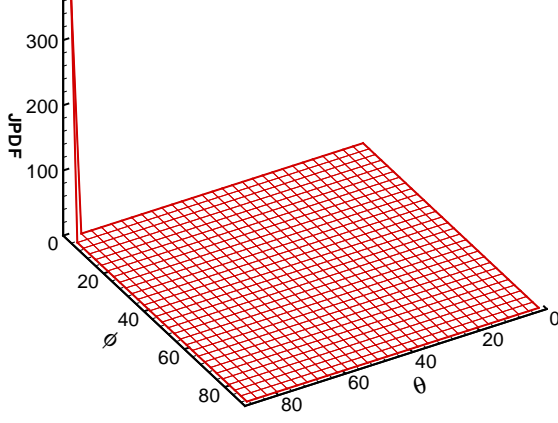
$$\Delta S \stackrel{\text{def}}{=} \iint_{\Delta\Sigma} \sin\theta d\theta d\phi \approx \sin\theta \Delta\theta \Delta\phi = -\Delta(\cos\theta) \Delta\phi, \quad (6.4)$$

where $\Delta\Sigma$ is the bin for statistics on the surface of the unit sphere. In view of this, and in order to obtain unbiased statistical results, the JPDF of θ and ϕ should be evaluated based on the concept of the solid angle; optionally, some researchers [54, 57] compute the JPDF of $\cos\theta$ and ϕ . By comparing Eqs. (6.1) with (6.4), it is understood the sample area represented by Eq. (6.1) can be directly obtained by integrating Eq. (6.4) over the co-longitude ϕ , indicating that Eq. (6.4) represents a more general approach for evaluating the orientation of a random vector in a 3-D Cartesian space.

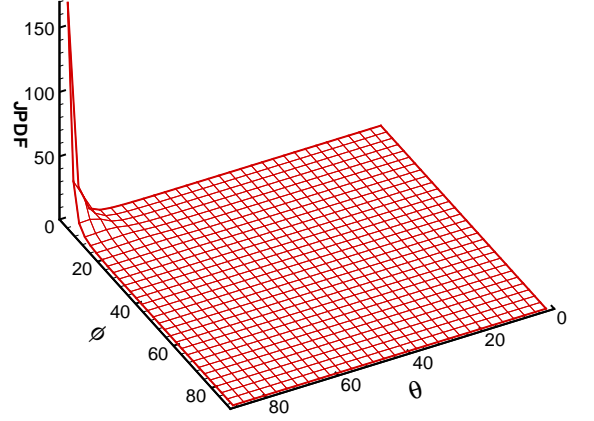
Figures 6.11(a)–(c) show the JPDF of Θ and Φ for describing the attitude of $\bar{\omega}$ with respect to the eigenframe of \bar{S}_{ij} in the hot wall region. Since the JPDF patterns predicted using the two different sets of dynamic SGS models are qualitatively similar to each other except for some differences in the magnitude of the JPDFs, we only present the results predicted using the DNM&DTDM-HF. Figure 6.11 shows that in all three flow regimes, $\bar{\omega}$ is preferentially aligned with the intermediate eigenvector, while simultaneously perpendicular to the most extensive and contracting eigenvectors, implying that the mode is located at $\theta = 90^\circ$ and $\phi = 0^\circ$. This observation is consistent with our previous analysis of the PDF of each individual alignment angle based on figures 6.7–6.9, and also consistent with previous *a priori* LES studies of Tao *et al.* [54] and Higgins *et al.* [57]. From the figure, it is also observed that as the wall is approached, this preferential state ($\Theta = 90^\circ$ and $\Phi = 0^\circ$) indicated by the JPDF becomes increasingly dominant. In effect, the JPDF of Θ and Φ degenerates to a 2-D Dirac delta function at the wall [156]:

$$P_{\Theta,\Phi}(\theta, \phi)|_{\text{wall}} = \delta_{2D}(\theta - 90^\circ, \phi), \quad (6.5)$$

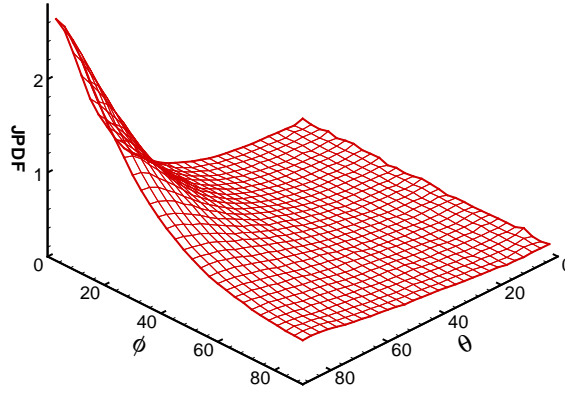
reflecting an intense near-wall anisotropic effect on the geometrical alignment pattern under discussion.



(a) Viscous sublayer ($x_2^+ = 4$)



(b) Buffer layer ($x_2^+ = 21$)



(c) Logarithmic layer ($x_2^+ = 80$)

FIGURE 6.11: JPDPF(θ, ϕ) for describing the attitude of $\bar{\omega}$ with respect to the eigen-frame of \bar{S}_{ij} in the hot wall region predicted using the DNM&DTDM-HF.

6.3.4 Attitude of the Resolved Temperature Gradient Vector with Respect to the Eigenframe of the Resolved Strain Rate Tensor

The geometry of the scalar gradient vector is essential for understanding the turbulent scalar transport and micro-mixing processes. As mentioned in Section 6.1, this subject has been extensively investigated based on a variety of DNS approaches [48, 63, 64, 155, 157, 158] over the past two decades; and recently, the method of LES has also been applied for studying this subject based on *a priori* analysis of experimental measurements of a heated wake flow [19] and thermal stratified atmospheric boundary layer flows [38, 66]. In this Subsection, we focus on examining the geometrical property of the resolved temperature gradient vector with respect to the eigenframe of the resolved strain rate tensor using the LES method, and provide a strict analytical explanation for some observed alignment features characteristic to a near-wall thermal flow. The geometrical relation between the resolved temperature gradient vector and the SGS HF vector will be discussed separately in Subsection 6.3.5.

Figures 6.12-6.14 show the geometrical alignment between the resolved temperature gradient vector $\nabla\bar{T}$ and the eigenvectors of \bar{S}_{ij} predicted using the DM&DEDM-HF and DNM&DTDM-HF. From Figures 6.12a and b, it is observed that $\nabla\bar{T}$ is preferentially aligned with $\mathbf{e}_{S\alpha}$ at $\psi = 45^\circ$ for both the viscous and buffer layers. As the distance from the wall increases, the probability corresponding to this mode decreases. In the logarithmic layer (cf. Figure 6.12c), this preferential alignment pattern can still be observed, however, other modes towards $\psi > 45^\circ$ also become prevalent. The performance of the DM&DEDM-HF and DNM&DTDM-HF shown in Figure 6.12 is similar: the PDF patterns predicted by both sets of SGS models exhibit a similar tendency, except that the magnitude of the predicted PDFs based on different model sets varies especially in the logarithmic layer. Figures 6.13 and 6.14 show the PDFs of the alignment patterns between $\nabla\bar{T}$ and $\mathbf{e}_{S\beta}$, and $\nabla\bar{T}$ and $\mathbf{e}_{S\gamma}$, respectively. These two figures can be analyzed similarly to Figure 6.12. In contrast to Figure 6.12, Figure 6.13 indicates that $\nabla\bar{T}$ is preferentially perpendicular to the intermediate eigenvector $\mathbf{e}_{S\beta}$ for all three flow layers. Figure 6.14 shows that the most probable alignment angle between $\nabla\bar{T}$ and the most contracting eigenvector

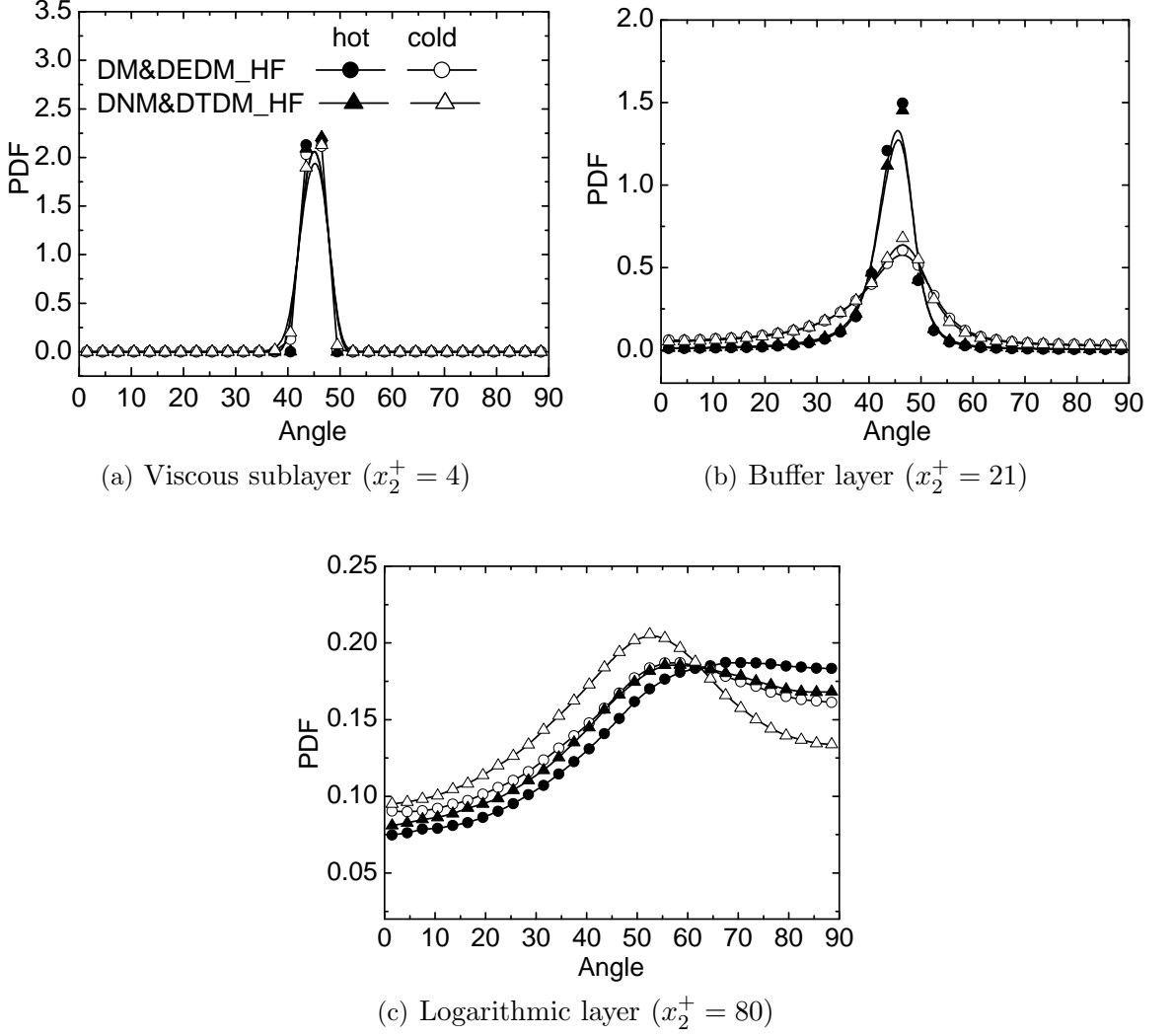


FIGURE 6.12: PDFs of the alignment angle between the resolved temperature gradient $\nabla \bar{T}$ and $\mathbf{e}_{S\alpha}$ predicted using two sets of SGS models: DM&DEDM-HF and DNM&DTDM-HF.

$\mathbf{e}_{S\gamma}$ is, in general, 45° , however, as the distance from the wall increases, other modes towards $\psi < 45^\circ$ become prevalent. A general interesting phenomenon observed from figures 6.12-6.14 is that the probability for $\nabla \bar{T}$ being aligned at $\psi = 90^\circ$ with $\mathbf{e}_{S\beta}$ and $\psi = 45^\circ$ with both $\mathbf{e}_{S\alpha}$ and $\mathbf{e}_{S\gamma}$ becomes increasingly high as the wall is approached. These special alignment patterns are characteristic to near-wall thermal flows, and the PDFs of these special alignment angles must collapse to Dirac delta functions in the vicinity of the wall in response to the wall boundary condition [156].

In order to describe the general attitude of $\nabla \bar{T}$ with respect to the eigenframe of \bar{S}_{ij} , a JPDF of two independent parameters needs to be considered. Following the method introduced in Subsection 6.3.3, we investigate the JPDF of the co-latitude Θ and co-longitude Φ evaluated using the solid angle. Since the JPDF pattern for the

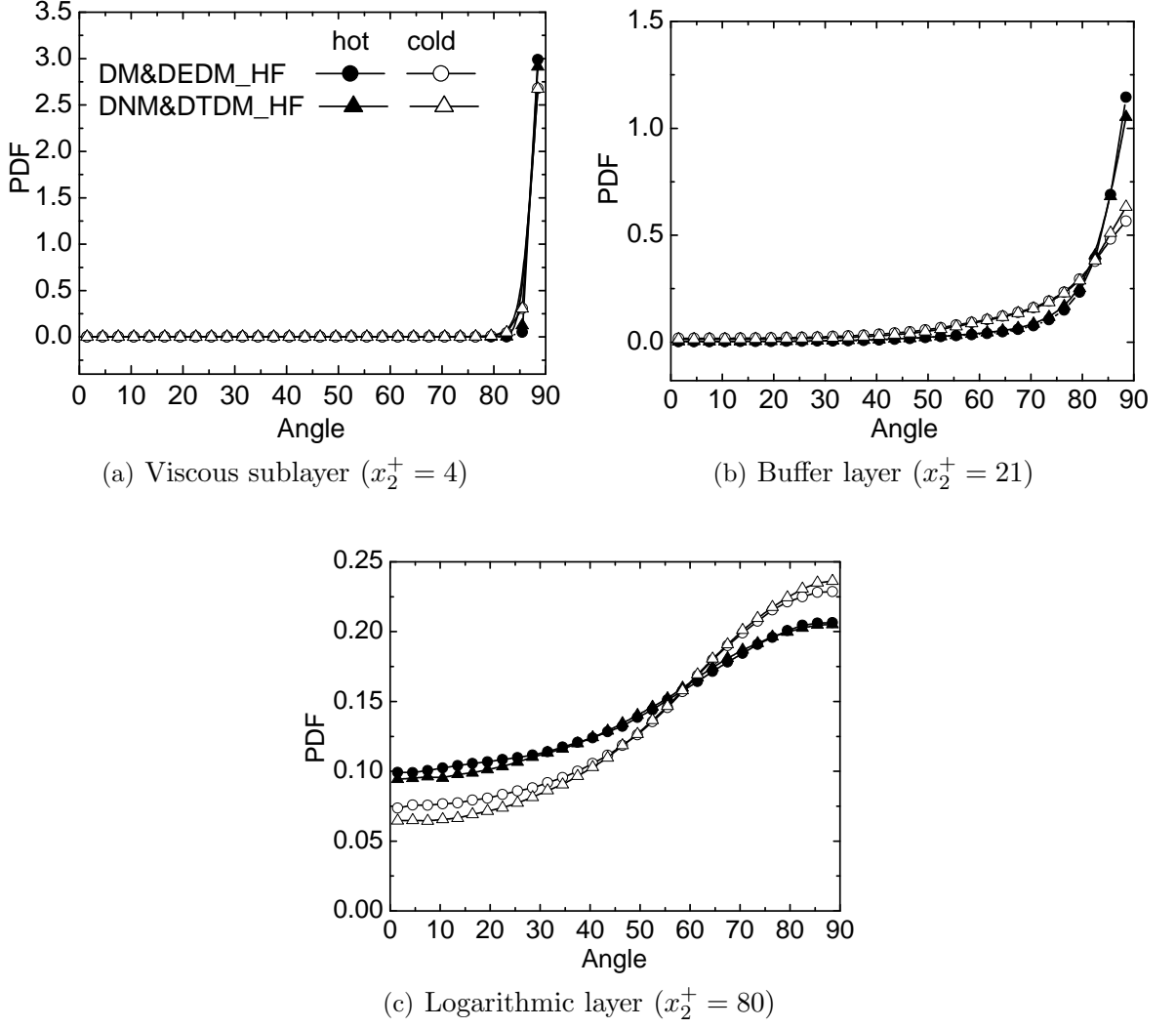


FIGURE 6.13: PDFs of the alignment angle between the resolved temperature gradient $\nabla \bar{T}$ and $\mathbf{e}_{S\beta}$ predicted using two sets of SGS models: DM&DEDM-HF and DNM&DTDM-HF.

cold wall region is similar to that for the hot wall region except for some differences in the magnitude of the JPDF, here we only show in Figure 6.15 the JPDF for three different layers in the hot wall region predicted using the DNM&DTDM-HF. Consistent with the PDFs of the alignment angle between $\nabla \bar{T}$ and each eigenvector of \bar{S}_{ij} as observed previously in figures 6.12-6.14, the most probable state for the attitude of $\nabla \bar{T}$ with respect to the eigenframe of \bar{S}_{ij} is $\theta = 45^\circ$ and $\phi = 90^\circ$ in the viscous sublayer and buffer layer. As the distance from the wall increases, the preference for this mode decreases. From Figure 6.15c, it is observed that modes $\theta < 45^\circ$ and $\phi = 90^\circ$ also become prevalent in the central core of the channel. The above observed near-wall anisotropic effect can be described in a more strict manner using an analytical approach. This JPDF mode necessarily collapses to a 2-D Dirac

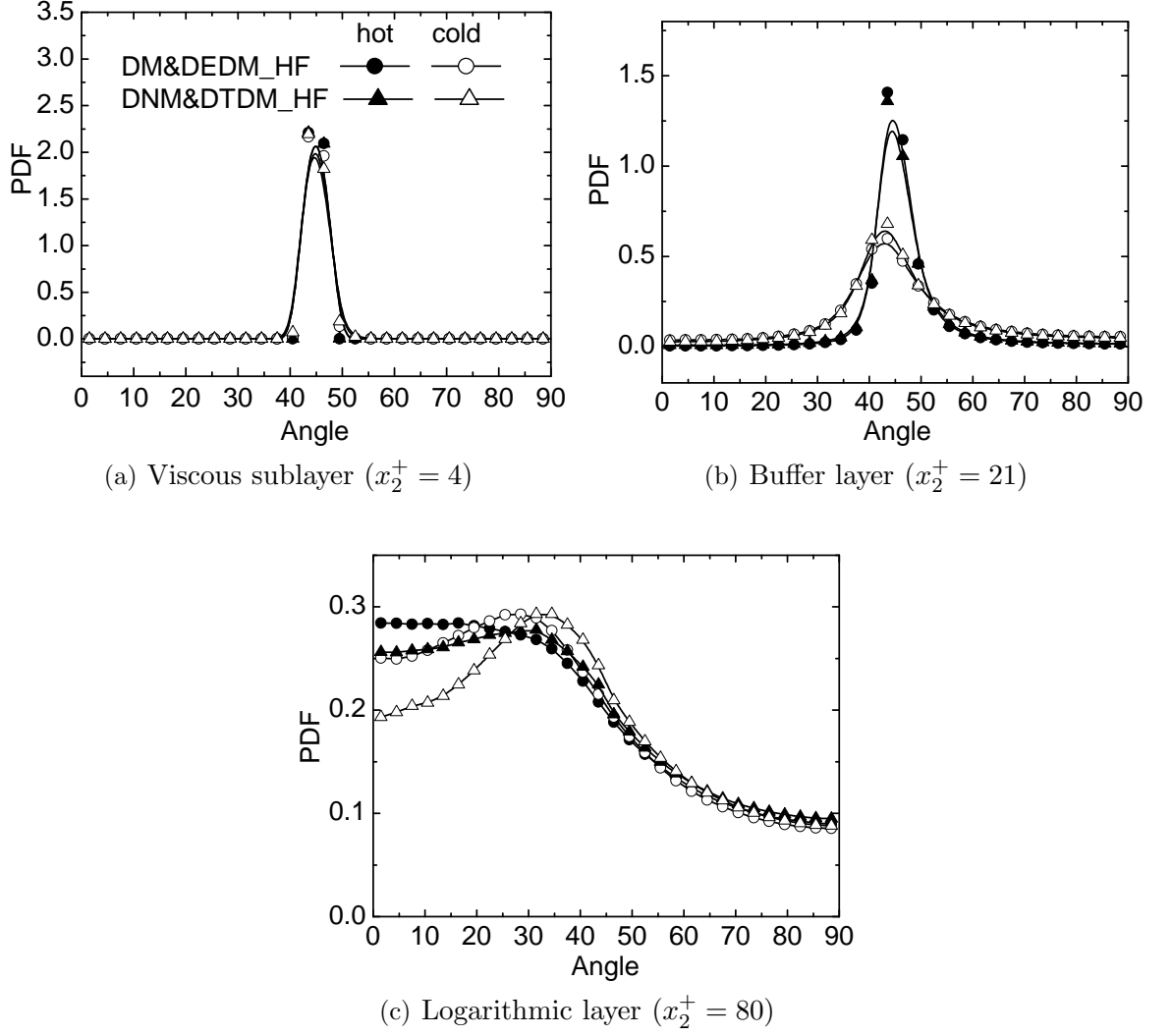


FIGURE 6.14: PDFs of the alignment angle between the resolved temperature gradient $\nabla \bar{T}$ and $\mathbf{e}_{S\gamma}$ predicted using two sets of SGS models: DM&DEDM-HF and DNM&DTDM-HF.

delta function at the wall, i.e. [156]

$$P_{\Theta, \Phi}(\theta, \phi)|_{\text{wall}} = \delta(\theta - 45^\circ, \phi - 90^\circ), \quad (6.6)$$

which explains the sharp JPDF peaks illustrated in Figure 6.15a.

It should be indicated that the JPDF for describing the general attitude of $\nabla \bar{T}$ with respect to the eigenframe of \bar{S}_{ij} shown in Figure 6.15 and the PDF of each individual alignment angle between $\nabla \bar{T}$ and an eigenvector of \bar{S}_{ij} demonstrated in Figures 6.12-6.14, are two closely related but different statistical objects. Both the PDF and JPDF are important for understanding the alignment pattern between $\nabla \bar{T}$ and the eigenvectors of \bar{S}_{ij} , and one cannot replace the other in terms of statistics.

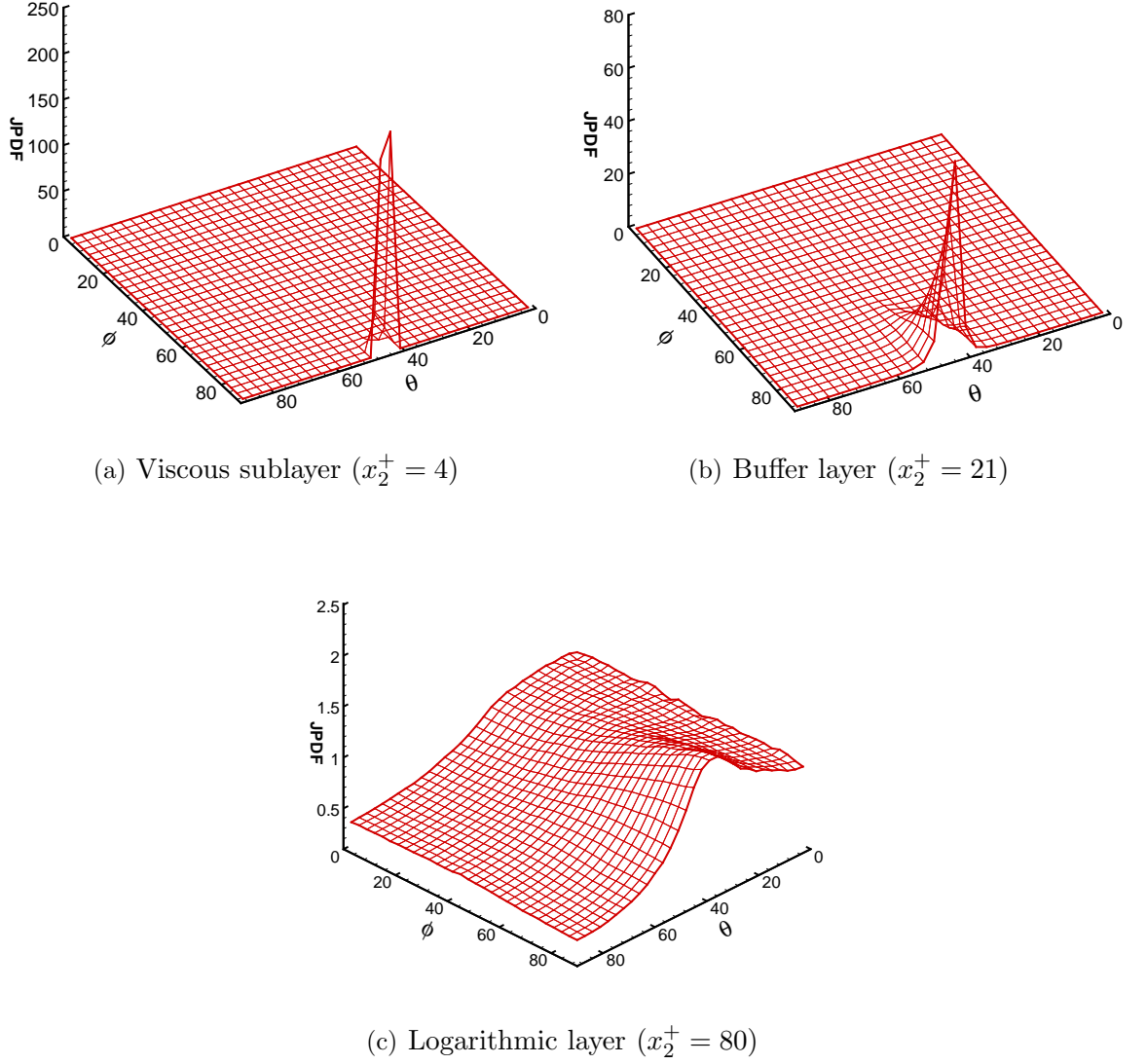


FIGURE 6.15: $\text{JPDF}(\theta, \phi)$ for describing the attitude of $\nabla \bar{T}$ with respect to the eigenframe of \bar{S}_{ij} in the hot wall region predicted using the DNM&DTDM-HF.

Finally, it is observed that the JPDF patterns predicted using the DM&DEDM-HF (not shown) are also similar to those predicted using the DNM&DTDM-HF except for some differences in the predicted magnitude of the JPDF, which is consistent with the previous comparison of the two sets of linear and nonlinear SGS models in terms of their prediction of the PDFs of the alignment angles demonstrated using Figures 6.12-6.14. This is not surprising, because both $\nabla \bar{T}$ and the eigenvectors of the \bar{S}_{ij} are resolved quantities which are directly computed at the resolved-scale in an LES approach. Although some of the predictions of the resolved-scale geometrical alignment patterns are similar for different SGS modelling approaches, we will demonstrate in the next Subsection that the performances of different SGS modelling

approaches can be drastically different at the unresolved subgrid-scales.

6.3.5 Orientation of the SGS Heat Flux Vector \mathbf{h}

The alignment angle Ψ between the modelled SGS HF vector \mathbf{h} and the temperature gradient $\nabla\bar{T}$, defined as:

$$\Psi \stackrel{\text{def}}{=} \cos^{-1}(\mathbf{h}, \nabla\bar{T}) = \cos^{-1}\left(\frac{\mathbf{h} \cdot \nabla\bar{T}}{|\mathbf{h}| \cdot |\nabla\bar{T}|}\right), \quad (6.7)$$

is an important vector invariant for characterizing the constitutive relation of a SGS HF model. For the conventional eddy thermal diffusivity type models (e.g., the DEDM-HF, which requires that \mathbf{h} be aligned with $-\nabla\bar{T}$), this alignment angle can only take one of two values: either 0° (when $C_T < 0$) or 180° (when $C_T > 0$). In the case of $\Psi = 180^\circ$, the physical mechanism of SGS heat flux transfer is analogous to the process of molecular heat conduction governed by Fourier's law. The case of $\Psi = 0^\circ$ is allowed only in a dynamic SGS HF modelling procedure, when C_T is allowed to assume negative values. For the DTDM-HF of Peng and Davidson [40], the value of Ψ can vary over a much larger range owing to the introduction of the tensor thermal diffusivity in the constitutive relation. Therefore, qualitatively, the value of Ψ reflects the degree of deviation of the constitutive relation of a SGS HF model from the equivalent of Fourier's law. Since the physics of turbulent heat transfer at the subgrid-scale is fundamentally different than the mechanism of molecular diffusion/conduction, the value of Ψ is expected to deviate from either 0° or 180° in a realistic turbulent flow.

Figure 6.16a shows the PDF of the Ψ predicted using the DEDM-HF (in conjunction with the DM for modelling the SGS stress tensor). As expected, for all three flow layers (viscous sublayer, buffer layer and logarithmic layer) in both the hot and cold wall regions, a dominant bi-modal distribution is observed indicating the value of Ψ is either 0° or 180° . Figure 6.16b shows the PDF of Φ predicted using the DTDM-HF (in conjunction with the DNM for modelling the SGS stress tensor) for three different flow layers. From figure 6.16b, it is interesting to observe that as the wall is approached (or, as the value of x_2^+ decreases), \mathbf{h} is preferentially aligned in a direction that is orthogonal to $\nabla\bar{T}$ in both the hot and cold wall regions. As

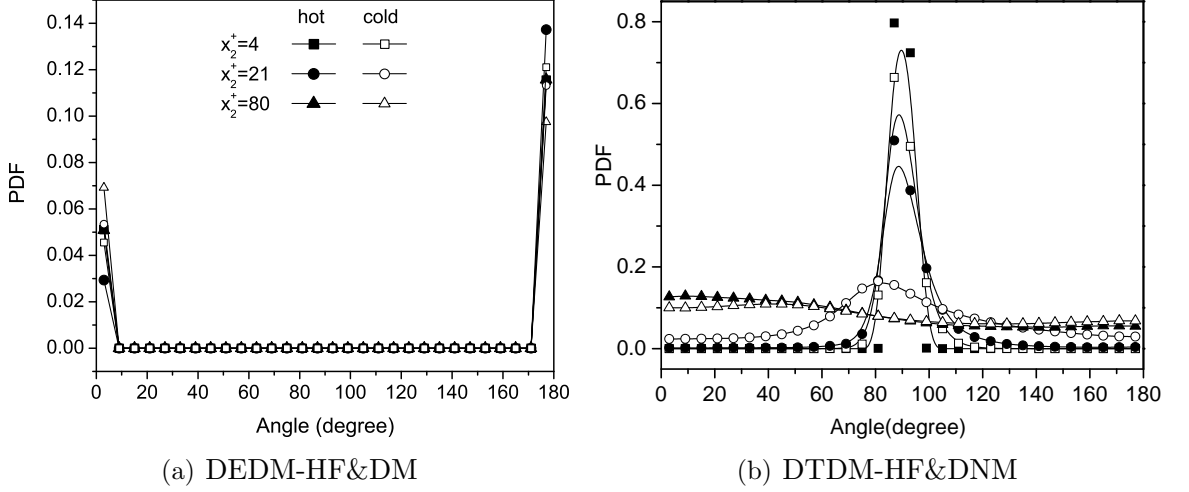
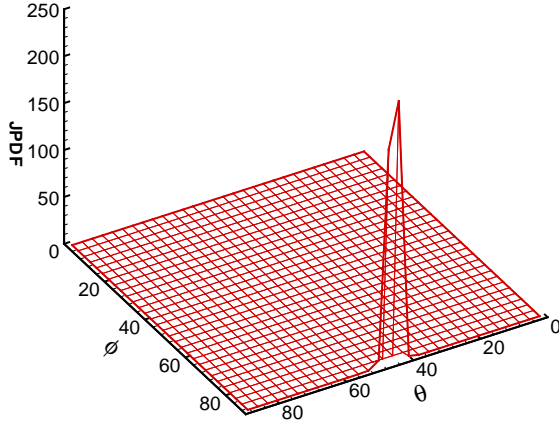


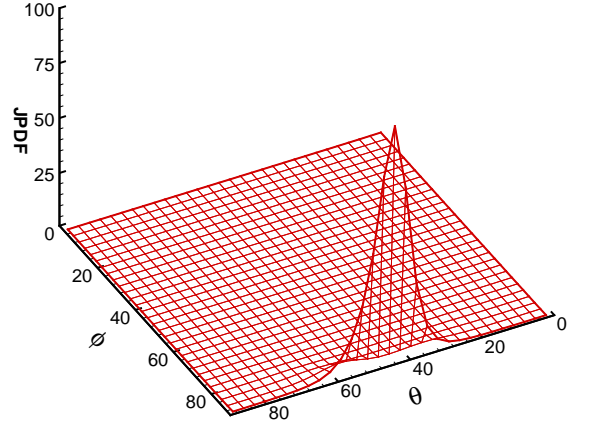
FIGURE 6.16: PDFs of the alignment angle between the SGS heat flux \mathbf{h} and the resolved temperature gradient $\nabla \bar{T}$.

discussed earlier, this special orthogonal alignment pattern cannot be predicted by the DEDM-HF (since this alignment pattern is different from either 0° or 180°). The new question is whether this special geometrical alignment feature is consistent with the physics. In effect, this question is well answered by an analysis of the near-wall effects on the magnitude and direction of \mathbf{h} and $\nabla \bar{T}$ [156]. As the wall is approached, the relative orientation between \mathbf{h} and $\nabla \bar{T}$ converges to an exact and unique orthogonal pattern, and correspondingly, the PDF of the angle degenerates to a Dirac delta function: $P_\Psi(\psi)|_{\text{wall}} = \delta_{1D}(\psi - \pi/2)$. As such, we have demonstrated that in contrast to the unsatisfactory performance of the DEDM-HF, the DTDM-HF can successfully predict the near-wall geometrical property of the SGS HF vector \mathbf{h} in terms of its relative orientation with respect to the resolved temperature gradient $\nabla \bar{T}$.

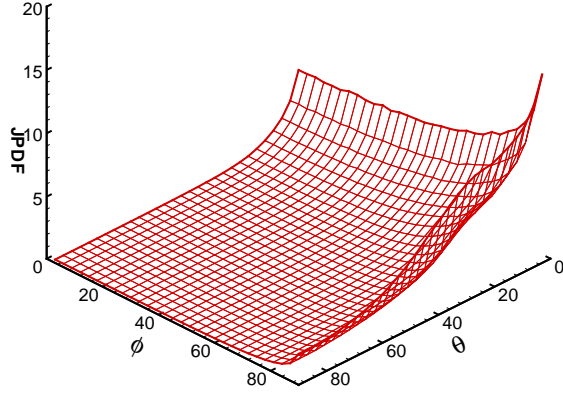
Figure 6.17 shows the JPDF for describing the attitude of the SGS heat flux vector \mathbf{h} with respect to the eigenframe of \bar{S}_{ij} in the hot wall region predicted using the DNM&DTDM-HF. Figures 6.17a and b indicate that \mathbf{h} tends to be aligned at an angle of 45° with $\mathbf{e}_{S\gamma}$ and simultaneously perpendicular to $\mathbf{e}_{S\beta}$ (i.e., $\theta = 45^\circ$ and $\phi = 90^\circ$) in the viscous sublayer and buffer layer. In the logarithmic layer, \mathbf{h} is also most likely perpendicular to $\mathbf{e}_{S\beta}$ but aligned with $\mathbf{e}_{S\gamma}$, i.e. $\theta = 0^\circ$, $\phi = 90^\circ$. A common feature from Figures 6.17a–c is that \mathbf{h} tends to lie in the $\mathbf{e}_{S\alpha}$ – $\mathbf{e}_{S\gamma}$ plane (being perpendicular to $\mathbf{e}_{S\beta}$) in all three flow regimes, with a preferential alignment angle



(a) Viscous sublayer ($x_2^+ = 4$)



(b) Buffer layer ($x_2^+ = 21$)



(c) Logarithmic layer ($x_2^+ = 80$)

FIGURE 6.17: $\text{JPDF}(\theta, \phi)$ for describing the attitude of \mathbf{h} with respect to the eigen-frame of \bar{S}_{ij} in the hot wall region predicted using the DNM&DTDM-HF.

between \mathbf{h} and $\mathbf{e}_{S\gamma}$ decreasing from 45° to 0° as the distance from the wall increases. The above numerical results based on LES are consistent with the near-wall physics of the flow, since it can be shown analytically that as the wall is approached, \mathbf{h} must be strictly aligned at 45° with $\mathbf{e}_{S\alpha}$ and $\mathbf{e}_{S\gamma}$, and 90° with $\mathbf{e}_{S\beta}$, resulting in a unique wall-limiting attitude corresponding to $\Theta|_{\text{wall}} = 45^\circ$ and $\Phi|_{\text{wall}} = 90^\circ$ [156].

6.4 Summary

In this research, we investigated the geometrical property of a thermal fluid flow field in the context of LES. The present research together with some recently reported LES studies [19, 54, 55, 57, 66] confirms that LES is an effective tool for investigating the geometrical property of a turbulent field at the resolved scales.

The presence of the wall has a significant anisotropic impact on many geometrical parameters. In the core region of the channel, the resolved vorticity $\bar{\omega}$ tends to align with the vortex stretching vector $\bar{\mathbf{w}}$, suggesting a dominant local vortex stretching flow configuration. However, in the viscous sublayer, both local vortex stretching and compression patterns are preferred. The local fluid element deformation configuration can be vividly demonstrated using the ratio of the eigenvalues of the resolved strain rate tensor \bar{S}_{ij} . The statistics based on the S^* parameter suggest that axisymmetric expansion ($\alpha_S : \beta_S : \gamma_S = 1 : 1 : -2$) is the most probable flow configuration in the core region of the channel. In contrast, in the viscous sublayer, the most likely local flow configuration in both the hot and cold wall regions is close to the PTD pattern ($\alpha_S : \beta_S : \gamma_S = 1 : 0 : -1$).

In the core region of the channel, the resolved vorticity vector $\bar{\omega}$ tends to align in the streamwise direction resulting in a large helicity value; however, as the wall is approached, $\bar{\omega}$ is preferentially aligned in the spanwise direction resulting in a negligible level of helicity. It is observed that the level of helical activities is higher in the cold wall region than in the hot wall region. This is due to the fact that helicity tends to reduce nonlinear interactions and inhibits the cascade of TKE to smaller scales for dissipation, and therefore, local helical structures are more active at the center of the channel especially on the cold wall side where large-scale turbulent motions are relatively more prevalent.

The present simulations based on different SGS models have all successfully reproduced the well-known conclusion that $\bar{\omega}$ is predominantly parallel to $\mathbf{e}_{S\beta}$ and perpendicular to $\mathbf{e}_{S\alpha}$ and $\mathbf{e}_{S\gamma}$, respectively. This particular alignment pattern between $\bar{\omega}$ and $\mathbf{e}_{S\beta}$ is found to be more characteristic of the viscous sublayer than the logarithmic region, which is consistent with the reported experimental [45] and the DNS [53]

studies. Furthermore, the present results demonstrated that the JPDF of Θ and Φ for describing the attitude of $\bar{\omega}$ with respect to the eigenframe of \bar{S}_{ij} degenerates to a 2-D Dirac delta function in the vicinity of the wall, i.e. $P_{\Theta,\Phi}(\theta, \phi)|_{\text{wall}} = \delta(\theta - 90^\circ, \phi)$. As the wall is approached, the attitude of the resolved temperature gradient $\nabla \bar{T}$ with respect to the eigenframe of \bar{S}_{ij} converges to a fixed pattern which also corresponds to a 2-D Dirac delta function at the wall, i.e. $P_{\Theta,\Phi}(\theta, \phi)|_{\text{wall}} = \delta(\theta - 45^\circ, \phi - 90^\circ)$.

Two sets of dynamic SGS models were tested in the simulations, i.e. the DM&DEDM-HF and the DNM&DTDM-HF. It is observed that the performances of these two sets of SGS models are in general comparable to each other at the resolved scale. This is because in an LES approach, large dominant turbulent motions are directly computed and the contribution from the SGS motions is usually limited. However, the performances of these two sets of SGS models can be markedly different at the unresolved subgrid-scale. The prediction from the DTDM-HF is able to demonstrate a non-alignment pattern between \mathbf{h} and $\nabla \bar{T}$ and successfully predict the near-wall physics that \mathbf{h} must be aligned towards 90° with $\mathbf{e}_{S\beta}$, and 45° with $\mathbf{e}_{S\alpha}$ and $\mathbf{e}_{S\gamma}$ in the vicinity of the wall. In contrast, the conventional DEDM-HF fails to reflect the geometrical property of \mathbf{h} and strictly requires that the alignment angle between \mathbf{h} and $\nabla \bar{T}$ be either 0° or 180° .

Chapter 7

Conclusions and Future Work

7.1 Summary of the Dissertation

Many engineering and industrial flows are characterized by the effects of buoyancy. Given that turbulent buoyant flows are inherently unsteady and feature important large-scale motions, time-dependent LES provides a good tool in both theoretical research and industrial applications on thermal flows. The objectives of this dissertation focus on the application of LES to buoyancy affected flows, especially, the effect of the SGS modelling in LES, and geometrical properties of the turbulent buoyant flows based on the resolved scales of motion obtained by LES. In this dissertation, an LES code using a collocated non-uniform mesh for wall-bounded turbulent flows is further developed and tested exhaustively before its application. To save computational resources, a multigrid method using a control strategy scheme is implemented in the 3-D LES code to accelerate the solution convergence of the pressure field. The kinetic energy conservation related to the numerical schemes used for the code is examined. The accuracy and robustness of the present code are investigated carefully using several benchmark flows, e.g. lid-driven cavity flow and low Reynolds number channel flow. In this dissertation, LES of channel flow at $Re_\tau = 395$ is performed to examine the performance of SGS stress models. The nonlinear DNM for SGS stress is investigated especially with respect to the turbulence kinetic energy dissipation issue. The geometrical properties of the resolved velocity field of wall-bounded turbulence are also studied using the LES prediction. Next, a combined forced and natural convection (or mixed convection) in a vertical channel with differentially heated side walls

is studied. The geometrical properties of the resolved thermal flow field are examined at the end of the dissertation. In this chapter, a general review of the contributions of this dissertation will be presented and possible future studies will be discussed.

7.2 Contributions of the Dissertation

1) A 3-D LES Code Developed for Wall-bounded Thermal Turbulence

To study wall-bounded thermal turbulence, a 3-D LES code based on a non-uniform collocated grid system has been developed and tested in chapter 3. The code is based on the fractional time-step technique [67, 88], in which the discretized Navier-Stokes equations (2.6) are solved in two separate steps: first, the velocity field is estimated without solving the pressure field, and then the pressure field is solved to satisfy the continuity equations and the estimated velocity field is corrected using the pressure field at new time level. To accelerate the convergence rate of the pressure Poisson equation, a MG-CS solver is employed in the present LES code. The approach and numerical implementation of MG-CS are presented in section 3.2. Compared to Gauss-Seidel (GS) type solvers, multigrid methods can greatly accelerate the convergence rate [91, 92]. Other than the strategies with fixed sequence and iteration number, a control strategy (CS) suggested by Brandt [95] and Hutchinson [93] employs a flexible procedure which is automatically adjusted to the convergence rate on each grid level, and thus saves CPU time. A lid-driven cavity flow at $Re = 400$ is chosen to test the performance of the MG-CS. Compared with that of the MG-V, the convergence rate of the MG-CS is much faster. To reduce the residuals of the pressure field by four orders of magnitude, the finest grid takes 33 iterations for the MG-CS, while for the MG-V, the finest grid takes 120 iterations. The computational cost of the MG-CS is only about one third that of the MG-V.

The discretized transport equations should recover the inherent conservation nature of the governing equations. However, since the mass and momentum equations alone are sufficient to obtain a solution and a kinetic energy equation is not solved separately, most discretization schemes only conserve the mass and momentum equations, but not the kinetic energy equation. Although a collocated grid system has

been applied to LES for many flows, it does not conserve the kinetic energy inherently [96]. Since the present code employs a collocated grid system, the conservation property of the collocated grid system and its effect on LES are investigated in this dissertation following the previous works of Morinishi *et al.* [96], Vasilyev [97] and Ham *et al.* [98]. To test the conservation properties, a uniform staggered code is also developed. Both the staggered and collocated grid system used a 2^{nd} CDS. The development of a periodic inviscid flow field is simulated on both grid systems. The error for the average kinetic energy on the staggered grid is second order with respect to time, since the second-order Adams-Bashforth time stepping scheme introduces only a slight dissipative error. However, the error on the collocated grid is first order with respect to time, which indicates that the collocated system introduces additional errors other than time stepping error. The staggered and collocated grid systems are also tested using a viscous flow, i.e. a laminar LDC at $Re_D = 400$. Although the collocated grid system introduces conservation errors, it yields a satisfactory prediction of the laminar flow, which is almost the same as that obtained on a staggered grid. This observation indicates that the kinetic energy conservation issue may not be very important for a steady flow, in which the time accurate advancement is not important. The ability of non-conservative collocated and conservative staggered codes to accurately advance an unsteady flow through time is also investigated using a start-up flow. Again, both the staggered and collocated grid systems give satisfactory results. It appears that the numerical dissipation (conservation error) of the collocated grid system is not significant for the specific test problems considered.

2) LES of Channel Flow and Investigation of the Dynamic Nonlinear SGS Stress Model using Turbulence Geometrical Statistics

(i) LES Prediction of Channel Flow using DNM and DM

In Chapter 4, the nonlinear DNM for the SGS stress tensor is investigated and compared to the DM in LES of a channel flow at $Re_\tau = 395$. The study of the mean and fluctuation properties of the flow indicates that the LES results agree fairly well with the DNS data. Both the DM and DNM models give satisfactory predictions with respect to the resolved velocity field. The SGS dissipation is specifically investigated

in this chapter. It is found that although a localized form of the DM can predict backscatter of TKE, a geometrical statistical study of the SGS dissipation indicates that not only the level but also the local distribution of backscatter predicted by the DM is incorrect. It is not surprising since the level of the backscatter is decided by the bounding scheme adopted rather than the local state of the flow. Compared to the DM, the nonlinear DNM is free from artificial ‘tuning’ of its coefficients and allows for a relatively large level of backscatter due to its constitutive relation.

(ii) PDF of the Non-dimensional State Parameters of the Resolved Strain Rate and SGS Stress Tensor

The local structures of the resolved strain rate and SGS stress tensor predicted by both DM and DNM are studied using turbulence geometrical statistics. The PDFs of the state parameters S^* and S_τ^* in the channel center predicted by both models indicate that, in this region, the most probable strain state tends to be axisymmetric extension ($S^* = 1$), while the most probable stress state is axisymmetric compression ($S_\tau^* = -1$). Towards the wall, both models show that the mode of the PDF of S^* shifts to $S^* = 0$, corresponding to an eigenvalue ratio of $\alpha_S : \beta_S : \gamma_S = 1 : 0 : 1$, which reflects the intrinsic QTD nature of the near-wall turbulence. In contrast to the PDF of S^* , the PDF of S_τ^* predicted by these two models are evidently different, e.g. the PDF of S_τ^* predicted by the DNM indicates that S_τ^* is independent with S^* and still peaks at $S_\tau^* = -1$ towards wall. However, S_τ^* predicted by the DM is coupled with S^* as $S^* = -S_\tau^*$ towards the wall due to the model’s constitutive relationship.

(ii) Relationship between the State Parameters S^* and S_τ^* and SGS Dissipation Rate

At the channel center, the mode of the JPDF of S^* and SGS dissipation (Π/Π_{mean}) predicted by the localized DM is located in the negative dissipation region, which implies that the DM tends to overpredict the backscatter. Although the local averaging scheme was able to constrain the overall level of backscatter to be positive, it cannot reduce the number of the excessive backscatter events. In contrast, the mode of the JPDF of S^* and Π/Π_{mean} in the channel center predicted by the DNM is located in the positive dissipation region. However, for the region $S^* < 0$, the peak

values of the JPDF will fall in the negative SGS dissipation region, which implies that for $S^* < 0$, the DNM probably overpredicts backscatter. Towards the wall, the mode of the JPDF of S^* and Π/Π_{mean} using the DNM moves from the axisymmetric extension region ($S^* = 1$) to the QTD flow region ($S^* = 0$). The JPDF profile of S_τ^* and Π/Π_{mean} using the DNM always peaks at $S_\tau^* = -1$ (axisymmetric compression) rather than $S_\tau^* = 1$ (axisymmetric extension) throughout the entire flow region.

3) LES of Mixed Convection in a Vertical Channel Using Different SGS Models

In Chapter 5, LES of mixed convection between two vertical plates at different temperatures has been performed and the LES results are compared to related DNS results. The mean flow features, e.g. resolved temperature and velocity fields predicted by LES are consistent with the DNS results. It is observed from the LES results that the buoyancy force has a significant impact on both the resolved and SGS quantities. Due to the buoyancy effects, the velocity and temperature fields are skewed across the channel. For instance, the wall-normal distribution of the mean resolved temperature and velocity, resolved turbulent and SGS shear stresses and heat fluxes, root-mean-square value of the fluctuation in the filtered velocity and temperature fields, and effective diffusivity for the resolved turbulent heat flux, are asymmetrical across the channel.

Two sets of dynamic SGS models, the DM&DEDM-HF and DNM&DTDM-HF, were used in the simulation. The performances of these two sets of SGS models are different in terms of the SGS motions. In particular, their predictions for the SGS shear stress and SGS heat fluxes are different. At the resolved scale, the difference between these two sets of SGS models is more evident with respect to the temperature field, especially in the cold wall region where the turbulent effect is the strongest due to the existence of buoyancy. In general, the performance of the nonlinear models is closer to the DNS data than that of the linear models.

4) Geometrical Properties of the Resolved Thermal Flow Field and SGS Heat Flux Vector

In Chapter 6, the geometrical properties of a mixed convection in a vertical slot were examined using LES. Prototypical geometrical patterns have been reproduced and compared with the reported DNS, experimental and *a priori* LES results. The present research together with some recently reported LES studies [19, 54, 55, 57, 66] confirm that LES is an effective tool for investigating the geometrical properties of a turbulent field at the resolved-scales.

(i) Structural Configurations of Local Fluid Element Deformation

The PDF of S^* suggests that axisymmetric expansion ($\alpha_S : \beta_S : \gamma_S = 1 : 1 : -2$) is the most probable flow configuration in the core region of the channel, which is consistent with previous observations [42, 53, 54, 120]. In contrast, in the viscous sublayer, the PDF of S^* indicates that the most likely local flow configuration is PTD pattern ($\alpha_S : \beta_S : \gamma_S = 1 : 0 : -1$). It is observed that the peak value of the PDF of S^* in the cold wall region is smaller than that of the hot wall region, indicating that the flow in the cold wall region more closely resembles 3-D axisymmetrical expansion and deviates from the PTD state. This observation is consistent with the physical notion that the flow is more “turbulent” in the cold wall region than in the hot wall region due to the existence of buoyancy.

In the core region of the channel, the resolved vorticity vector $\bar{\omega}$ tends to align in the streamwise direction resulting in a large helicity value; however, as the wall is approached, $\bar{\omega}$ is preferentially aligned in the spanwise direction resulting in a negligible level of helicity. It is observed that the level of helical activities is higher in the cold wall region than in the hot wall region. This is due to the fact that helicity tends to reduce nonlinear interactions and inhibits the cascade of TKE to smaller scales for dissipation, and therefore, local helical structures are more active at the center of the channel especially on the cold wall side where large-scale turbulent motions are relatively more prevalent.

(ii) Resolved Enstrophy Generation and Helicity

The present study predicts a strong alignment between the resolved vorticity $\bar{\omega}$ and vortex stretching vector $\bar{\mathbf{w}}$ in the core (logarithmic) region of the channel,

which suggests a dominant local vortex stretching flow configuration in that region. This feature is expected and has been reported previously based on DNS and experimental studies [41, 44, 123, 125]. However, near the wall, a bi-modal distribution of $\bar{\sigma}_n$ is observed, indicating both local vortex stretching and compression patterns are preferred.

Near the wall, $\bar{\omega}$ is preferentially aligned in the spanwise direction resulting in a negligible level of helicity. As the distance from the wall increases, helical activities increase significantly in both the hot and cold wall regions. However, it is observed that the level of helical activities is higher in the cold wall region than in the hot wall region, which implies that the helical behavior is more related to large-scale turbulent motions near the cold wall.

(iii) Attitude of the Resolved Vorticity, Temperature Gradient and SGS heat flux Vector with Respect to the Eigenframe of the Resolved Strain Rate Tensor

In all three flow regimes, $\bar{\omega}$ is preferentially aligned with the intermediate eigenvector $\mathbf{e}_{S\beta}$, and simultaneously perpendicular to the most extensive eigenvector $\mathbf{e}_{S\alpha}$ and contracting eigenvectors $\mathbf{e}_{S\gamma}$, implying that the mode is located at $\theta = 90^\circ$ and $\phi = 0^\circ$ with respect to the eigenframe of \bar{S}_{ij} . It is also observed that as the wall is approached, this preferential state ($\theta = 90^\circ$ and $\phi = 0^\circ$) indicated by the JPDF becomes increasingly dominant. The temperature gradient vector $\nabla\bar{T}$ tends to be perpendicular to $\mathbf{e}_{S\beta}$, and simultaneously aligned at 45° with $\mathbf{e}_{S\alpha}$ and $\mathbf{e}_{S\gamma}$ for both the viscous and buffer layer. As the distance from the wall increases, the specific preference decreases. In the logarithmic layer, this preferential alignment pattern, i.e. $\theta = 45^\circ$ and $\phi = 90^\circ$, can still be observed, but is not dominant.

(iv) Orientation of the SGS Heat Flux Vector

Both the DM&DEDM-HF and DNM&DTDM were used in this study. Although the performance of these two sets of SGS models are in general comparable to each other at the resolved scale, in performance is clearly different at the unresolved subgrid-scale. The prediction from the DTDM-HF of Peng and Davidson [40] demon-

strated a non-alignment pattern between the SGS heat flux and resolved temperature gradient vector, and successfully predict the near-wall physics that \mathbf{h} must be aligned at 90° with $\mathbf{e}_{S\beta}$, and 45° with $\mathbf{e}_{S\alpha}$ and $\mathbf{e}_{S\gamma}$ in the vicinity of the wall. In contrast, the conventional DEDM-HF fails to reflect the geometrical property of the SGS HF vector \mathbf{h} , since it strictly requires that the alignment angle between \mathbf{h} and $\nabla\bar{T}$ be either 0° or 180° .

7.3 Future Studies

In this study, the SGS stress and heat flux models are studied in terms of two combinations, i.e. DM&DEDM-HF and DNM&DTDM-HF. It is observed that the nonlinear combination (DNM&DTDM-HF) generally yields better predictions of the buoyant flow, especially with respect to the temperature field. Since the temperature and velocity field are coupled, the specific contribution of either the SGS stress or heat flux model to the thermal field is often unclear. It is reported by Jiménez *et al.* [87] in their study of scalar transfer in a mixing layer that although the DEDM-HF cannot yield proper reverse TKE transfer, it can still result in a good LES prediction of the scalar evolution, provided that a proper SGS stress model is adopted. In other words, the SGS heat flux model does not have a significant impact on the LES predictions in their case. To further study the performance of SGS models for thermal flows, different combinations of SGS models, for instance, DM&DTDM-HF and DNM&DEDM-HF, should be investigated. A mixed dynamic two-parameter model for the SGS heat flux [33] is found to be able to reproduce the proper forward and backward TKE transfer [87], and therefore should be considered in any future study.

Although impressive progress has been made over the past two decades to improve our understanding of the geometrical property of turbulent flows, this subject still presents multiple challenges for future studies. For instance, the geometrical property of the velocity and temperature gradients is still less understood in the core region of the channel than in the near-wall regions; and according to our knowledge, although some interesting local structure-based SGS stress models have already appeared in the literature [60–62], the potential for designing local structure-based SGS

heat flux models is yet to be explored. Turbulence topology is another interesting methodology to study the local structures of turbulence. Based on critical-point theory, the technique provides an unambiguous way to interpret and understand the local flow patterns [151, 159–161]. It is found that the cubic discriminant of the velocity gradient tensor is closely related to the Reynolds stress and turbulence kinetic energy generating events. For instance, Blackburn *et al.* [53] and Chong *et al.* [150] used the discriminant as a marker of coherent motions in the flow. Future study should consider utilizing this methodology to further explore the physics of the thermal fluid flow and evaluate the SGS models.

The present results show that for many flows, LES captures much of the resolved scales. Future study may consider the application of LES to other thermal engineering flow in which the SGS scales also play a significant role, such as room fire and engine combustion. LES application of such reacting flows is a relatively new field and much of the theory of the modelling of reacting processes needs to be developed. In a nonpremixed combustion, chemical reactions occur essentially at the smallest scales and strongly depend on the small-scale mixing process [162], which requires accurate prediction on small-scale structure of the scalar field.

References

- [1] L. Davidson, D. Čuturić, and S.-H. Peng, “DNS in a plane vertical channel with and without buoyancy,” in *Turbulence Heat and Mass Transfer 4* (K. Hanjalić, Y. Nagano, and M. J. Tummers, eds.), (Begell House), pp. 401–408, 2003.
- [2] K. Hanjalić, “One-point closure models for buoyancy-driven turbulent flows,” *Ann. Rev. Fluid Mech.*, vol. 34, pp. 321–347, 2002.
- [3] R. Boudjemadi, V. Maupu, D. Laurence, and P. L. Quéré, “Budgets of turbulent stresses and fluxes in a vertical slot natural convection flow at Rayleigh $Ra = 10^5$ and 5.410^5 ,” *Int. J. Heat Fluid Flow*, vol. 18, pp. 70–79, 1997.
- [4] J. Smagorinsky, “General circulation experiments with the primitive equations, I. the basic experiment,” *Month. Weath. Rev.*, vol. 91, pp. 99–165, 1963.
- [5] D. K. Lilly, “The representation of small-scale turbulence in numerical simulation experiments,” in *Proc. IBM Sci. Comp. Symp. on Environ. Sci.*, p. 195, 1967.
- [6] M. Germano, U. Piomelli, P. Moin, and W. H. Cabot, “A dynamic subgrid-scale eddy viscosity model,” *Phys. Fluids A*, vol. 3, pp. 1760–1765, 1991.
- [7] D. K. Lilly, “A proposed modification of the Germano subgrid-scale closure method,” *Phys. Fluids A*, vol. 4, pp. 633–635, 1992.
- [8] U. Piomelli, “High Reynolds number calculations using the dynamic subgrid-scale stress model,” *Phys. Fluids A*, vol. 5, pp. 1484–1490, 1993.

- [9] B.-C. Wang and D. J. Bergstrom, “A dynamic nonlinear subgrid-scale stress model,” *Phys. Fluids*, vol. 17(035109), 2005.
- [10] C. G. Speziale, “On nonlinear $k-l$ and $k-\epsilon$ models of turbulence,” *J. Fluid Mech.*, vol. 178, pp. 459–475, 1987.
- [11] T. B. Gatski and C. G. Speziale, “On explicit algebraic stress models for complex turbulent flows,” *J. Fluid Mech.*, vol. 254, pp. 59–78, 1993.
- [12] B.-C. Wang, E. Yee, and D. J. Bergstrom, “Geometrical description of the subgrid-scale stress tensor based on euler axis/angle,” *AIAA J.*, vol. 44, pp. 1106–1110, 2006.
- [13] T. S. Lund and E. A. Novikov, “Parameterization of subgrid-scale stress by the velocity gradient tensor,” *Annu. Res. Briefs*, pp. 27–43, 1992. Center for Turbulence Research, Stanford Univ.
- [14] V. C. Wong, “A proposed statistical-dynamic closure method for the linear and nonlinear subgrid-scale stresses,” *Phys. Fluids A*, vol. 4, pp. 1080–1082, 1992.
- [15] B. Kosović, “Subgrid-scale modelling for the large-eddy simulation of high-Reynolds-number boundary layers,” *J. Fluid Mech.*, vol. 336, pp. 151–182, 1997.
- [16] G. S. Winckelmans, A. A. Wray, O. V. Vasilyev, and H. Jeanmart, “Explicit-filtering large-eddy simulation using the tensor-diffusivity model supplemented by a dynamic Smagorinsky term,” *Phys. Fluids*, vol. 13, pp. 1385–1403, 2001.
- [17] N. Liu, X. Lu, and L. Zhuang, “An improved dynamic subgrid-scale model and its application to large eddy simulation of rotating channel flows,” *Sci. China, Ser. G*, vol. 47, pp. 463–476, 2004.
- [18] Z. Warhaft, “Passive scalars in turbulent flows,” *Ann. Rev. Fluid Mech.*, vol. 32, pp. 203–240, 2000.

- [19] H. S. Kang and C. Meneveau, “Passive scalar anisotropy in a heated turbulent wake: new observations and implications for large-eddy simulations,” *J. Fluid Mech.*, vol. 442, pp. 161–170, 2001.
- [20] P. Moin, K. Squires, W. Cabot, and S. Lee, “A dynamic subgrid-scale model for compressible turbulence and scalar transport,” *Phys. Fluids A*, vol. 3, pp. 2746–2757, 1991.
- [21] W.-P. Wang and R. H. Pletcher, “On the large eddy simulation of a turbulent channel flow with significant heat transfer,” *Phys. Fluids*, vol. 8, pp. 3354–3366, 1996.
- [22] A. R. V. R. and P. R. H., “Large eddy simulation of the turbulent flow past a backward-facing step with heat transfer and property variations,” *Int. J. Heat Fluid Flow*, vol. 23, pp. 601–614, 2002.
- [23] L. D. Dailey, N. Wang, and R. H. Pletcher, “Large eddy simulation of constant heat flux turbulent channel flow with property variations: quasi-developed model and mean flow results,” *ASME J. Heat Trans.*, vol. 125, pp. 27–38, 2003.
- [24] L. Wang and X.-Y. Lu, “An investigation of turbulent oscillatory heat transfer in channel flows by large eddy simulation,” *Int. J. Heat. Mass. Trans.*, vol. 47, pp. 2161–2172, 2004.
- [25] O. Labbé, P. Sagaut, and E. Montreuil, “Large-eddy simulation of heat transfer over a backward-facing step,” *Numer. Heat Trans.: Part A*, vol. 42, pp. 73–90, 2002.
- [26] J. Pallares and L. Davidson, “Large-eddy simulations of turbulent heat transfer in stationary and rotating square ducts,” *Phys. Fluids*, vol. 14, pp. 2804–2816, 2002.

- [27] A. Keating, U. Piomelli, K. Bremhorst, and S. Nešić, “Large-eddy simulation of heat transfer downstream of a backward-facing step,” *J. Turb.*, vol. 5, pp. 1–27, 2004.
- [28] M. M. Afonso, A. Celani, R. Festa, and A. Mazzino, “Large-eddy-simulation closures of passive scalar turbulence: a systematic approach,” *J. Fluid Mech.*, vol. 496, pp. 355–364, 2003.
- [29] J. Yin, B.-C. Wang, and D. J. Bergstrom, “Les of buoyant turbulent convection in a vertical slot based on a novel dynamic nonlinear subgrid-scale model,” in *Proc. 4th Int. Conf. Comput. Heat Mass Trans.*, (Paris-Cachan, France), pp. 51–56, 2005.
- [30] A. Yoshizawa, “A statistical theory of thermally-driven turbulent shear flows, with the derivation of a subgrid model,” *J. Phys. Soc. Japan*, vol. 52, pp. 1194–1205, 1983.
- [31] J. Bardina, J. H. Ferziger, and W. C. Reynolds, “Improved subgrid-scale models for large-eddy simulation,” in *Proc. AIAA 13th Fluid & Plasma Dynamics Conference*, (Snowmass, Colorado), 1980. AIAA Paper 80-1357.
- [32] A. Leonard, “Large-eddy simulation of chaotic convection and beyond,” in *AIAA Paper 97-0204*, (Reno, Nevada), 1997.
- [33] M. V. Salvetti and S. Banerjee, “*A priori* Tests of a new dynamic subgrid-scale model for finite-difference large-eddy simulations,” *Phys. Fluids*, vol. 7, pp. 2831–2847, 1995.
- [34] Y. Zang, R. L. Street, and J. R. Koseff, “A dynamic mixed subgrid-scale model and its application to turbulent recirculating flows,” *Phys. Fluids*, vol. 5, pp. 3186–3196, 1993.

- [35] M. Tyagi and S. Acharya, “Large eddy simulations of flow and heat transfer in rotating ribbed duct flows,” *ASME J. Heat Trans.*, vol. 127, pp. 486–498, 2005.
- [36] F. A. Jaber and P. J. Colucci, “Large eddy simulation of heat and mass transport in turbulent flows, part 2: scalar field,” *Int. J. Heat. Mass. Trans.*, vol. 46, pp. 1827–1840, 2003.
- [37] E. Porté-Agel, M. B. Parlange, C. Meneveau, and W. E. Eichinger, “A priori field study of the subgrid-scale heat fluxes and dissipation in the atmospheric surface layer,” *J. Atmos. Sci.*, vol. 58, pp. 2673–2698, 2001.
- [38] E. Porté-Agel, M. Pahlow, C. Meneveau, and M. B. Parlange, “Atmospheric stability effect on subgrid-scale physics for large-eddy simulation,” *Adv. Water Resources*, vol. 24, pp. 1085–1102, 2001.
- [39] H. S. Kang and C. Meneveau, “Universality of large eddy simulation model parameters across a turbulent wake behind a heated cylinder,” *J. Turb.*, vol. 3, pp. 1–27, 2002.
- [40] S.-H. Peng and L. Davidson, “On a subgrid-scale heat flux model for large eddy simulation of turbulent thermal flow,” *Int. J. Heat. Mass. Trans.*, vol. 45, pp. 1393–1405, 2002.
- [41] L. Shtilman, M. Spector, and A. Tsinober, “On some kinematic versus dynamic properties of homogeneous turbulence,” *J. Fluid Mech.*, vol. 247, pp. 65–77, 1993.
- [42] T. S. Lund and M. M. Rogers, “An improved measure of strain state probability in turbulent flows,” *Phys. Fluids*, vol. 6, pp. 1838–1847, 1994.
- [43] M. M. Rogers and P. Moin, “Helicity fluctuations in incompressible turbulent flows,” *Phys. Fluids*, vol. 30, pp. 2662–2671, 1987.

- [44] A. Tsinober, E. Kit, and T. Dracos, “Experimental investigation of the field of velocity gradients in turbulent flows,” *J. Fluid Mech.*, vol. 242, pp. 169–192, 1992.
- [45] A. Honkan and Y. Andreopoulos, “Vorticity, strain-rate and dissipation characteristics in the near-wall region of turbulent boundary layers,” *J. Fluid Mech.*, vol. 350, pp. 29–96, 1997.
- [46] P. Vieillefosse, “Internal motion of a small element of fluid in an inviscid flow,” *Physica A*, vol. 125, pp. 150–162, 1984.
- [47] R. B. Pelz, V. Yakhot, and S. A. Orszag, “Velocity-vorticity patterns in turbulent flows,” *Phys. Rev. Let.*, vol. 54, pp. 2505–2508, 1985.
- [48] W. T. Ashurst, A. R. Kerstein, R. M. Kerr, and C. H. Gibson, “Alignment of vorticity and scalar gradient with strain rate in simulated Navier-Stokes turbulence,” *Phys. Fluids*, vol. 30, pp. 2343–2353, 1987.
- [49] R. M. Kerr, “Histograms of helicity and strain in numerical turbulence,” *Phys. Rev. Let.*, vol. 59, pp. 783–786, 1987.
- [50] Z.-S. She, E. Jackson, and S. A. Orszag, “Structure and dynamics of homogeneous turbulence: Models and simulations,” *Proc. R. Soc. Lond. A*, vol. 434, pp. 101–124, 1991.
- [51] K. K. Nomura and G. K. Post, “The structure and dynamics of vorticity and rate of strain in incompressible homogeneous turbulence,” *J. Fluid Mech.*, vol. 377, pp. 65–97, 1998.
- [52] A. Tsinober, J. G. M. Eggels, and F. T. M. Nieuwstadt, “On alignments and small scale structure in turbulent pipe flow,” *Fluid Dyn. Res.*, vol. 16, pp. 297–310, 1995.

- [53] H. M. Blackburn, N. N. Mansour, and B. J. Cantwell, “Topology of fine-scale motions in turbulent channel flow,” *J. Fluid Mech.*, vol. 310, pp. 269–292, 1996.
- [54] B. Tao, J. Katz, and C. Meneveau, “Statistical geometry of subgrid-scale stresses determined from holographic particle image velocimetry measurements,” *J. Fluid Mech.*, vol. 457, pp. 35–78, 2002.
- [55] K. Horiuti, “Roles of non-aligned eigenvectors of strain-rate and subgrid-scale stress tensors in turbulence generation,” *J. Fluid Mech.*, vol. 491, pp. 65–100, 2003.
- [56] V. Borue and S. A. Orszag, “Local energy flux and subgrid-scale statistics in three-dimensional turbulence,” *J. Fluid Mech.*, vol. 366, pp. 1–31, 1998.
- [57] C. W. Higgins, M. B. Parlange, and C. Meneveau, “Alignment trends of velocity gradients and subgrid-scale fluxes in the turbulent atmospheric boundary layer,” *Boundary-Layer Meteorology*, vol. 109, pp. 59–83, 2003.
- [58] C. Fureby and F. F. Grinstein, “Large eddy simulation of high-reynolds-number free and wall-bounded flows,” *J. Comp. Phys.*, vol. 181, pp. 68–97, 2002.
- [59] B.-C. Wang, D. J. Bergstrom, J. Yin, and E. Yee, “Turbulence topologies predicted using large eddy simulation,” *J. Turb.*, vol. 7(3), pp. 1–28, 2006.
- [60] D. I. Pullin, “A vortex-based model for the subgrid flux of a passive scalar,” *Phys. Fluids*, vol. 12, pp. 2311–2319, 2000.
- [61] A. Misra and D. I. Pullin, “A vortex-based subgrid stress model for large-eddy simulation,” *Phys. Fluids*, vol. 9, pp. 2443–2454, 1997.
- [62] T. Voelkl, D. I. Pullin, and D. C. Chan, “A physical-space version of the stretched-vortex subgrid-stress model for large-eddy simulation,” *Phys. Fluids*, vol. 12, pp. 1810–1825, 2000.

- [63] K. K. Nomura and S. E. Elghobashi, “Mixing characteristics of an inhomogeneous scalar in isotropic and homogeneous sheared turbulence,” *Phys. Fluids A*, vol. 4, pp. 606–625, 1992.
- [64] J. Martín, C. Dopazo, and L. Valiño, “Joint statistics of the scalar gradient and the velocity gradient in turbulence using linear diffusion models,” *Phys. Fluids*, vol. 17, 2005. 028101.
- [65] O. N. Boratav, S. E. Elghobashi, and R. Zhong, “On the alignment of strain, vorticity and scalar gradient in turbulent, buoyant, nonpremixed flames,” *Phys. Fluids*, vol. 10, pp. 2260–2267, 1998.
- [66] C. W. Higgins, M. B. Parlange, and C. Meneveau, “The heat flux and the temperature gradient in the lower atmosphere,” *Geophysical Research Letters*, vol. 31, p. L22105, 2004.
- [67] J. Kim and P. Moin, “Application of a fractional-step method to incompressible Navier-Stokes equations,” *J. Comp. Phys.*, vol. 59, pp. 308–323, 1985.
- [68] S. B. Pope, *Turbulent Flows*. Cambridge, UK: Cambridge Univ., 2000.
- [69] C. Meneveau and J. Katz, “Scale-invariance and turbulence models for large-eddy simulation,” *Ann. Rev. Fluid Mech.*, vol. 32, pp. 1–32, 2000.
- [70] U. Piomelli, *Large-Eddy and Direct Simulation of Turbulent Flows, Lecture Notes for CFD2001*. Kitchener, Ontario, May 27-29 2001. The 9th Annual Conference of the CFD Society of Canada.
- [71] U. Piomelli, W. H. Cabot, P. Moin, and S. Lee, “Subgrid-scale backscatter in turbulent and transitional flows,” *Phys. Fluids A*, vol. 3, pp. 1766–1771, 1991.
- [72] S. Liu, C. Meneveau, and J. Katz, “On the properties of similarity subgrid-scale models as deduced from measurements in a turbulent jet,” *J. Fluid Mech.*, vol. 275, pp. 83–119, 1994.

- [73] U. Piomelli and J. Liu, “Large-eddy simulation of rotating channel flows using a localized dynamic model,” *Phys. Fluids*, vol. 7, pp. 839–848, 1995.
- [74] S. Liu, C. Meneveau, and J. Katz, “Experimental study of similarity subgrid-scale models of turbulence in the far-field of a jet,” *Appl. Sci. Res.*, vol. 54, pp. 177–190, 1995.
- [75] B. Vreman, B. Geurts, and H. Kuerten, “On the formulation of the dynamic mixed subgrid-scale model,” *Phys. Fluids*, vol. 6, pp. 4057–4059, 1994.
- [76] K. Horiuti, “A new dynamic two-parameter mixed model for large-eddy simulation,” *Phys. Fluids*, vol. 9, pp. 3443–3464, 1997.
- [77] R. A. Clark, J. H. Ferziger, and W. C. Reynolds, “Evaluation of subgrid-scale models using an accurately simulated turbulent flow,” *J. Fluid Mech.*, vol. 91, pp. 1–16, 1979.
- [78] J. L. Lumley, “Toward a turbulent constitutive relation,” *J. Fluid Mech.*, vol. 41, pp. 413–434, 1970.
- [79] S. B. Pope, “A more general effective-viscosity hypothesis,” *J. Fluid Mech.*, vol. 72, pp. 331–340, 1975.
- [80] P. Sagaut, *Large Eddy Simulation for Incompressible Flows: An Introduction*. Berlin: Springer, 2nd ed., 2002.
- [81] A. W. Cook, “Determination of the constant coefficient in scale similarity models of turbulence,” *Phys. Fluids*, vol. 9, pp. 1485–1487, 1997.
- [82] B. Vreman, B. Geurts, and H. Kuerten, “Large-eddy simulation of the turbulent mixing layer,” *J. Fluid Mech.*, vol. 339, pp. 357–390, 1997.
- [83] W. Cabot, “Large-eddy simulation of time-dependent and buoyancy-driven channel flow,” *Annu. Res. Briefs*, pp. 45–60, 1992.

- [84] V. C. Wong and D. K. Lilly, “A comparison of two dynamic subgrid closure methods for turbulent thermal convection,” *Phys. Fluids*, vol. 6, pp. 1016–1023, 1994.
- [85] A. K. and K. Suga, “Towards the development of a Reynolds-averaged algebraic turbulent scalar-flux model,” *Int. J. Heat Fluid Flow*, vol. 22, pp. 19–29, 2001.
- [86] U. Piomelli, “Large-eddy simulation: achievements and challenges,” *Progress in Aerospace Sciences*, vol. 35, pp. 335–362, 1999.
- [87] C. Jiménez, L. Valiño, and C. Dopazo, “*A priori* and *a posteriori* test of subgrid scale models for scalar transport,” *Phys. Fluids*, vol. 13, pp. 2433–2436, 2001.
- [88] A. J. Chorin, “Numerical solution of the Navier-Stokes equations,” *Math. Comp.*, vol. 22, pp. 745–762, 1968.
- [89] J. H. Ferziger and P. M., *Computational Methods for Fluid Dynamics*. Berlin: Springer, 2nd ed., 1999.
- [90] W. Hackbusch, *Multi-Grid Methods and Applications*. Berlin: Springer-Verlag, 1985.
- [91] A. Brandt, *Multigrid Techniques: 1984 Guide With Applications to Fluid Dynamics, von Karman Institute, Lecture Series 1984-04*, 1984.
- [92] U. Stüben, K. and Trottenberg, *Multigrid Methods, Lecture Notes in Mathematics*, vol. 960. Berlin: Springer-Verlag, 1982.
- [93] B. R. Hutchinson, P. F. Galpin, and G. D. Raithby, “Application of additive correction multigrid to the coupled fluid flow equations,” *Numer. Heat Trans.*, vol. 13, pp. 133–147, 1988.
- [94] P. S. Sathiyamurthy and S. V. Patankar, “Block-correction-based multigrid method for fluid flow problem,” *Numer. Heat Trans.: Part B*, vol. 25, pp. 375–394, 1994.

- [95] A. Brandt, J. E. Dendy, and H. Ruppel, “The multigrid method for semi-implicit hydrodynamics codes,” *J. Comp. Phys.*, vol. 34, pp. 348–370, 1980.
- [96] Y. Morinishi, T. S. Lund, O. V. Vasilyev, and P. Moin, “Fully conservative higher order finite difference schemes for incompressible flow,” *J. Comp. Phys.*, vol. 143, pp. 90–124, 1998.
- [97] O. V. Vasilyev, “Higher order finite difference schemes on non-uniform meshes with good conservation properties,” *J. Comp. Phys.*, vol. 157, pp. 746–761, 2000.
- [98] F. Ham, F. S. Lien, and A. Strong, “A new method direct numerical simulation that discretely conserves mass, momentum, and kinetic energy, turbulence and shear flow phenomena,” *Turbulence and shear flow phenomena*, vol. 2, pp. 365–370, 2001.
- [99] R. Verstappen and A. Veldman, “Spectro-consistent discretization of navier-stokes: a challenge to rans and les,” *J. Eng. Math.*, vol. 34, pp. 163–104, 1998.
- [100] R. Verstappen and A. Veldman, “Symmetry-preserving discretization of turbulent flow,” *J. Comp. Phys.*, vol. 187, pp. 343–368, 2003.
- [101] U. Ghia, K. Ghia, and C. Shin, “High-re solutions for incompressible flow using the navier-stokes equations and a multigrid method,” *J. Comp. Phys.*, vol. 48, pp. 387–411, 1982.
- [102] H. C. Ku, R. Hirsh, and T. Taylor, “A pseudospectral method for solution of the three-dimensional incompressible navier-stokes equations,” *J. Comp. Phys.*, vol. 70, pp. 439–426, 1987.
- [103] G. B. Deng, J. Piquet, P. Queutey, and M. Visonneau, “Incompressible flow calculations with a consistent physical interpolation finite volume approach,” *Comput. Fluids*, vol. 23, pp. 1029–1047, 1994.

- [104] V. Babu and S. Korpela, “Numerical study of three-dimensional navier-stokes equations,” *Comput. Fluids*, vol. 23, pp. 675–691, 1994.
- [105] X. Huang, *Volume Average Technique for Turbulent Flow Simulation and Its Application to Room Airflow Prediction*. PhD thesis, Univ. of Saskatchewan, 1998.
- [106] J.-L. Guermond, C. Migeon, G. Pineau, and L. Quartapelle, “Start-up flows in a three-dimensional rectangular driven cavity of aspect ratio 1:1:2 at $re = 1000$,” *J. Fluid Mech.*, vol. 450, pp. 169–199, 2002.
- [107] P. Moin and J. Kim, “Numerical investigation of turbulence channel flow,” *J. Fluid Mech.*, vol. 118, pp. 341–377, 1982.
- [108] J. Kim, P. Moin, and R. Moser, “Turbulence statistics in fully developed channel flow at low Reynolds number,” *J. Fluid Mech.*, vol. 177, pp. 133–166, 1987.
- [109] R. D. Moser, J. Kim, and N. N. Mansour, “Direct numerical simulation of turbulent channel flow up to $re_\tau = 590$,” *Phys. Fluids*, vol. 11, pp. 943–945, 1999.
- [110] S. Lyons, T. Hanratty, and J. McLaughlin, “Large-scale computer simulation of fully-developed turbulent channel flow with heat transfer,” *Int. J. Numer. Meth. Fluids*, vol. 13, pp. 999–1028, 1991.
- [111] J. Rutledge and C. Sleicher, “Direct simulation of turbulent flow and heat transfer in a channel. part i: Smooth walls,” *Int. J. Numer. Meth. Fluids*, vol. 16, pp. 1051–1078, 1993.
- [112] N. Kasagi, Y. Tomita, and A. Kuroda, “Direct numerical simulation of passive scalar field in a turbulent channel flow,” *ASME J. Heat Trans.*, vol. 114, pp. 598–606, 1992.

- [113] J. Smagorinsky and S. Manabe, “Numerical model for study of global general circulation,” *Bull. Amer. Meteorol. Soc.*, vol. 43, pp. 673–673, 1962.
- [114] J. W. Deardorff, “A numerical study of three-dimensional turbulent channel flow at large Reynolds numbers,” *J. Fluid Mech.*, vol. 41, pp. 453–480, 1970.
- [115] U. Schumann, “New subgrid scale motion model for numerical simulation of turbulent flows,” *Bull. Amer. Phys. Soc.*, vol. 18, pp. 1469–1469, 1973.
- [116] U. Schumann, “Subgrid scale model for finite difference simulations of turbulent flows in plane channels and annuli,” *J. Comp. Phys.*, vol. 18, pp. 376–404, 1975.
- [117] P. Moin, W. Reynolds, and J. Ferziger, “Large eddy simulation of incompressible turbulent channel flow,” *Dept Mech. Engng, Stanford Univ., Rep. TF-12*, 1978.
- [118] J. Kim, P. Moin, and R. Moser, “Turbulence statistics in fully developed channel flow at low Reynolds number,” *J. Fluid Mech.*, vol. 177, pp. 133–166, 1987.
- [119] R. Betchov, “An inequality concerning the production of vorticity in isotropic turbulence,” *J. Fluid Mech.*, vol. 1, pp. 497–504, 1956.
- [120] J. Soria, R. Sondergaard, B. J. Cantwell, M. S. Chong, and A. E. Perry, “A study of the fine-scale motions of incompressible time-developing mixing layers,” *Phys. Fluids*, vol. 6, pp. 871–884, 1994.
- [121] H. Tennekes and J. L. Lumley, *A First Course in Turbulence*. Cambridge, MA: MIT, 1972.
- [122] G. I. Taylor, “Production and dissipation of vorticity in a turbulent fluid,” *Proc. R. Soc. Lond. A*, vol. 164, pp. 15–23, 1938.
- [123] G. R. Ruetsch and M. R. Maxey, “Small-scale features of vorticity and passive scalar fields in homogeneous isotropic turbulence,” *Phys. Fluids A*, vol. 3, pp. 1587–1597, 1991.

- [124] B. Andreotti, “Studying Burgers’ models to investigate the physical meaning of the alignments statistically observed in turbulence,” *Phys. Fluids*, vol. 9, pp. 735–742, 1997.
- [125] A. Tsinober, L. Shtilman, and H. Vaisburd, “A study of properties of vortex stretching and enstrophy generation in numerical and laboratory turbulence,” *Fluid Dyn. Res.*, vol. 21, pp. 477–494, 1997.
- [126] R. B. Pelz, L. Shtilman, and A. Tsinober, “The helical nature of unforced turbulent flows,” *Phys. Fluids*, vol. 29, pp. 3506–3508, 1986.
- [127] M. Lesieur, *Turbulence in Fluids*. Dordrecht: Kluwer Academic, 2nd ed., 1990.
- [128] J. C. André and M. Lesieur, “Influence of helicity on the evolution of isotropic turbulence at high Reynolds number,” *J. Fluid Mech.*, vol. 81, pp. 187–207, 1977.
- [129] J. O’Neil and C. Meneveau, “Subgrid-scale stresses and their modelling in a turbulent plane wake,” *J. Fluid Mech.*, vol. 349, pp. 253–293, 1997.
- [130] K. Horiuti, “The role of the Bardina model in large eddy simulation of turbulent channel flow,” *Phys. Fluids A*, vol. 1, pp. 426–428, 1989.
- [131] U. Piomelli, Y. Yu, and R. J. Adrian, “Subgrid-scale energy transfer and near-wall turbulence structure,” *Phys. Fluids*, vol. 8, pp. 215–224, 1996.
- [132] G.-H. Cottet and O. V. Vasilyev, “Comparison of dynamic Smagorinsky and anisotropic subgrid-scale models,” in *Proc. of the Summer Program 1998, Center for Turbulence Research*, 1998.
- [133] B. Tao, J. Katz, and C. Meneveau, “Geometry and scale relationships in high Reynolds number turbulence determined from three-dimensional holographic velocimetry,” *Phys. Fluids*, vol. 12, pp. 941–944, 2000.

- [134] B. Tao, J. Katz, and C. Meneveau, “Alignment of the strain-rate, SGS stress, and SGS force relative to parameters based on the filtered velocity gradients,” in *Proc. ASME FEDSM’01, ASME 2001 Fluids Engineering Division Summer Meeting*, (New Orleans, Louisiana), 2001.
- [135] W. A. Rosenkrantz, *Introduction to Probability and Statistics for Scientists and Engineers*. New York, NY: McGraw-Hill, 1997.
- [136] B. Metais and E. R. G. Eckert, “Forced, mixed and free convection regimes,” *ASME J. Heat Trans.*, vol. 86, pp. 295–296, 1964.
- [137] J. P. Easby, “The effect of buoyancy on flow and heat transfer for a gas passing down a vertical pipe at low turbulent Reynolds numbers,” *Int. J. Heat. Mass. Trans.*, vol. 21, pp. 791–801, 1978.
- [138] M. Nakajima, K. Fukui, H. Ueda, and T. Mizushima, “Buoyancy effects on turbulent transport in combined free and forced convection between vertical parallel plates,” *Int. J. Heat. Mass. Trans.*, vol. 23, pp. 1325–1336, 1980.
- [139] A. M. Abdelmeguid and D. B. Spalding, “Turbulent flow and heat transfer in pipes with buoyancy effects,” *J. Fluid Mech.*, vol. 94, pp. 383–400, 1979.
- [140] H. Tanaka, S. Maruyama, and S. Hatano, “Combined forced and natural convection heat transfer for upward flow in a uniformly heated vertical pipe,” *Int. J. Heat. Mass. Trans.*, vol. 30, pp. 165–174, 1987.
- [141] N. Kasagi and M. Nishimura, “Direct numerical simulation of combined forced and natural turbulent convection in a vertical plane channel,” *Int. J. Heat Fluid Flow*, vol. 18, pp. 88–99, 1997.
- [142] J. D. Jackson, M. A. Cotton, and B. P. Axcell, “Studies of mixed convection in vertical tubes,” *Int. J. Heat Fluid Flow*, vol. 10, pp. 2–15, 1989.

- [143] J. S. Lee, X. Xu, and R. H. Pletcher, “Large eddy simulation of heated vertical annular pipe flow in fully developed turbulent mixed convection,” *Int. J. Heat. Mass. Trans.*, vol. 47, pp. 437–446, 2004.
- [144] W. Zhang and Q. Chen, “Large eddy simulation of natural and mixed convection air flow indoors with two simple filtered dynamic subgrid scale models,” *Numer. Heat Trans.: Part A*, vol. 37, pp. 447–463, 2000.
- [145] Z. H. Yan, “A numerical study of effect of initial condition on large eddy simulation of thermal plume,” *Numer. Heat Trans.: Part B*, vol. 43, pp. 167–178, 2003.
- [146] A. Kuroda, N. Kasagi, and M. Hirata, “Direct numerical simulation of turbulent plane couette-poiseuille flows: effect of mean shear rate on the near-wall turbulence structures,” in *Proc. Turbul. Shear Flows 9* (F. Durst, N. Kasagi, B. E. Launder, F. W. Schmidt, K. Suzuki, and e. Whitelaw, J. H., eds.), (Berlin: Springer-Verlag), pp. 241–257, 1995.
- [147] P. Sagaut and R. Grohens, “Discrete filters for large eddy simulation,” *Int. J. Numer. Meth. Fluids*, vol. 31, pp. 1195–1220, 1999.
- [148] Y. Na and T. J. Hanratty, “Limiting behavior of turbulent scalar transport close to a wall,” *Int. J. Heat. Mass. Trans.*, vol. 43, pp. 1749–1758, 2000.
- [149] A. A. Townsend, “On the fine-scale structure of turbulence,” *Proc. R. Soc. Lond. A*, vol. 208, pp. 534–542, 1951.
- [150] M. S. Chong, J. Soria, A. E. Perry, J. Chacin, B. J. Cantwell, and Y. Na, “Turbulence structures of wall-bounded shear flows found using DNS data,” *J. Fluid Mech.*, vol. 357, pp. 225–247, 1998.
- [151] B. J. Cantwell, “Exact solution of a restricted Euler equation for the velocity gradient tensor,” *Phys. Fluids A*, vol. 4, pp. 782–793, 1992.

- [152] E. Dresselhaus and M. Tabor, “The kinematics of stretching and alignment of material elements in general flow fields,” *J. Fluid Mech.*, vol. 236, pp. 415–444, 1991.
- [153] A. Vincent and M. Meneguzzi, “The dynamics of vorticity tubes in homogeneous turbulence,” *J. Fluid Mech.*, vol. 258, pp. 245–254, 1994.
- [154] K. K. Nomura and P. J. Diamessis, “The interaction of vorticity and rate-of-strain in homogeneous sheared turbulence,” *Phys. Fluids*, vol. 12, pp. 846–864, 2000.
- [155] P. J. Diamessis and K. K. Nomura, “Interaction of vorticity, rate-of-strain, and scalar gradient in stratified homogeneous sheared turbulence,” *Phys. Fluids*, vol. 12, pp. 1166–1188, 2000.
- [156] J. Yin, B.-C. Wang, and D. J. Bergstrom, “Local statistical geometry of the resolved-scale velocity and temperature gradient fields in a vertical slot flow,” *Flow Turbulence and Combustion*, 2007. accepted.
- [157] A. Tsinober and B. Galanti, “Exploratory numerical experiments on the differences between genuine and ‘passive’ turbulence,” *Phys. Fluids*, vol. 15, pp. 3514–3531, 2003.
- [158] A. Garcia and M. Gonzalez, “Analysis of passive scalar gradient alignment in a simplified three-dimensional case,” *Phys. Fluids*, vol. 18, 2006. 058101.
- [159] A. E. Perry and M. S. Chong, “A description of eddying motions and flow patterns using critical-point concepts,” *Ann. Rev. Fluid Mech.*, vol. 19, pp. 125–155, 1987.
- [160] M. S. Chong, A. E. Perry, and B. J. Cantwell, “A general classification of three-dimensional flow fields,” *Phys. Fluids A*, vol. 2, pp. 765–777, 1990.

- [161] B. J. Cantwell, “On the behavior of velocity gradient tensor invariants in direct numerical simulations of turbulence,” *Phys. Fluids A*, vol. 5, pp. 2008–2013, 1993.
- [162] H. Pitsch, “Large-eddy simulation of turbulent combustion,” *Ann. Rev. Fluid Mech.*, vol. 38, pp. 453–482, 2006.